



**HAL**  
open science

# Crystallization of mixed clathrate hydrates under equilibrium and non-equilibrium conditions: PVTx measurements and thermodynamic modeling

Saheb Maghsoodloobabakhani

► **To cite this version:**

Saheb Maghsoodloobabakhani. Crystallization of mixed clathrate hydrates under equilibrium and non-equilibrium conditions: PVTx measurements and thermodynamic modeling. Other. Université de Lyon, 2018. English. NNT : 2018LYSEM027 . tel-02885353

**HAL Id: tel-02885353**

**<https://theses.hal.science/tel-02885353>**

Submitted on 30 Jun 2020

**HAL** is a multi-disciplinary open access archive for the deposit and dissemination of scientific research documents, whether they are published or not. The documents may come from teaching and research institutions in France or abroad, or from public or private research centers.

L'archive ouverte pluridisciplinaire **HAL**, est destinée au dépôt et à la diffusion de documents scientifiques de niveau recherche, publiés ou non, émanant des établissements d'enseignement et de recherche français ou étrangers, des laboratoires publics ou privés.



N°d'ordre NNT : 2018LYSEM027

**THESE de DOCTORAT DE L'UNIVERSITE DE LYON**  
opérée au sein de  
**l'École des Mines de Saint-Etienne**

**Ecole Doctorale N° 488**  
**Sciences, Ingénierie, Santé**

**Spécialité de doctorat** : Génie des Procédés  
**Discipline** : DS8 Sciences pour l'ingénieur

Soutenue prévue le 14/12/2018, par :  
**Saheb Maghsoodloo Babakhani**

---

**Cristallisation à l'équilibre et hors équilibre d'hydrates mixtes de gaz : Mesures PVTx et modélisation thermodynamique**

**Crystallization of mixed clathrate hydrates under equilibrium and non-equilibrium conditions: PVTx measurements and thermodynamic modeling**

---

Devant le jury composé de :

Christelle Miqueu	Maître de Conférences HDR, Université De Pau Et Des Pays De L'adour, France	Présidente
Karine Ballerat-Busserolles	Ingénieure de Recherche - CNRS, Institut de Chimie de Clermont-Ferrand, France. Chercheure Associée - Mines ParisTech, France	Rapporteure
Nicolas von Solms	Associate professor, Technical University of Denmark, Denmark	Rapporteur
Bertrand Chazallon	Professeur, Université de Lille 1, France	Examineur
Jean-Michel HERRI	Professeur, École Nationale Supérieure des Mines de Saint-Étienne, Saint-Étienne, France	Directeur de thèse
Baptiste Bouillot	Maître de Conférences, École Nationale Supérieure des Mines de Saint-Étienne, Saint-Étienne, France	Co-Directeur de thèse
Arnaud Desmedt	Chercheur CNRS - Université Bordeaux 1, France	Invité

**Spécialités doctorales**  
 SCIENCES ET GENIE DES MATERIAUX  
 MECANIQUE ET INGENIERIE  
 GENIE DES PROCÉDES  
 SCIENCES DE LA TERRE  
 SCIENCES ET GENIE DE L'ENVIRONNEMENT

**Responsables :**  
 K. Wolki Directeur de recherche  
 S. Drapier, professeur  
 F. Gruy, Maître de recherche  
 B. Guy, Directeur de recherche  
 D. Graillot, Directeur de recherche

**Spécialités doctorales**  
 MATHEMATIQUES APPLIQUEES  
 INFORMATIQUE  
 SCIENCES DES IMAGES ET DES FORMES  
 GENIE INDUSTRIEL  
 MICROELECTRONIQUE

**Responsables**  
 O. Roustant, Maître-assistant  
 O. Foissier, Professeur  
 J.C. Pinoli, Professeur  
 X. Delorme, Maître assistant  
 Ph. Lalevée, Professeur

**EMSE : Enseignants-chercheurs et chercheurs autorisés à diriger des thèses de doctorat (titulaires d'un doctorat d'Etat ou d'une HDR)**

ARSI	Nabil	CR	Génie industriel	CMP
AUGUSTO	Vincent	CR	Image, Vision, Signal	CIS
AVRIL	Stéphane	PR2	Mécanique et ingénierie	CIS
BADEL	Pierre	MA(MDC)	Mécanique et ingénierie	CIS
BALBO	Flavien	PR2	Informatique	FAYOL
BASSEREAU	Jean-François	PR	Sciences et génie des matériaux	SMS
BATTON-HUBERT	Mireille	PR2	Sciences et génie de l'environnement	FAYOL
BEGBEDER	Michel	MA(MDC)	Informatique	FAYOL
BLAYAC	Sylvain	MA(MDC)	Microélectronique	CMP
BOISSIER	Olivier	PR1	Informatique	FAYOL
BONNEFOY	Olivier	MA(MDC)	Génie des Procédés	SPIN
BORBELY	Andras	M(R)(DR2)	Sciences et génie des matériaux	SMS
BOUCHER	Xavier	PR2	Génie Industriel	FAYOL
BRODHAG	Christian	DR	Sciences et génie de l'environnement	FAYOL
BRUCHON	Julien	MA(MDC)	Mécanique et ingénierie	SMS
CAMERAO	Ara	MA(MDC)	Génie des Procédés	SPIN
CHRISTIAN	Frédéric	PR	Science et génie des matériaux	SMS
DAUZERE-PERES	Stéphane	PR1	Génie Industriel	CMP
DEBAYLE	John	MR	Sciences des Images et des Formes	SPIN
DEGEORGE	Jean-Michel	MA(MDC)	Génie industriel	Fayol
DELAFOISSE	David	PR0	Sciences et génie des matériaux	SMS
DELORME	Xavier	MA(MDC)	Génie industriel	FAYOL
DESRAYAUD	Christophe	PR1	Mécanique et ingénierie	SMS
DJENIZIAN	Thierry	PR	Science et génie des matériaux	CMP
DOUCE	Sandrine	PR2	Sciences de gestion	FAYOL
DRAPIER	Sylvain	PR1	Mécanique et ingénierie	SMS
FAUCHEU	Jenny	MA(MDC)	Sciences et génie des matériaux	SMS
FAVERGON	Loté	CR	Génie des Procédés	SPIN
FEILLET	Dominique	PR1	Génie Industriel	CMP
FOREST	Valérie	MA(MDC)	Génie des Procédés	CIS
FRACZKIEWICZ	Ara	DR	Sciences et génie des matériaux	SMS
GARCIA	Daniel	M(R)(DR2)	Sciences de la Terre	SPIN
GAVET	Yann	MA(MDC)	Sciences des Images et des Formes	SPIN
GERINGER	Juan	MA(MDC)	Sciences et génie des matériaux	CIS
GOEURBOT	Dominique	DR	Sciences et génie des matériaux	SMS
GONDRAN	Natasha	MA(MDC)	Sciences et génie de l'environnement	FAYOL
GONZALEZ FELIU	Josua	MA(MDC)	Sciences économiques	FAYOL
GRAILLOT	Didier	DR	Sciences et génie de l'environnement	SPIN
GROSSEAU	Philippe	DR	Génie des Procédés	SPIN
GRUY	Frédéric	PR1	Génie des Procédés	SPIN
GUY	Bernard	DR	Sciences de la Terre	SPIN
HAN	Woo-Suck	MR	Mécanique et ingénierie	SMS
HERRI	Jean Michel	PR1	Génie des Procédés	SPIN
KERMOUCHE	Ouillatne	PR2	Mécanique et Ingénierie	SMS
KLOCKER	Helmut	DR	Sciences et génie des matériaux	SMS
LAFORÉST	Valérie	M(R)(DR2)	Sciences et génie de l'environnement	FAYOL
LERICHE	Rodolphe	CR	Mécanique et ingénierie	FAYOL
MALLIARAS	Georges	PR1	Microélectronique	CMP
MOLMARD	Jérôme	PR2	Mécanique et ingénierie	CIS
MOUTTE	Jacques	CR	Génie des Procédés	SPIN
NEUBERT	Gilles			FAYOL
NIKOLOVSKI	Jean-Pierre	Ingénieur de recherche	Mécanique et ingénierie	CMP
NORTIER	Patrice	PR1	Génie des Procédés	SPIN
O'CONNOR	Rodney Philip	MA(MDC)	Microélectronique	CMP
OWENS	Rosin	MA(MDC)	Microélectronique	CMP
PERES	Véronique	MR	Génie des Procédés	SPIN
PICARD	Gauthier	MA(MDC)	Informatique	FAYOL
PUOLAT	Christophe	PR0	Génie des Procédés	SPIN
PENOLI	Jean Charles	PR0	Sciences des Images et des Formes	SPIN
POURCHEZ	Jérémy	MR	Génie des Procédés	CIS
ROUSSY	Agnes	MA(MDC)	Microélectronique	CMP
ROUSTANT	Olivier	MA(MDC)	Mathématiques appliquées	FAYOL
SANAUR	Sébastien	MA(MDC)	Microélectronique	CMP
STOLAREZ	Jacques	CR	Sciences et génie des matériaux	SMS
TRIA	Assia	Ingénieur de recherche	Microélectronique	CMP
VALDIVIESO	François	PR2	Sciences et génie des matériaux	SMS
VIRICELLE	Jean Paul	DR	Génie des Procédés	SPIN
WOLSKI	Krzysztof	DR	Sciences et génie des matériaux	SMS
XIE	Xiaolan	PR0	Génie industriel	CIS
YUOMA	Gulian	CR	Génie industriel	CMP

## Remerciements

« La pierre n'a point d'espoir d'être autre chose qu'une pierre. Mais, de collaborer, elle s'assemble et devient temple. »

Antoine de St Exupéry

C'est avec une certaine émotion et beaucoup de sincérité que je voudrais remercier toutes les personnes ayant soutenu et apprécié mon travail.

Je remercie tout particulièrement Jean-Michel Herri, Baptiste Bouillot et Ana Cameirao pour m'avoir accepté et accueilli dans leur équipe, « GasHyDyn » à l'Ecole des Mines de Saint-Etienne. Ils m'ont encadré tout au long de cette thèse avec leur gentillesse, leur disponibilité permanente, leurs nombreux encouragements, leurs implications et suggestions scientifiques constructives.

Je tiens à remercier les membres du jury de ma thèse, Karine Ballerat-Busserolles, Nicolas von Solms, Christelle Miqueu, Bertrand Chazallon et Arnaud Desmedt pour avoir accepté de participer à ce jury de thèse et pour leurs commentaires constructifs qui m'ont permis d'améliorer mon rapport. Je remercie chaleureusement Arnaud Desmedt de l'Institut des Sciences Moléculaires-Université Bordeaux de m'avoir accueilli dans son laboratoire pour effectuer des mesures en bénéficiant de son expertise et de ses précieux conseils. J'adresse également mes remerciements à Georg Janicki, Baerbel Egenolf-Jonkmanns et Fabienne Knappitsch de l'institut Fraunhofer (UMSICHT, Allemagne) pour m'avoir accueilli durant un mois au sein de leur laboratoire et pour la qualité de leur collaboration et leur aide précieuse.

J'adresse mes remerciements à Fabien Chauvy pour son aide technique et également Maxime Minot, Son Ho-Van, Kien Pham Trung, Richard Drogo, Marc Rouvière et Hubert Faure pour leur aide et les bons moments passés. Je tiens à remercier particulièrement Michèle et Christophe Pijolat qui m'ont accompagné tout au long de ces trois années, pour toutes nos discussions et leurs conseils. Je remercie également Christopher Yukna pour son aide lors de la relecture de mes articles. Je désire en outre remercier tous les membres du personnel du Centre SPIN pour leur aide et leur bonne humeur. Je remercie enfin l'Ecole des Mines de Saint-Etienne pour m'avoir accepté et avoir financé cette thèse.

Mention spéciale à Jérôme Douzet qui m'a aidé, conseillé et supporté scientifiquement et personnellement tout au long de ces trois années de thèse. Je voudrais te dire merci pour ta gentillesse, ta générosité, ton honnêteté, ta modestie. Grâce à toi, ta patience et ta bonne humeur, j'ai appris le français et je l'améliore de jour en jour.

J'adresse toute mon affection et ma gratitude à ma famille pour m'avoir soutenu dans mes efforts. Malgré mon éloignement depuis longtemps, leur confiance et leur tendresse me portent et me guident tous les jours.



Enfin, je voudrais remercier vivement et sincèrement ma femme, Gita. Merci pour ta tendresse, ta confiance, ta bonne humeur et ta grande patience. Je t'exprime ici mes remerciements pour ton soutien et tes encouragements constants durant les moments difficiles. Je voudrais te dire merci pour ton amour et ton affection. Je t'adresse toute ma gratitude du fond du cœur.

NNT : 2018LYSEM027

Saheb Maghsoodloo Babakhani

Crystallization of mixed clathrate hydrates under equilibrium and non-equilibrium conditions: PVTx measurements and thermodynamic modeling

Speciality : Chemical Engineering

Keywords : clathrate hydrates, phase equilibria, crystallization, non-equilibrium thermodynamics, Raman spectroscopy, flash calculation.

## Abstract

In this work, in order to investigate the non-equilibrium behaviors of mixed clathrate hydrates, vapor-liquid-hydrate phase equilibria of mixed gas hydrates from  $\text{CH}_4\text{-C}_2\text{H}_6\text{-C}_3\text{H}_8\text{-nC}_4\text{H}_{10}\text{-CO}_2\text{-N}_2$  are studied. Two different experimental procedures are used: at quick and slow crystallization rates. The aim is to examine the effects of crystallization rate on the final state, either under usual dynamic (quick formation) or steady state conditions (slow formation).

Unlike most of the literature data, providing temperature-pressure-vapor composition (PTy) results, this study also furnishes hydrate composition, volume, storage capacity, density, or hydration number and water conversion. At quick crystallization, hydrate volume increases from 2% to 69% according to the gas mixture. Moreover, storage capacity decreases with increasing rate of crystallization. In addition, a thermodynamic model, based on classical van der Waals and Platteuw method and Kihara potential, has been used. A new set of Kihara parameters for propane, based on slow crystallization, has been obtained successfully and compared to the literature.

Besides, a review on guest composition in hydrates from experimental results is suggested, based on open literature. Then, the capability of thermodynamic modeling to simulate these rare data has been investigated. While simulation tools are interesting to predict phase equilibria for light molecules, they become less reliable when phase transition occurs in the system, or when heavier molecules are involved. In addition, the use of RAMAN spectroscopy has illustrated phase transition for  $\text{CO}_2/\text{C}_3\text{H}_8$  mixed hydrates under  $\text{CO}_2$  rich gas conditions.

To conclude, the rate of crystallization significantly influences the process of mixed hydrates formation. The use of a thermodynamic flash shows that slow crystallization is necessary to satisfy the thermodynamic equilibrium, and thus increase storage capacity, and optimize hydrate processes.

NNT : 2018LYSEM027

Saheb Maghsoodloo Babakhani

Cristallisation à l'équilibre et hors équilibre d'hydrates mixtes de gaz : Mesures PVTx et modélisation thermodynamique

Spécialité: Génie des Procédés

Mots clefs : clathrate hydrates, cristallisation, équilibre de phases, thermodynamique hors équilibre, spectroscopie Raman, calculs flash.

## Résumé

Dans ce travail, afin d'étudier la formation à l'équilibre et hors équilibre des hydrates mixtes de gaz, deux procédures de formation, rapide et lente, ont été appliquées à des mélanges de  $\text{CH}_4\text{-C}_2\text{H}_6\text{-C}_3\text{H}_8\text{-nC}_4\text{H}_{10}\text{-CO}_2\text{-N}_2$ . L'objectif de ces deux procédures est d'examiner les effets cinétiques de la vitesse de cristallisation sur l'état final, soit dans des conditions dynamiques habituelles (formation rapide) soit en régime permanent (formation lente). Contrairement à la plupart des données de la littérature, qui fournissent uniquement des données de température-pression-composition gaz (PTy), cette étude fournit également la composition, le volume, la capacité de stockage, la densité de la phase hydrate, ou encore le nombre d'hydratation et la conversion d'eau. Les résultats montrent que, lors d'une cristallisation rapide, le volume d'hydrate augmente de 2% à 69% selon le mélange gazeux. De plus, la capacité de stockage diminue avec l'augmentation de la vitesse de cristallisation. En outre, un modèle thermodynamique, basé sur la méthode classique de van der Waals et Platteuw avec le potentiel de Kihara, a été utilisé. Un nouvel ensemble de paramètres Kihara pour le propane, basé sur une cristallisation lente, a été obtenu avec succès et comparé à la littérature. Les données sur la phase hydrates étant rares dans la littérature, ces dernières ont été collectées, et comparées au modèle thermodynamique précédent. Cela permet de mettre en évidence la capacité de la simulation à prédire la composition de la phase hydrate. Bien que ces outils soient intéressants pour prédire les équilibres de phase des molécules légères, ils deviennent moins fiables lorsque des transitions de phase se produisent (coexistence de structures) ou lorsque des molécules plus lourdes sont impliquées. Une analyse par spectroscopie RAMAN a d'ailleurs mis en évidence la coexistence de structures I et II pour un gaz riche en  $\text{CO}_2$  à partir d'un mélange  $\text{CO}_2/\text{C}_3\text{H}_8$ .

Pour conclure, la vitesse de cristallisation influence significativement le procédé de formation d'un hydrate mixte. L'utilisation d'un flash thermodynamique, combinant thermodynamique et bilan de masse, montre bien qu'une cristallisation lente est nécessaire pour satisfaire l'équilibre thermodynamique, et donc augmenter la capacité de stockage, et optimiser les procédés hydrate.

***à ma femme, Gita***

***et à ma famille :***

***Ali, Safieh, Sareh, Morteza, Safa, Sahar, Sepehr, Sahel***



# List of contents

Remerciements .....	3
Abstract .....	5
Résumé .....	6
List of contents .....	9
List of figures .....	12
List of tables .....	15
General introduction.....	17
1. Introduction .....	19
1.1. Definition of gas hydrate.....	19
1.2. Molecular structures and properties .....	19
1.3. Gas hydrates, an issue in oil and gas industry .....	21
1.4. Natural gas hydrates deposits, an unconventional energy resource .....	22
1.5. Potential applications of gas hydrates .....	23
2. State of the art.....	27
2.1. Background of phase equilibria of gas hydrates.....	27
2.1.1. Hydrates of pure components .....	30
2.1.2. Multicomponent clathrate hydrates .....	35
2.2. Modeling of gas hydrates phase equilibria .....	37
2.2.1. Gas-gravity charts.....	37
2.2.2. K-value method .....	39
2.2.3. Empirical correlations .....	39
2.2.4. Neural network approaches .....	40
2.2.5. van der Waals and Platteeuw approach .....	43
2.2.5.1. Liquid phase .....	43
2.2.5.2. Hydrate phase .....	45
2.2.5.3. Kihara potential .....	47
2.2.5.4. Simulation procedures .....	48
2.2.5.5. Kihara parameters determination by GasHyDyn.....	50
2.2.5.6. Comments on the modeling.....	52
2.3. Non-equilibrium crystallization of mixed gas hydrates; experimental clues and modeling evidence .....	52
2.4. Motivations and objectives.....	54

3. Capability of thermodynamic modeling to simulate hydrate composition.....	55
3.1. Introduction .....	55
3.2. Methods to measure hydrate composition .....	55
3.2.1. Dissociation of whole hydrate phase .....	56
3.2.2. Material balance and volumetric properties evaluated from equation of state .....	62
3.2.3. Gas uptake at isobaric equilibrium condition .....	69
3.2.4. Using a tracer and mass balance.....	73
3.2.5. Microscopic measurements tools .....	82
3.2.6. Issues of hydrate composition calculation from cage occupancy.....	88
3.3. Conclusion.....	89
4. Experimental description.....	91
4.1. Materials.....	91
4.2. Apparatus.....	92
4.3. Gas chromatography.....	93
4.4. Ion Chromatography.....	98
4.5. Experimental procedures .....	100
4.5.1. Quick crystallization process.....	100
4.5.2. Slow crystallization process .....	101
4.6. Mass balance and hydrate phase properties calculation .....	102
4.6.1. Liquid phase .....	103
4.6.2. Gas phase.....	104
4.6.3. Hydrate phase .....	105
4.6.4. Hydrate phase properties .....	106
4.7. Experimental and instrumental uncertainties and assumptions.....	107
5. Experimental results and modeling .....	109
5.1. Initial conditions.....	109
5.2. Pressure and temperature evolution during the quick crystallization .....	110
5.3. Pressure and temperature evolution during the slow crystallization .....	111
5.4. Experimental results .....	112
5.4.1. New phase equilibrium data .....	112
5.4.2. Hydrate phase properties results.....	122
5.5. Modeling results .....	128
5.5.1. Kihara parameters optimization for propane .....	128

5.5.2. Test of the thermodynamic model based on the new set of Kihara parameters for propane to other sets in the literature .....	130
5.5.3. Experimental data versus thermodynamic modeling results .....	133
5.6. Raman spectroscopic measurements of clathrate hydrates.....	142
5.6.1. Basic principles of Raman spectroscopy .....	142
5.6.2. Raman spectra of CO <sub>2</sub> /C <sub>3</sub> H <sub>8</sub> binary hydrate at isochoric conditions.....	143
5.6.2.1. High pressure optical cell and Raman spectrometer.....	143
5.6.2.2. Experimental protocol .....	145
5.6.2.3. Raman spectra of CO <sub>2</sub> and C <sub>3</sub> H <sub>8</sub> during crystallization.....	146
5.6.2.4. Raman spectra of CO <sub>2</sub> and C <sub>3</sub> H <sub>8</sub> during dissociation process .....	150
5.6.2.5. Compositional analysis.....	153
5.6.3. Raman spectra of CO <sub>2</sub> /C <sub>3</sub> H <sub>8</sub> binary hydrate at isobaric conditions.....	156
6. Flash calculations .....	162
6.1. Standard flash calculations .....	163
6.2. Flash calculations for clathrate hydrates .....	164
6.3. Non-equilibrium flash calculations .....	166
6.4. Flash calculations results.....	170
Conclusions, final remarks and perspectives.....	175
References .....	178
Scientific production (2015-2018) .....	196
Appendix A .....	198



## List of figures

Figure 1. Hydrate crystal structures and the number of each type cavities [3].	20
Figure 2. P-T diagram of deep water pipeline including hydrate formation regions with/without methanol [12].	22
Figure 3. Schematic of hydrate-based desalination process [38]	25
Figure 4. A typical schematic diagram of hydrocarbon and water systems [1]	29
Figure 5. Three phase equilibrium data of methane hydrate (sI) [60–70].	31
Figure 6. Three phase equilibrium data for simple propane hydrate (sII) [62,71–76].	32
Figure 7. Three phase equilibrium of simple carbon dioxide hydrate (sI) [60,77–80].	33
Figure 8. Three phase equilibrium data for simple ethane hydrate (sI) [62,72,80–82]	34
Figure 9. Three phase equilibrium data for simple nitrogen hydrate (sII) [72,83–85]	34
Figure 10. V-L <sub>w</sub> -H equilibrium data of simple methane hydrate (sI) [67], simple iso-butane hydrate (sII) [93] and methane/iso-butane binary hydrate (sII) [94].	36
Figure 11. V-L <sub>w</sub> -H equilibrium data of simple ethane hydrate (sI) [62], simple propane hydrate (sII) [95] and ethane/propane binary hydrate (sI and sII) [96].	37
Figure 12. Gas-gravity curves for prediction of hydrate formation (from Sloan and Koh [1]).	38
Figure 13. The schematic of the feed-forward algorithm developed and used by Maghsoodloo Babakhani et al. [109]	42
Figure 14. The algorithm of Kihara parameters optimization	48
Figure 15. The procedure for calculating hydrate equilibrium pressure and composition	49
Figure 16. A typical procedure of submitting a calculation in GasHyDyn and provided results	50
Figure 17. $\varepsilon/k$ versus $\sigma$ at the minimum deviation with experimental data for: a) CO <sub>2</sub> [120], b) CH <sub>4</sub> [120] and c) C <sub>2</sub> H <sub>6</sub> [121]	51
Figure 18. P-x diagram of nitrogen-methane mixed hydrate (sI) [68]	57
Figure 19. Experimental H-V equilibrium data for N <sub>2</sub> /CO <sub>2</sub> mixture by Kang et al. [143] and the simulation results (sI)	60
Figure 20. Carbon dioxide-methane hydrates phase equilibria at 280.3 K. Experimental [24] and simulation results (sI). Error bars correspond to the standard uncertainty of experimental hydrate composition.	63
Figure 21. Hydrate composition for methane-carbon dioxide hydrates. Experimental data [146] and simulation results (sI).	66
Figure 22. Hydrate composition for nitrogen-carbon dioxide hydrates at two isotherms. Experimental data [147] and simulation results (sI).	69
Figure 23. Pressure-gas composition diagram for nitrogen-carbon dioxide at three isotherms (sI). Experimental data from Seo et al. [148] and our prediction results	70
Figure 24. P-x diagram of N <sub>2</sub> -CO <sub>2</sub> hydrate based on the experimental results of Seo et al. (sI) [148] and our simulation results	73
Figure 25. The diagram of experimental procedure	76
Figure 26. Experimental data from Herri et al. [113] for methane-carbon dioxide hydrate (sI) and simulation results	78
Figure 27. P-T diagram of mixed CO <sub>2</sub> /CH <sub>4</sub> and CO <sub>2</sub> /N <sub>2</sub> hydrates, experimental data [121] and simulation results (sI). The vapor and hydrate compositions were listed in Table 18.	80

Figure 28. Experimental data from Raman spectroscopic measurements by Sum et al. [165] and our thermodynamic simulations .....	84
Figure 29. CO <sub>2</sub> composition in gas and hydrate phase versus pressure for CO <sub>2</sub> -N <sub>2</sub> system at 272.1 K (sI). Experimental [166] and our simulation results .....	86
Figure 30. Schematic of experimental set-up .....	93
Figure 31. Typical analysis of gas chromatography for a mixture of methane/ethane/propane/butane .....	94
Figure 32. GC calibration results. <i>S</i> is peak area and <i>y</i> is gas composition. Circles are experimental point for calibration. C1, C2, C3 and C4 correspond to methane, ethane, propane and n-butane, respectively. The numbers indicate the bottles composition provided in Table 27 .....	97
Figure 33. A typical analysis of IC for lithium .....	99
Figure 34. A typical calibration curve of IC for lithium (the axis <i>x</i> is the amount of lithium in ppm). Experimental data for IC calibration are shown by points and calibration curves by lines. ....	100
Figure 35. Schematic of the experimental procedures: a) Quick crystallization process. b) Slow crystallization process .....	102
Figure 36. The evolution of pressure and temperature during the course of experiments for methane-propane mixture: a) Quick crystallization process and b) Slow crystallization process .....	102
Figure 37. Mass balance calculation at equilibrium conditions .....	106
Figure 38. The pressure change versus temperature during the quick crystallization process in the case of ethane-butane mixture. The numbers in the figure correspond to the time of taking samples (from beginning of experiment) .....	111
Figure 39. Temperature- pressure evolution during the slow crystallization procedure for ethane-butane mixture. The numbers in the figure correspond to the time of taking samples (from beginning of experiment).....	112
Figure 40. Pressure-temperature diagram of two different methods for methane/propane, ethane/propane and carbon dioxide/propane mixtures .....	119
Figure 41. Pressure-temperature diagram of two different methods for methane/n-butane, ethane/n-butane and methane/ethane/n-butane, carbon dioxide/ethane/propane and methane/ethane/propane/n-butane mixtures .....	119
Figure 42. Composition of propane in hydrate phase in different mixed gas hydrates according to the rate of crystallization .....	120
Figure 43. The changes in compositions of propane and butane in gas and hydrate phases.....	121
Figure 44. Storage capacity of mixed gas hydrates at final state according to the rate of crystallization .	125
Figure 45. Hydrate density of mixed gas hydrates at final state concerning the both crystallization methods .....	126
Figure 46. Hydrate volume for different mixtures for quick and slow crystallization procedures.....	127
Figure 47. $\epsilon/K$ versus $\sigma$ for pure propane and three different mixtures including propane corresponding to average deviation by implementing experimental data from this paper and literature [61,62,72] .....	130
Figure 48. The average deviation of thermodynamic model based on different Kihara parameters of propane in literature and our work (The deviation results from Moradi and Khosravani were not presented in the figure since its deviation was significantly larger than others). ....	133
Figure 49. The experimental data versus simulation results in terms of pressure and hydrate composition for methane/propane mixed hydrate, sII.....	139
Figure 50. Experimental and simulation results of hydrate pressure and ethane composition in solid phase at slow crystallization for CO <sub>2</sub> -N <sub>2</sub> -C <sub>2</sub> H <sub>6</sub> mixed hydrates (sI).....	141

Figure 51. Schematic of experimental set-up used for Raman spectroscopic measurements .....	144
Figure 52. Pressure-Temperature evolution during hydrate formation and dissociation of CO <sub>2</sub> /C <sub>3</sub> H <sub>8</sub> mixed hydrate .....	146
Figure 53. The gas phase changes during the crystallization. (B. H. corresponds to “before hydrate formation”) .....	147
Figure 54. Hydrate phase changes during the crystallization process. Top left: C-C stretch of propane. Top right: C-H stretch of propane. Bottom: CO <sub>2</sub> Fermi resonance .....	149
Figure 55. The gas phase changes during the dissociation process .....	151
Figure 56. Hydrate phase analyses and Raman spectra of CO <sub>2</sub> /C <sub>3</sub> H <sub>8</sub> binary hydrate. Left: C-C stretch of propane vibrations. Right: C-H stretch of propane .....	151
Figure 57. Hydrate phase analysis CO <sub>2</sub> in hydrate phase compared to CO <sub>2</sub> gas .....	152
Figure 58. Calibration curve of carbon dioxide/propane mixture based on vapor measurements to estimate vapor and hydrate compositions (points a, b and c are the mixtures presented in Table 40) .....	154
Figure 59. A typical gas-water interface before the cooling process .....	158
Figure 60. Vibrational bands of CO <sub>2</sub> gas, simple hydrate and CO <sub>2</sub> /C <sub>3</sub> H <sub>8</sub> mixed hydrate .....	159
Figure 61. C-C stretch mode of propane in gas, simple hydrate and mixed hydrate.....	160
Figure 62. C-H stretch mode of propane in gas, simple hydrate and mixed hydrate .....	161
Figure 63. Isothermal flash calculation .....	163
Figure 64. Two mechanisms for hydrate growth [122] .....	167
Figure 65. Non-stoichiometric flash calculations, algorithm and procedure [122] .....	168
Figure 66. Stoichiometric flash algorithm [122] .....	170
Figure 67. Thermodynamic path of mixed N <sub>2</sub> -CO <sub>2</sub> -C <sub>2</sub> H <sub>6</sub> hydrate at slow and quick crystallization.....	171

## List of tables

Table 1. The properties of three most known hydrate structures [3].....	20
Table 2. quadrupole points of different gases [1].....	30
Table 3. Thermodynamic and reference properties of two different structures of gas hydrates [1].....	44
Table 4. A and B parameters for equation 15 [115]. .....	46
Table 5. Kihara parameters of the gas molecules used in this paper.....	47
Table 6. Experimental results of Jhaveri and Robinson [68] for methane-nitrogen mixture hydrates and simulation results (uncertainties not provided by the authors).....	58
Table 7. Gas composition in different phases at 3MPa (uncertainties not provided by the authors). .....	59
Table 8. Experimental results of Kang et al. [143] and simulation (composition uncertainties not provided by the authors).....	61
Table 9. Experimental data of Ohgaki et al. [24] for CH <sub>4</sub> /CO <sub>2</sub> mixture hydrates and simulation results. ..	63
Table 10. Experimental results of Belandria et al. [146] for methane-carbon dioxide hydrates and simulation results.....	65
Table 11. Experimental results of Belandria et al. [147] for nitrogen-carbon dioxide mixed hydrate and simulation results.....	67
Table 12. Experimental results of carbon dioxide-nitrogen hydrate equilibrium pressure and composition from Seo et al. [148] and our simulation results (composition uncertainties not provided by authors).....	70
Table 13. Experimental results of carbon dioxide-methane hydrate equilibrium pressure and composition from Seo et al. [148] and our simulation results (composition uncertainties not provided by authors).....	71
Table 14. Feed composition of different mixtures [149].....	74
Table 15. Experimental results of Ng [149] and our modeling results.....	74
Table 16. Experimental results from Herri et al. [113] and simulation results for carbon dioxide-nitrogen mixture .....	76
Table 17. Experimental results from Herri et al. [113] and simulation results for carbon dioxide-methane mixture .....	77
Table 18. Carbon dioxide-methane and carbon dioxide-nitrogen hydrate mixtures, experimental data [121] and simulation results.....	79
Table 19. Experimental results of Carbon dioxide-methane-ethane hydrate from Le Quang et al. [121] and simulation results.....	81
Table 20. Experimental data of methane-ethane-propane-butane hydrate from Le Quang et al. [121] and simulation results.....	82
Table 21. Experimental data from Sum et al. [165] and simulation results .....	83
Table 22. Experimental data from Subramanian et al. [89] for methane-ethane mixture and simulation results .....	85
Table 23. Experimental results from Seo and Lee [166] and our simulation results.....	86
Table 24. Evidence of structural change or co-existence of structures in mixed gas hydrates .....	88
Table 25. Materials used in this study .....	91
Table 26. The operational conditions of GC in our analyses .....	94
Table 27. Composition of bottles used for GC calibration.....	95
Table 28. The values of A and B for calculating the Henry's constants [180] .....	104
Table 29. The experimental and instrumental uncertainties.....	108
Table 30. Initial conditions of the experiments .....	110

Table 31. Experimental results of guest composition in all phases regarding to the equilibrium temperature and pressure for two rates of crystallization.....	113
Table 32. Gas solubility in liquid phase during the course of experiments.....	116
Table 33. Hydrate phase properties during the course of experiments for two different crystallization rates .....	122
Table 34. $\epsilon/K$ and $\sigma$ for the guest molecules from our previous work [113,120], “a” from literature [119,183] .....	129
Table 35. Different sets of Kihara parameters for propane .....	131
Table 36. The comparison between the different sets of propane Kihara parameters for predicting hydrate equilibrium pressure .....	132
Table 37. Results of thermodynamic model for hydrate pressure and composition .....	135
Table 38. The Raman shifts for CO <sub>2</sub> and C <sub>3</sub> H <sub>8</sub> in gas phase, obtained in this work and in literature .....	148
Table 39. The Raman spectra for CO <sub>2</sub> and C <sub>3</sub> H <sub>8</sub> in hydrate phase, during the crystallization.....	148
Table 40. Mixtures used for calibration of Raman spectroscopic measurements .....	153
Table 41. Compositional analysis of CO <sub>2</sub> /C <sub>3</sub> H <sub>8</sub> mixed hydrate by Raman spectroscopy; vapor and hydrate phases .....	155
Table 42. Hydrate composition simulation of CO <sub>2</sub> /C <sub>3</sub> H <sub>8</sub> mixed hydrate with GasHyDyn .....	156
Table 43. Experimental results for N <sub>2</sub> -CO <sub>2</sub> -C <sub>2</sub> H <sub>6</sub> mixed hydrates at final state of quick and slow crystallization .....	171
Table 44. Experimental versus prediction results of N <sub>2</sub> -CO <sub>2</sub> -C <sub>2</sub> H <sub>6</sub> mixed hydrates at quick crystallization rate by considering non-stoichiometric and stoichiometric flash algorithms .....	172
Table 45. Experimental hydrate composition of N <sub>2</sub> -CO <sub>2</sub> -C <sub>2</sub> H <sub>6</sub> mixed hydrates at quick crystallization versus non-stoichiometric and stoichiometric flash algorithms .....	172
Table 46. Experimental versus prediction results of N <sub>2</sub> -CO <sub>2</sub> -C <sub>2</sub> H <sub>6</sub> mixed hydrates at slow crystallization rate by considering non-stoichiometric and stoichiometric flash algorithms .....	173
Table 47. Experimental hydrate composition of N <sub>2</sub> -CO <sub>2</sub> -C <sub>2</sub> H <sub>6</sub> mixed hydrates at quick crystallization versus non-stoichiometric and stoichiometric flash algorithms .....	173

## General introduction

Based on the data obtained in this work, we suggest that the pressure and guest distribution in hydrate phase at final state are sometimes significantly influenced by the crystallization speed. Additionally, the hydrate volume at slow crystallization was noticeably less than at quick crystallization. This concept should help to regulate more realistically the amount of kinetic inhibitors (KHI) or anti-agglomerants (AA) to use in flow-assurance issues. Furthermore, the storage capacity at slow crystallization was larger than quick crystallization. This information could be essential for increasing gas storage in the form of hydrates especially pertinent in transportation use etc.

The results of the thermodynamic model showed that for both crystallization methods, the kinetic effects had a non-negligible impact on the thermodynamic equilibrium of mixed gas hydrates. However, the results of thermodynamic model agreed better with the experimental data from slow crystallization for hydrate pressure and composition. This means that hydrate formation at slow crystallization is closer to thermodynamic equilibrium.

Another objective of this study was to collect and classify the experimental data on guest composition in hydrate phase at equilibrium conditions in the open literature, since this information provides new insights into the enclathration of guest molecules. Then, the capability of thermodynamic modeling to simulate hydrate composition was investigated. The modeling results reveal the drawbacks and advantages of the thermodynamic model according to the equilibrium conditions. Previous experimental data shows that guest distribution in hydrate phase depends noticeably on vapor phase composition. In addition, composition of larger molecules, such as propane or butane, in the hydrate phase, is notably higher than in vapor phase. Our simulation results demonstrated that the hydrate composition data from direct measurement (microscopic tools) have been well evaluated by the thermodynamic model. Nevertheless, when structural transition can occur in a system, the thermodynamic model is no longer accurate. In the case of indirect measurements, the thermodynamic model usually predicts well the hydrate composition. Nonetheless, its capability does vary with differing hydrate composition and equilibrium pressure, to the extent that in some cases, it completely fails to predict hydrate composition. To sum up, we believe that this information could be very useful to develop and improve the processes involving hydrate formation and dissociation.

During our investigation of CO<sub>2</sub>/C<sub>3</sub>H<sub>8</sub> mixed hydrates, a strong change in hydrate composition was observed in both crystallization procedures. Therefore, the vapor and solid phase were then analyzed by Raman spectroscopy in order to obtain qualitative and quantitative information about hydrate composition, structure and guest enclathration. The results of Raman spectra revealed a co-existence of sI and sII which occurred at both isobaric and isochoric conditions under CO<sub>2</sub> rich gas feed.

Moreover, classical thermodynamic modeling is coupled with mass balance calculations during hydrate formation and two algorithms concerning thermodynamic flash calculations at constant volume is presented. The final hydrate volume, composition and pressure of N<sub>2</sub>-CO<sub>2</sub>-C<sub>2</sub>H<sub>6</sub> mixture at two mentioned crystallization rates have been simulated and discussed. The final hydrate pressure at slow crystallization rate was better simulated by stoichiometric flash algorithm by an average deviation is almost two times less than by non-stoichiometric algorithm (5.8% compared to 11.8%). Furthermore, the final hydrate volume was also satisfactorily predicted by stoichiometric framework (average deviation was 8%). The final hydrate composition was efficiently predicted by stoichiometric framework (average deviation near zero). This means that at slow crystallization rate which the kinetic effects are not significant, the hydrate phase was almost homogenous.

Finally, the concepts presented in this study would help to express and suggest new ideas about the non-equilibrium crystallization of mixed gas hydrates. Additionally, Moreover, these elucidations could have a significant impact on clathrate hydrate applications which thermodynamic equilibrium is essentially taken into account such as energy storage and transportation or carbon capture sequestration.

# 1. Introduction

## 1.1. Definition of gas hydrate

Water molecules, in the presence of gas molecules at high pressure and low temperature, can form some polyhedral hydrogen-bonded cavities encaging the aforementioned guest molecules, like CO<sub>2</sub>, N<sub>2</sub>, CH<sub>4</sub>, C<sub>2</sub>H<sub>6</sub> etc. This solid ice-like structure is called gas hydrate, or clathrate hydrate. The guest molecules stabilize the clathrate hydrate framework. Since they could not occupy all the cavities of hydrate structure, the number of water molecules is usually more than the ideal composition. Hence, the gas hydrates are also called “non-stoichiometric hydrates” to discriminate them from stoichiometric salt hydrates [1].

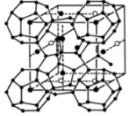
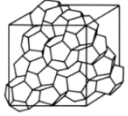
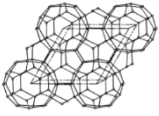
## 1.2. Molecular structures and properties

Gas hydrates form different structures depending on the nature of guest molecules as well as thermodynamic conditions. There are three principal structures of clathrate hydrates: sI, sII and sH.

Cubic structure I (sI) is composed of two pentagonal dodecahedron ( $5^{12}$ ) and six tetrakaidecahedron ( $5^{12}6^2$ ) cavities and usually forms in presence of small molecules (diameter between 4.2 and 6 Å) like methane or carbon dioxide. Larger molecules (diameter between 6 and 7 Å) like propane and small molecules (diameter less than 4.2 Å) such as nitrogen form cubic structure II (sII). This structure comprises sixteen pentagonal dodecahedron ( $5^{12}$ ) and eight hexakaidecahedron ( $5^{12}6^4$ ) cavities. Combination of large molecules (typically between 7 and 9 Å) such as iso-pentane or neohexane, and small molecules such as methane or nitrogen, can form hexagonal structure H (sH). It contains three pentagonal dodecahedron ( $5^{12}$ ), two irregular dodecahedron ( $4^35^66^3$ ) and one icosahedron ( $5^{12}6^8$ ) cavities [1]. Given the fact that the hydrate structures are constructed by at least 85% (mole fraction) of water molecules, mechanical properties of three hydrate structures are somehow similar to ice, except thermal conductivity and thermal expansivity [2]. Table 1 and Figure 1 detail the molecular differences between the various structures of gas hydrates.



**Table 1. The properties of three most known hydrate structures [3]**

Hydrate structures	sI		sII		sH		
Shape							
Cavity	Small	Large	Small	Large	Small	Medium	Large
Description	$5^{12}$	$5^{12}6^2$	$5^{12}$	$5^{12}6^4$	$5^{12}$	$4^35^66^3$	$5^{12}6^8$
Number of cavities per unit cell ( $m_i$ )	2	6	16	8	3	2	1
Average cavity radius (Å)	3.95	4.33	3.91	4.73	3.91	4.06	5.71
Coordination number <sup>a</sup>	20	24	20	28	20	20	36
(a) The number of oxygen atom per cavity							

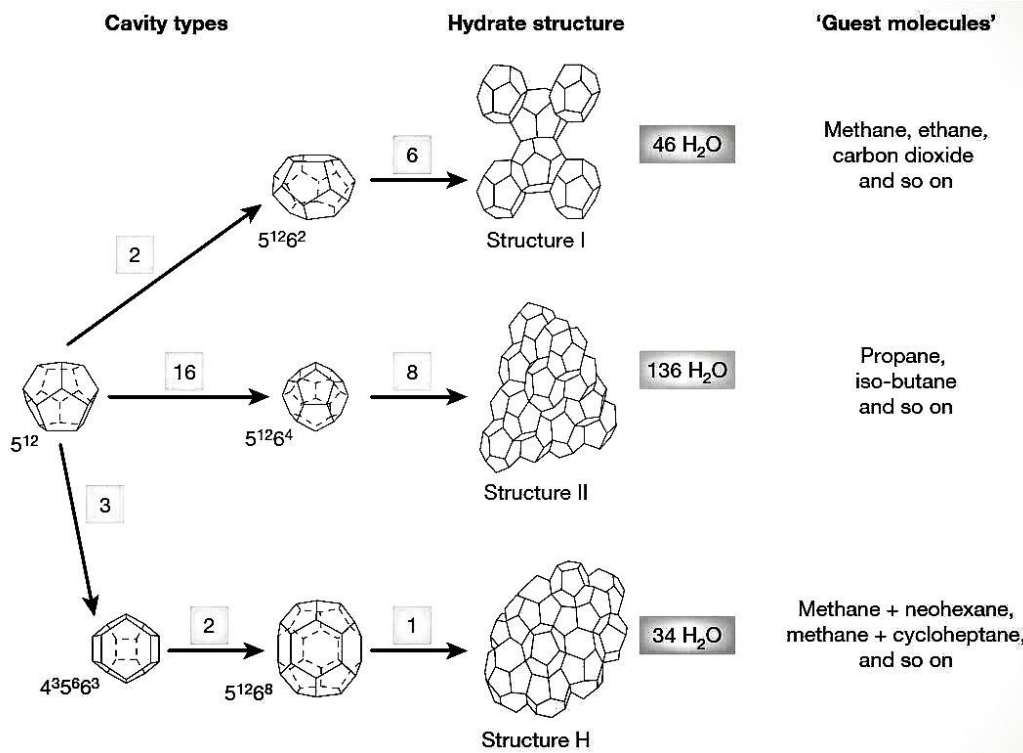


**Figure 1. Hydrate crystal structures and the number of each type cavities [3].**

Sloan and Koh [1], by reviewing the work of von Stackelberg [4], stated that, if a molecule occupies the small vacant cavity of a structure, it could also go into the large cavities of that structure. Conversely, large molecules such as propane and iso-butane only stabilize the large

cavities of sII and they cannot enter the small cavities. Furthermore, at normal pressures, each cavity can be accommodated by at most one guest molecules. However, the double occupancy of guest molecules in hydrate cavities has been also observed and reported in literature. For instance, Kuhs et al. [5,6] by neutron powder diffraction indicated that double occupancy of nitrogen molecules in large cavities of hydrate structure can be occurred at high pressure. In addition, Chazallon and Kuhs [7] investigated the hydrate structure of nitrogen and oxygen hydrates by neutron powder diffraction and reported the double occupancy of large molecules at high pressures. Moreover, based on experimental and mathematical investigations of non-stoichiometric properties of clathrate hydrates, it has been shown that only occupation of a fraction of cavities is required to stabilize the hydrate structure [1].

### **1.3. Gas hydrates, an issue in oil and gas industry**

One of the main issues in flow assurance during oil and gas production is gas hydrate formation due to the presence of water and light hydrocarbons at high pressure and low temperature conditions (about 4°C and 80bar) [8]. Gas hydrate formation in offshore and inshore pipelines causes an extreme risk of blockage. Consequently, in the history of gas hydrates, the primary focus has always been how to prevent hydrate formation in oil and gas industries. Therefore, the safety and economic costs of avoiding gas hydrates has been of great interest.

One of the primary attempts to prevent hydrate formation in oil and gas pipelines has been to inject sufficient amount of thermodynamic hydrate inhibitors (THIs), such as methanol or glycol to shift the hydrate stability region outside the operational range of temperature and pressure [9]. Figure 2 provides an overview of pressure-temperature diagram of liquid-hydrate-vapor equilibrium curve of hydrate formation for typical offshore flowline system with/without methanol. It is clear on the figure that a significant length of pipeline is located in the hydrate forming region (left hand side of hydrate formation curve). By adding methanol, the hydrate forming equilibrium curve is shifted to the lower temperature. In this case, about 30 wt% methanol is required to ensure that the operational conditions are not in the hydrate formation area. It is obvious that in high water-cut systems, the larger amount of methanol is needed to prevent hydrate formation. As a result, the operational cost may become prohibitively expensive [8,10,11].

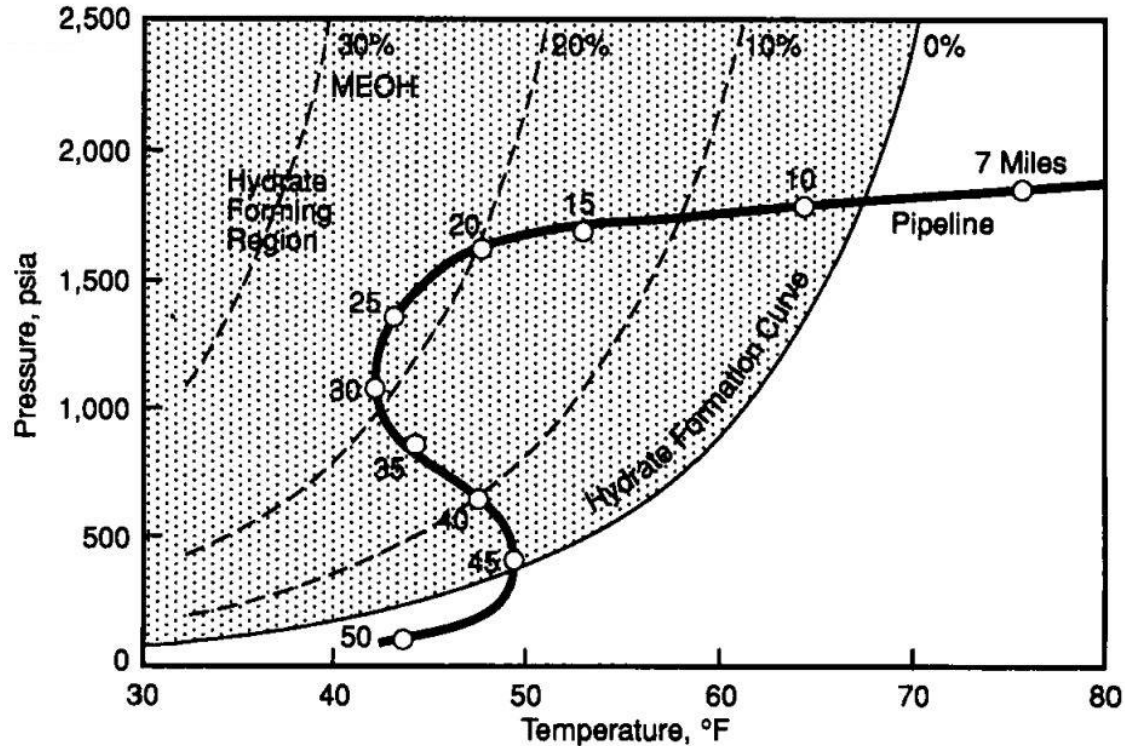


Figure 2. P-T diagram of deep water pipeline including hydrate formation regions with/without methanol [12].

Kinetic hydrate inhibitors (KHIs) and anti-agglomerants (AAs) have received much attention in over the last two decades. They both hinder hydrate formation nucleation and prevent crystal growth and they could be utilized at considerably lower concentrations (0.5-2 wt% compared to 30-60 wt% of thermodynamic inhibitors). Additionally, by using these low dosages hydrate inhibitors (LDHIs), recovery stage is not necessary. Hence, leakage risk of storage and transportations services can be significantly reduced [13,14]. However, they have some limitations. At low temperature and very high pressure with sufficient time, even by using KHIs, hydrate crystals can significantly grow and plug the pipelines. Moreover, in systems in which water cut is higher than 60%, the AAs cannot be efficient [1,9,15,16]. In general, the strategy concerning flow assurance in gas and oil industry is changing from preventing hydrate formation by thermodynamic inhibitors to risk management by low dosages hydrate inhibitors.

#### 1.4. Natural gas hydrates deposits, an unconventional energy resource

A huge resource of natural gas in the form of hydrate is assumed to be located in permafrost and seafloor sediments surrounding continental margins [17]. The quantity of these natural gas was

estimated about  $1.2 \times 10^{17} \text{ m}^3$  at standard temperature and pressure ( $0^\circ\text{C}$  and 1bar) [18]. This range of amount of natural gas hydrates is noticeably larger than conventional gas reserves for all fossil fuels [19,20]. Makogon [21] estimated that 15 to 20% of total volume of natural gas hydrates could provide energy for 200 years.

There are several techniques to recover natural gas from deposits such as thermal stimulation, depressurization, chemical inhibitors injection and  $\text{CH}_4/\text{CO}_2$  exchange. Among these methods,  $\text{CH}_4/\text{CO}_2$  exchange is attracting widespread interest due to the possibility of exploitation of natural gas from hydrate fields by injection and isolation of  $\text{CO}_2$  in these regions [22–24]. In 2012, ConocoPhillips Company performed a short term test by using  $\text{CO}_2/\text{N}_2$  (0.225 mole fraction  $\text{CO}_2$ ) injection to recover methane from a single well and demonstrated the  $\text{CO}_2/\text{CH}_4$  exchange concept at larger-than-lab scale. During six weeks, about  $2.4 \times 10^4 \text{ m}^3$  methane extracted from the well and 40% of  $1.3 \times 10^3 \text{ m}^3$  injected  $\text{CO}_2$  was isolated in the gas hydrate field [25].

Nevertheless, Makogon [21] stated that the cost of natural gas production from hydrate deposits might be 15 to 20% higher than conventional gas fields in the same area. Hence, more research is required to develop economically the natural gas exploitation from hydrate fields. Another significant issue is how the transfer of natural gas from its solid state into gas phase with effective technologies [21]. Moreover, Li et al. [26] reviewed the achievements for the natural gas hydrate exploitation researches and reported that the current techniques could not be utilized for a long-term exploitation since characteristics of the flow, the issues of heat and mass transfer as well as the risk assessment are still not completely understood [26].

In conclusion, Sloan and Koh [1] stated that countries are currently focused on gas production from permafrost, because deep-placing hydrates are expensive to exploit. Nonetheless, in near future natural gas could be produced in the ocean where high concentration of hydrates exist and near the distribution infrastructure [1,27].

## **1.5. Potential applications of gas hydrates**

Gas hydrate has received much attention over the last two decades since researchers realized that it could be a novel technical solution in different domains of industry. Unique structural features and physical and chemical properties of gas hydrates could provide a sustainable future technology for separation and storage applications. However, there is still a need for more

experimental and mathematical investigations to evaluate the efficiency and sustainability of hydrate-based applications. In this section, a summary of potential applications of gas hydrates is reviewed.

Safe and cheap transport of natural gas from fields to consumption places is nowadays under the consideration due to increasing energy demand. Transport of natural gas as LNG (liquefied natural gas) or through pipes is unsafe or expensive. To reduce the risk in gas transport, hydrate formation technology may be employed. In this technology large volumes of hydrocarbons can be stored in cavities of hydrate matrices [28–30]. For example, 150-180 Nm<sup>3</sup> of methane gas at standard conditions can be stored in one m<sup>3</sup> of gas hydrate [31,32]. Gas storage in hydrate does not require low temperature condition compared to the LNG. Additionally, hydrate formation installations may be located on the platforms offshore. It has been reported that transportation of natural gas through hydrate is about 18-24% cheaper than through LNG [33,34].

Furthermore, the next decade is likely to witness a considerable rise in hydrogen to benefit of its renewable and sustainable energy. Common requirements for the hydrogen-based systems are hydrogen storage method. The storage of hydrogen in the form of hydrates is found to require the minimum annual depreciation and utility expense compared to other processes [35]. Recent developments and future directions of using hydrogen clathrate hydrates have been comprehensively reviewed by Strobel et al. [36] and Veluswamy et al. [37].

Seawater desalination or treatment of salty wastewater is also a potential application of gas hydrates. The idea is based on salt elimination. When gas hydrates form in seawater or salty wastewater, the salts remain in the concentrated aqueous solution and they can be removed by a physical process. The process has been carefully explained by Cha and Seol [38] and schematically presented in Figure 3.

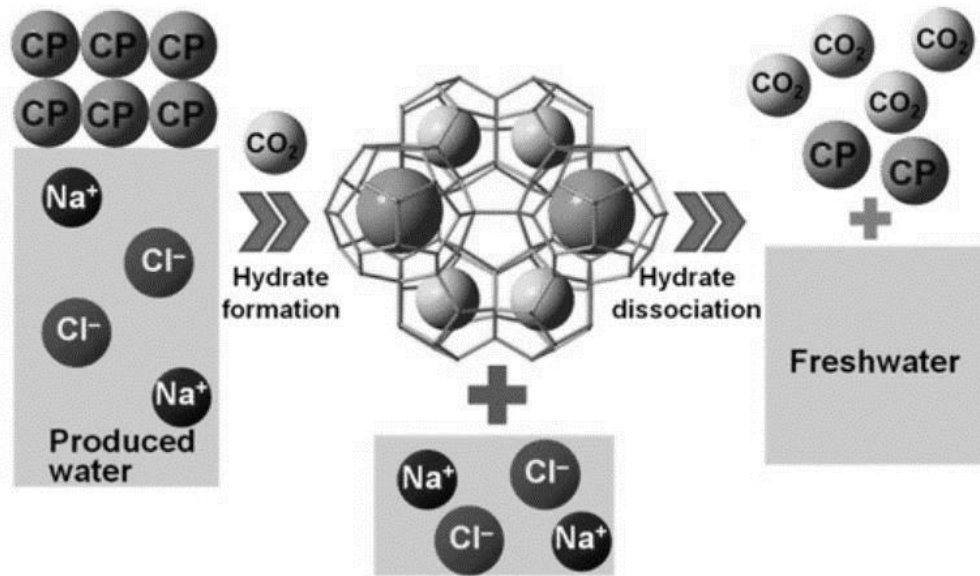


**Figure 3. Schematic of hydrate-based desalination process [38]**

The advantage of employing hydrate formation process for water desalination is that operational cost and energy consumption could be economical compared to other techniques of desalination [39]. Makogon [31] stated that desalination based on hydrate process could be cost-effective compared to membrane processes. Barduhn et al. [40] reported that hydrate-based desalination has not only all advantages of freezing-desalination process, but also it operates at higher temperature. In addition, gas hydrate formation process could be used as a pre-treatment method for reverse osmosis process to enhance the efficiency of salt removal [41]. However, developments are still required to increase the efficiency and safety of hydrate-based desalination process [42].

At last, gas separation is another potential application of gas hydrates. A remarkable feature of hydrate crystallization process is that guest composition in hydrate phase is different from feed gas. Hence, researchers proposed that this property of gas hydrates could be advantageous to separate and concentrate the desired molecules [43–47]. Recently, separating CO<sub>2</sub> by gas hydrate crystallization process attracts academic and industrial attentions in different fields of separation such as flue gas (CO<sub>2</sub>/N<sub>2</sub>) [48–50], shifted syngas (CO<sub>2</sub>/H<sub>2</sub>) [51,52], natural gas and biogas (CO<sub>2</sub>/CH<sub>4</sub>) separation [53,54]. The benefits of hydrate-based separation methods are simple and moderate operation conditions, low temperature and pressure loss, high environmental compatibility and low energy consumption [55,56].

In order to commercialize mentioned potential applications of gas hydrates, more investigations are still required as follows:

- a. Studying thermodynamics, crystallization mechanisms and pathways, as well as guest enclathration
- b. Determination of hydrate composition, volume and storage capacity
- c. Discovering physical and chemical properties of gas hydrates
- d. Molecular-scale measurements of the hydrate phase characterizations
- e. Reliable and accurate prediction tools to simulate equilibrium conditions and hydrate phase properties

In the present study, we intend to extend potentially our knowledge about these challenging subjects. In other words, we aim to provide further understanding and indications which could be useful to design, improve and develop hydrate-based applications such as energy storage and transportation or carbon capture sequestration or flow assurance issues, not only for academic studies, but also for serious managerial implications. Additionally, since thermodynamic equilibrium is essentially taken into account in clathrate hydrate applications, vital modifications will be investigated in this work.

## 2. State of the art

### 2.1. Background of phase equilibria of gas hydrates

Phase equilibrium measurements and calculations are among the most commonly discussed properties of gas hydrates. There are numerous experimental and prediction data on gas hydrate equilibria over a wide range of temperature, pressure and vapor phase composition. This information provides a fundamental understanding of thermodynamic equilibrium phenomena as well as tools for process design of potential applications.

Hydrate phase equilibria data are usually measured throughout hydrate dissociation process, like standard solubility measurement methods in crystallization (isothermal or polythermal methods etc. [57]). Indeed, induction time can be long (days). However, measurements in dissociation process pose several challenges such as suitable heating rate and self-preservation phenomenon. Therefore, V-L-H equilibrium analyses are commonly more difficult than VLE or SLE measurements. There are various techniques to investigate phase equilibria of gas hydrates depending on operational conditions, nature of hydrate former, type of required data, etc. Nonetheless, isochoric pressure search and differential scanning calorimetry (DSC) are among the most used frequently methods [58].

There are five common measurable variables in phase equilibria of gas hydrates: pressure, temperature, guest composition in co-existing phases (gas, liquid and hydrate), phase amounts (density) and volume. The hydrate composition, volume or density and phase amounts are usually ignored due to the experimental difficulties. This requires special instruments or technics. Nonetheless, the pressure, temperature and vapor composition are frequently provided in each process in the literature since they can be simply measured by commonly available instruments.

Phase diagrams of gas hydrates equilibria provide fundamental knowledge of phase's boundaries and present the co-existence of different phases at desired conditions. The structure of phase diagram for a system depends on the Gibbs' phase rule. The number of degrees of freedom for a non-reacting heterogeneous system at thermodynamic equilibrium can be expressed by Gibbs' phase rule as following:

$$F = 2 + C - P \tag{1}$$



where  $F$  is degree of freedom which presents the number of intensive variables required to identify the system,  $C$  corresponds to the number of components in the system and  $P$  is the number of co-existing phases in the system. The Gibbs' phase rule represents the number of specified intensive variables to define a solution for thermodynamic equilibrium calculations. Nota bene: the intensive variables are temperature, pressure and guest composition in gas, liquid and hydrate phases, or density. Conversely, phase amounts and volume are extensive variables and they cannot be considered by Gibbs' phase rule.

A schematic temperature-pressure diagram for water and hydrocarbon systems is illustrated in Figure 4. In the figure,  $I$ ,  $V$ ,  $H$ ,  $L_W$  and  $L_{HC}$  are ice, vapor, hydrate, liquid water and liquid hydrocarbon phases. The phase diagrams contain points which represent four phases equilibrium, lines correspond to the three phase equilibrium and areas between the lines are two phases existence. The hydrate region is located at the left of the three phase lines  $I$ - $H$ - $V$ ,  $L_W$ - $H$ - $V$  and  $L_W$ - $H$ - $L_{HC}$ . At the intersection of three phase lines, there are two points.  $Q_1$  corresponds to the lower hydrate quadruple point which four different phases are at equilibrium ( $I$ - $L_W$ - $V$ - $H$ ). The upper quadruple point is  $Q_2$ , which accounts for the coexistence of  $L_W$ - $H$ - $V$ - $L_{HC}$ . These two quadruple points provide a quantitative classification for each hydrate former and they are unique according to the nature of each guest.

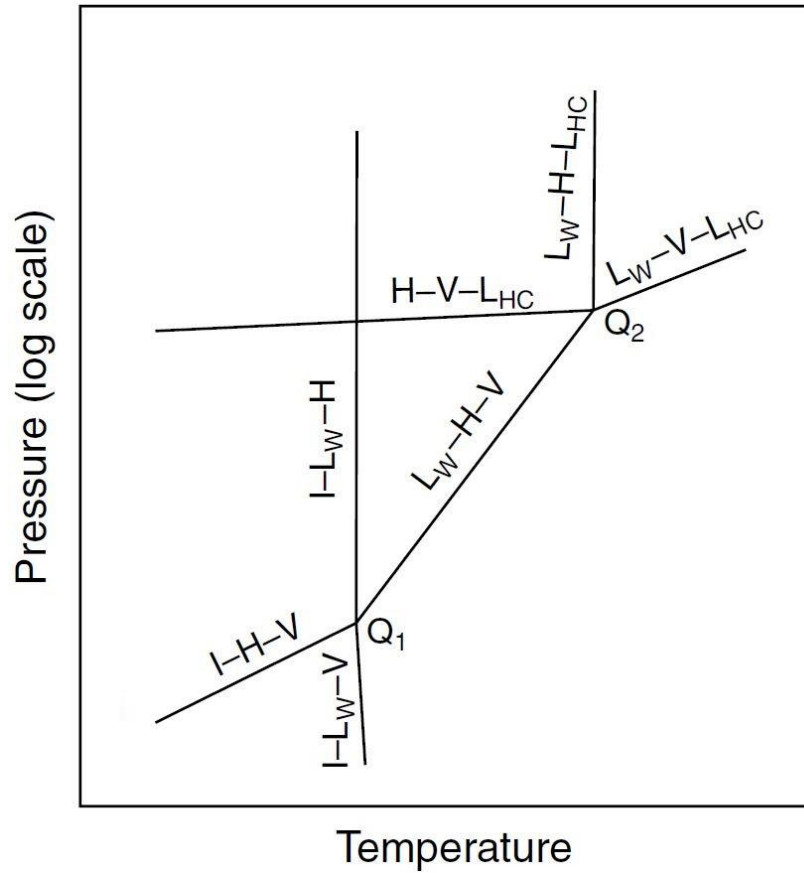


**Figure 4. A typical schematic diagram of hydrocarbon and water systems [1]**

The lower quadruple point denotes the transition of liquid water to ice and hydrate formation from ice and vapor. The upper quadruple point represents the upper temperature limit for hydrate formation. Some hydrate formers have no upper quadruple point due to low vapor pressure at the critical temperature, such as methane and nitrogen. This means that for nitrogen or methane, there is no temperature limit to form hydrate [1]. The quadrupole points of different gases are listed in Table 2.

**Table 2. quadrupole points of different gases [1]**

Component	Q1		Q2	
	T (K)	P (MPa)	T (K)	P (MPa)
Methane	272.9	2.563	No Q <sub>2</sub>	
Ethane	273.1	0.530	287.8	3.39
Propane	273.1	0.172	278.8	0.556
Isobutane	273.1	0.113	275.0	0.167
Carbon dioxide	273.1	1.256	283.0	4.499
Nitrogen	271.9	14.338	No Q <sub>2</sub>	
Hydrogen sulfide	272.8	0.093	302.7	2.239

It is obvious on the figure 4 that for the I-L<sub>W</sub>-H and L<sub>W</sub>-H-L<sub>HC</sub> lines, small change in temperature leads to a significant change in pressure in a close system as there exists three incompressible phases. It should be noted that since both ice and hydrate phases cause major problems when they occur in oil and gas flow lines, the pipelines condition are kept to the right of L<sub>W</sub>-H-V and I-H-V lines and system temperature above the ice point. Hence, the most interest in gas hydrate systems is the L<sub>W</sub>-H-V line. In the present work, we aim to extend the current knowledge of three phase equilibrium of L<sub>W</sub>-H-V in hydrocarbon and water systems.

In the following sections, the phase equilibria of simple methane, propane and carbon dioxide will be discussed in details. Furthermore, the phase diagrams of some binary and multicomponent clathrate hydrates will be presented.

### 2.1.1. Hydrates of pure components

Among the hydrate formers, methane has been extensively studied in a wide range of temperature (below the ice point and 327 K) and pressure up to 1000 MPa. Three phase equilibrium boundaries of simple methane hydrate which forms sI is illustrated in Figure 5. As clear on the figure, the V-L<sub>W</sub>-H(sI) line is steeper than V-I-H(sI) line. This is due to existence of two incompressible phases at I-H(sI)-V equilibrium conditions. In other words, at a desire temperature change, the pressure variation in V-L<sub>W</sub>-H(sI) condition is significantly higher than in I-H(sI)-V equilibrium. Moreover, the intersection of these lines presents lower quadruple point

( $Q_1$ ) or four phase equilibrium point (I-H(sI)-L<sub>W</sub>-V) which is 272.9 K and 2.563 MPa [1]. As aforementioned, methane has no upper quadruple point ( $Q_2$ ) since its critical temperature (190.56 K [59]) is noticeably lower than  $Q_1$ . This means that there is no temperature or pressure limits for V-L<sub>W</sub>-H(sI) equilibrium of methane.

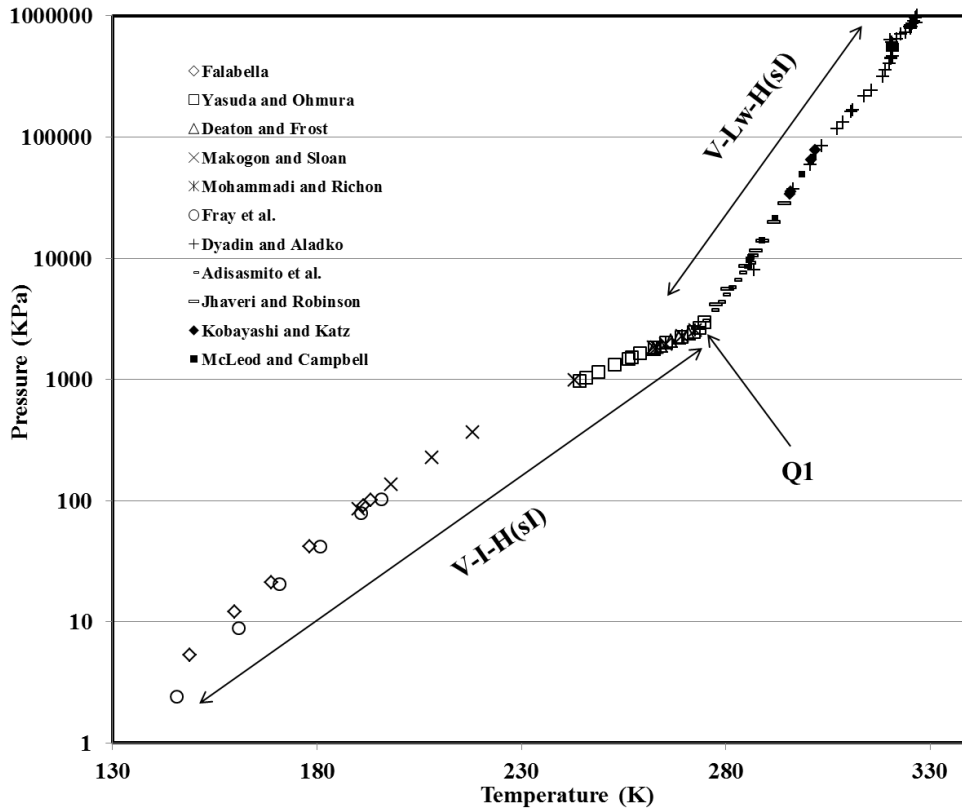


Figure 5. Three phase equilibrium data of methane hydrate (sI) [60–70].

Three phase equilibrium data for pure propane and pure carbon dioxide hydrates are illustrated in Figure 6 and Figure 7, respectively. Carbon dioxide and propane form sI and sII, respectively. As clear on the figures, unlike methane, carbon dioxide and propane have upper quadruple points ( $Q_2$ ). This means that at higher temperatures than  $Q_2$  (in hydrate region), there is a phase transition from V-L<sub>W</sub>-H to L<sub>W</sub>-H-L<sub>HC</sub> (whether sI CO<sub>2</sub> hydrate or sII C<sub>3</sub>H<sub>8</sub> hydrate). Obviously due to co-existence of three incompressible phases, large pressure changes for small temperature variations can be observed (the L<sub>W</sub>-H-L<sub>HC</sub> line is almost vertical). Hence, the maximum temperatures for hydrate formation of simple carbon dioxide and simple propane hydrates are 278.8 and 283.0K, respectively [1].

Furthermore, the lower quadruple temperature for both gases is identical (273.1K) since the phase transition of liquid water to ice or vice versa occurs at the intersection of I-H-V and V-L<sub>W</sub>-H lines. Nonetheless, the lower quadruple pressure of simple propane hydrate is noticeably lower than of simple carbon dioxide hydrate. This can be explained by the provided three phase equilibrium data in Figure 6 and Figure 7. Evidently, at a desired temperature, the equilibrium curve of CO<sub>2</sub> hydrate is located at an upper pressure than of C<sub>3</sub>H<sub>8</sub> hydrate.

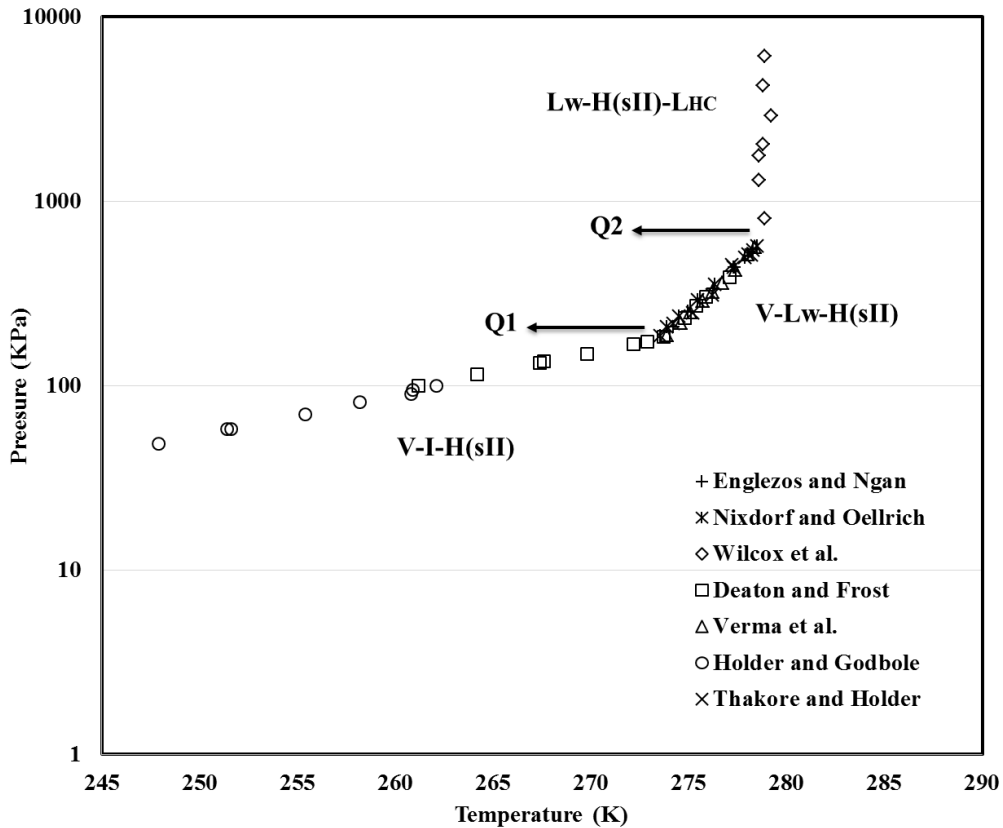


Figure 6. Three phase equilibrium data for simple propane hydrate (sII) [62,71–76].

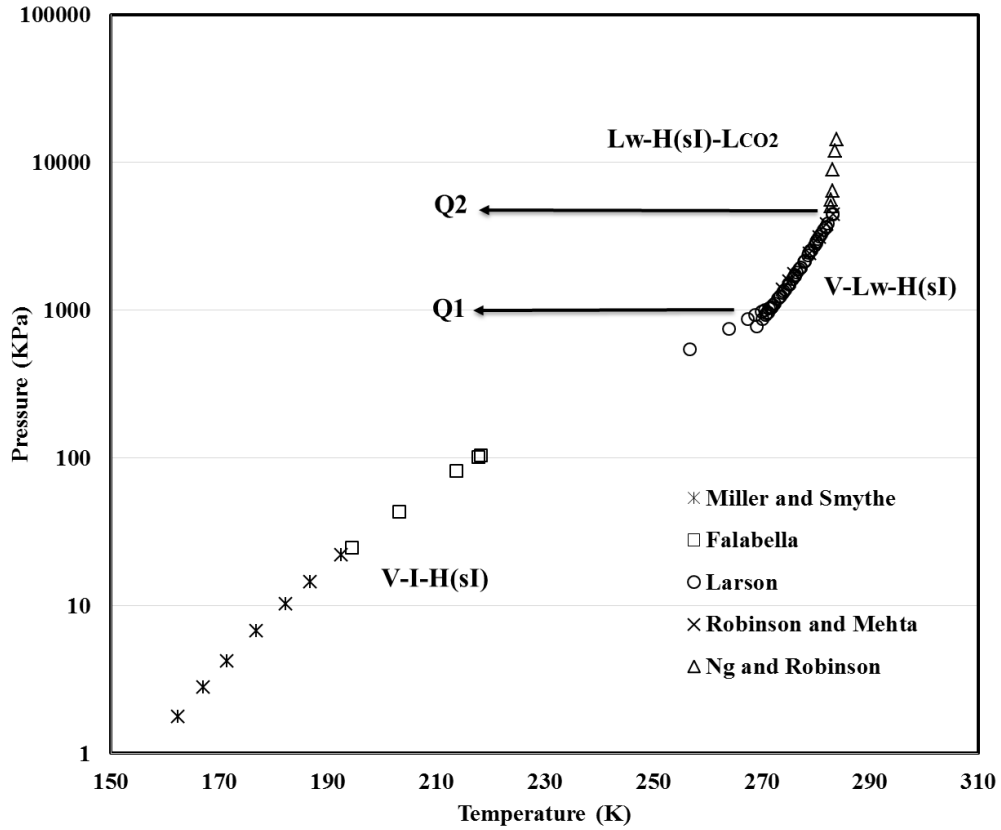


Figure 7. Three phase equilibrium of simple carbon dioxide hydrate (sI) [60,77–80].

Three-phase equilibrium diagrams of ethane and nitrogen are presented in Figure 8 and Figure 9. This should be considered that for nitrogen, only V-L<sub>W</sub>-H(sII) data is available in open literature. Therefore, only this line is illustrated in Figure 9.

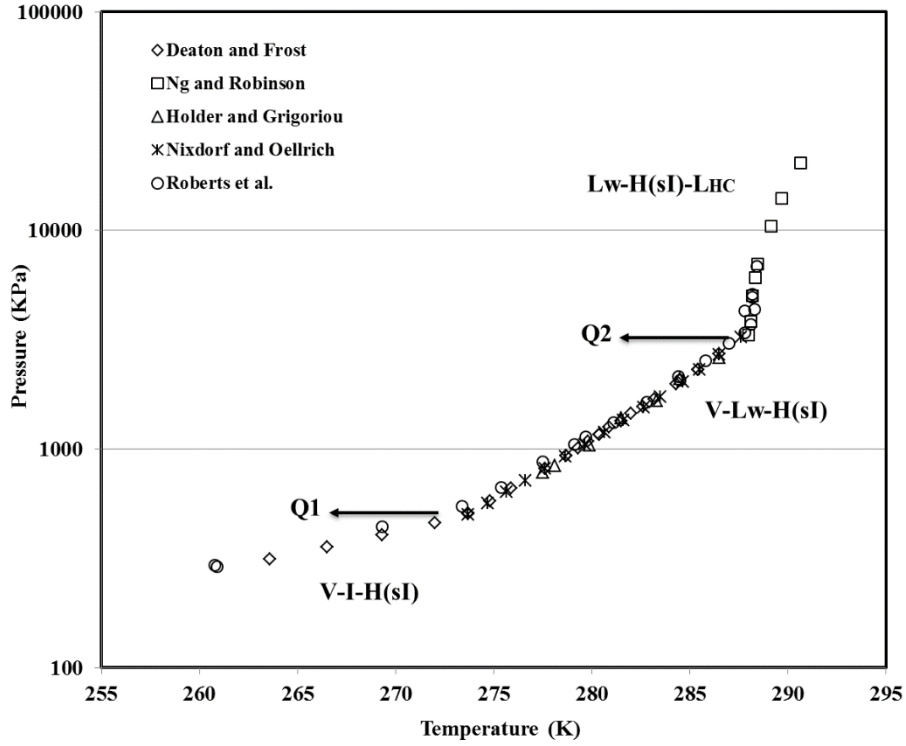


Figure 8. Three phase equilibrium data for simple ethane hydrate (sI) [62,72,80–82]

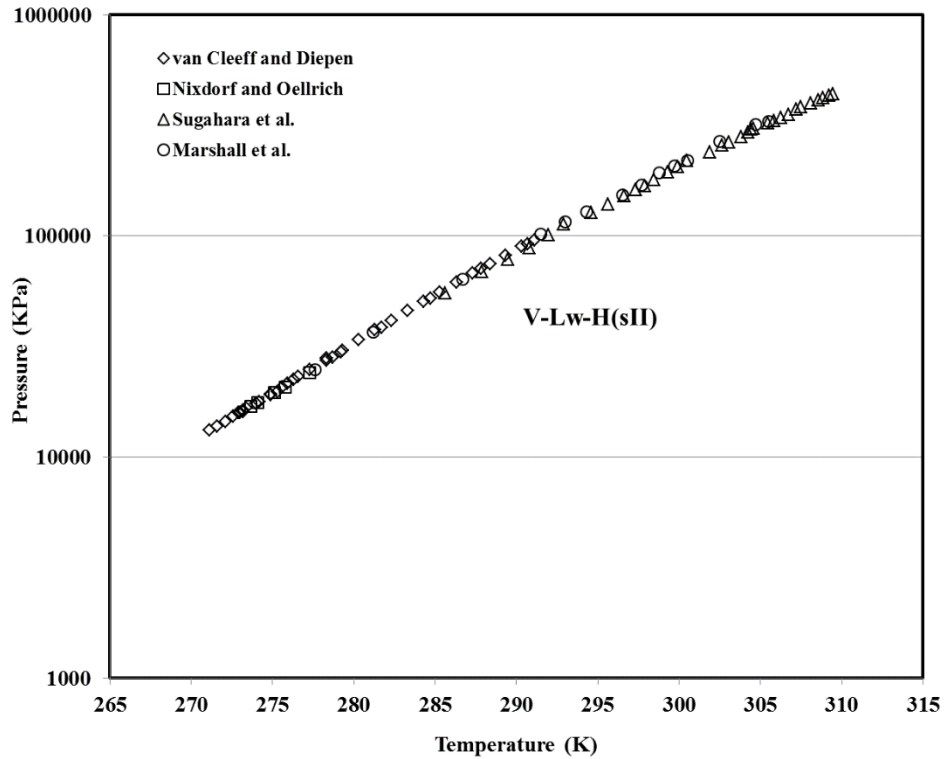


Figure 9. Three phase equilibrium data for simple nitrogen hydrate (sII) [72,83–85]

### 2.1.2. Multicomponent clathrate hydrates

To draw the phase equilibrium diagram for a multicomponent gas hydrate, a third dimension which corresponds to the composition of feed gas is required. Nevertheless, by fixing the feed composition at a desired value, the P-T equilibrium diagram of a binary or multicomponent hydrate can be illustrated.

Moreover, hydrate structure is also a key factor which should be taken into account. Each structure is a unique solid phase and they have different properties and characterizations. Indeed, for a mixture including both sI and sII hydrate formers, can form whether sI or sII, depending on the guest feed composition and operational conditions. Furthermore, co-existence of both structures or structural transition can be also occurred [86,87]. Subramanian et al. [88,89], Ballard and Sloan [90], Kwon et al. [91] and Ohno et al. [92] already reported that although methane and ethane which are sI hydrate formers, their mixture can form sII hydrate at specific feed composition and temperature.

As mentioned earlier, the V-L<sub>W</sub>-H equilibrium line is of great interest in natural gas hydrate systems. Therefore, P-T diagrams of two different gas mixtures concerning the V-L<sub>W</sub>-H equilibrium conditions at fixed feed compositions are presented and discussed in this section. For each equilibrium diagram of multicomponent gas hydrate system, the equilibrium data of simple component hydrates are also provided to present clearly how the equilibrium conditions varies according to the changes in the feed compositions.

Figure 10 presents the V-L<sub>W</sub>-H equilibrium data of simple methane hydrate, simple iso-butane hydrate and methane/iso-butane binary hydrate. As seen in the figure, the equilibrium lines of simple CH<sub>4</sub> hydrate and simple i-C<sub>4</sub>H<sub>10</sub> hydrate are located at the top and bottom of figure, respectively. The lower and upper quadruple temperatures of i-C<sub>4</sub>H<sub>10</sub> are 273.1 and 275K, respectively. Hence, the V-L<sub>W</sub>-H equilibrium curve of iso-butane is significantly shorter than of methane. Nevertheless, even a small amount of iso-butane in the mixture could remarkably increase the value of upper quadruple temperature. Additionally, the equilibrium curves of binary CH<sub>4</sub>/i-C<sub>4</sub>H<sub>10</sub> at different gas concentrations are placed between the V-L<sub>W</sub>-H lines of simple iso-butane and methane hydrates. Interestingly, only 1.2% mole fraction of i-C<sub>4</sub>H<sub>10</sub> shifted considerably the V-L<sub>W</sub>-H equilibrium curve compared to simple methane hydrate. Furthermore,



at a desired temperature, the equilibrium pressure of  $\text{CH}_4/\text{i-C}_4\text{H}_{10}$  hydrate is closer to the equilibrium pressure of simple  $\text{i-C}_4\text{H}_{10}$  hydrate (for  $y_{\text{i-C}_4\text{H}_{10}} > 0.152$  mole fraction).

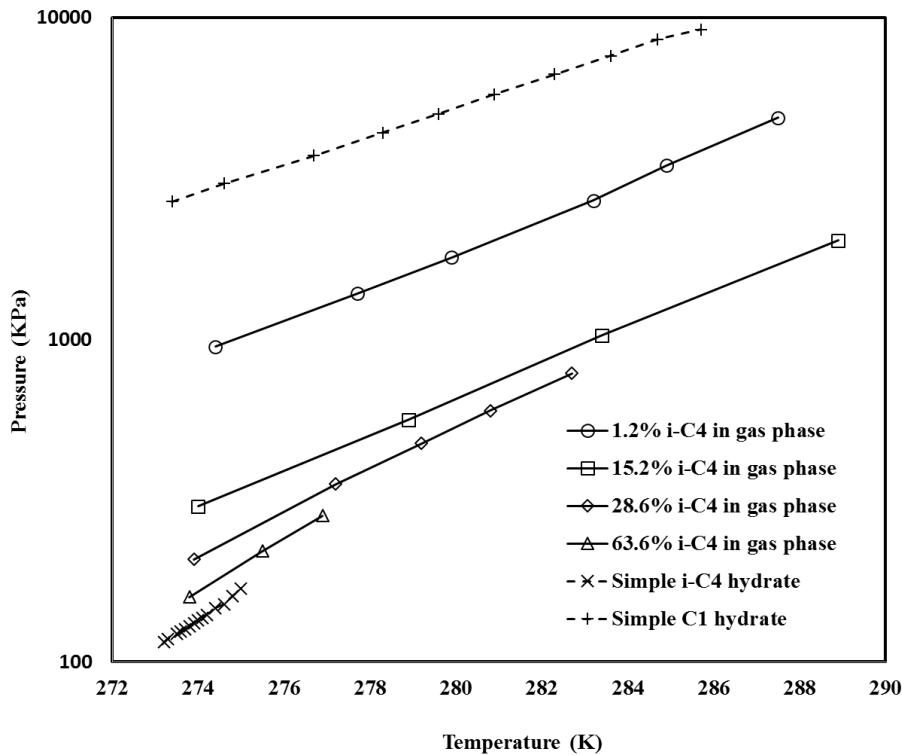


**Figure 10. V-L<sub>w</sub>-H equilibrium data of simple methane hydrate (sI) [67], simple iso-butane hydrate (sII) [93] and methane/iso-butane binary hydrate (sII) [94].**

Figure 11 shows the V-L<sub>w</sub>-H equilibrium data of simple ethane hydrate, simple propane hydrate as well as ethane/propane binary hydrate at different gas compositions. This is clear that the hydrate equilibrium lines of binary  $\text{C}_2\text{H}_6/\text{C}_3\text{H}_8$  hydrate at high composition of ethane are located at upper positions than of  $\text{C}_2\text{H}_6$  hydrate curve (unlike the  $\text{CH}_4/\text{i-C}_4\text{H}_{10}$  binary hydrate data). One of the remarkable observations of both figures is that the P-T locus of all V-L<sub>w</sub>-H lines is straight except the line of  $\text{C}_2\text{H}_6/\text{C}_3\text{H}_8$  hydrate at 34.2% propane. At this concentration, the equilibrium curve includes two straight lines with a significant increase in pressure at 275.8K. This behavior can be explained by the fact that that simple ethane and propane form different hydrate structures. Ethane forms sI, whereas propane forms sII. Hence, a structural transition from sII to sI might occur for ethane/propane binary hydrate at these conditions in the mixture.

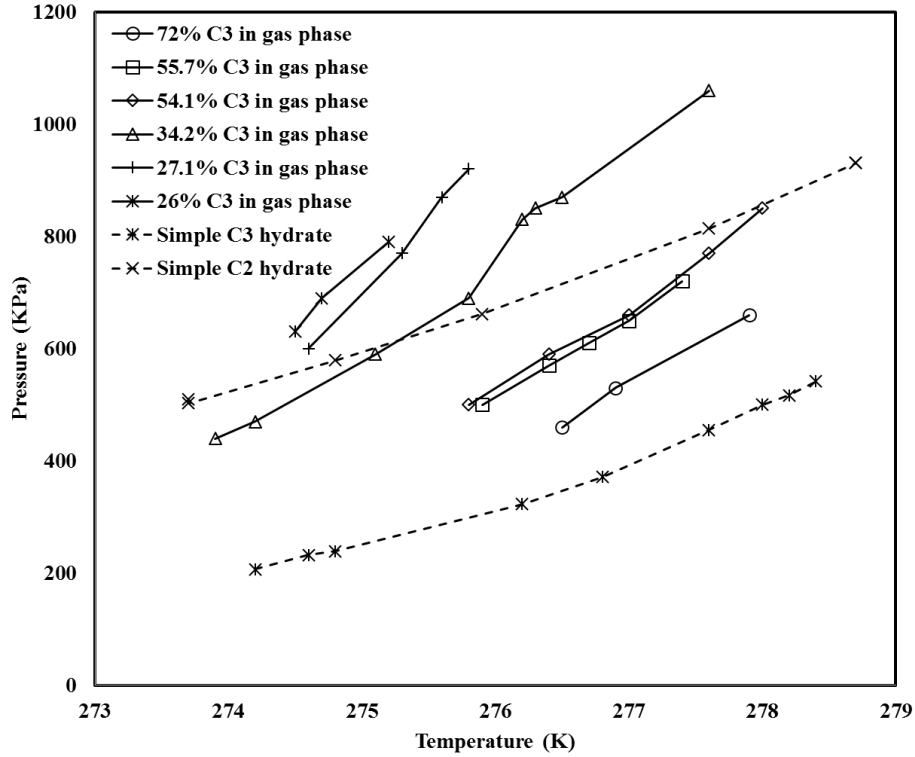


Figure 11. V-L<sub>w</sub>-H equilibrium data of simple ethane hydrate (sI) [62], simple propane hydrate (sII) [95] and ethane/propane binary hydrate (sI and sII) [96].

## 2.2. Modeling of gas hydrates phase equilibria

The most useful equilibrium condition of clathrate hydrates in industrial and academic application is V-L<sub>w</sub>-H, since other three-phase equilibrium conditions are energy consuming (like V-I-H which low temperatures below zero are required) or risk management consideration must be taken into account (for instance for L<sub>w</sub>-H-L<sub>HC</sub> much greater system pressures are needed). Hence, predicting hydrate equilibrium pressure, temperature and composition is of great interest. Since it is not practical to perform experiments for each gas mixture and composition, approaches to calculate hydrate equilibrium pressure (temperature) at desired conditions (like temperature and guest composition in vapor phase) have received much attention in the past decades. In the following sections, a brief description of methods to evaluate gas hydrates phase equilibria is provided. Require

### 2.2.1. Gas-gravity charts

In a major advance in 1945, Katz provided charts that hydrate equilibrium pressure and temperature conditions (V-L<sub>w</sub>-H) at given gas gravities of feed could be determined [97]. Gas

gravity is the molar mass of the gas divided by the molar mass of air. The gas gravity limits in the charts were between 0.6 and 1.0. Figure 12 presents a gas-gravity chart which is reproduced from Katz [97] by Sloan and Koh [1]. As the figure shows, at a given temperature (pressure), only the gravity of gas or gas mixture is required to read directly the hydrate formation pressure (temperature) from the chart. Hence, this method is a simple technique to predict V-L<sub>W</sub>-H equilibrium conditions.

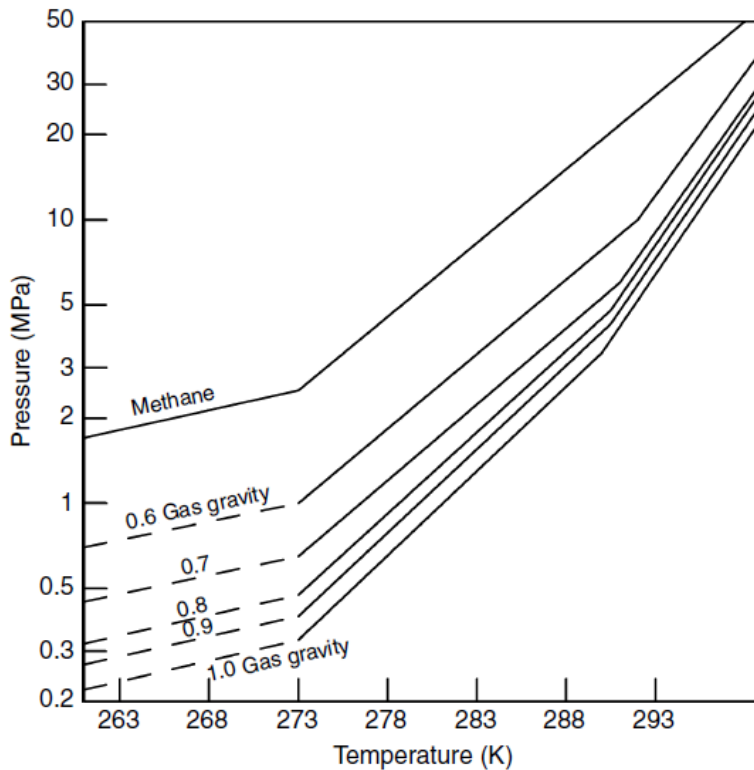


**Figure 12. Gas-gravity curves for prediction of hydrate formation (from Sloan and Koh [1])**

As explained, this method is a simple technique to predict V-L<sub>W</sub>-H equilibrium conditions. Nevertheless, it has major limitations. Since in this technique, only one parameter (gas gravity) is taken into account, it cannot be very accurate. Loh and James [98] reported that gas-gravity charts are not capable to predict hydrate formation conditions at gravities between 0.9 to 1.0. Furthermore, the prediction results from this method for the components which have similar gravities are the same. But there are different components with the same gravity that have different hydrate equilibrium behavior. In addition, these charts were produced from very limited data of methane, ethane, propane, butane and normal pentanes. Therefore, prediction results for a component excluding the mentioned gases, may lead to a considerable deviation [99]. In

conclusion, the gas-gravity charts can be used as a first estimate for hydrate equilibrium predictions, since the procedure of calculations is very simple. This provides an approximation of hydrate equilibrium behavior which may be used for the other techniques.

### 2.2.2. K-value method

In the K-value approach, the hydrate equilibrium conditions can be predicted by considering the hydrate phase as a solid solution. Then, a vapor–solid distribution coefficient ( $K_{vsi}$ ) is utilized for each component at equilibrium as following [73,100]:

$$K_{vsi} = \frac{y_i}{x_{si}} \quad (2)$$

where  $y_i$  stands for mole fraction of gas  $i$  in vapor phase and  $x_{si}$  is mole fraction of gas  $i$  in hydrate phase. This should be noted that  $y_i$  and  $x_{si}$  are on water-free basis. Therefore, the V-L<sub>W</sub>-H conditions can be calculated based on the K-value charts in a manner which satisfies the following equation:

$$\sum_{i=1}^n \frac{y_i}{K_{vsi}} = 1 \quad (3)$$

Elgibaly and Elkamel [101] reported that this method is limited to the equilibrium pressures up to 4000 psia (27.6MPa) for methane, ethane and propane; up to 2000 psia (13.8MPa) for iso-butane and hydrogen sulfide; and up to 1000 psia (6.9MPa) for carbon dioxide. Moreover, the both mentioned techniques, gas-gravity charts and K-value method were generated from experimental data of components which form sI and sII. Hence, these methods cannot be used for the equilibrium predictions of sH.

### 2.2.3. Empirical correlations

As reading charts can be time and energy consuming, correlations to predict hydrate formation pressure (temperature) have been frequently used. In this section, several correlations of hydrate formation prediction will be discussed. This should be noted that, since empirical correlations include many coefficients and values for each hydrate former and they are out of interest of this work, only a brief description of correlations is provided to analyze their advantages and disadvantages. For further information, the readers are referred to the original works.

Kobayashi et al. [102] proposed a correlation based on the gas-gravity charts to predict hydrate equilibrium conditions. Since the gas gravity curves were used to generate this correlation, the same limitations as mentioned in the section 2.2.1 can be considered. In addition, this correlation may have large deviations at temperatures higher than 289K, pressure above 1500 psia (10.3MPa) and gas gravities above 0.9 [101].

Bahadori [103] developed a correlation for calculating the hydrate pressure equilibrium of light hydrocarbons as well as sweet gases and nitrogen. The correlation was as a function of molecular weight and temperature as following:

$$P = a + bT + cT^2 + dT^3 \quad (4)$$

where  $P$  is pressure (kPa),  $T$  is temperature (K) and  $a$ ,  $b$ ,  $c$ ,  $d$  are coefficients which can be calculated as functions of gas molecular weight. The author stated that the average absolute deviations for light hydrocarbons and non-hydrocarbons were 3.0 and 1.4%, respectively. Nevertheless, the temperature range in his work was between 263 and 293K. Moreover, the correlation cannot be utilized for phase equilibrium behaviors of mixed gas hydrates like natural gas.

Since hydrate formation is considered as a physical process rather than chemical, Omole et al. [104] developed a correlation by temperature, pressure, gas gravity as well as adding a coefficient which corresponds to water vapor pressure. The authors compared the new correlation with other correlations in literature and reported that less average absolute deviations have been obtained compared to other correlation. Nevertheless, their correlation had an error about 5.5K to calculate equilibrium temperature in some cases. Moreover, they stated that the insufficient available data in the literature was a limitation to improve the accuracy of the correlation. At last, another main drawback of this method is incapability of these empirical correlations to simulate phase equilibria of clathrate hydrates where more than one component exists in the system.

#### **2.2.4. Neural network approaches**

In the last two decades, artificial neural networks (ANNs) have received attention due to their capability in modeling the linear and non-linear systems without needing the prior empirical models [105,106]. ANNs are powerful tools for experimental correlations and fitting parameters compared to the conventional fitting methods [107]. A set of experimental data is required to

develop an ANN. This is obvious that training the algorithm with more experimental data improves the accuracy of this approach.

Mohammadi et al. [108] developed a feed-forward artificial neural network algorithm to study the phase behavior of binary mixtures including tetrahydrofuran (THF). They trained the algorithm by the experimental data in literature for different concentrations of THF. Then, the capability of the algorithm to predict hydrate dissociation pressures was evaluated by their obtained experimental data. They reported that the developed algorithm successfully predicted the phase behavior of binary mixtures including THF for concentration below 0.056 mole fraction (the stoichiometric concentration of THF).

Maghsoodloo Babakhani et al. [109] investigated forecasting of hydrate formation pressure of binary mixtures including at least one hydrocarbon using a feed-forward multi-layer artificial neural network. For this purpose, 895 experimental data which cover a wide range of temperatures and compositions were collected from different studies cited in the literatures. In order to find the best model, they tested different ANN types through the absolute average relative deviation percent (AARD), mean square error (MSE) and the regression coefficient ( $R^2$ ) with a procedure as shown in Figure 13. They found that the selected ANN model based on the statistical analysis had an excellent agreement (AARD=1.02, MSE= $1.27 \times 10^{-5}$  and  $R^2=0.9938$ ) with the collected experimental data. The obtained results revealed that the developed MLPNN model is an applicable and feasible tool to predict hydrate formation pressure with high accuracy with respect to CSMHYD Program.

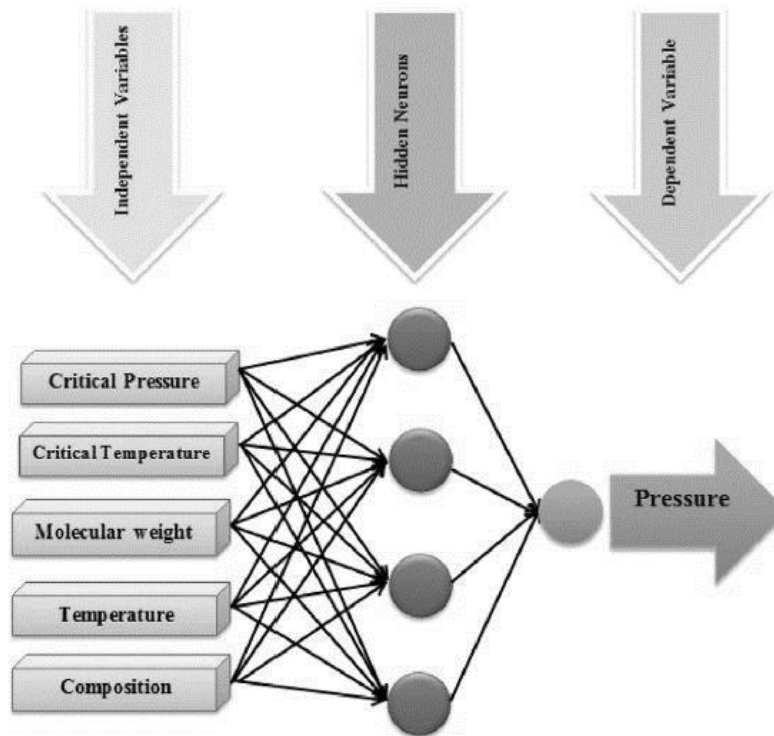


Figure 13. The schematic of the feed-forward algorithm developed and used by Maghsoodloo Babakhani et al. [109]

Zahedi et al. [110] tested two correlations for estimating the hydrate formation temperature as a function of temperature and specific gravity based on Berge and Sloan and Kobayashi models and they compared the prediction results from the correlations to an artificial neural network. They reported that the ANN was more accurate than the correlations.

In conclusion, the ANNs are commonly capable to predict the phase behavior of gas hydrates as the authors reported the good agreements between the experimental and prediction results. However, a large database is required to train the ANN models. This means that the convergence of the model could be long. On the other hand, for the hydrate formers that limited data is available, these models cannot be utilized. In addition, the independent variables that are frequently used as input parameters are not sufficient to predict phase transition, structural changes, cage occupancy, hydration number etc. Furthermore, since these ANNs are incorporated in programming software like Matlab and models are hidden, users should be familiar with the software applications environment.

### 2.2.5. van der Waals and Platteeuw approach

Thermodynamic equilibrium can be described by the equality of chemical potential at each phase. In the case of gas hydrates, the equality of chemical potential of water in liquid phase ( $\mu_W^L$ ) and hydrate phase ( $\mu_W^H$ ) is usually considered:

$$\mu_W^L = \mu_W^H \quad (5)$$

In 1959, van der Waals and Platteeuw proposed a model by considering the gas hydrate equilibria [111]. Some of the assumptions required for this model should be noted. First, cavities are hypothesized to be spherical and only a single gas molecule can be trapped in one cavity. Second, a pair potential function of gas-molecule is used to describe the interaction between the guest molecule and water. Third, there is no interaction among the guest molecules and additionally these guest molecules do not deform the cavities. Given the fact that the assumptions in the model are restrictive, but it could work for many cases to predict phase behavior of clathrate hydrates [99].

Van der Waals and Platteeuw model also includes a hypothetical phase  $\beta$  which corresponds to the empty cavities in hydrate phase. So the equation 5 can be re-written as the equality of difference between chemical potential of water in liquid phase and  $\beta$  phase ( $\Delta\mu_W^{L-\beta}$ ) and the difference between chemical potential of water in hydrate phase and  $\beta$  phase ( $\Delta\mu_W^{H-\beta}$ ).

$$\Delta\mu_W^{L-\beta} = \Delta\mu_W^{H-\beta} \quad (6)$$

The both sides of equation 6 are discussed in details in the following sections.

#### 2.2.5.1. Liquid phase

In the left hand side of equation 6, the difference in chemical potential of water in liquid phase and  $\beta$  phase, can be described by classical thermodynamics using Gibbs-Duhem equation:

$$\Delta\mu_W^{L-\beta} = T \frac{\Delta\mu_W^{L-\beta}|_{T^0, P^0}}{T^0} - T \int_{T^0}^T \frac{\Delta h_{W,m}^{L-\beta}|_{P^0}}{T^2} dT + \int_{P^0}^P \Delta v_{W,m}^{L-\beta}|_T dP - RT \ln a_W^L|_{T,P} \quad (7)$$

Where  $T^0=273.15\text{K}$  and  $P^0=0$  bar are the reference temperature and pressure, respectively.  $a_W^L$  is the water activity in liquid phase. It can be described by an activity coefficient model. However, as we consider pure water without any additives, the water activity can be approximated by



$a_W^L = x_W^L$ . This should be noted that the water activity can be notably differed from ideality in the presence of salt and polar molecules (such as thermodynamic inhibitors: for instance alcohols).  $\Delta v_{W,m}^{L-\beta} \Big|_T$  is the molar volume difference between the liquid phase and  $\beta$  phase. von Stackelberg measured its value by X-ray diffraction [112].  $\Delta h_{W,m}^{L-\beta} \Big|_{p_0}$  is the difference in enthalpy between the liquid phase and  $\beta$  phase. It can be expressed by using the classical thermodynamics [1]:

$$\Delta h_{W,m}^{L-\beta} \Big|_{p_0} = \Delta h_{W,m}^{L-\beta} \Big|_{p_0 T^0} + \int_{T^0}^T \Delta C_{p,w}^{L-\beta} \Big|_{p_0} dT \quad (8)$$

By assuming linear dependence of  $\Delta C_{p,w}^{L-\beta} \Big|_{p_0}$  on temperature:

$$\Delta C_{p,w}^{L-\beta} \Big|_{p_0} = \Delta C_{p,w}^{L-\beta} \Big|_{p_0 T^0} + b_{p,w}^{L-\beta} (T - T^0) \quad (9)$$

$\Delta h_{W,m}^{L-\beta} \Big|_{p_0 T^0}$  and  $\Delta \mu_W^{L-\beta} \Big|_{T^0 p_0}$  are the thermodynamic properties with various values corresponding to each author. Based on a previous study of our team, by comparing several predicted thermodynamics data, it was concluded that the values from Handa and Tse are the best set to use for gas hydrates modeling [113]. The values of all reference and thermodynamic properties are in Table 3.

**Table 3. Thermodynamic and reference properties of two different structures of gas hydrates [1]**

Parameters (units)	Structure I	Structure II
$\Delta C_{p,w}^{L-\beta} \Big _{p_0 T^0}$ (J/mol/K)	-38.12	-38.12
$b_{p,w}^{L-\beta}$ (J/mol/K <sup>2</sup> )	0.141	0.141
$\Delta v_{W,m}^{L-\beta} \Big _{T^0 p_0}$ (10 <sup>-6</sup> m <sup>3</sup> /mol)	4.5959	4.99644
$\Delta \mu_W^{L-\beta} \Big _{T^0 p_0}$ (J/mol)	1287	1068
$\Delta h_{W,m}^{L-\beta} \Big _{p_0 T^0}$ (J/mol)	934	764

Hence by re-writing equation 7, the difference in chemical potential of water in liquid and  $\beta$  phases can be expressed by following equation:

$$\begin{aligned} \Delta\mu_W^{L-\beta} = & T \frac{\Delta\mu_W^{L-\beta}|_{T^0, P^0}}{T^0} + \left( b_{P,W}^{L-\beta} T^0 - \Delta C_{p,W}^{L-\beta} \Big|_{P^0, T^0} \right) - T \ln \frac{T}{T^0} + \frac{1}{2} b_{P,W}^{L-\beta} T (T - T^0) + \left( \Delta h_{W,m}^{L-\beta} \Big|_{P^0, T^0} + \right. \\ & \left. T^0 \left( b_{P,W}^{L-\beta} T^0 - \Delta C_{p,W}^{L-\beta} \Big|_{P^0, T^0} \right) - \frac{1}{2} b_{P,W}^{L-\beta} T^{0^2} \right) \left( 1 - \frac{T}{T^0} \right) + \Delta v_{W,m}^{L-\beta} \Big|_{T^0} (P - P^0) - RT \ln x_W^L \end{aligned} \quad (10)$$

### 2.2.5.2. Hydrate phase

The right hand side of equation 6 is the difference between chemical potential of water in hydrate phase and  $\beta$  phase ( $\Delta\mu_W^{H-\beta}$ ) and can be described by statistical thermodynamic functions. In the model of van der Waals and Platteuw, this parameter was expressed based on the occupancy factor of the guest molecule  $i$  in cavity  $j$  ( $\theta_j^i$ ).

$$\Delta\mu_W^{H-\beta} = RT \sum_i v_i \ln(1 - \sum_j \theta_j^i) \quad (11)$$

where  $v_i$  is the number of cavities type  $i$  per mole of water. The occupancy factor can be described by considering the analogy among gas adsorption in the three dimensional hydrate structures and two-dimensional Langmuir adsorption [1].

$$\theta_j^i = \frac{C_j^i f_j(T, P)}{1 + \sum_j C_j^i f_j(T, P)} \quad (12)$$

where  $f_j(T, P)$  is the fugacity of guest molecule  $j$  at a desired temperature and pressure. The value of fugacity in the gas phase can be calculated based on an appropriate EoS (for example SRK), because at equilibrium condition, fugacities in all phases, including vapor phase, are the same. By re-writing equation 11:

$$\Delta\mu_W^{H-\beta} = RT \sum_i v_i \ln(1 - \sum_j C_j^i f_j(T, P)) \quad (13)$$

In this equation,  $C_j^i$  is the Langmuir constant of guest molecule  $j$  in the cavity type  $i$ . The Langmuir constant depends on the interaction potential between the trapped guest molecules and the surrounding water molecules cage, and for spherical guest-cages potentials can be expressed as follows:

$$C_j^i = \frac{4\pi}{kT} \int_0^\infty \exp\left(-\frac{w(r)}{kT}\right) r^2 dr \quad (14)$$

where  $w(r)$  is the interaction potential between the guest molecule and the cavity based on the distance between the gas and water molecules in the structure ( $r$ ). Parrish and Prausnitz [114] proposed a model to calculate the Langmuir constant of each hydrate former in different cavities as following:

$$C_j^i = \frac{A_j^i}{T} \exp\left(\frac{B_j^i}{T}\right) \quad (15)$$

where  $T$  is temperature (K),  $A_j^i$  and  $B_j^i$  are fitting parameters from experimental data. Their values for several guest molecules according to the hydrate structure and cavity type are provided by Munck et al. [115] and presented in Table 4.

**Table 4. A and B parameters for equation 15 [115].**

Guest	Structure	Small cavity		Large cavity	
		$A \times 10^3$ (K/atm)	B (K)	$A \times 10^3$ (K/atm)	B (K)
Methane	I	0.7228	3187	23.35	2653
	II	0.2207	3453	100	1916
Ethane	I	0	0	3.039	3861
	II	0	0	240	2967
Propane	II	0	0	5.455	4638
Iso-butane	II	0	0	189.3	3800
n-butane	II	0	0	30.51	3699
Nitrogen	I	1.617	2905	6.078	2431
	II	0.1742	3082	18	1728
Carbon dioxide	I	0.2474	3410	42.46	2813
	II	0.0845	3615	851	2025

The interaction potential and consequently the Langmuir constant can be also determined by Kihara potential as following:

$$w(r) = 2Z\varepsilon \left[ \frac{\sigma^{12}}{R^{11}r} \left( \Delta^{10} + \frac{a}{R} \Delta^{11} \right) - \frac{\sigma^6}{R^5 r} \left( \Delta^4 + \frac{a}{R} \Delta^5 \right) \right] \quad (16)$$

$$\Delta^N = \frac{1}{N} \left[ \left( 1 - \frac{r}{R} - \frac{a}{R} \right)^{-N} - \left( 1 + \frac{r}{R} - \frac{a}{R} \right)^{-N} \right] \quad (17)$$

Parameters  $\varepsilon$ ,  $\sigma$  and  $a$  are Kihara parameters and they correspond to minimum energy, collision diameter and shell radius, respectively. McKoy and Sinagoglu stated that using Kihara parameters can be a reliable approach to calculate the interaction potential [116]. Hence in this study, this approach has been used.

### 2.2.5.3. Kihara potential

Kihara parameters for each guest molecules are unique and they do not depend on the type of cavity. Two of the Kihara parameters are fitted according to the experimental data of pure gas hydrates. The hard-core radius is calculated from viscosity [117] or by values of the second virial coefficient [118] and the radius value for each gas does need to be optimized again. In this work, a new set of Kihara parameters for propane was optimized based on an algorithm shown in Figure 14. The results of optimization will be discussed in the next chapters. Table 5 presents the Kihara parameters for the guest molecules used in this study.

**Table 5. Kihara parameters of the gas molecules used in this paper**

Guest molecule	$a$ [119]	$\varepsilon/\kappa$	$\sigma$	Reference
CO <sub>2</sub>	0.6805	178.21	2.873	[120]
N <sub>2</sub>	0.3526	133.13	3.099	[120]
CH <sub>4</sub>	0.3834	166.36	3.050	[120]
C <sub>2</sub> H <sub>6</sub>	0.5651	177.46	3.205	[121]
C <sub>3</sub> H <sub>8</sub>	0.6502	195.00	3.340	This work
nC <sub>4</sub> H <sub>10</sub>	0.9379	209.00	2.912	[119]
$a$ is the hard-core radius $\varepsilon$ corresponds to the maximum attractive potential $\sigma$ is the distance from the center of cavity at maximum attractive potential				

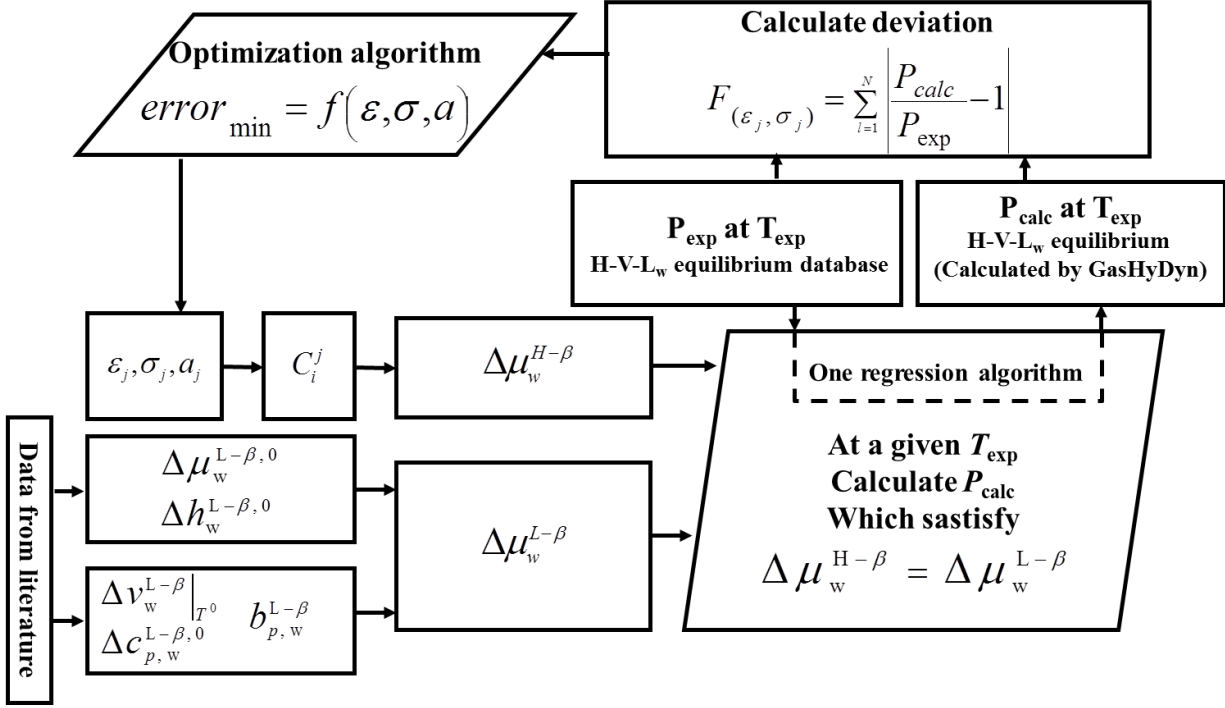


Figure 14. The algorithm of Kihara parameters optimization

#### 2.2.5.4. Simulation procedures

First, for a gas mixture at a desired temperature, the equilibrium pressure which satisfies equation (6) is calculated. Subsequently, the occupancy factor is determined based on equation (12). Then, the hydrate composition is calculated as following:

$$x_j^H = \frac{\sum_i v_i \theta_j^i}{\sum_i \sum_j v_i \theta_j^i} \quad (18)$$

The procedure for calculating hydrate equilibrium pressure and composition of mixed gas hydrates is shown in Figure 15.

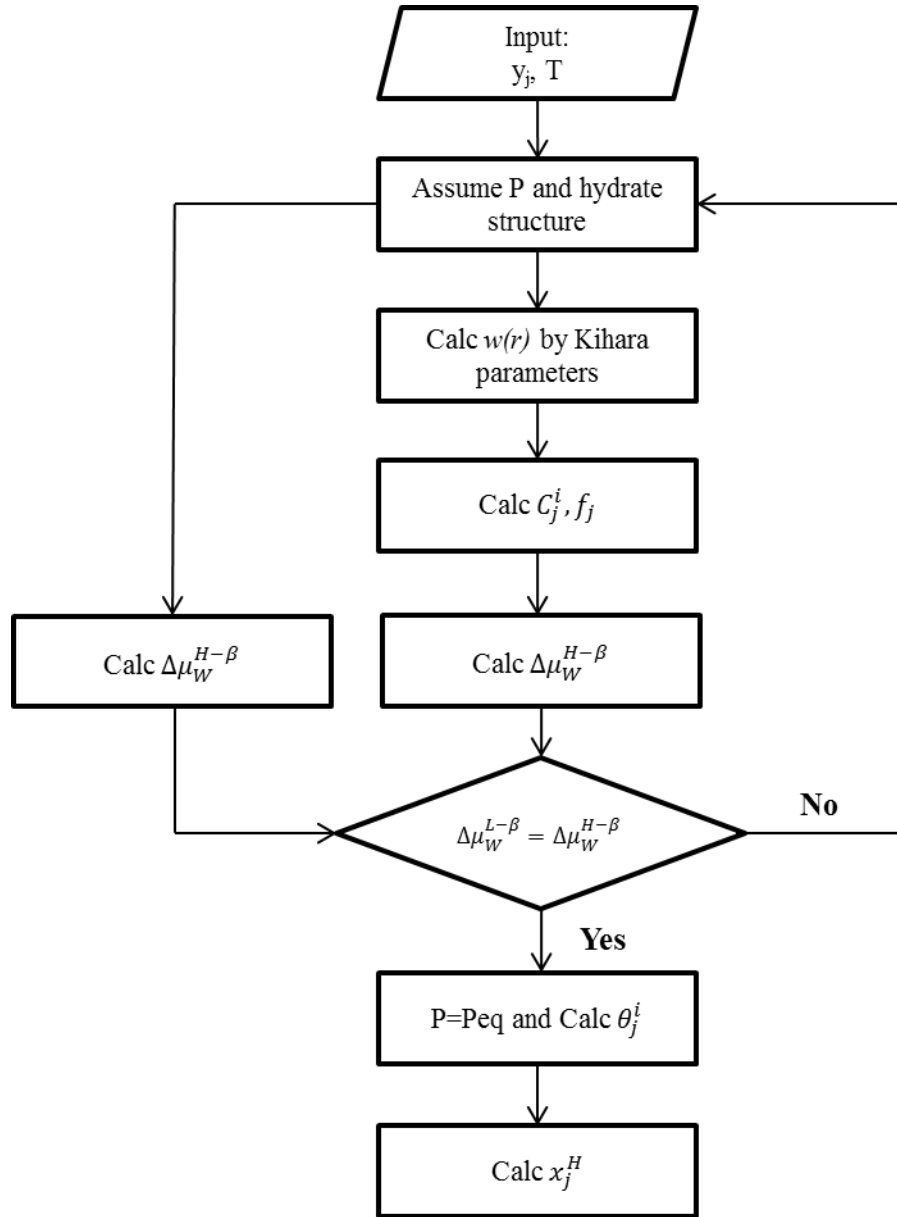


Figure 15. The procedure for calculating hydrate equilibrium pressure and composition

The average deviations for pressure and hydrate composition have been calculated based on equations 19 and 20, respectively.

$$AADp\% = \frac{100}{N} \sum_i^N \left( \left| \frac{P_i^{exp} - P_i^{pre}}{P_i^{exp}} \right| \right) \quad (19)$$

$$AADc = \frac{1}{N} \sum_i^N (|x_i^{exp} - x_i^{pre}|) \quad (20)$$

where  $i$  is equilibrium point,  $N$  total number of equilibrium points,  $P$  pressure,  $x$  hydrate composition,  $exp$  experimental data and  $pre$  prediction results.  $AAD_p$  and  $AAD_c$  are average absolute deviations for equilibrium pressure and hydrate composition, respectively.

### 2.2.2.5. Kihara parameters determination by GasHyDyn

All the thermodynamic modelling part (section 2.2.5) has been implemented in our in-house software, GasHyDyn. This software has shown a very good capability of liquid-hydrate equilibrium predictions [113,121], and will be used to discuss the experimental results for both pressure and hydrate composition. The procedure of submitting a calculation in GasHyDyn is illustrated in Figure 16.

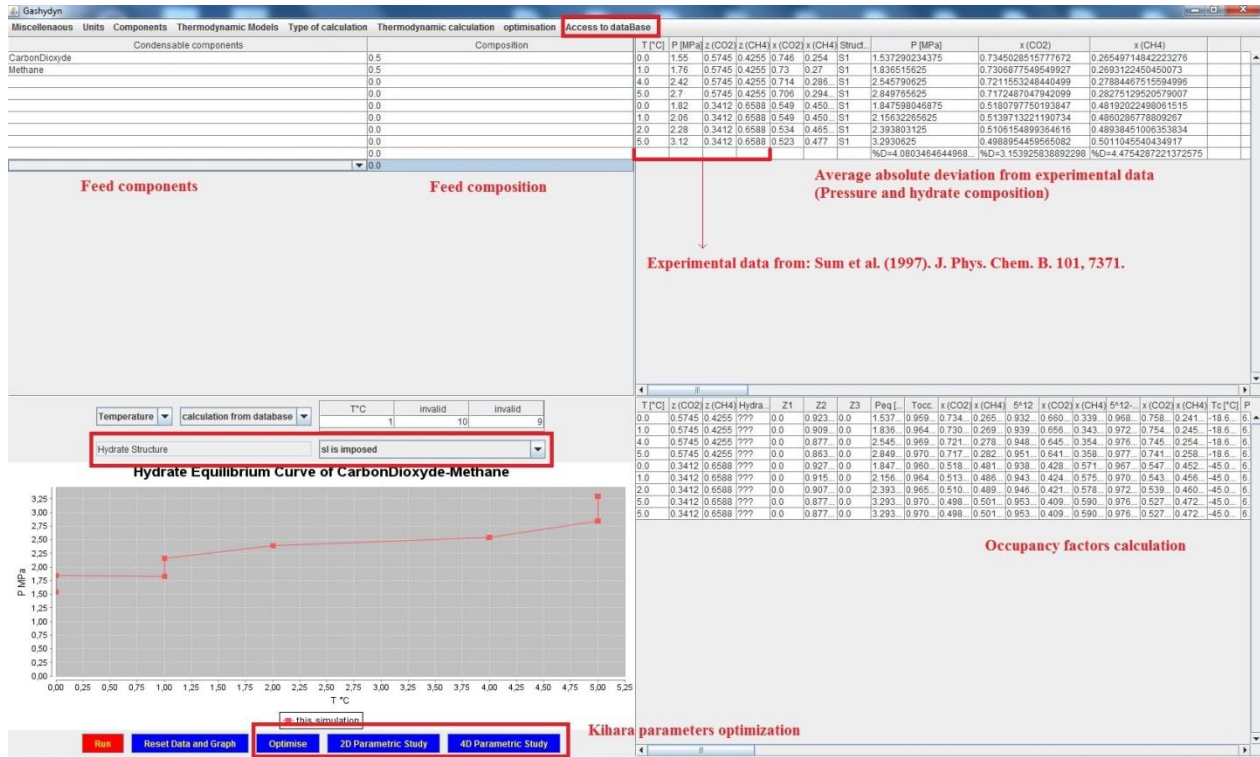
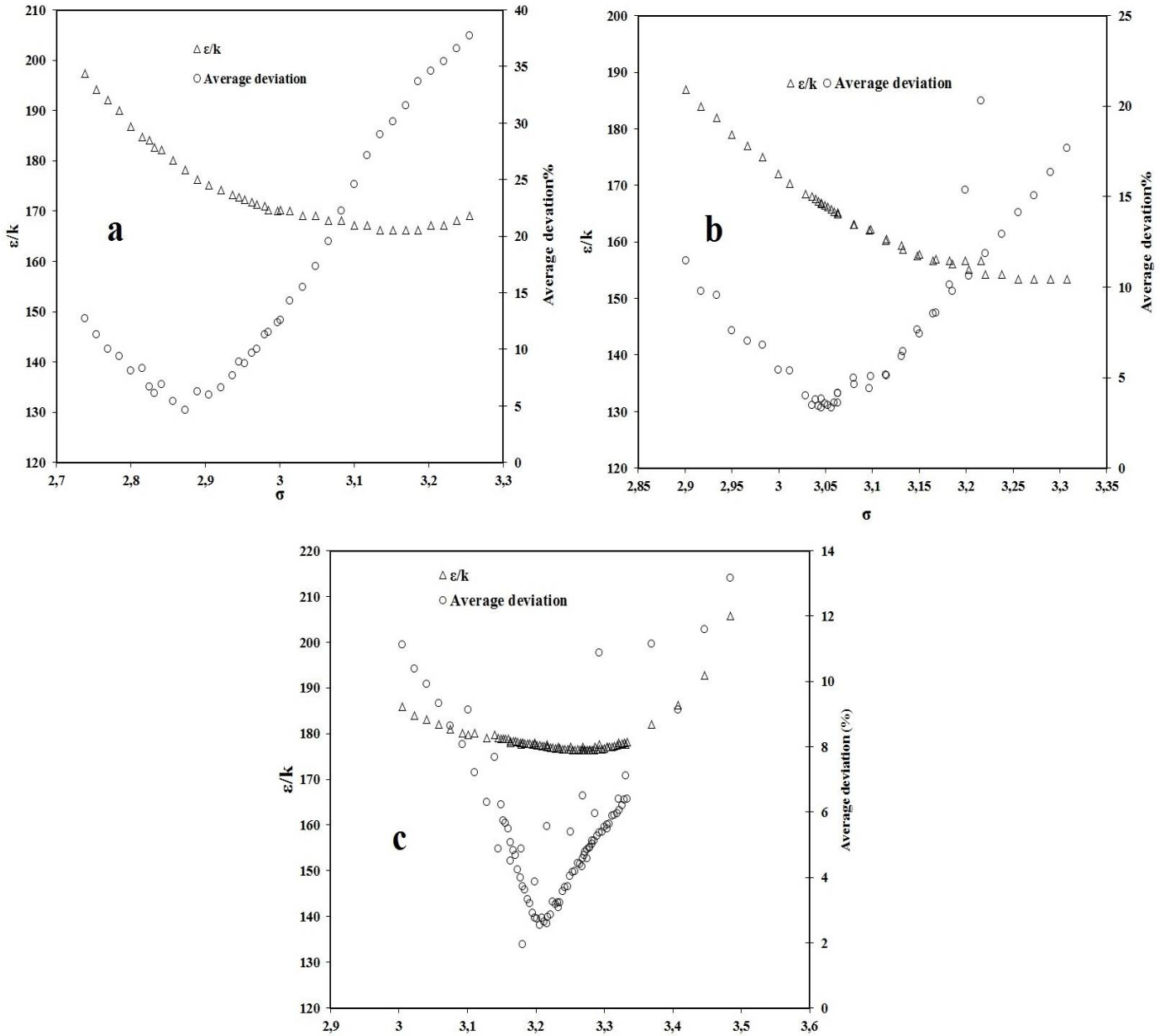


Figure 16. A typical procedure of submitting a calculation in GasHyDyn and provided results

Moreover, Kihara parameters of pure  $N_2$ , pure  $CO_2$ , pure  $CH_4$  and pure  $C_2H_6$  hydrates have been also retrieved from a wide range of temperature and pressure by our research team and presented elsewhere [120,121]. A brief illustration of the results is provided in Figure 17 (the optimization result for  $N_2$  was only provided in table).



**Figure 17.**  $\epsilon/k$  versus  $\sigma$  at the minimum deviation with experimental data for: a) CO<sub>2</sub> [120], b) CH<sub>4</sub> [120] and c) C<sub>2</sub>H<sub>6</sub> [121]

As the figure shows, in all cases, the average deviation provides a clear minimum which is considered as the best values of  $\epsilon/k$  and  $\sigma$  for each guest molecule. The optimized Kihara parameters were then used to simulate the simple hydrate equilibrium data and good accordance with experimental data has been obtained. The values of Kihara parameters for gases used in this study have been already presented in Table 5.



### **2.2.5.6. Comments on the modeling**

In equation 16,  $z$  is the total number of water molecules per cavity (coordination number) and  $R$  the free cavity radius. Their values were already measured by x-ray diffraction and informed by Sloan and Koh [1]. It should be noted that, the values of  $z$  and  $R$  do never change according to the type of guest molecules. Furthermore, the model supposes that there is only one guest molecule at each cavity and the guest molecules do not deform the cavities. The guest-guest interaction has been also neglected. In addition, it was assumed that the internal motion function of the guest molecules in the cavities is similar to an ideal gas. This means that the guest enclathration has no significant impacts on vibrational or electronic energies [1].

Moreover, several assumptions have been taken into account for the Langmuir adsorption analogy. First, the enclathration of guest molecules takes place at separate cavities on the crystal unit cell. Secondly, the energy of enclathration does not depend on the presence of the other molecules. Finally, the dissociation rate is only governed by the amount of guest molecules in the crystal unit cell [1].

## **2.3. Non-equilibrium crystallization of mixed gas hydrates; experimental clues and modeling evidence**

The driving force for clathrate hydrate formation is normally defined as difference in temperature or pressure from the equilibrium conditions. Since the driving force controls the kinetics of hydrate formation process, it is of great importance. Hence, concerns have been raised about the kinetic effects on clathrate hydrates formation and composition since cage occupancy and consequently hydrate composition depends on local fluid composition which can change during the crystallization [122].

Kvamme et al. [123] reported that mixed gas hydrates might not be theoretically reached at equilibrium by reassessing the Gibbs phase rule and the laws of thermodynamics. According to their investigations based on coupling the classical thermodynamic and molecular dynamics simulations, they stated that crystallization occurs not only in the bulk, but also at interfaces in the system or gas phase. Consequently, the driving force could be different due to diverging chemical potentials. Therefore, the Gibbs phase rule could over-determine the thermodynamic equilibrium without considering existence of any unforeseen phases.

Before going any further, let us state that thermodynamic equilibrium is the most stable state, the one that minimizes free energy of the system. Therefore, we consider that the system can reach an equilibrium point (no longer any change in state parameters), without being at thermodynamic equilibrium, as stated by Kvamme et al. [123]. Thus, it is metastable.

Some evidence shows how a metastable system could evolve toward a most stable state, or stay as it is. For instance, there are several indications of structural transition or co-existence of different structures during the crystallization of mixed gas hydrates.

Subramanian et al. [88,89] and Uchida et al. [124] reported structural transition from sI to sII for methane-ethane mixture under certain range of vapor compositions. Schicks and Ripmeester [125] observed both sI and sII methane hydrate under moderate conditions. In addition, Herri et al. [126] and Peytavi et al. [127] experimentally investigated that the mass transfer limitation from gas to aqueous solution could hinder the crystallization process. Therefore, the guest composition in liquid phase appears mainly driven by kinetics. Hence, guest distribution in the hydrate phase should be affected during crystal growth.

Murphy and Roberts [128] studied the fluid inclusion in CO<sub>2</sub>-rich gases and reported that there was not a single homogenous equilibrium clathrate composition. In fact, clathrate may form in different phases in the system with different compositions. Finally, they concluded that clathrate composition does not change quickly after crystallization.

Salamatin et al. [129] studied mathematically the gas diffusion during gas replacement process by “hole-in-cage-wall” diffusive mechanism. They showed that gas exchange could be started by a rapid crystallization of a hydrate layer on the hydrate surface and then it can be continued by a much slower permeation process. Molecular dynamics simulation also support the idea that the hydrate structure that forms is not necessarily the most stable one, but the one that show the highest growth rate [130–134]. According to these studies, the question then arises, “Is thermodynamic equilibrium reached in short term processes?”

Our previous investigations on mixed hydrates showed this non-equilibrium phenomenon while comparing different crystallization rates [121,135]. Some of these experiments have been simulated with a “non-equilibrium flash model” with some success [136].

## 2.4. Motivations and objectives

Most previous studies on mixed gas hydrates have only focused on classic P-T-y measurements (y stands for guest composition in gas phase) of mixed gas hydrates at thermodynamic equilibrium. Nonetheless, there has been little discussion about hydrate composition and volume at equilibrium due to their difficulties of measurements. Thus, it was the first motivation of this work to investigate experimentally vapor-liquid-hydrate equilibrium data (V-L<sub>w</sub>-H) for different mixed gas hydrates, not only at equilibrium but also during the crystallization at non-equilibrium conditions. Furthermore, the available data in literature on guest composition in hydrate phase was also reviewed and discussed. Then, the capability of thermodynamic modeling to simulate hydrate pressure and composition was investigated and evaluated.

Furthermore, although several studies report data at final state of equilibrium for gas hydrates, is thermodynamic equilibrium actually reached? How does the rate of crystallization affect the final state? Hence, the second motivation of this thesis was to study the influence of the crystallization rate on the final state of a system in a closed batch reactor. The results include not only the classical temperature-pressure, but also hydrate composition and volume, storage capacity, density and water conversion according to the rate of crystallization.

Given the fact that it is not practical to perform experiments for each gas mixture and composition, a thermodynamic model based on classical van der Waals and Platteeuw approach and Kihara potential (as explained in section 2.2.5) was chosen to investigate the effects of kinetics during the crystallization and final state. Obtaining a new set of Kihara parameters for propane was another objective of this work since the prediction results based on the sets of Kihara from literature had shown poor agreement with experimental data.

We aim that this study go some way towards enhancing our understanding of non-equilibrium crystallization of mixed gas hydrates as well as guest distribution in hydrate phase. In addition, the findings of this research could play an important role in design and development of application of gas hydrates which the assumption of thermodynamic equilibrium is made.

### **3. Capability of thermodynamic modeling to simulate hydrate composition**

#### **3.1. Introduction**

Numerous studies have investigated phase equilibria of clathrate hydrates [1,58,99,137–141]. Nonetheless, to the best of our knowledge, there are still few studies on the hydrate composition which depends on the pressure, temperature and gas phase composition. Thanks to gas chromatography, the composition of the gas phase can be easily measured, but solid phase analysis is still challenging, often leading to experimental errors. In addition, some researchers studied the hydrate composition of gas mixtures by different methods making them exceedingly difficult to compare. Indeed, quantifying hydrate equilibrium composition presents several obstacles such as water occlusion, heterogeneous solid phase and the analysis itself of the solid phase concentration [1]. Thus, experimental data on hydrate composition has been rare. However, these publications do include some valuable information about fundamental hydrate phase composition, enclathration process as well as guest distribution in hydrate phase. Hence, in the present chapter, studies providing hydrate composition in open literature were collected and presented. Moreover, the capability of thermodynamic modeling (by our in-house software, GasHyDyn, see section 2.2.5) to predict hydrate pressure and composition was evaluated to detect divergences from this standard approach and collected experimental data. Differences will be discussed, considering that experimental data may not be at thermodynamic equilibrium.

#### **3.2. Methods to measure hydrate composition**

In this section, the collected data from open literature is categorized based on their methods of hydrate composition measurements. This should be noted that there are some studies on the hydrate composition of gas mixtures that do not furnish exact values of hydrate composition. Sometimes, only figures are shown and quantitative data are not available.

It should be considered that the hydrate structure for modeling was chosen based on the statement of each research. Unfortunately in some cases, the authors did not provide the structure. Therefore, we simulated their experimental data for both structures I and II. Consequently, the structure which agreed better with the simulation results was chosen and presented. However, the

prediction results concerning the undesired structure were also provided in Appendix A, if required.

### **3.2.1. Dissociation of whole hydrate phase**

One of the first systematic reports on the mixed hydrate composition was carried out by Jhaveri and Robinson [68]. They studied the gas hydrate equilibrium curves of methane-nitrogen mixture as well as the guest composition in gas and hydrate phases. They introduced gas mixture and water inside a batch reactor at a pressure 25% more than the equilibrium pressure at a desired temperature. After completion of hydrate formation, the gas phase was analyzed chromatographically. The gas was then removed from the reactor and the hydrate crystals dissociated. The decomposed gas was analyzed to obtain the hydrate composition. They measured hydrate composition at three temperatures 273.2, 277.4 and 279.8K for various ranges of pressure and gas compositions. Their results are illustrated in Figure 18. Clearly, at a constant temperature, by increasing the molar composition of nitrogen in the gas phase, the equilibrium pressure increased. Since the hydrate equilibrium pressure of nitrogen at a desired temperature is higher than of methane. Moreover, the simulation results of equilibrium pressure were in a good accordance with the experimental data.

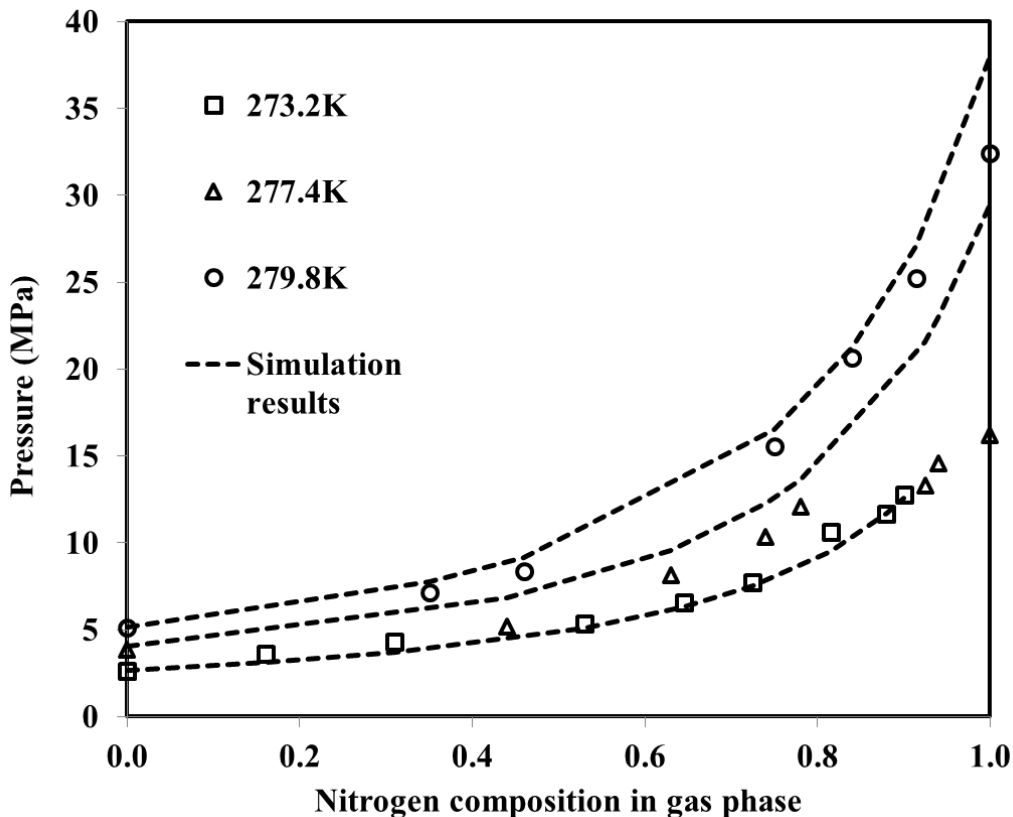


Figure 18. P-x diagram of nitrogen-methane mixed hydrate (sI) [68]

The results of thermodynamic simulation for hydrate pressure and composition are detailed in Table 6. At 273.2 K and 279.8 K, the equilibrium pressures are successfully predicted (by our software, GasHyDyn, readers are referred to section 2.2.5). Nonetheless, the equilibrium pressures at 277.4 K for nitrogen compositions more than 90%mol (in gas phase) were poorly simulated (sI). As nitrogen forms sII, we suspected a phase transition in this case. Hence, the experimental data were also simulated by considering sII (see Appendix A). The results revealed that sII simulations are also unsuccessful to predict the equilibrium pressures for the 277 K isotherm at high concentrations of nitrogen in the mixture of CH<sub>4</sub>/N<sub>2</sub>. This might be due to whether the co-existence of sI and sII at this condition (which cannot be predicted by the model as it is implemented in our software) or the experimental measurement uncertainties.

**Table 6. Experimental results of Jhaveri and Robinson [68] for methane-nitrogen mixture hydrates and simulation results (uncertainties not provided by the authors).**

T <sub>exp</sub> (K)	P <sub>exp</sub> (MPa)	P <sub>pre</sub> (MPa)	S	Gas composition (exp)		Hydrate composition (exp)		Hydrate composition (pre)	
				N <sub>2</sub>	CH <sub>4</sub>	N <sub>2</sub>	CH <sub>4</sub>	N <sub>2</sub>	CH <sub>4</sub>
273.2	2.640	2.660	I	0.000	1.000	0.000	1.000	0.000	1.000
273.2	3.620	3.116	I	0.160	0.840	0.065	0.935	0.034	0.966
273.2	4.310	3.708	I	0.310	0.690	0.098	0.902	0.078	0.922
273.2	5.350	5.092	I	0.530	0.470	0.200	0.800	0.176	0.824
273.2	6.550	6.301	I	0.645	0.355	0.350	0.650	0.259	0.741
273.2	7.750	7.517	I	0.725	0.275	0.425	0.575	0.339	0.661
273.2	10.640	9.525	I	0.815	0.185	0.620	0.380	0.466	0.534
273.2	11.650	11.716	I	0.880	0.120	0.710	0.290	0.597	0.403
273.2	12.770	12.577	I	0.900	0.100	0.765	0.235	0.646	0.354
277.4	3.860	4.028	I	0.000	1.000	0.000	1.000	0.000	1.000
277.4	5.200	6.839	I	0.440	0.560	0.180	0.820	0.138	0.862
277.4	8.110	9.575	I	0.630	0.370	0.310	0.690	0.262	0.738
277.4	10.340	12.286	I	0.740	0.260	0.470	0.530	0.378	0.622
277.4	12.060	13.628	I	0.780	0.220	0.560	0.440	0.433	0.567
277.4	13.320	21.582	I	0.925	0.075	0.810	0.190	0.734	0.266
277.4	14.590	22.950	I	0.940	0.060	0.860	0.140	0.779	0.221
277.4	16.210	29.486	I	1.000	0.000	1.000	0.000	1.000	0.000
279.8	5.140	5.161	I	0.000	1.000	0.000	1.000	0.000	1.000
279.8	7.140	7.751	I	0.350	0.650	0.091	0.909	0.102	0.898
279.8	8.370	9.170	I	0.460	0.540	0.224	0.776	0.155	0.845
279.8	15.550	16.516	I	0.750	0.250	0.550	0.450	0.404	0.596
279.8	20.670	21.253	I	0.840	0.160	0.680	0.320	0.549	0.451
279.8	25.230	27.054	I	0.914	0.086	0.802	0.198	0.715	0.285
279.8	32.420	37.997	I	1.000	0.000	1.000	0.000	1.000	0.000
<b>AADp</b>		<b>16.32%</b>		<b>AADc</b>				<b>0.067</b>	

The hydrate composition predictions are slightly different. The simulation results at low and high percentages of nitrogen in the hydrate phase agree satisfactorily with the experimental data. But when there is no significant difference between the compositions of methane and nitrogen, the

simulation results deviated from experimental. Still, the average absolute deviation of hydrate composition was less than 0.07 in mole fraction.

Kawasaki et al. [142] studied the guest content in hydrate phase for a gas mixture of methane, ethane, propane and iso-butane with initial molar concentrations 0.885, 0.046, 0.054 and 0.015, respectively. They used the same procedure as Jhaveri and Robinson [68] by removing the gas and dissociating the hydrate to measure the hydrate composition at two different temperatures, 274.15 and 278.15 K. The experimental and simulation results are presented in Table 7.

**Table 7. Gas composition in different phases at 3MPa (uncertainties not provided by the authors).**

Gas	T=274.15 K			T=278.15 K		
	Gas and hydrate phase compositions			Gas and hydrate phase compositions		
	Gas (exp)	Hydrate (exp)	Hydrate (Pre)	Gas (exp)	Hydrate (exp)	Hydrate (Pre)
Methane	0.987	0.760	0.827	0.979	0.702	0.784
Ethane	0.011	0.089	0.031	0.017	0.104	0.034
Propane	0.002	0.117	0.141	0.004	0.150	0.181
iso-Butane	0.0	0.034	N/A	0.0	0.044	N/A

The authors remarked that all i-butane molecules concentrated in the hydrate phase, irrespective of the temperature. In fact, it is supposed that the order of stabilization of hydrate structure is iso-butane, propane, ethane and methane. Thus, all the iso-butane molecules are encapsulated in solid phase to stabilize the hydrate structure. They also considered that the concentration of heavier hydrocarbon in hydrate phase at 278.15 K is higher at 274.15 K. Moreover, the deviation of simulation results for the hydrate composition of methane, ethane and propane were 0.074, 0.064 and 0.027, respectively. The deviations between the experimental and prediction values could be due to uncertainties in the experimental procedure. In fact, Kawasaki et al. removed the gas mixture from the reactor after hydrate formation to measure hydrate composition. Hence, the hydrate phase could be dissociated during the gas removing step due to the pressure drop, leading to the measurement uncertainties.

Kang et al. [143] measured the hydrate composition of CO<sub>2</sub>-N<sub>2</sub> mixture at three isotherms of vapor-hydrate equilibrium condition. After hydrate formation, they purged the gas outside the



cell and dissociated the hydrate by increasing temperature. Figure 19 presents the equilibrium pressure versus nitrogen composition in the gas phase at H-V equilibrium condition for three isotherms. Our simulation results are also shown by dash lines in the figure. The simulation of hydrate composition is detailed in Table 8 as well as the experimental results.

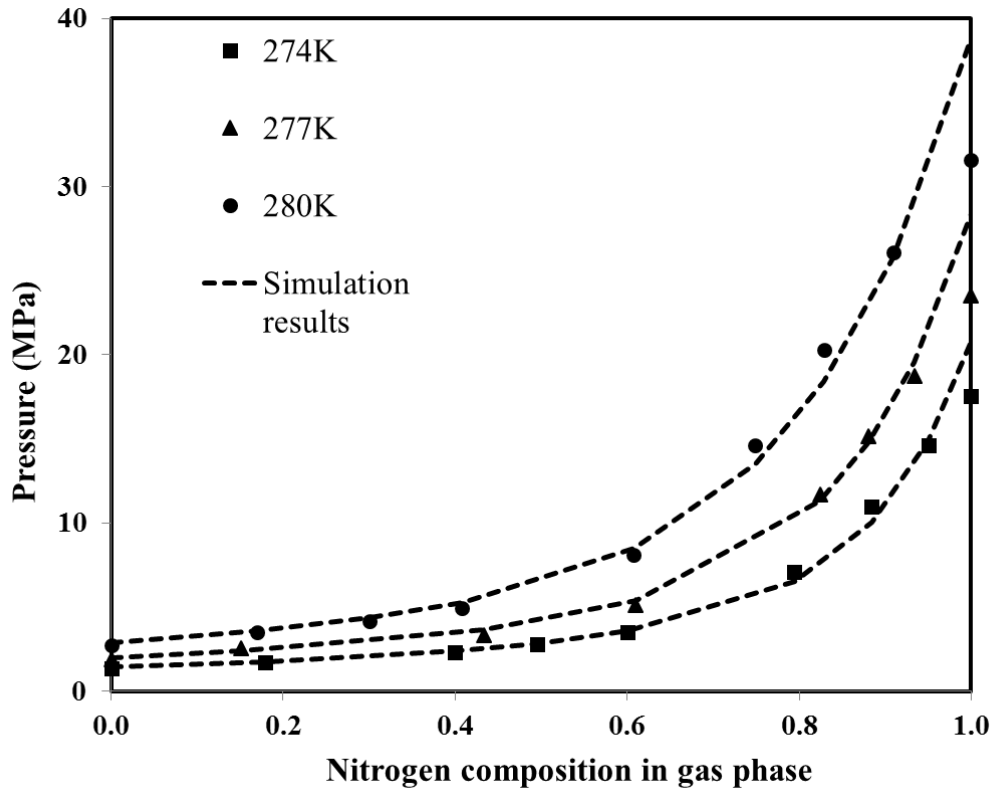


**Figure 19. Experimental H-V equilibrium data for N<sub>2</sub>/CO<sub>2</sub> mixture by Kang et al. [143] and the simulation results (sI)**

As Figure 19 and Table 8 indicate, the thermodynamic model acceptably predicted the equilibrium pressure (average deviation 6.5%). The hydrate composition simulation can be categorized in two parts. The first part is when carbon dioxide is dominant in the hydrate phase. In this case, the simulation results were well predicted (average absolute deviation for 13 equilibrium points was 0.016 mole fraction). When nitrogen is dominant in the hydrate phase, the average absolute deviation is 0.071 in mole fraction.

Indeed, pure carbon dioxide and pure nitrogen form sI and sII, respectively. Thus, a mixture of these two hydrate formers at high concentration of nitrogen is generally expected to form sII.

Nonetheless, the model based on sI fits pretty well with data of Kang et al. [143], even at high concentration of nitrogen in vapor phase. On the other hand, although hydrate composition is also well simulated by considering sII, pressure by according to sII is poorly predicted (see Appendix A).

**Table 8. Experimental results of Kang et al. [143] and simulation (composition uncertainties not provided by the authors).**

T <sub>exp</sub> (K) (±0.1)	P <sub>exp</sub> (MPa) (±0.01)	P <sub>pre</sub> (MPa)	S	Gas composition (exp)		Hydrate composition (exp)		Hydrate composition (pre)	
				CO <sub>2</sub>	N <sub>2</sub>	CO <sub>2</sub>	N <sub>2</sub>	CO <sub>2</sub>	N <sub>2</sub>
274.0	1.36	1.42	I	1.00	0.00	1.00	0.00	1.00	0.00
274.0	1.73	1.74	I	0.82	0.18	0.99	0.02	0.98	0.02
274.0	2.30	2.39	I	0.60	0.40	0.95	0.05	0.94	0.06
274.0	2.77	2.84	I	0.50	0.50	0.93	0.07	0.92	0.08
274.0	3.48	3.57	I	0.40	0.60	0.90	0.10	0.87	0.13
274.0	7.07	6.55	I	0.21	0.79	0.58	0.42	0.71	0.29
274.0	10.95	10.03	I	0.12	0.88	0.34	0.66	0.53	0.47
274.0	14.59	14.91	I	0.05	0.95	0.18	0.82	0.28	0.72
274.0	17.52	20.81	I	0.00	1.00	0.00	1.00	0.00	1.00
277.0	1.91	1.99	I	1.00	0.00	1.00	0.00	1.00	0.00
277.0	2.54	2.38	I	0.85	0.15	0.98	0.02	0.98	0.02
277.0	3.30	3.65	I	0.57	0.43	0.95	0.05	0.93	0.07
277.0	5.12	5.40	I	0.39	0.61	0.89	0.11	0.85	0.15
277.0	11.71	11.30	I	0.18	0.82	0.54	0.46	0.62	0.38
277.0	15.15	14.81	I	0.12	0.88	0.35	0.65	0.49	0.51
277.0	18.74	19.56	I	0.07	0.93	0.19	0.81	0.31	0.69
277.0	23.50	28.37	I	0.00	1.00	0.00	1.00	0.00	1.00
277.0	1.91	1.99	I	1.00	0.00	1.00	0.00	1.00	0.00
277.0	2.54	2.38	I	0.85	0.15	0.98	0.02	0.98	0.02
280.0	2.74	2.86	I	1.00	0.00	1.00	0.00	1.00	0.00
280.0	3.52	3.57	I	0.83	0.17	0.98	0.02	0.98	0.02
280.0	4.14	4.35	I	0.70	0.30	0.96	0.04	0.95	0.05
280.0	4.95	5.29	I	0.59	0.41	0.94	0.06	0.92	0.08
280.0	8.09	8.50	I	0.39	0.61	0.86	0.14	0.83	0.17
280.0	14.64	13.50	I	0.25	0.75	0.64	0.36	0.68	0.32

280.0	20.29	18.39	I	0.17	0.83	0.45	0.55	0.55	0.45
280.0	26.09	25.74	I	0.09	0.91	0.22	0.78	0.35	0.65
280.0	31.58	38.81	I	0.00	1.00	0.00	1.00	0.00	1.00
<b>AADp</b>		<b>6.5%</b>	<b>AADc</b>				<b>0.04</b>		

### 3.2.2. Material balance and volumetric properties evaluated from equation of state

Ohgaki et al. investigated the phase equilibrium of carbon dioxide-methane hydrate at 280.3 K [24]. They obtained the guest composition in gas, liquid and hydrate phases at isothermal conditions in a batch reactor. Their experimental procedure is briefly described as follows: They injected separately carbon dioxide and methane to the reactor. Pure water was then introduced to the reactor. The amount of each material was weighed. Thanks to a gas chromatograph, they determined the gas composition of carbon dioxide and methane at equilibrium temperature and pressure. The solubility of carbon dioxide and methane in water was calculated based on Henry constants. They assumed that the general formula for mixed carbon dioxide-methane hydrate is  $zCO_2 \cdot (1 - z) \cdot qH_2O$ , where  $z$  is the mole fraction of carbon dioxide in hydrate phase and  $q$  is the hydration number at ideal condition. They also hypothesized that the molar volume of hydrate is  $130.1 \text{ cm}^3/\text{mol}$  [24]. They calculated the volumetric properties from Soave-Redlich-Kwong equation of state or IUPAC recommended equation of state for carbon dioxide and methane [24,119,144,145]. The hydrate compositions were then calculated by the material balance.

Figure 20 shows their experimental results for hydrate phase composition and our simulation results. Furthermore, they observed that at each equilibrium condition, the mole fraction of carbon dioxide in hydrate phase is significantly larger than in gas phase. Hence, based on the idea of methane exploration by carbon dioxide injection and by defining the average distribution coefficient of methane, they concluded that methane in hydrate phase can be replaced by carbon dioxide; as a result, methane concentration in the gas phase will be increased.

Table 9 summarizes the experimental and modeling results by details for carbon dioxide-methane hydrate at 280.3 K.

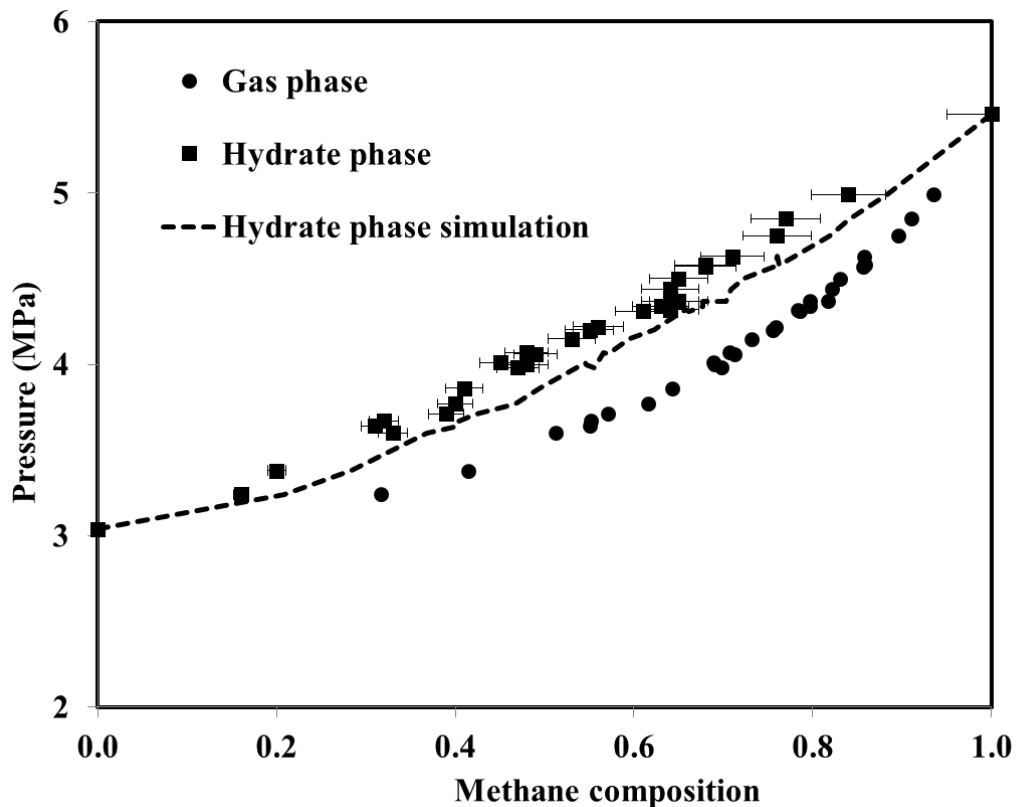


Figure 20. Carbon dioxide-methane hydrates phase equilibria at 280.3 K. Experimental [24] and simulation results (sl). Error bars correspond to the standard uncertainty of experimental hydrate composition.

Table 9. Experimental data of Ohgaki et al. [24] for CH<sub>4</sub>/CO<sub>2</sub> mixture hydrates and simulation results.

P <sub>exp</sub> (MPa) (±0.005)	P <sub>pre</sub> (MPa)	S	Gas composition (exp)		Hydrate composition (exp) (±5%)		Hydrate composition (pre)	
			CO <sub>2</sub>	CH <sub>4</sub>	CO <sub>2</sub>	CH <sub>4</sub>	CO <sub>2</sub>	CH <sub>4</sub>
3.04	2.98	I	1.00	0.00	1.00	0.00	1.00	0.00
3.24	3.46	I	0.68	0.32	0.84	0.16	0.79	0.21
3.38	3.55	I	0.59	0.42	0.80	0.20	0.72	0.28
3.60	3.85	I	0.49	0.51	0.67	0.33	0.63	0.37
3.64	3.93	I	0.45	0.55	0.69	0.31	0.60	0.40
3.67	3.93	I	0.45	0.55	0.68	0.32	0.60	0.40
3.71	3.98	I	0.43	0.57	0.61	0.39	0.58	0.42
3.77	4.09	I	0.38	0.62	0.60	0.40	0.53	0.47
3.86	4.16	I	0.36	0.64	0.59	0.41	0.50	0.50
4.22	4.49	I	0.24	0.76	0.44	0.56	0.37	0.63
4.31	4.57	I	0.22	0.79	0.39	0.61	0.34	0.66

4.32	4.57	I	0.22	0.78	0.36	0.64	0.34	0.66	
4.34	4.61	I	0.20	0.80	0.37	0.63	0.32	0.68	
4.37	4.61	I	0.20	0.80	0.35	0.65	0.32	0.68	
4.37	4.68	I	0.18	0.82	0.36	0.64	0.30	0.70	
4.44	4.70	I	0.18	0.82	0.36	0.64	0.29	0.71	
4.50	4.73	I	0.17	0.83	0.35	0.65	0.28	0.72	
4.57	4.82	I	0.14	0.86	0.32	0.68	0.24	0.76	
3.98	4.31	I	0.30	0.70	0.53	0.47	0.44	0.56	
4.00	4.29	I	0.31	0.69	0.52	0.48	0.45	0.55	
4.01	4.28	I	0.31	0.69	0.55	0.45	0.45	0.55	
4.06	4.35	I	0.29	0.71	0.51	0.49	0.43	0.57	
4.07	4.33	I	0.29	0.71	0.52	0.48	0.43	0.57	
4.15	4.41	I	0.27	0.73	0.47	0.53	0.41	0.59	
4.20	4.48	I	0.25	0.76	0.45	0.55	0.38	0.62	
4.58	4.83	I	0.14	0.86	0.32	0.68	0.24	0.76	
4.63	4.83	I	0.14	0.86	0.29	0.71	0.24	0.76	
4.75	4.96	I	0.10	0.90	0.24	0.76	0.18	0.82	
4.85	5.03	I	0.09	0.91	0.23	0.77	0.16	0.84	
4.99	5.14	I	0.07	0.94	0.16	0.84	0.12	0.88	
5.46	5.44	I	0.00	1.00	0.00	1.00	0.00	1.00	
<b>AADp</b>	<b>5.8%</b>		<b>AADc</b>				<b>0.06</b>		

The simulation results agreed well with the experimental data for hydrate equilibrium pressure (AADp 5.8%). Additionally, the mole fraction deviation of hydrate composition calculations was about 0.06.

Belandria et al. investigated the compositional analysis of carbon dioxide-methane hydrate by the same method as Ohgaki et al. [24,146]. Our simulation results based on the experimental data of Belandria et al. are presented in Table 10 and Figure 21. As it is clear on the table, the thermodynamic model predicted hydrate equilibrium pressure with an acceptable error (7.8%). Although the hydrate composition simulation had mostly an adequate agreement with the data obtained, several experimental equilibrium points were poorly simulated (for instance 280 K and 3.54MPa). Additionally, they reported that CSMGem model was not capable to converge three

phase flash calculations in some cases, in comparison, the thermodynamic model had no problem with three phase flash calculations [146].

**Table 10. Experimental results of Belandria et al. [146] for methane-carbon dioxide hydrates and simulation results.**

T (K) (±0.02)	P <sub>exp</sub> (MPa) (±0.002)	P <sub>pre</sub> (MPa)	S	Gas composition (exp)		Hydrate composition (exp) (±1%)		Hydrate composition (pre)	
				CO <sub>2</sub>	CH <sub>4</sub>	CO <sub>2</sub>	CH <sub>4</sub>	CO <sub>2</sub>	CH <sub>4</sub>
273.6	2.44	2.55	I	0.08	0.92	0.10	0.90	0.16	0.84
273.6	1.84	2.03	I	0.35	0.66	0.55	0.45	0.52	0.48
273.6	1.94	2.12	I	0.29	0.71	0.39	0.61	0.46	0.54
273.6	2.05	2.24	I	0.22	0.78	0.29	0.71	0.37	0.63
273.6	1.51	1.67	I	0.63	0.37	0.88	0.12	0.77	0.23
273.6	1.61	1.77	I	0.55	0.46	0.80	0.20	0.71	0.29
275.2	2.58	2.77	I	0.17	0.83	0.34	0.66	0.29	0.71
275.2	2.77	2.98	I	0.09	0.91	0.18	0.82	0.16	0.84
275.2	2.12	2.33	I	0.38	0.62	0.65	0.35	0.56	0.44
275.2	2.22	2.48	I	0.30	0.70	0.59	0.41	0.47	0.53
275.2	2.40	2.63	I	0.23	0.77	0.37	0.63	0.38	0.62
275.2	1.79	1.96	I	0.66	0.34	0.83	0.17	0.79	0.21
275.2	1.87	2.07	I	0.57	0.44	0.75	0.25	0.72	0.28
276.1	2.81	3.00	I	0.18	0.82	0.26	0.74	0.31	0.69
276.1	3.03	3.12	I	0.13	0.87	0.24	0.76	0.24	0.76
276.1	3.03	3.23	I	0.10	0.90	0.24	0.76	0.18	0.82
276.1	2.32	2.43	I	0.41	0.60	0.64	0.36	0.57	0.43
276.1	2.50	2.70	I	0.32	0.69	0.40	0.60	0.48	0.52
276.1	2.69	2.88	I	0.23	0.77	0.31	0.69	0.38	0.62
276.1	1.99	2.14	I	0.67	0.33	0.88	0.12	0.80	0.20
276.1	2.17	2.26	I	0.58	0.42	0.78	0.22	0.73	0.27
278.1	3.42	3.64	I	0.20	0.80	0.23	0.77	0.33	0.67
278.1	3.63	3.83	I	0.14	0.86	0.23	0.78	0.24	0.76
278.1	3.80	3.95	I	0.10	0.90	0.15	0.85	0.19	0.81
278.1	3.04	3.33	I	0.32	0.68	0.46	0.54	0.48	0.52
278.1	3.32	3.55	I	0.23	0.77	0.27	0.73	0.37	0.63
278.1	2.58	2.77	I	0.61	0.39	0.79	0.21	0.74	0.26
279.2	3.57	4.09	I	0.20	0.80	0.27	0.73	0.33	0.67

280.2	4.49	4.76	I	0.15	0.85	0.31	0.69	0.25	0.75	
280.2	4.66	4.90	I	0.11	0.89	0.25	0.76	0.19	0.81	
280.2	3.54	4.14	I	0.34	0.66	0.73	0.27	0.49	0.51	
280.2	4.11	4.46	I	0.24	0.77	0.34	0.66	0.37	0.63	
280.2	3.14	3.53	I	0.62	0.38	0.86	0.14	0.74	0.26	
280.2	3.48	3.75	I	0.49	0.51	0.79	0.21	0.64	0.36	
282.2	5.77	6.08	I	0.11	0.89	0.28	0.72	0.19	0.81	
284.2	7.19	7.65	I	0.12	0.89	0.11	0.89	0.18	0.82	
<b>AADp</b>		<b>7.8%</b>	<b>AADc</b>					<b>0.07</b>		

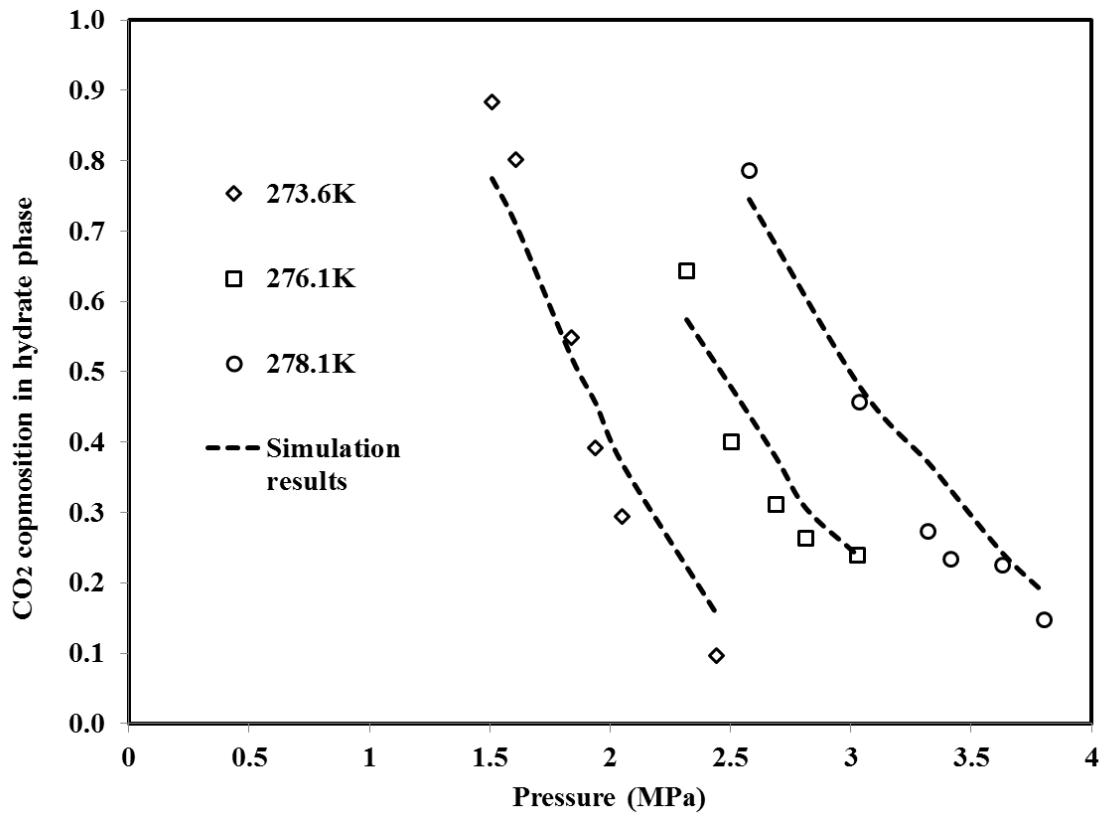


Figure 21. Hydrate composition for methane-carbon dioxide hydrates. Experimental data [146] and simulation results (sI).

Belandria et al. also studied the hydrate composition of carbon dioxide-nitrogen mixture using the same method [24,147]. They calculated the guest composition in gas, liquid and hydrate phases based on the material balance and volumetric properties evaluated from equation of state. Table 11 details their experimental data and our simulation results. Moreover, Figure 22

illustrates the experimental [147] and simulation results for two isotherms of N<sub>2</sub>/CO<sub>2</sub> binary hydrates.

**Table 11. Experimental results of Belandria et al. [147] for nitrogen-carbon dioxide mixed hydrate and simulation results.**

T (K) (±0.02)	P <sub>exp</sub> (MPa) (±0.002)	P <sub>pre</sub> (MPa)	S	Gas composition (exp)		Hydrate composition (exp) (±1%)		Hydrate composition (pre)	
				CO <sub>2</sub>	N <sub>2</sub>	CO <sub>2</sub>	N <sub>2</sub>	CO <sub>2</sub>	N <sub>2</sub>
273.6	2.03	2.22	I	0.62	0.38	0.97	0.03	0.95	0.05
273.6	8.15	7.22	I	0.17	0.83	0.66	0.34	0.66	0.34
273.6	11.94	6.94	I	0.18	0.82	0.37	0.63	0.67	0.33
273.6	2.96	3.17	I	0.43	0.57	0.90	0.10	0.89	0.11
274.6	2.54	2.10	I	0.73	0.27	0.74	0.26	0.97	0.03
274.9	5.20	2.21	I	0.72	0.28	0.79	0.21	0.96	0.04
275.2	2.29	2.51	I	0.66	0.34	0.90	0.10	0.95	0.05
275.2	2.64	2.25	I	0.73	0.27	0.89	0.11	0.97	0.03
275.2	3.26	3.69	I	0.45	0.55	0.88	0.12	0.89	0.11
275.2	7.45	8.83	I	0.17	0.83	0.82	0.18	0.64	0.36
275.2	8.25	8.74	I	0.18	0.82	0.80	0.20	0.65	0.35
275.2	12.75	9.32	I	0.16	0.84	0.38	0.62	0.62	0.38
275.6	2.71	2.36	I	0.73	0.27	0.76	0.24	0.97	0.03
275.8	5.38	2.45	I	0.72	0.28	0.80	0.20	0.96	0.04
276.1	2.50	2.69	I	0.68	0.32	0.98	0.02	0.96	0.04
276.1	2.87	2.50	I	0.73	0.27	0.79	0.21	0.97	0.03
276.1	3.70	3.80	I	0.49	0.51	0.70	0.30	0.90	0.10
276.1	4.40	4.70	I	0.40	0.60	0.69	0.31	0.86	0.14
276.1	8.58	9.07	I	0.20	0.80	0.57	0.43	0.67	0.33
276.7	3.70	4.11	I	0.49	0.51	0.70	0.30	0.90	0.10
277.1	2.71	2.94	I	0.71	0.30	0.84	0.16	0.96	0.04
277.3	3.13	2.89	I	0.73	0.27	0.83	0.17	0.96	0.04
277.8	6.16	3.01	I	0.75	0.25	0.86	0.14	0.97	0.03
278.1	2.97	3.21	I	0.73	0.27	0.89	0.11	0.96	0.04
278.1	3.41	3.19	I	0.73	0.27	0.75	0.25	0.96	0.04
278.1	4.19	4.63	I	0.52	0.48	0.66	0.35	0.91	0.09
278.1	9.15	10.69	I	0.23	0.77	0.54	0.46	0.69	0.31
278.1	14.26	16.69	I	0.13	0.87	0.51	0.49	0.49	0.51



279.7	4.82	5.42	I	0.56	0.44	0.70	0.30	0.91	0.09	
279.7	10.02	12.26	I	0.26	0.74	0.61	0.39	0.71	0.29	
279.7	15.82	19.25	I	0.15	0.85	0.55	0.45	0.50	0.50	
281.2	17.63	21.78	I	0.18	0.82	0.58	0.42	0.53	0.47	
281.7	6.33	5.22	I	0.75	0.25	0.81	0.19	0.96	0.04	
<b>AADp</b>		<b>17.4%</b>	<b>AADc</b>					<b>0.13</b>		

From Table 11 and Figure 22, notice that neither equilibrium pressure nor hydrate composition were well simulated. Nevertheless, at equilibrium pressures below 7MPa, the simulation results were satisfactory. In contrast, equilibrium pressures more than 7MPa were poorly simulated. In the case of hydrate composition, the average deviation was large ( $\pm 0.13$  mole fraction) compared to the simulation of experimental data of Kang et al. ( $\pm 0.04$  mole fraction) for the same mixture. This divergence might be due to different experimental procedures.

This should be considered that thermodynamic model based on sII hydrate do not also adequately fit with the experimental data of Belandria et al. [147] (see Appendix A). This should be due to whether phase transition and/or co-existence of structures or uncertainties in measurements. However our modeling results for CO<sub>2</sub>/N<sub>2</sub> mixtures based on the experimental data of Seo et al. [148] showed that a phase transition seems to be probable at high concentration of nitrogen.

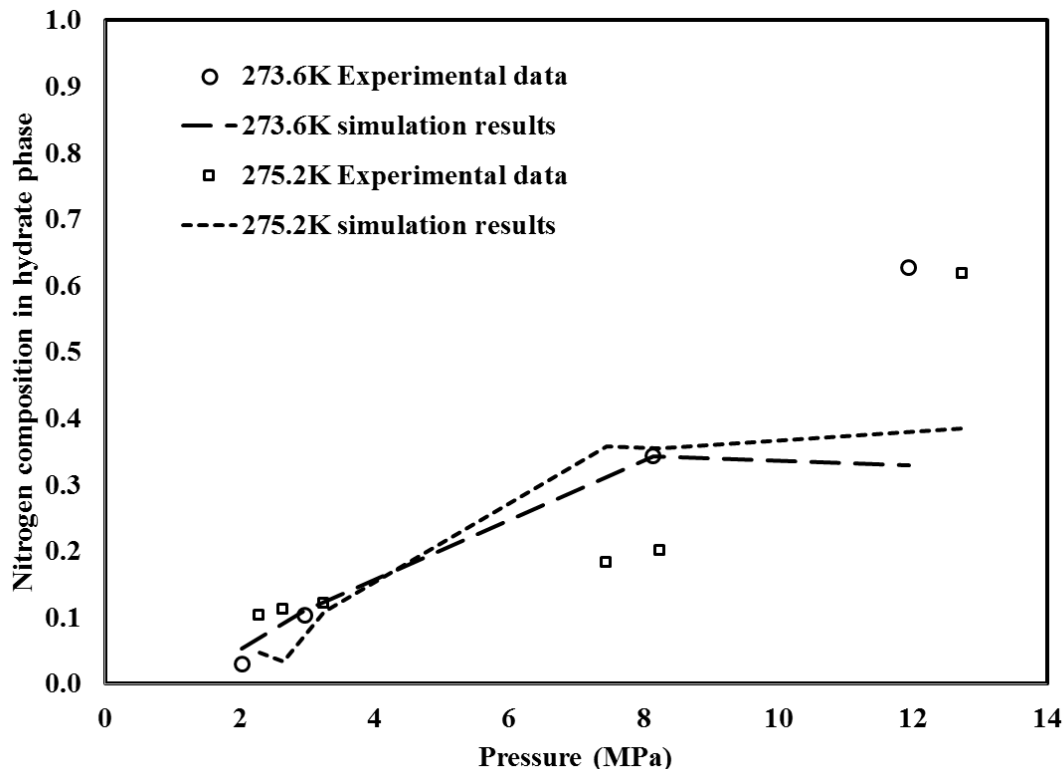


Figure 22. Hydrate composition for nitrogen-carbon dioxide hydrates at two isotherms. Experimental data [147] and simulation results (sI).

### 3.2.3. Gas uptake at isobaric equilibrium condition

Seo et al. studied the vapor-liquid-hydrate equilibrium conditions of nitrogen-carbon dioxide and methane-carbon dioxide mixtures at isobaric condition [148]. They performed their experiments in a batch reactor by injecting gas mixtures and water by a syringe pump at a desired pressure. Then they decreased the temperature to 5 K below the hydrate formation temperature. Hydrate formation led to a decrease in pressure. In order to keep it constant, they recharged the reactor by the gas mixtures. Then, they increased the temperature by the rate of 1-2 K per hour. The pressure then increased due to hydrate dissociation. Later, the dissociated gases were vented. When only a small amount of hydrate crystals remained in the cell, at a constant pressure, this was considered to be the three phase equilibrium [148]. Both their experimental and our simulation results for nitrogen-carbon dioxide mixture are listed and presented in Table 12 and Figure 23. Moreover, the results for methane-carbon dioxide mixture are presented in Table 13.

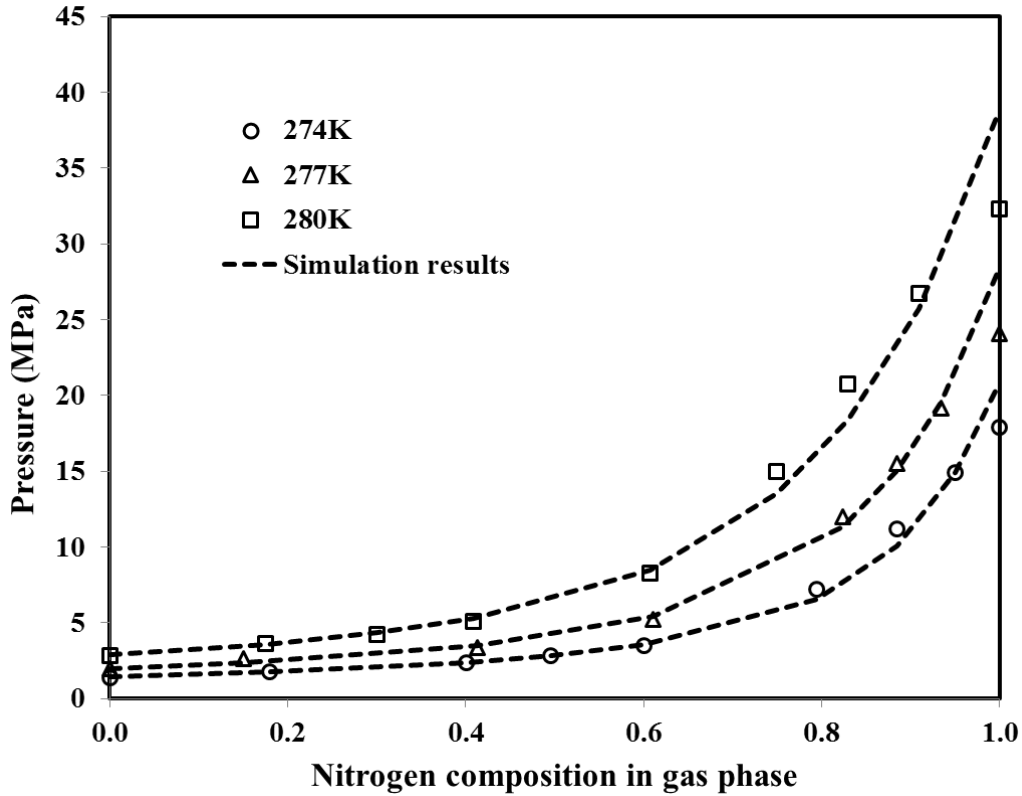


Figure 23. Pressure-gas composition diagram for nitrogen-carbon dioxide at three isotherms (sI).  
Experimental data from Seo et al. [148] and our prediction results

Table 12. Experimental results of carbon dioxide-nitrogen hydrate equilibrium pressure and composition from Seo et al. [148] and our simulation results (composition uncertainties not provided by authors).

T (K) (±0.1)	P <sub>exp</sub> (MPa) (±0.01)	P <sub>pre</sub> (MPa)	S	Gas composition (exp)		Hydrate composition (exp)		Hydrate composition (pre)	
				CO <sub>2</sub>	N <sub>2</sub>	CO <sub>2</sub>	N <sub>2</sub>	CO <sub>2</sub>	N <sub>2</sub>
274	1.39	1.42	I	1.00	0.00	1.00	0.00	1.00	0.00
274	1.77	1.74	I	0.82	0.18	0.99	0.02	0.98	0.02
274	2.35	2.39	I	0.60	0.40	0.95	0.05	0.94	0.06
274	2.84	2.84	I	0.50	0.50	0.93	0.07	0.92	0.08
274	3.46	3.57	I	0.40	0.60	0.90	0.10	0.87	0.13
274	7.24	6.55	I	0.21	0.79	0.58	0.42	0.71	0.29
274	11.20	10.03	I	0.12	0.88	0.34	0.66	0.53	0.47
274	14.93	14.91	I	0.05	0.95	0.18	0.82	0.28	0.72
274	17.93	20.81	I	0.00	1.00	0.00	1.00	0.00	1.00
277	1.95	1.99	I	1.00	0.00	1.00	0.00	1.00	0.00

277	2.60	2.38	I	0.85	0.15	0.98	0.02	0.98	0.02	
277	3.38	3.52	I	0.59	0.41	0.95	0.05	0.93	0.07	
277	5.23	5.40	I	0.39	0.61	0.89	0.11	0.85	0.15	
277	11.98	11.30	I	0.18	0.82	0.54	0.46	0.62	0.38	
277	15.50	15.07	I	0.12	0.88	0.35	0.65	0.48	0.52	
277	19.17	19.56	I	0.07	0.93	0.19	0.81	0.31	0.69	
277	24.04	28.37	I	0.00	1.00	0.00	1.00	0.00	1.00	
280	2.80	2.86	I	1.00	0.00	1.00	0.00	1.00	0.00	
280	3.60	3.59	I	0.83	0.18	0.98	0.02	0.98	0.02	
280	4.23	4.35	I	0.70	0.30	0.96	0.04	0.95	0.05	
280	5.07	5.29	I	0.59	0.41	0.94	0.06	0.92	0.08	
280	8.28	8.50	I	0.39	0.61	0.86	0.14	0.83	0.17	
280	14.97	13.50	I	0.25	0.75	0.64	0.36	0.68	0.32	
280	20.75	18.39	I	0.17	0.83	0.45	0.55	0.55	0.45	
280	26.69	25.74	I	0.09	0.91	0.22	0.78	0.35	0.65	
280	32.31	38.81	I	0.00	1.00	0.00	1.00	0.00	1.00	
<b>AADp</b>		<b>5.7%</b>	<b>AADc</b>					<b>0.04</b>		

**Table 13. Experimental results of carbon dioxide-methane hydrate equilibrium pressure and composition from Seo et al. [148] and our simulation results (composition uncertainties not provided by authors).**

T (K) ( $\pm 0.1$ )	P <sub>exp</sub> (MPa) ( $\pm 0.01$ )	P <sub>pre</sub> (MPa)	S	Gas composition (exp)		Hydrate composition (exp)		Hydrate composition (pre)	
				CO <sub>2</sub>	CH <sub>4</sub>	CO <sub>2</sub>	CH <sub>4</sub>	CO <sub>2</sub>	CH <sub>4</sub>
273.1	2.00	1.92	I	0.28	0.72	0.92	0.09	0.45	0.55
274.1	2.00	2.03	I	0.40	0.60	0.94	0.06	0.58	0.42
275.4	2.00	2.06	I	0.61	0.39	0.98	0.02	0.75	0.25
276.3	2.00	2.04	I	0.79	0.21	1.00	0.00	0.88	0.12
273.8	2.60	2.48	I	0.13	0.87	0.66	0.34	0.24	0.76
274.9	2.60	2.54	I	0.23	0.77	0.85	0.15	0.38	0.62
276.3	2.60	2.56	I	0.42	0.59	0.93	0.07	0.58	0.42
277.5	2.60	2.55	I	0.64	0.36	0.98	0.02	0.77	0.23
278.1	2.60	2.46	I	0.83	0.17	0.99	0.01	0.90	0.10
276.6	3.50	3.29	I	0.13	0.87	0.65	0.35	0.24	0.76
277.6	3.50	3.32	I	0.25	0.75	0.73	0.27	0.40	0.60
279.0	3.50	3.45	I	0.42	0.58	0.89	0.11	0.57	0.43

279.9	3.50	3.43	I	0.61	0.39	0.95	0.05	0.74	0.26	
280.5	3.50	3.30	I	0.83	0.17	0.99	0.01	0.90	0.10	
<b>AAD</b>		<b>3.3%</b>						<b>0.29</b>		

It is clear from Table 12, Table 13 and Figure 23 that, the thermodynamic model predicts the equilibrium pressure with adequate deviations (average deviations for methane-carbon dioxide and nitrogen-carbon dioxide hydrate pressure were 3.3 and 5.7%, respectively).

As seen in Table 12, at low concentrations of nitrogen, the hydrate phase compositions were acceptably simulated (sI). Nevertheless, when nitrogen was the dominate component in hydrate phase, the simulation results deviated from the experimental data. Hence, the hydrate phase compositions were again simulated by taking into account both structures, sI and sII. Prediction results for two isotherms of N<sub>2</sub>/CO<sub>2</sub> binary hydrate are presented in Figure 24. This figure shows that, at higher pressures, the hydrate preferentially encapsulates nitrogen from the N<sub>2</sub>/CO<sub>2</sub> mixture. Consequently, the nitrogen composition in hydrate phase increases. As clear on the figure, at high concentrations of nitrogen in hydrate phase, sII simulation results are in better agreement with experimental data compared to sI results. This can be explained by the fact that pure nitrogen forms sII hydrates. Thus, when nitrogen is the major component in the mixture, there might be a structural transition from sI to sII. Finally, for CO<sub>2</sub>/N<sub>2</sub> mixtures, it might be concluded that when nitrogen composition in vapor phase is more than 70% mole fraction and system pressure is more than 8 MPa, a phase transition from sI to sII may be occurred.

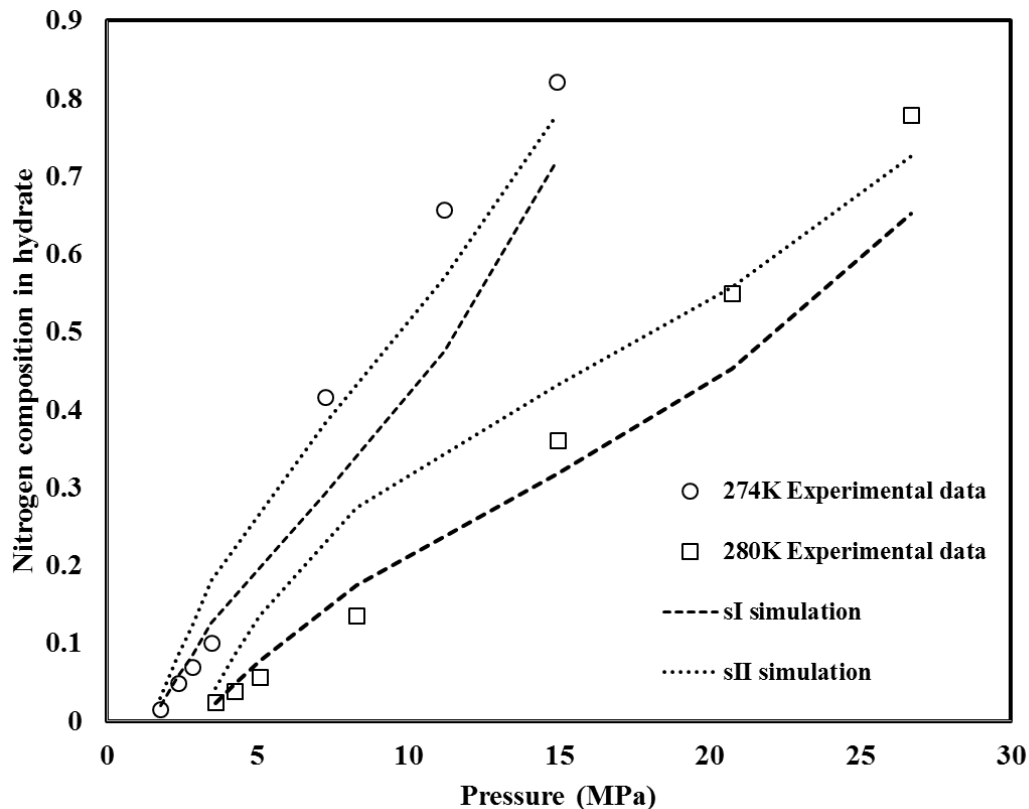


Figure 24. P-x diagram of N<sub>2</sub>-CO<sub>2</sub> hydrate based on the experimental results of Seo et al. (sI) [148] and our simulation results

For the methane-carbon dioxide mixture, although the equilibrium pressure were satisfactorily simulated (average absolute deviation 3.3%), the thermodynamic model failed to evaluate the hydrate composition (average absolute deviation 0.29 mole fraction).

### 3.2.4. Using a tracer and mass balance

Using a tracer in gas or liquid phase could help to measure hydrate composition. A tracer must not be able to form hydrates and only a small amount should be utilized to avoid any thermodynamic influence on equilibrium. This section presents a short report of publications which have used a tracer in their experiment to measure hydrate composition. Of course, based on the experimental results of these papers, the capability of the thermodynamic model to simulate hydrate composition is evaluated.

**Table 14. Feed composition of different mixtures [149]**

Gas	Mixtures (Concentration mole %) ( $\pm 0.003$ )					
	a	b	c	d	e	f
Carbon dioxide	0	0	0	2	0	2
Methane	90	99	84	88	80	86.5
Ethane	0	0	10	0	10	0
Propane	10	1	4	8	5	4
iso-Butane	0	0	2	2	2	0.5
n-Butane	0	0	0	0	3	1

**Table 15. Experimental results of Ng [149] and our modeling results**

T (C) ( $\pm 0.05$ )	P (MPa) ( $\pm 0.007$ )	Feed	Experimental hydrate composition ( $\pm 0.003$ )						Hydrate composition simulation					
			C <sub>1</sub>	C <sub>2</sub>	C <sub>3</sub>	iC <sub>4</sub>	nC <sub>4</sub>	CO <sub>2</sub>	C <sub>1</sub>	C <sub>2</sub>	C <sub>3</sub>	iC <sub>4</sub>	nC <sub>4</sub>	CO <sub>2</sub>
11.4	2.07	a	0.586	-	0.414	-	-	-	0.61	-	0.39	-	-	-
20.1	6.89	a	0.657	-	0.343	-	-	-	0.64	-	0.36	-	-	-
AADc														
3.7	2.07	b	0.726	-	0.274	-	-	-	0.65	-	0.35	-	-	-
13.2	6.89	b	0.771	-	0.229	-	-	-	0.67	-	0.33	-	-	-
AADc									0.05					
10.9	2.07	c	0.606	0.087	0.182	0.124	-	-	0.62	0.01	0.2	0.17	-	-
19.4	6.89	c	0.59	0.087	0.2	0.123	-	-	0.64	0.01	0.2	0.15	-	-
AADc									0.03	0.07	0.009	0.02		
12.9	2.07	d	0.6	-	0.297	0.092	-	0.0102	0.6	-	0.28	0.1	-	0.02
21.6	6.89	d	0.63	-	0.289	0.078	-	0.0104	0.62	-	0.27	0.09	-	0.02
AADc									0.005	-	0.018	0.01	-	0.01
11.3	2.07	e	0.581	0.074	0.206	0.107	0.031	-	0.62	0.01	0.22	0.14	0.01	-
19.6	6.89	e	0.617	0.089	0.181	0.087	0.027	-	0.64	0.01	0.23	0.11	0.01	-
AADc									0.031	0.07	0.03	0.02	0.02	
9.8	2.07	f	0.584	0.076	0.265	0.044	0.018	0.011	0.6	0.006	0.31	0.06	0.007	0.017
18.7	6.89	f	0.621	0.077	0.238	0.039	0.011	0.01	0.63	0.007	0.29	0.05	0.006	0.017
AADc									0.01	0.07	0.05	0.01	0.008	0.006

Ng determined the hydrate composition for six gas mixture including methane, ethane, propane, iso-butane, n-butane and carbon dioxide. He used n-pentane as a tracer in gas phase. Thanks to a gasometer and composition of n-pentane at the end of experiments, he successfully determined the amount of original gas mixture and overall gas dissociation [149]. Table 14 shows the different gas mixtures in the study. Ng's experimental data and our simulation results are presented in Table 15.

Obviously, in Table 15, there is a wide range of average absolute deviation according to the number and type of components in the feed gas, between 0.006 and 0.07. This variation could be explained by the fact that for the ternary or quaternary mixtures, kinetic considerations might affect experimental results. Note: the largest deviation belongs to ethane in all the mixtures.

At the beginning of the 21st century, researchers at Ecole Nationale Supérieure des Mines de Saint-Etienne (Mines Saint-Etienne) developed a new method to determine the hydrate composition not only at equilibrium condition, but also during the crystallization under non-equilibrium conditions. Their new procedure was based on tracing the concentration of lithium salt in liquid phase and material balance (see section 4.6). The protocol is as follows: after gas injection inside the reactor, water solution with 10 ppm concentration of lithium salt was inserted in the reactor. By decreasing the temperature at a desire value, hydrate formation started. After several days, the system reached at equilibrium. At this point a gas and liquid sample was taken. The gas sample was analyzed by gas chromatography to determine the gas composition in vapor phase. The liquid sample was analyzed by ion chromatograph to measure the concentration of lithium salt in liquid phase. As lithium does not participate in hydrate formation, it is possible to calculate the amount of water at equilibrium according to the lithium concentration. Then, the system temperature increased stepwise and gas and liquid samples were taken [113,121]. A diagram of their experiments is shown in Figure 25.



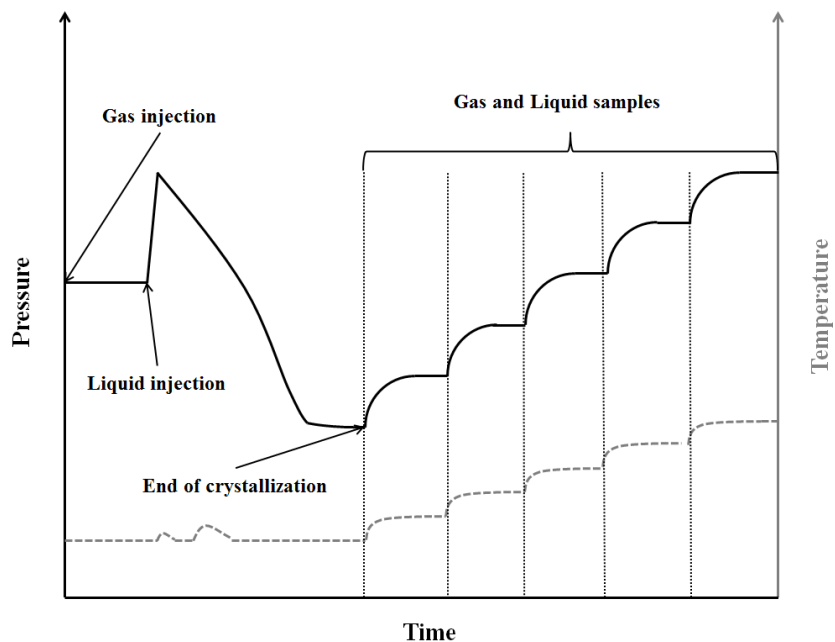


**Figure 25. The diagram of experimental procedure**

Based on this procedure (see section 4.6), Herri et al. [113] studied the equilibrium conditions of carbon dioxide-nitrogen and carbon dioxide-methane hydrates. Table 16 and Table 17 present their experimental results and our corresponding simulation results for carbon dioxide-nitrogen and carbon dioxide-methane mixtures, respectively.

**Table 16. Experimental results from Herri et al. [113] and simulation results for carbon dioxide-nitrogen mixture**

T (K) (±0.1)	P <sub>exp</sub> (MPa) (±0.01)	P <sub>pre</sub> (MPa)	S	Gas composition (exp) (±0.001)		Hydrate composition (exp) (±0.003)		Hydrate composition (pre)	
				CO <sub>2</sub>	N <sub>2</sub>	CO <sub>2</sub>	N <sub>2</sub>	CO <sub>2</sub>	N <sub>2</sub>
273.4	6.10	7.51	I	0.16	0.84	0.66	0.34	0.63	0.37
274.5	6.20	8.31	I	0.16	0.84	0.66	0.34	0.63	0.37
275.4	6.40	8.64	I	0.19	0.82	0.66	0.34	0.66	0.34
276.5	6.60	9.42	I	0.20	0.80	0.58	0.42	0.67	0.33
273.9	5.90	5.40	I	0.25	0.75	0.75	0.25	0.77	0.23
274.7	5.90	5.93	I	0.26	0.75	0.73	0.27	0.76	0.24
276.0	5.90	6.90	I	0.26	0.74	0.70	0.30	0.76	0.24
276.9	6.00	7.70	I	0.27	0.74	0.70	0.30	0.75	0.25
277.8	6.30	8.14	I	0.29	0.71	0.67	0.33	0.77	0.23

278.1	6.40	8.41	I	0.30	0.71	0.69	0.31	0.77	0.23	
278.4	6.40	8.82	I	0.30	0.71	0.72	0.29	0.76	0.24	
278.6	6.50	8.93	I	0.30	0.70	0.70	0.31	0.77	0.23	
275.4	6.10	7.99	I	0.20	0.80	0.67	0.33	0.69	0.31	
276.0	6.20	8.14	I	0.22	0.78	0.65	0.35	0.70	0.30	
280.1	5.30	5.75	I	0.56	0.44	0.85	0.16	0.91	0.09	
281.1	5.60	6.42	I	0.59	0.42	0.82	0.18	0.91	0.09	
<b>AADp</b>		<b>25.6%</b>		<b>AADc</b>				<b>0.05</b>		

**Table 17. Experimental results from Herri et al. [113] and simulation results for carbon dioxide-methane mixture**

T (K) (±0.1)	P <sub>exp</sub> (MPa) (±0.01)	P <sub>pre</sub> (MPa)	S	Gas composition (exp) (±0.001)		Hydrate composition (exp) (±0.003)		Hydrate composition (pre)		
				CO <sub>2</sub>	CH <sub>4</sub>	CO <sub>2</sub>	CH <sub>4</sub>	CO <sub>2</sub>	CH <sub>4</sub>	
277.15	2.04	2.03	I	1.00	0.00	1.00	0.00	1.00	0.00	
277.15	2.36	2.45	I	0.64	0.36	0.77	0.23	0.77	0.23	
277.15	2.55	2.63	I	0.52	0.48	0.68	0.32	0.68	0.32	
277.15	2.80	2.92	I	0.36	0.64	0.54	0.47	0.53	0.47	
277.15	3.55	3.55	I	0.11	0.89	0.21	0.79	0.20	0.80	
277.15	3.90	3.94	I	0.00	1.00	0.00	1.00	0.00	1.00	
<b>AADp</b>		<b>2.10%</b>		<b>AADc</b>				<b>0.004</b>		

In the case of carbon dioxide-nitrogen, the simulation results for hydrate equilibrium pressure are not very reliable. Since nitrogen composition in vapor phase is more than carbon dioxide in most of cases, sII is more probable. But the prediction results revealed that the structure might be sI, as hydrate pressure concerning sII is poorly simulated (average deviation of 60% for sII compared to 25% for sI). Nonetheless, the average absolute deviation for prediction of hydrate composition according to both structures is small (0.05). The prediction results concerning sII are also provided in Appendix A. For carbon dioxide-methane mixture, the simulation results are in respectable agreement with the experimental results. As it can be seen in Table 17, the average deviation of equilibrium pressure was about 2%. The thermodynamic model better predicts the hydrate composition. The average deviation for carbon dioxide and methane compositions in

hydrate phase was 0.004. Figure 26 presents clearly the excellent match between the experimental and simulation results for carbon dioxide-methane hydrate mixture.

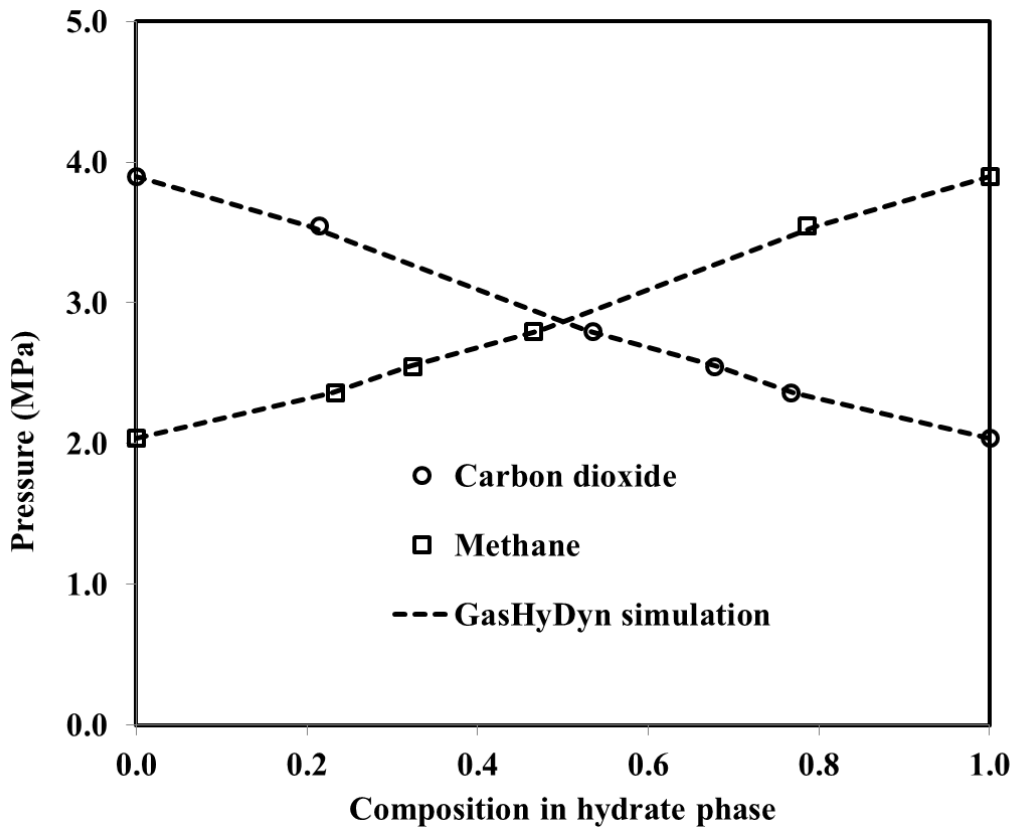


Figure 26. Experimental data from Herri et al. [113] for methane-carbon dioxide hydrate (sI) and simulation results

Le Quang et al. [121] studied the equilibrium conditions of several gas mixtures from  $N_2$ - $CO_2$ - $CH_4$ - $C_2H_6$ - $C_3H_8$ - $nC_4H_{10}$ . They also determined the guest composition in vapor and hydrate phases [121]. They used the same method as Herri et al [113] to analyze guest composition in different phases. In addition, they studied the influence of crystallization rate on the final equilibrium pressure and composition during the crystallization of  $CO_2$ - $CH_4$ - $C_2H_6$  mixed hydrate. All the experimental data and our equivalent simulation results are listed in Table 18, Table 19 and Table 20. They reported that, for the equilibrium points near total dissociation, hydrate composition was suspected to have large errors. Thus, they were not used for our purposes. As Table 18 shows, the thermodynamic model realistically predicts the equilibrium pressures of binary mixtures including carbon dioxide. The average deviation of the equilibrium pressure predictions for  $CO_2$ - $CH_4$  and  $CO_2$ - $N_2$  are about 2 and 3%, respectively. For hydrate

composition extrapolation, the average absolute deviations are 0.05 and 0.04 for CO<sub>2</sub>-CH<sub>4</sub> and CO<sub>2</sub>-N<sub>2</sub>, respectively. It should be noticed that the carbon dioxide composition of vapor phase in CO<sub>2</sub>-N<sub>2</sub> mixture was significantly larger than nitrogen. As a result, sI was considered for the CO<sub>2</sub>-N<sub>2</sub> mixed hydrate. The simulation results concerning sII (see Appendix A) validate adequately this assumption.

**Table 18. Carbon dioxide-methane and carbon dioxide-nitrogen hydrate mixtures, experimental data [121] and simulation results**

Gas	T <sub>exp</sub> (°C) (±0.1)	P <sub>exp</sub> (MPa) (±0.01)	P <sub>pre</sub> (MPa)	S	Gas composition (exp) (±0.001)			Hydrate composition (exp) (±0.003)			Hydrate composition (Pre)		
					N <sub>2</sub>	CO <sub>2</sub>	CH <sub>4</sub>	N <sub>2</sub>	CO <sub>2</sub>	CH <sub>4</sub>	N <sub>2</sub>	CO <sub>2</sub>	CH <sub>4</sub>
CO <sub>2</sub> -CH <sub>4</sub>	3.4	3.33	3.29	I	-	0.13	0.87	-	0.32	0.68	-	0.23	0.77
	4.4	3.53	3.62	I	-	0.13	0.87	-	0.32	0.68	-	0.24	0.76
	4.9	3.71	3.80	I	-	0.14	0.86	-	0.32	0.68	-	0.24	0.76
	5.8	4.03	4.14	I	-	0.15	0.85	-	0.32	0.68	-	0.26	0.74
	6.8	4.45	4.57	I	-	0.16	0.84	-	0.32	0.68	-	0.27	0.73
	7.8	4.93	5.06	I	-	0.18	0.83	-	0.30	0.70	-	0.28	0.72
	2.2	2.91	2.93	I	-	0.12	0.88	-	0.29	0.71	-	0.22	0.78
	2.5	2.97	3.00	I	-	0.13	0.87	-	0.28	0.72	-	0.23	0.77
	3.6	3.18	3.33	I	-	0.14	0.87	-	0.28	0.72	-	0.24	0.76
	4.5	3.47	3.63	I	-	0.15	0.85	-	0.27	0.73	-	0.25	0.75
	5.2	3.80	3.85	I	-	0.16	0.84	-	0.23	0.77	-	0.27	0.73
<b>AADp</b>		<b>2.4%</b>		<b>AADc</b>						<b>0.05</b>			
CO <sub>2</sub> -N <sub>2</sub>	2.3	2.46	2.53	I	0.33	0.67	-	0.06	0.94	-	0.05	0.95	-
	3.1	2.60	2.69	I	0.31	0.69	-	0.07	0.93	-	0.04	0.96	-
	3.3	2.66	2.73	I	0.30	0.70	-	0.07	0.93	-	0.04	0.96	-
	4.3	2.87	2.99	I	0.28	0.72	-	0.09	0.91	-	0.04	0.96	-
	5.2	3.13	3.22	I	0.25	0.75	-	0.12	0.88	-	0.03	0.97	-
	<b>AADp</b>		<b>3.16%</b>		<b>AADc</b>						<b>0.04</b>		

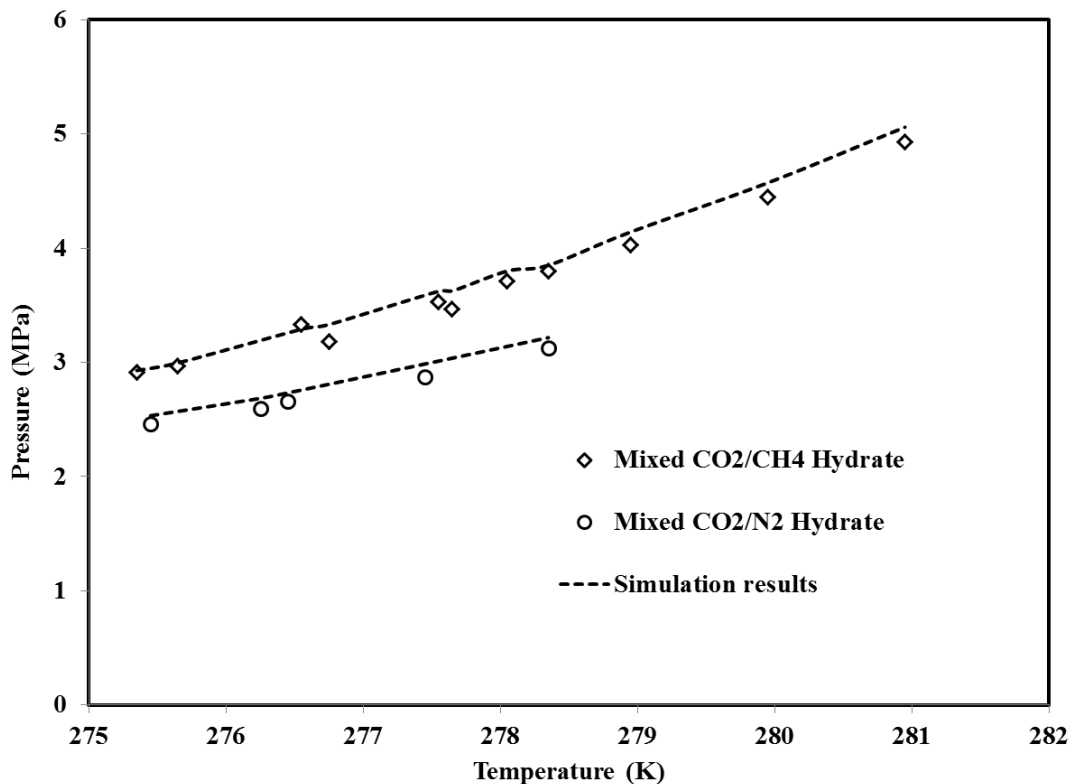


Figure 27. P-T diagram of mixed CO<sub>2</sub>/CH<sub>4</sub> and CO<sub>2</sub>/N<sub>2</sub> hydrates, experimental data [121] and simulation results (sI). The vapor and hydrate compositions were listed in Table 18.

As aforementioned, Le Quang et al. investigated the effect of crystallization rate on hydrate equilibrium pressure and composition of CO<sub>2</sub>-CH<sub>4</sub>-C<sub>2</sub>H<sub>6</sub> ternary mixture. They reported that the hydrate equilibrium pressure and composition at final state differed according to the rate of crystallization. They concluded that at quick crystallization rate, mixed gas hydrate could not be at thermodynamic equilibrium [121]. Table 19 reveals that the results of thermodynamic model is closer to the slow crystallization data. The average deviations of equilibrium pressure prediction for slow and quick crystallization are about 2 and 8%, respectively. The average deviations for carbon dioxide in hydrate phase for slow and quick crystallization are similar (0.01). This is not the case for methane and ethane compositions in hydrate phase, where the deviation of simulation for slow crystallization are much better compared to quick rate (e.g. ethane, 0.009 for slow compared to 0.05 for quick).

**Table 19. Experimental results of Carbon dioxide-methane-ethane hydrate from Le Quang et al. [121] and simulation results**

Gas	T <sub>exp</sub> (°C) (±0.1)	P <sub>exp</sub> (MPa) (±0.01)	P <sub>pre</sub> (MPa)	S	Gas composition (exp) (±0.001)			Hydrate composition (exp) (±0.003)			Hydrate composition (Pre)		
					CO <sub>2</sub>	CH <sub>4</sub>	C <sub>2</sub> H <sub>6</sub>	CO <sub>2</sub>	CH <sub>4</sub>	C <sub>2</sub> H <sub>6</sub>	CO <sub>2</sub>	CH <sub>4</sub>	C <sub>2</sub> H <sub>6</sub>
CO <sub>2</sub> -CH <sub>4</sub> -C <sub>2</sub> H <sub>6</sub> Quick crys.	2.75	3.54	3.11	I	0.03	0.96	0.01	0.07	0.89	0.04	0.05	0.87	0.08
	3.65	3.81	3.35	I	0.03	0.96	0.01	0.07	0.89	0.04	0.05	0.86	0.09
	5.15	4.23	3.79	I	0.03	0.95	0.02	0.07	0.89	0.04	0.05	0.83	0.11
	6.55	4.56	4.33	I	0.03	0.95	0.02	0.07	0.89	0.04	0.06	0.83	0.12
	7.80	5.12	4.76	I	0.04	0.94	0.02	0.07	0.89	0.04	0.06	0.81	0.13
	9.25	5.99	5.67	I	0.04	0.94	0.02	0.04	0.90	0.07	0.07	0.82	0.12
	<b>AADp</b>		<b>8.6%</b>		<b>AADc</b>						<b>0.01</b>	<b>0.05</b>	<b>0.05</b>
CO <sub>2</sub> -CH <sub>4</sub> -C <sub>2</sub> H <sub>6</sub> Slow crys.	4.60	3.78	3.64	I	0.04	0.95	0.01	0.08	0.80	0.12	0.06	0.84	0.09
	4.20	3.56	3.50	I	0.03	0.95	0.01	0.08	0.83	0.09	0.06	0.84	0.10
	3.25	3.18	3.27	I	0.03	0.96	0.01	0.08	0.85	0.08	0.06	0.87	0.07
	1.30	2.76	2.76	I	0.03	0.96	0.01	0.08	0.86	0.06	0.06	0.89	0.05
	4.20	3.57	3.46	I	0.04	0.95	0.02	0.06	0.84	0.09	0.07	0.83	0.10
	<b>AADp</b>		<b>2.2%</b>		<b>AADc</b>						<b>0.01</b>	<b>0.02</b>	<b>0.01</b>

As seen in Table 20, the average deviation of the equilibrium pressures calculated for the quaternary mixture of methane-ethane-propane-butane is about 13% which is expected due to more significant kinetic effects in quaternary mixtures.

Hydrate composition for the methane and butane is well simulated (AADc=0.01), while for ethane and propane, the average deviation of hydrate composition are 0.06 and 0.07, respectively.

**Table 20. Experimental data of methane-ethane-propane-butane hydrate from Le Quang et al. [121] and simulation results**

Texp (°C) (±0.1)	Pexp (MPa) (±0.01)	Ppre (MPa)	S	Gas composition (exp) (±0.001)				Hydrate composition (exp) (±0.003)				Hydrate composition (Pre)				
				C <sub>1</sub>	C <sub>2</sub>	C <sub>3</sub>	C <sub>4</sub>	C <sub>1</sub>	C <sub>2</sub>	C <sub>3</sub>	C <sub>4</sub>	C <sub>1</sub>	C <sub>2</sub>	C <sub>3</sub>	C <sub>4</sub>	
2.40	2.28	1.70	II	0.97	0.02	0.00	0.01	0.73	0.11	0.11	0.05	0.75	0.03	0.16	0.06	
3.45	2.31	1.82	II	0.97	0.02	0.01	0.01	0.73	0.11	0.11	0.05	0.74	0.03	0.18	0.06	
7.60	2.75	2.50	II	0.94	0.04	0.01	0.02	0.71	0.10	0.14	0.05	0.72	0.04	0.18	0.07	
9.15	2.97	2.70	II	0.93	0.04	0.01	0.02	0.68	0.10	0.17	0.05	0.70	0.03	0.20	0.06	
9.90	3.05	2.78	II	0.92	0.04	0.02	0.02	0.68	0.10	0.17	0.05	0.70	0.03	0.22	0.05	
10.80	3.12	2.86	II	0.92	0.05	0.02	0.02	0.69	0.10	0.17	0.05	0.69	0.03	0.24	0.04	
11.70	3.22	2.94	II	0.91	0.05	0.03	0.02	0.69	0.10	0.16	0.05	0.68	0.02	0.25	0.04	
12.65	3.34	3.09	II	0.90	0.05	0.03	0.02	0.70	0.09	0.16	0.05	0.68	0.02	0.26	0.04	
13.65	3.46	3.32	II	0.89	0.05	0.04	0.02	0.70	0.09	0.16	0.05	0.68	0.02	0.27	0.03	
14.70	3.48	3.75	II	0.89	0.05	0.04	0.02	0.70	0.09	0.16	0.05	0.68	0.02	0.27	0.03	
15.65	3.52	4.20	II	0.89	0.05	0.04	0.02	0.70	0.09	0.16	0.05	0.68	0.02	0.27	0.03	
16.60	3.61	4.61	II	0.88	0.05	0.04	0.02	0.71	0.09	0.16	0.05	0.68	0.02	0.27	0.03	
2.75	2.14	1.52	II	0.96	0.02	0.01	0.01	0.73	0.08	0.15	0.04	0.71	0.03	0.19	0.07	
4.30	2.16	1.80	II	0.96	0.02	0.01	0.01	0.73	0.08	0.15	0.04	0.72	0.03	0.18	0.07	
4.85	2.18	1.82	II	0.95	0.03	0.01	0.01	0.73	0.08	0.15	0.04	0.71	0.02	0.21	0.06	
5.90	2.21	1.98	II	0.95	0.03	0.01	0.01	0.72	0.08	0.16	0.04	0.71	0.02	0.21	0.06	
6.80	2.26	2.14	II	0.95	0.03	0.01	0.01	0.72	0.08	0.16	0.04	0.71	0.02	0.22	0.05	
7.45	2.36	2.12	II	0.94	0.03	0.02	0.02	0.72	0.08	0.16	0.04	0.69	0.02	0.24	0.05	
9.20	2.53	2.31	II	0.93	0.04	0.02	0.02	0.71	0.08	0.17	0.04	0.68	0.02	0.26	0.04	
11.05	2.82	2.55	II	0.91	0.04	0.03	0.02	0.71	0.07	0.18	0.04	0.67	0.02	0.27	0.04	
<b>AADp</b>		<b>13%</b>	<b>AADc</b>								<b>0.01</b>	<b>0.06</b>	<b>0.07</b>	<b>0.01</b>		

### 3.2.5. Microscopic measurements tools

In the previous sections, various indirect methods of determining hydrate composition have been reviewed. All approaches were based on measuring fluid and system properties like pressure, temperature, gas phase composition etc. and then calculating the hydrate composition according to the material balance and hydrate properties. Recently, innovative microscopic instruments helped researchers to measure directly the properties and molecular aspects of clathrate hydrates such as hydrate structure, cage occupancy, hydrate composition and guest molecule position [150–163]. For instance, the reader is referred to a comprehensive review book of Desmedt et al.

[164] on optical microscopic tools (for instance; Raman, infrared (IR) and X-ray) and their implications for gas hydrates.

One of the first studies using Raman spectroscopy was performed by Sum et al [165] to explore the properties of clathrate hydrates for pure guest molecules such as CH<sub>4</sub>, CO<sub>2</sub>, C<sub>3</sub>H<sub>8</sub> and binary mixtures CH<sub>4</sub>-CO<sub>2</sub>, CD<sub>4</sub>-C<sub>3</sub>H<sub>8</sub>, CH<sub>4</sub>-N<sub>2</sub>, CH<sub>4</sub>-THF<sub>d8</sub> and CH<sub>4</sub>-C<sub>7</sub>D<sub>14</sub>. As to hydrate composition, they only reported the guest composition in hydrate phase for CH<sub>4</sub>-CO<sub>2</sub> binary mixture. Their procedure included several steps; preparation of hydrate sample in cell and setting the cell into the sample chamber of the Raman. Then, the pressure was adjusted to a value which was within 5% of the predicted pressure at a desired temperature. They predicted hydrate equilibrium pressure by CSMHYD [119,165]. Spectra were then collected at the equilibrium conditions for hydrate composition analyses. Table 21 and Figure 28 present their experimental data and reciprocal simulation results by the thermodynamic model.

**Table 21. Experimental data from Sum et al. [165] and simulation results**

T (K)	Gas composition (exp)		S	Hydrate composition (exp) (±1%)		Hydrate composition (pre)	
	CO <sub>2</sub>	CH <sub>4</sub>		CO <sub>2</sub>	CH <sub>4</sub>	CO <sub>2</sub>	CH <sub>4</sub>
273.15	0.57	0.43	I	0.75	0.25	0.73	0.27
274.15	0.57	0.43	I	0.73	0.27	0.73	0.27
277.15	0.57	0.43	I	0.71	0.29	0.72	0.28
278.15	0.57	0.43	I	0.71	0.29	0.72	0.28
273.15	0.34	0.66	I	0.55	0.45	0.52	0.48
274.15	0.34	0.66	I	0.55	0.45	0.51	0.49
275.15	0.34	0.66	I	0.53	0.47	0.51	0.49
278.15	0.34	0.66	I	0.52	0.48	0.50	0.50
					<b>AADc</b>	<b>0.02</b>	



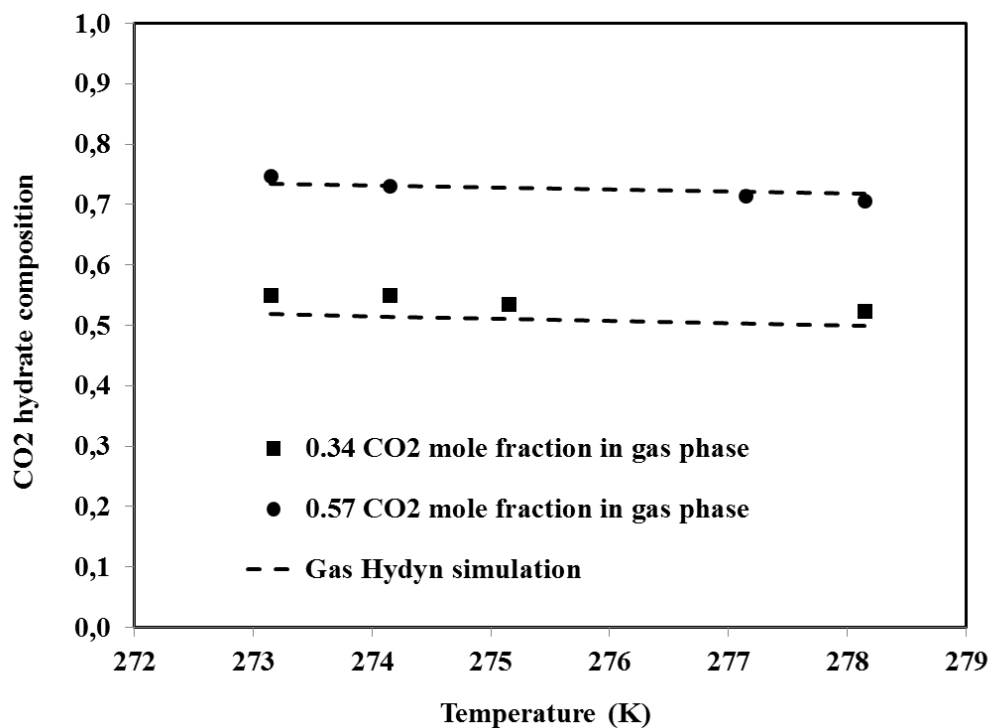


**Figure 28. Experimental data from Raman spectroscopic measurements by Sum et al. [165] and our thermodynamic simulations**

The results illustrate that the thermodynamic model satisfactorily simulated the hydrate composition. The average absolute deviation for hydrate composition was 0.02. Moreover, the simulation results concerning higher concentration of carbon dioxide in the gas phase had a better accordance with experimental measurements.

Subramanian et al. studied the structural transition of methane-ethane hydrate mixture based on Raman spectroscopy and  $^{13}\text{C}$  NMR measurements [88,89]. According to the Raman spectra, they reported that for methane-ethane hydrate mixture at 274.2 K, there was a structural transition from structure I to II, when the methane composition in gas phase is over 72.2-75 mole %. Moreover, they observed that the structure changed from sII to sI, once the methane composition in vapor phase is over 0.992-0.994 mole %. Furthermore, Raman spectra showed that structural transition leads to a 20% variation in hydrate composition. They also measured the hydrate composition by  $^{13}\text{C}$  NMR at six different vapor compositions. Their results are listed in Table 22.

**Table 22. Experimental data from Subramanian et al. [89] for methane-ethane mixture and simulation results**

T (K)	P <sub>exp</sub> (MPa) (±0.014)	P <sub>pre</sub> (MPa)	S	Gas composition (exp)		Hydrate composition (exp) (±0.1%)		Hydrate composition (Pre)	
				CH <sub>4</sub>	C <sub>2</sub> H <sub>6</sub>	CH <sub>4</sub>	C <sub>2</sub> H <sub>6</sub>	CH <sub>4</sub>	C <sub>2</sub> H <sub>6</sub>
274.2	0.88	0.82	I	0.63	0.37	0.28	0.72	0.30	0.70
274.2	0.96	0.88	I	0.68	0.32	0.36	0.64	0.32	0.68
274.2	0.97	0.96	I	0.72	0.28	0.37	0.63	0.35	0.65
<b>AADp</b>		<b>5.3%</b>	I	<b>AADc</b>				<b>0.02</b>	
274.2	0.99	1.02	II	0.75	0.25	0.57	0.43	0.37	0.63
274.2	1.17	1.34	II	0.85	0.15	0.65	0.35	0.47	0.53
274.2	1.45	1.76	II	0.92	0.08	0.70	0.30	0.61	0.39
<b>AADp</b>		<b>41.6%</b>	II	<b>AADc</b>				<b>0.09</b>	

Clearly, in Table 20, the thermodynamic simulation concurs with the experimental results for structure I. While for the structure II, the simulations fail. This reveals that the thermodynamic model cannot be proficient to well evaluate the hydrate equilibrium conditions when the structure transition occurs in the system.

Seo and Lee [166] analyzed the structure and gas distribution of nitrogen-carbon dioxide hydrate at different vapor compositions. They revealed from X-ray diffraction patterns that when carbon dioxide composition in gas phase was between 3 and 20% mole, structure sI formed. While for CO<sub>2</sub> composition under 1%, the hydrate structure seemed to be sII. Additionally, they measured the hydrate composition by NMR spectroscopic analyses. They noticed that the CO<sub>2</sub> molecules were mostly localized in the large sI cages. Also, the hydrate composition was significantly augmented by a small increase of CO<sub>2</sub> in the vapor phase. Table 23 and Figure 29 present their experimental and our simulation results for hydrate guest distribution. This is clear from the figure that the results of thermodynamic model for hydrate composition prediction corresponds well with the experimental data (average deviation of hydrate phase prediction is 0.02).

**Table 23. Experimental results from Seo and Lee [166] and our simulation results**

T (K)	P <sub>exp</sub> (MPa)	P <sub>pre</sub> (MPa)	S	Gas composition (exp)		Hydrate composition (exp) ( $\pm 0.1\%$ )		Hydrate composition (Pre)	
				CO <sub>2</sub>	N <sub>2</sub>	CO <sub>2</sub>	N <sub>2</sub>	CO <sub>2</sub>	N <sub>2</sub>
272.1	14.50	13.57	I	0.01	0.99	0.09	0.91	0.07	0.93
272.1	13.00	12.11	I	0.03	0.97	0.15	0.85	0.17	0.83
272.1	10.50	8.79	I	0.10	0.90	0.47	0.54	0.41	0.59
272.1	7.70	6.24	I	0.18	0.82	0.59	0.41	0.61	0.39
272.1	5.00	3.99	I	0.33	0.67	0.74	0.26	0.79	0.21
272.1	4.10	2.80	I	0.50	0.50	0.86	0.14	0.88	0.12
272.1	3.50	2.14	I	0.67	0.34	0.94	0.06	0.94	0.06
272.1	3.20	1.69	I	0.85	0.15	0.97	0.04	0.98	0.02
<b>AADp</b>		<b>23.3%</b>		<b>AADc</b>				<b>0.02</b>	

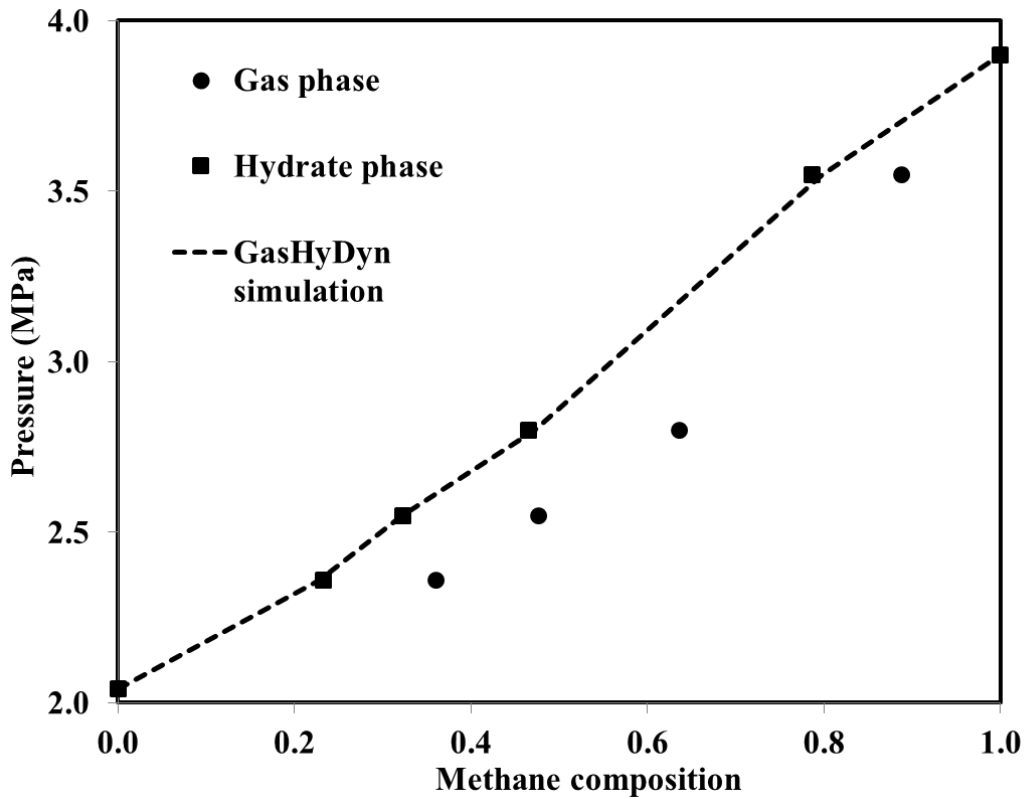


**Figure 29. CO<sub>2</sub> composition in gas and hydrate phase versus pressure for CO<sub>2</sub>-N<sub>2</sub> system at 272.1 K (sI). Experimental [166] and our simulation results**

Uchida et al. [124] investigated cage occupancy, hydrate composition and structure of methane-ethane mixture by Raman spectroscopy and XRD analyses [124]. They prepared the mixed methane-ethane hydrates from ice powder at different feed guest compositions. In the case of hydrate structure by Raman spectroscopy, they reported that, when the composition of ethane in the gas phase is below 2% or over 22% mole, only structure I exists. However, there was a coexistence of both structures I and II at ethane concentrations between 12 and 22% mol. Results of XRD analyses confirmed these investigations. They also observed that ethane molecules were only encapsulated in large cavities, while the methane molecules occupied both small and large cavities. Interestingly, their results revealed that the vapor composition had a significant influence on the cage occupancy in large cavities [124].

Uchida et al. [167] expanded their experiments for  $C_2H_6-C_3H_8$ ,  $CH_4-C_2H_6-C_3H_8$  and  $CH_4-C_2H_6-C_3H_8-iC_4H_{10}$  mixed hydrates. Based on the Raman spectra and confirmation of X-ray diffraction, they reported that for  $C_2H_6-C_3H_8$  mixed hydrates, only structure II existed when the vapor composition of ethane ranged from 28 to 73% mole fraction. They also stated that both molecules occupied the  $5^{12}6^4$  cages (sII large cages). Moreover, they concluded that the preferential occupancy of  $5^{12}6^4$  cages is  $C_3H_8 > C_2H_6 > CH_4$ . For  $CH_4-C_2H_6-C_3H_8$  hydrates, the initial methane composition in gas phase was between 90 and 98%. Their work showed that, at final state, the composition of methane in gas phase increased, whereas the ethane and propane composition decreased. In hydrate phase, propane enriched more than other guest molecules. Furthermore, if the cage occupancy of ethane and propane was less than 33%, the methane molecules can occupy some  $5^{12}6^4$  cages. For the quaternary hydrate mixture, they reported the existence of structure II. In addition, all the molecules except methane, occupied the  $5^{12}6^4$  cages and the ratio is  $C_2H_6-C_3H_8-iC_4H_{10} = 2:3:5$ . They concluded that at a desired temperature, the larger molecules with lower dissociation pressure, enriched more in hydrate phase [167].

Schicks et al. [86] studied the phase behavior of methane-propane and methane-ethane-propane hydrates in a temperature range between 260 and 290 K and a pressure range from 1 to 6MPa. They investigated the phase transition, hydrate structure and composition by Raman spectroscopy and x-ray diffraction. They observed two different types of crystals after hydrate formation; light and dark. They reported the presence of occluded gas in the structure of light hydrate crystals. However, there was no evidence of the occluded gas in the dark crystals which was supposed to

be structure II. Their approach demonstrated that there was a transformation process near the decomposition line. During the transformation, the crystal formation and decomposition was quick. They suggested that this is due to the occluded of free gas or water. Below this, they observed both structure I and II [86].

A summary of all these observations concerning structure change of mixed gas hydrates is tabulated in Table 24.

**Table 24. Evidence of structural change or co-existence of structures in mixed gas hydrates**

Mixture	Condition (mole fraction)	Structure change or co-existence	Technique	Ref.
CH <sub>4</sub> /C <sub>2</sub> H <sub>6</sub>	CH <sub>4</sub> > 72.2-75	sI → sII	RAMAN + NMR	[89]
CH <sub>4</sub> /C <sub>2</sub> H <sub>6</sub>	CH <sub>4</sub> > 99.2-99.4	sII → sI	RAMAN + NMR	[88]
CH <sub>4</sub> /C <sub>2</sub> H <sub>6</sub>	2 < C <sub>2</sub> H <sub>6</sub> < 22	sI + sII	XRD + RAMAN	[124]
CH <sub>4</sub> /C <sub>3</sub> H <sub>8</sub>	CH <sub>4</sub> > 94	sI + sII	XRD + RAMAN	[86]
CO <sub>2</sub> /N <sub>2</sub>	N <sub>2</sub> > 99	sI → sII	XRD + NMR	[166]

### 3.2.6. Issues of hydrate composition calculation from cage occupancy

Although there are a lot of studies on the pure hydrate formers or kinetic investigation of mixed hydrates by microscopic measurements tools [168–175], there is still little research based on these tools to measure mixed hydrates composition at equilibrium. Furthermore, even in these pertinent studies, they sometimes did not mention clearly their experimental data on hydrate composition (reporting experimental results only on figures, for instance). Therefore, it was impossible to compare their experimental results with the thermodynamic model. In some studies, researchers measured the rate of cage occupancy for mixtures based on Raman spectroscopy. Then, based on the statistical thermodynamics, they calculated absolute cage occupancy. Hydrate composition could be calculated based on the absolute cage occupancy [89].

Since this information was retrieved from statistical thermodynamics, they are of less interest for this work (the reader is referred to the review article of Maghsoodloo et al. [176]).

### **3.3. Conclusion**

While equilibrium conditions of clathrate hydrates, such as temperature, pressure and gas phase composition have been widely studied, the hydrate composition is usually ignored due to the experimental difficulties, like the non-homogenous hydrate phase, water and free gas occlusion, etc. [1]. However, vital data for hydrate composition can be compiled from literature. This information provides comprehensive, representative, and additional knowledge about hydrate composition according to the different equilibrium conditions. Hence, this was the motivation to assemble the relevant research on the hydrate composition by different experimental procedures and compare these methods via simulation based on the van der Waals and Platteeuw approach and Kihara potential for hydrate equilibrium pressure and composition.

Hydrate composition of binary mixtures of carbon dioxide, methane and nitrogen were usually studied since the idea of methane exploration from the hydrate resources by carbon dioxide isolation and gas separation was presented. Experimental data indicated that hydrate composition strongly depends on guest composition in gas phase. A small change in gas composition could lead to a substantial change in hydrate composition. Furthermore, the composition of heavier hydrocarbons (propane and butane) in the hydrate phase was significantly higher than in the gas phase.

Our simulations showed that generally, the thermodynamic model predicted adequately the hydrate equilibrium composition. In fact, the thermodynamic model had the best accordance with the experimental data obtained by the microscopic tools like Raman spectroscopy. This suggests that using these direct measurement techniques might help researchers to get closer to reality. Nevertheless, the existence of structural transition led to a significant deviation. Failure to predict structure change could be one of the main challenges for applying effectively the thermodynamic models.

Furthermore, at pressures higher than 7 MPa or when CO<sub>2</sub> was the minor component in hydrate phase, the deviation of the thermodynamic model from the experimental data was considerable.

Unfortunately, there were some cases which the agreement between the results of thermodynamic model and experimental data were not satisfactory. This might be explained by kinetic effects during the crystallization as well as the experimental methodology which could have a significant influence on the experiment. Furthermore, Bouillot and Herri reported that a small change of Kihara parameters had a considerable effect on the hydrate pressure and composition calculations [136]. Hence, it is essential to extend the experimental database in order to well optimize the Kihara parameters. Interestingly, there is still a lack of data concerning storage capacity of hydrates. This information could be used to re-design and develop chemical processes which the volume of gas stored in hydrate phase has been taken into account. Finally, consistent, reliable and extensive experimental data is still needed to examine the ability of thermodynamic modeling to predict hydrate composition as well as its developments.

## 4. Experimental description

### 4.1. Materials

In this study, CO<sub>2</sub>, N<sub>2</sub>, CH<sub>4</sub>, C<sub>2</sub>H<sub>6</sub>, C<sub>3</sub>H<sub>8</sub> and n-C<sub>4</sub>H<sub>10</sub> were provided by Air Products were used. Gas mixtures were prepared by injection of pure gases (from the less volatile to most volatile) and weighting the bottle after each injection. The bottle composition was calculated from the mass of each gas.

Deionized water was obtained through a water purifier from a cleansing system “Millipore”. This system is equipped with a cartridge “Milli-Q®-AdvantageA10” which lowers the conductivity of the water to 0.055 μS.cm<sup>-1</sup>. The total organic carbon content was less than 5 ppb. Moreover, about 10 ppm of lithium nitrate was used in our experiments as a liquid tracer. The lithium solution was purchased from Merck. Since lithium does not participate in hydrate formation process and also remains in solution, the volume of water converted to hydrate can be calculated from the concentration of lithium in the remaining liquid. The lithium concentration in the liquid phase is analyzed by an ion chromatography (IC) system. Helium was also used as a carrier gas for chromatography analyses. This is supplied by Air Product. The materials used in this work are listed by details in Table 25.

**Table 25. Materials used in this study**

Component	Supplier	Purity grade
Carbon dioxide	Air products	mole fraction 0.99999
Methane	Air products	mole fraction 0.9995
Nitrogen	Air products	mole fraction 0.99999
Ethane	Air products	mole fraction 0.995
Propane	Air products	mole fraction 0.9995
Butane	Air products	mole fraction 0.9995
Helium	Air products	mole fraction 0.99999
Li <sup>+</sup> Tracer	Merck	1001±5 mgdm <sup>-3</sup> Li <sup>+</sup> LiNO <sub>3</sub> in 0.5 moldm <sup>-3</sup> HNO <sub>3</sub> aqueous solution
Water	Milli-Q®- AdvantageA10	Organic content<5 ppb Salinity: conductivity of σ = 0.055 μScm <sup>-1</sup>



## 4.2. Apparatus

A schematic of the experimental set-up is presented in Figure 30. Two batch reactors named ACACIA and SECOHYA with the same characteristics and specifications were utilized (except the inner volume: 2.36 L for the first and 2.23 L for the second). Both are equipped with windows which allow direct observation and they can resist pressure up to 100 bar.

Agitation systems include vertical stirrers with two sets of blades. The top set of blades is in the gas phase and the bottom set in liquid (approximately 25mm from bottom of the reactors). This allows stirring the contents up to 25 Hz (1500 rpm) to increase the surface contact.

The autoclave is surrounded by a cooling jacket and the temperature is controlled by a cryostat, LAUDA RC6 CS ranging from -15 to 50°C. Temperature inside the reactor is monitored by two Pt100 probes (temperature accuracy  $\pm 0.2^\circ\text{C}$ ), for gas and liquid phases. In fact, the temperature probes send the voltage signals to a WEST 8010 electronic device. This converts the voltage signals to temperature, here degree Celsius. The pressure is also measured by a pressure sensor in the range 0-10 MPa (pressure accuracy  $\pm 0.01$  MPa). The liquid is injected in the reactor under pressure by using a HPLC pump (KNAUER P4.1S). The working rate of the pump is between 0.1 and 50 ml/min at pressures up to 10 MPa.

An online ROLSI sampler is mounted on the reactor for sampling the gas and subsequently sending it into a gas chromatograph VARIAN equipped with a TCD detector and two columns PoraBOND Q and CP-Molsieve. Peak integration is possible with software provided by Varian Galaxie. The liquid samples throughout the experiments are taken by a mechanical valve and a capillary tube which is located in the liquid phase. The sampling tube is positioned according to the density of hydrate crystals formed. The samples are then analyzed by ion chromatography system Dionex ICS-5000<sup>+</sup>. Data acquisition is controlled on a personal computer running Labview.

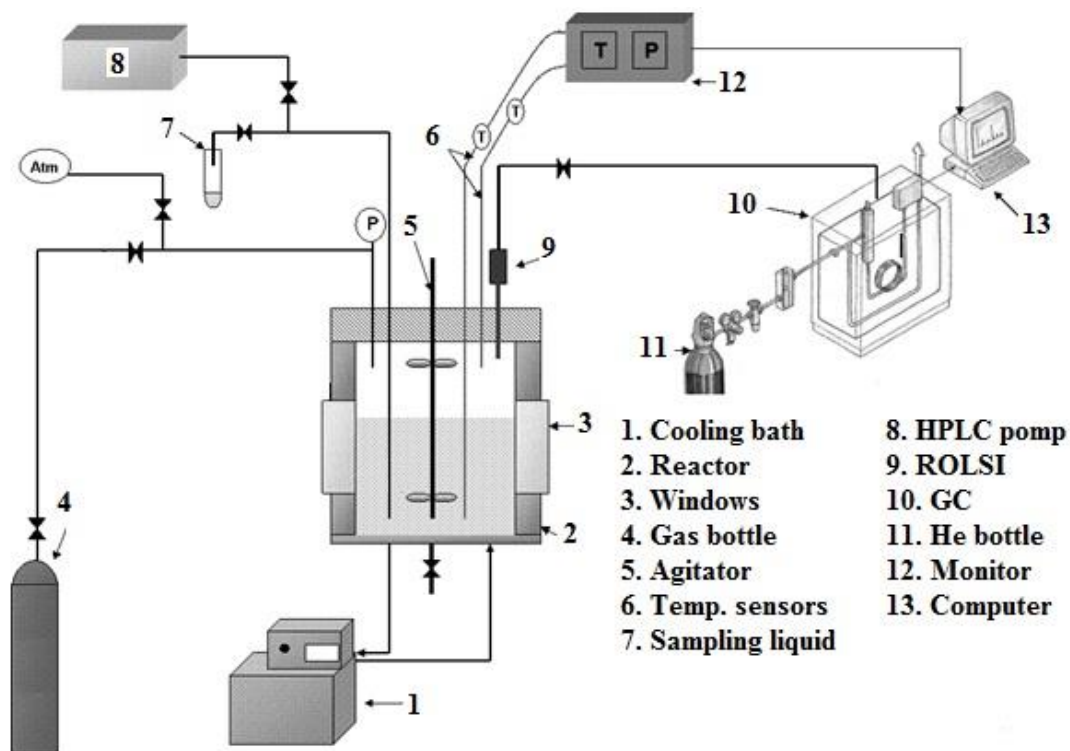


Figure 30. Schematic of experimental set-up

### 4.3. Gas chromatography

Gas chromatography (GC) is an analytical technique to identify and quantify components in a mixture. It allows detecting very small amount quantity of compounds as long as they are thermally stable and reasonably volatile. A mobile and a stationary phase are required for chromatographic techniques and the separation of compounds is based on the different strengths of interaction of the compounds with the stationary phase. The most common factors which influence the separation of components are carrier gas type and flow rate, column temperature, injectors and detector temperatures. Two gas chromatographs were used in this work, VARIAN CP-3800 (connected to SECOHYA reactor) and VARIAN 450-GC (connected to ACACIA reactor). The GCs are equipped with two columns which allow identifying a large number of gases. First column is CP-Molsive 5A with the diameter of 0.32 mm and the length of 10 m. Hydrogen, carbon dioxide, carbon monoxide, methane etc. can be detected by this column. The other column is PoraBOND Q with the diameter of 0.53 mm and the length of 50 m which is used to detect and identify hydrocarbon (C<sub>1</sub>-C<sub>9</sub>), carbon dioxide and nitrogen [177]. The

operational conditions of both gas chromatographs in our analyses are listed in Table 26. A typical gas analysis of GC for a mixture of methane/ethane/propane/butane is also presented in Figure 31.

**Table 26. The operational conditions of GC in our analyses**

Carrier gas	Helium
Carrier gas flow rate	40 ml/min
Column temperature	80°C
Injector temperature	200°C
Detector temperature	220°C

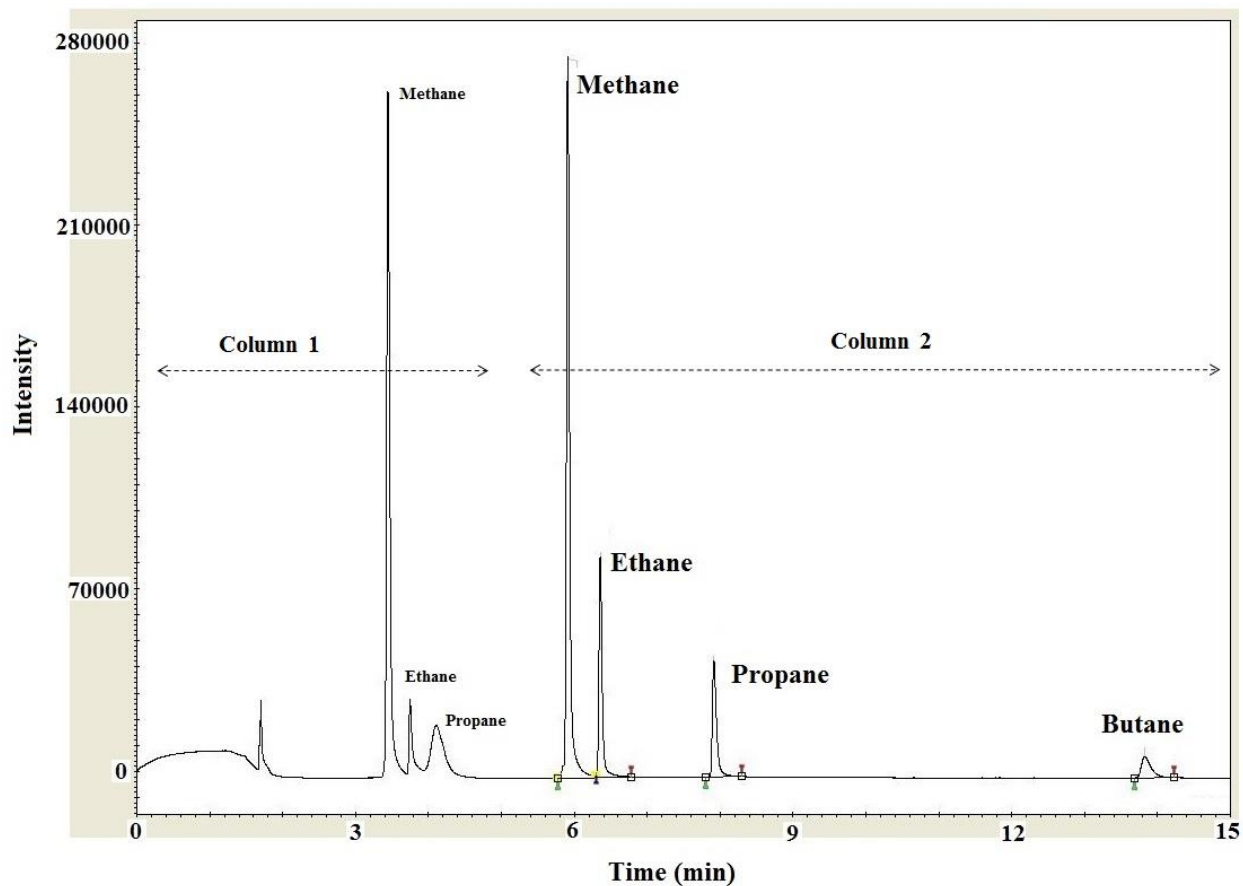


**Figure 31. Typical analysis of gas chromatography for a mixture of methane/ethane/propane/butane**

Generally, in gas chromatography technique for a mixture, the area of a peak ( $S_i$ ) is proportional to the amount of component introduced ( $n_i$ ) as follow:

$$S_i = k_i n_i \quad (21)$$

where  $k_i$  is proportionality constant of component  $i$  in the mixture. Hence by knowing the amount of component injected, the proportionality constant can be determined. However in our experiments, the exact amount of components sampled cannot be determined. Because ROLSI instrument which is used for gas sampling, is a valve that can be opened for a period of time. Therefore, the amount of sample is proportional to the gas flow rate and consequently the gas pressure. Since the operational conditions (pressure and temperature) vary during the course of experiment, the exact amount of components cannot be precisely determined.

Therefore, a relative calibration of GC was applied to determine the proportionality constants. Four gas bottles of  $\text{CH}_4\text{-C}_2\text{H}_6\text{-C}_3\text{H}_8\text{-nC}_4\text{H}_{10}$  with different compositions were prepared. Table 27 presents the composition of these four mixtures.

**Table 27. Composition of bottles used for GC calibration**

Mixture	Gas composition (%) ( $\pm 0.1\%$ )			
	$\text{CH}_4$	$\text{C}_2\text{H}_6$	$\text{C}_3\text{H}_8$	$\text{nC}_4\text{H}_{10}$
1	84.99	9.01	4.00	2.00
2	73.93	14.69	8.05	3.33
3	89.67	7.35	1.88	1.10
4	73.16	11.38	13.40	2.10

Each gas mixture was injected in the reactor and analyzed by GC. To assess reproducibility and to ascertain the quality of evaluations, each mixture was analyzed four times. The methane gas was taken into account as a reference since it was the dominant component in all mixtures. By equation 21 for methane:

$$S_{\text{CH}_4} = k_{\text{CH}_4} n_{\text{CH}_4} = k_{\text{CH}_4} n_t y_{\text{CH}_4} \quad (22)$$

By dividing the equations 21 and 22:

$$\frac{S_i}{S_{CH_4}} = k_{i,CH_4} \frac{y_i}{y_{CH_4}} \quad (23)$$

The peak area of each component is provided by GC. The composition of each gas in the bottles was already determined during the gas mixture preparation. Therefore, the proportional constant  $k_{i,CH_4}$  can be determined. The calibration curves with different slopes ( $K_{i,CH_4} = \frac{1}{k_{i,CH_4}}$ ) were then provided.

The results of GC calibration are illustrated in Figure 32. As the figures show, the area ratios to concentrations ratio are in linear forms. The slopes of these curves provide the proportional constants.

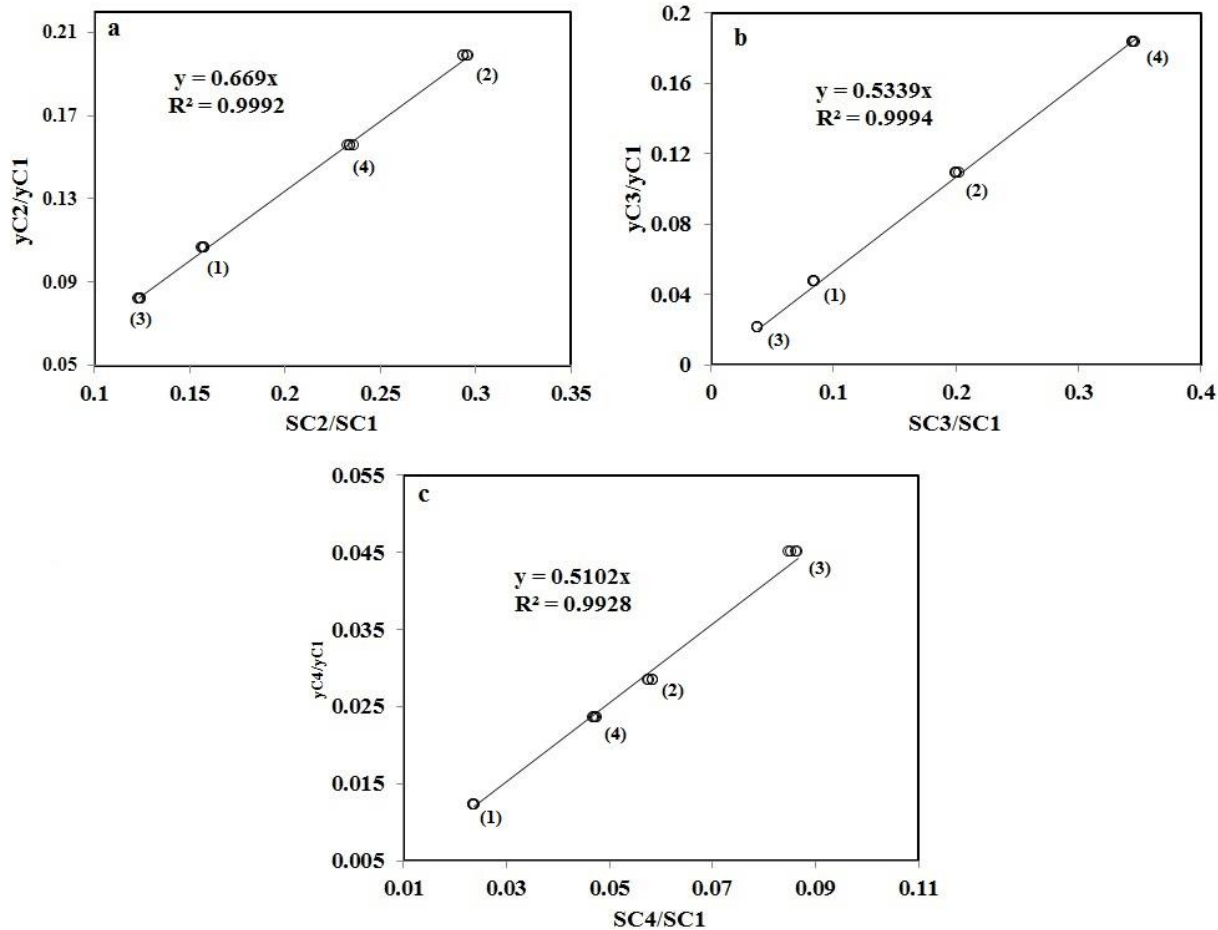


**Figure 32.** GC calibration results. *S* is peak area and *y* is gas composition. Circles are experimental point for calibration. C1, C2, C3 and C4 correspond to methane, ethane, propane and n-butane, respectively. The numbers indicate the bottles composition provided in Table 27

Once the proportional constants have been determined, the gas composition during the experiments for each analysis can be calculated as following:

$$y_{CH_4} = \frac{1}{1 + \sum_{i \neq CH_4} K_{i,CH_4} \frac{S_i}{S_{CH_4}}} \quad (24)$$

$$y_{i \neq CH_4} = \frac{S_i}{S_{CH_4}} y_{CH_4} K_{i,CH_4} \quad (25)$$

This should be noted that the GC connected to the SECOHYA reactor, had been already calibrated for carbon dioxide, methane, ethane, propane and n-butane [178]. In this work, only

the GC connected to ACACIA has been calibrated. The error of determination of each peak area is estimated by  $\Delta S/S = 0.05$ . The results of calibration curve provide relative compositions by an error of  $\pm 1\%$ .

#### **4.4. Ion Chromatography**

Ion Chromatograph (IC) or Ion-Exchange Chromatograph (IEC) is an instrument which separates ions according to their interactions with a stationary phase and a mobile phase. An anion column attracts cations and a cation column attracts anions. The columns measure the conductivity of ions attracted by an electrical conductivity detector. The detector produces a chromatogram which designs conductivity versus time. Each ion has a peak on this diagram and the height and area of each peak depends on the relative concentration in the injected solution. These measurements can then be utilized to determine concentrations of components in a sample. The ion chromatograph used in this work is ThermoFisher ICS-5000+.

As aforementioned, liquid samples were taken during the experiments for tracing the concentration of lithium in order to measure the volume of water converted to hydrate. The amount of samples were between 1 and 2 ml. Since the minimum volume of sample required to be analyzed by IC is 5ml, the samples were diluted by a factor of 5. Then, they were loaded in the sampler of IC. A typical analysis of IC for lithium is presented in Figure 33. As clear on the figure, the peak of lithium with a good resolution is at the retention time of 4.701.

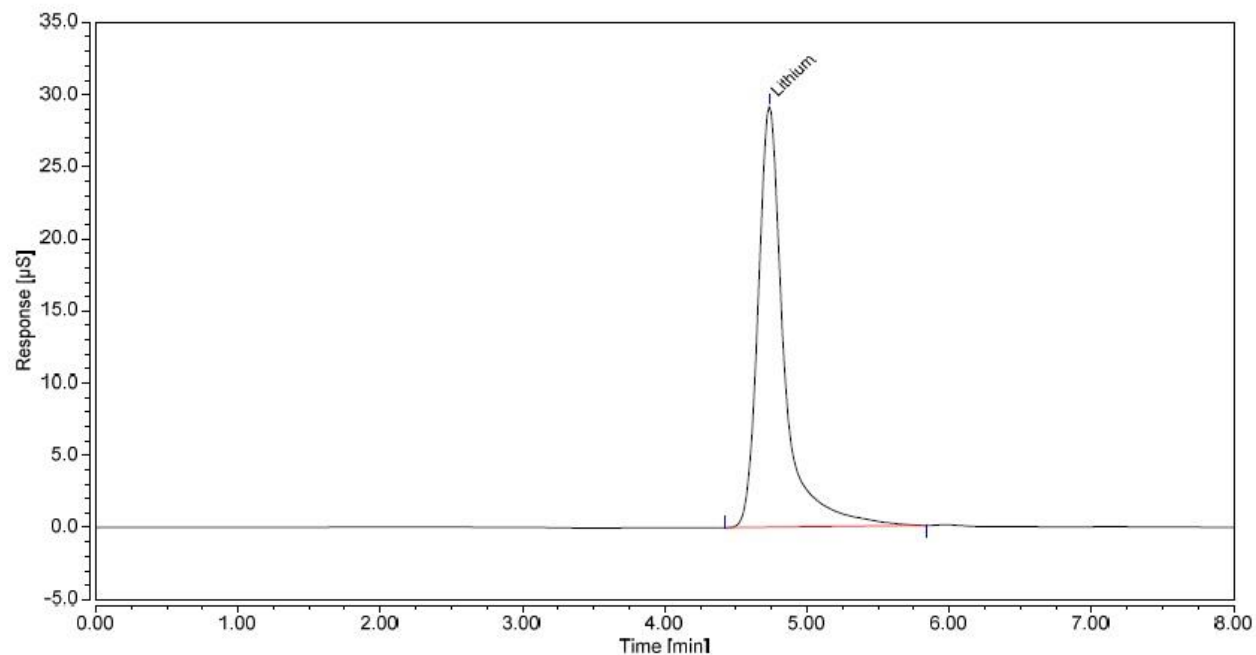


**Figure 33. A typical analysis of IC for lithium**

Given the fact that the concentration of mobile phase may vary for different sequences of analyses, a calibration curve were provided at each series of measurements. For this, standard solution with known concentrations of lithium were prepared and analyzed. Then, the relationship between the peak areas and lithium concentrations were obtained. Figure 34 illustrates a typical calibration curve of IC for lithium. A linear relationship between the peak area and concentration (ppm) was achieved which can be used to determine the concentration of lithium at a measured peak area. This should be considered that the IC used in this study, provides lithium concentration by an adequate precision ( $\Delta[Li^+]/[Li^+] = 0.001$ ).



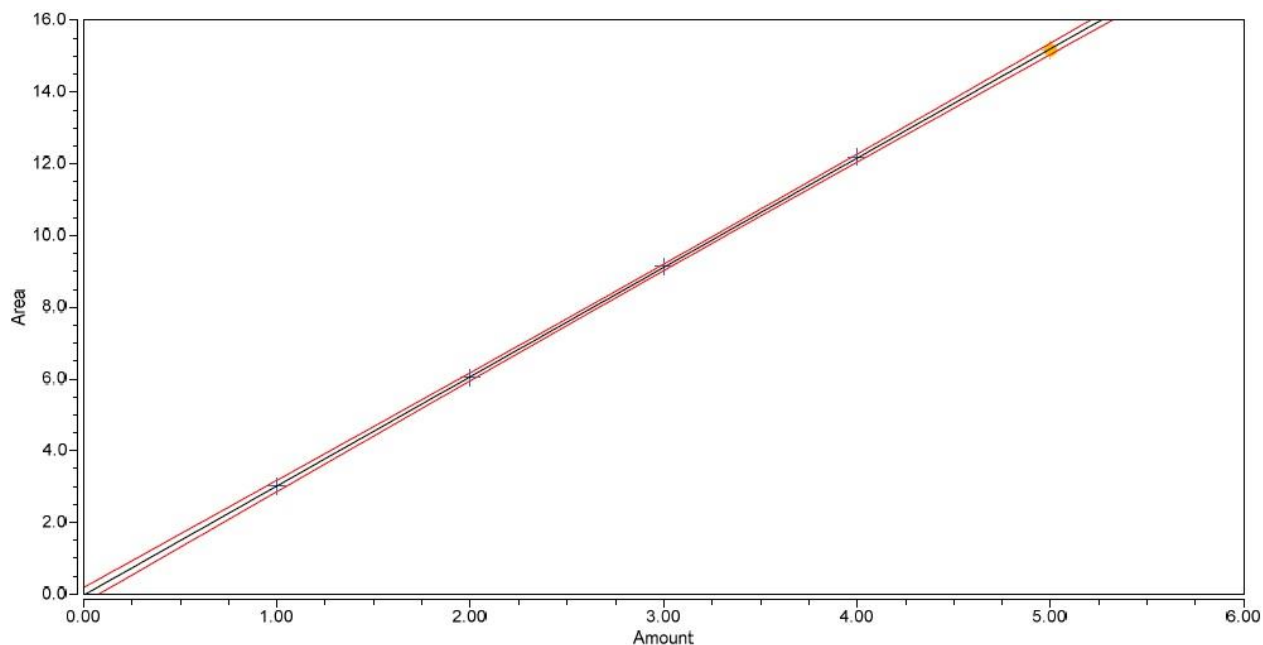


**Figure 34. A typical calibration curve of IC for lithium (the axis x is the amount of lithium in ppm).**

**Experimental data for IC calibration are shown by points and calibration curves by lines.**

## **4.5. Experimental procedures**

To evaluate effects of crystallization rate on the equilibrium condition at final state, both quick and slow crystallization were investigated. Quick crystallization evaluates the formation and dissociation of mixed gas hydrates at high initial supersaturation. Whereas at slow crystallization, the aim is to neglect the kinetic effects as much as possible. This means that we expect to be closer to the thermodynamic equilibrium condition, which usually occurs in steady state processes.

### **4.5.1. Quick crystallization process**

Using the same previous procedure as we did on gas hydrates equilibria [113,121], the crystallization occurs at a “high rate” (or at a high initial supersaturation). At first, the reactor is filled by nitrogen up to 50 bar in order to check the cell for the leakage. The pressure is monitored between 24 to 48 hours to ensure that there is no pressure drop. The reactor is then cleaned and vacuumed (for 40-50 minutes). The cell is filled with the prepared gas mixture at chosen expected pressure. Pressure and temperature are measured and the gas composition is checked with GC analysis. Thanks to these measurements, the amount of each gas molecules can be calculated using an appropriate Equation of State (EoS), here Soave-Redlich-Kwong. About

800-1200 mL of water (including 10 ppm  $\text{Li}^+$ ) is then prepared and inserted into the cell *via* the HPLC pump. The water is ultrapure water (first category, 18.2 M $\Omega$ .cm) and  $\text{LiNO}_3$  acts as a tracer to monitor the water volume. It does not influence hydrate equilibrium. An increase of pressure, due to the added volume of liquid, is observed. Then, the cryostat temperature is set to 1°C and the batch is stirred at the rate of 400 rpm on both the upper gas and lower liquid sections. After the gas dissolution into the liquid phase, and the induction time, the crystallization begins (normally after several hours to days). As a result of hydrate formation, a pressure drop is observed. Additionally, due to the exothermicity of the reaction, a short-term increase of temperature is detected. At this point, it is necessary to wait (3-8 days) for equilibrium to be attained (no more changes in temperature or pressure). After equilibrium is reached, a sample of the gas phase is taken and injected into the gas chromatograph to determine the molar composition. A liquid sample is also taken to be analyzed by ionic chromatography (about 1-2mg). Then, the dissociation of the hydrate begins. Temperature is increased by about 1-2°C, over about 24 hours with a maximum of three days. Then when second equilibrium is reached, new samples of the fluid phases are taken. The process is iterated until there is no longer a hydrate phase into the reactor. The whole procedure takes about 25 days for each mixture. A schematic diagram summarizing the whole quick crystallization process is illustrated in Figure 35(a).

#### **4.5.2. Slow crystallization process**

At the end of quick crystallization process, the amount of water samples taken is measured. The same amount of water is then replaced into the reactor to have almost the same initial pressure and temperature conditions. Pressure, temperature and guest compositions are analyzed to assure that the same initial conditions are going to be considered. At this point, slow crystallization procedure starts. However, instead of decreasing quickly the temperature, the cooling rate is very slow (0.3-0.5°C per 12 hours and we wait to reach equilibrium at each temperature drop iteration). Gas and liquid samples are taken during, and at the end, of crystallization. In this case, the process takes about 60 days for each mixture as opposed to 25. Moreover, the final point at which the hydrate volume is the highest is obtained in about 60 days, compared to around 5 days for quick process. A schematic of procedure is illustrated in Figure 35(b).

At last, in order to exemplify the both procedures, the evolution of pressure and temperature during the course of experiments (both crystallization methods) for methane-propane mixture is provided in Figure 36.

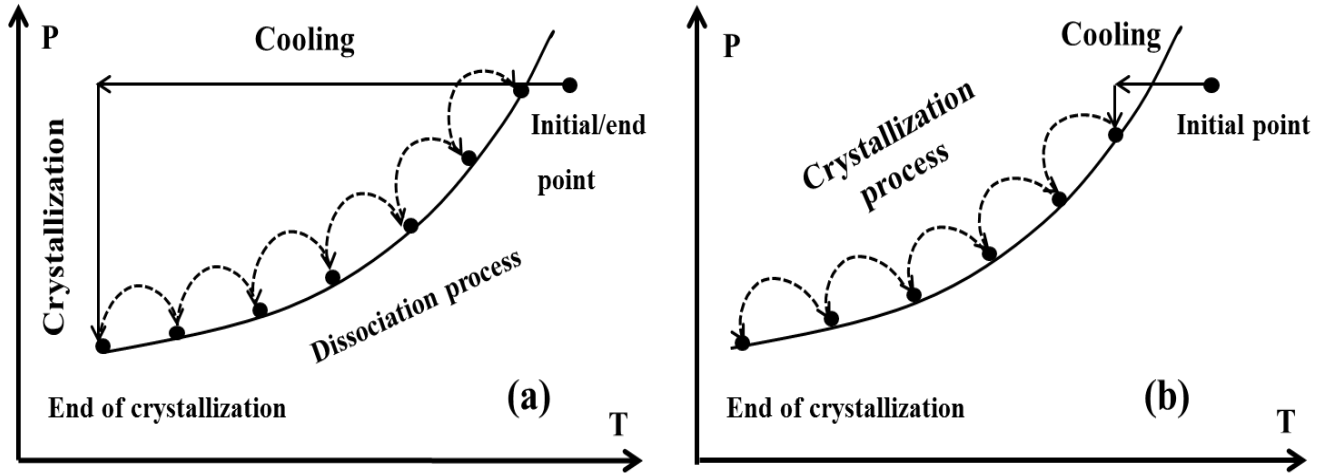


Figure 35. Schematic of the experimental procedures: a) Quick crystallization process. b) Slow crystallization process

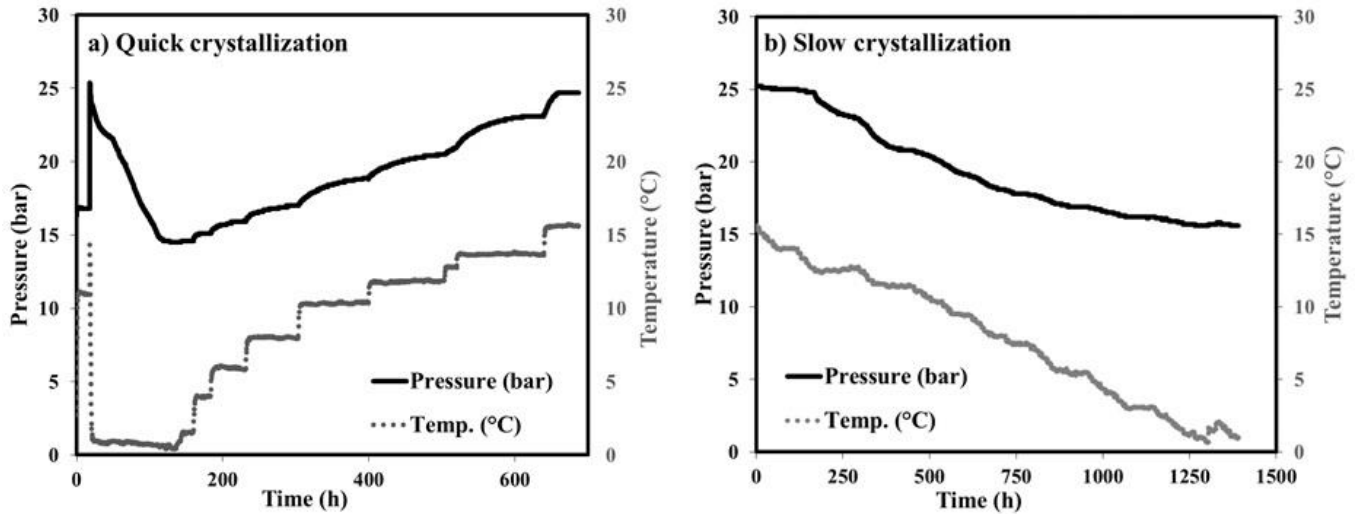


Figure 36. The evolution of pressure and temperature during the course of experiments for methane-propane mixture: a) Quick crystallization process and b) Slow crystallization process

#### 4.6. Mass balance and hydrate phase properties calculation

The mass balance for each molecule is used to determine the amount of gas molecules in the hydrate phase ( $n_j^g$ ):

$$n_j^0 = n_j^L + n_j^H + n_j^g \quad (26)$$

Where  $j$  is guest molecule,  $0$  indicates the initial condition,  $n$  is mole number,  $L$ ,  $H$  and  $g$  stand for the liquid, hydrate and gas phases, respectively.

Fluid phases are analyzed through GC and ionic chromatography. The amount of gas sampled is very small (about  $\mu\text{m}^3$ ), so it can be neglected. For liquid analysis, at each point, about 1-2 ml of solution is taken. Hence its removal was taken into account at each step when evaluating the actual mass of water and lithium concentration in the solution.

#### 4.6.1. Liquid phase

As aforementioned, about 10ppm  $\text{Li}^+$  was used for each experiment as a tracer. The volume of the water phase can be calculated based on the mass balance of the lithium concentrations:

$$V^L = \frac{V_0^L [Li_0^+]}{[Li^+]} \quad (27)$$

where  $V^L$  is the volume of liquid at equilibrium,  $V_0^L$  is the volume of injected solution,  $[Li_0^+]$  the initial concentration of Lithium and  $[Li^+]$  is the concentration of lithium at equilibrium. The two last parameters can be measured by an ion-chromatograph.

It should be noted that, in order to take samples, we always stop the agitation. Due to differences in density of water and hydrate, hydrate and liquid phases are separated; liquid phase at the bottom of reactor and hydrate phase at the top (in most cases). The sampling tube is located at the bottom of reactor. Furthermore, we saw neither crystals nor turbidity showing presence of crystals in the samples with our naked eyes. Hence, we assumed that hydrate crystals were not sampled with the liquid.

The mole number of each gas in liquid phase can be then determined from gas solubility in water. Note that the effect of  $\text{LiNO}_3$  is neglected. Gas solubility is calculated according to the Henry's law under the following form [179]:

$$n_j^L = \frac{V^L \rho_w^0}{M_w} \frac{y_i \phi_j^G P}{K_{H,j}^\infty \exp\left(\frac{P v_j^\infty}{RT}\right)} \quad (28)$$

where  $\rho_w^0$  and  $M_w$  stand for the density and molecular weight of water, respectively,  $\varphi_j^G$  fugacity coefficient of gas  $j$ ,  $v_j^\infty$  is the partial molar volume of the gas  $j$  in the solvent water ( $v_j^\infty=32$  cm<sup>3</sup>mol<sup>-1</sup> [179]) and  $K_{H,j}^\infty$  is Henry's constant and can be calculated from the following equation [180]:

$$K_{H,j}^\infty = \exp\left(A + \frac{B}{T}\right) \quad (29)$$

The values of  $A$  and  $B$  for gases used in this study are in Table 2.

**Table 28. The values of  $A$  and  $B$  for calculating the Henry's constants [180]**

Gas	$A$	$B$ (K)
CO <sub>2</sub>	14.283146	-2050.3269
N <sub>2</sub>	17.934347	-1933.3810
CH <sub>4</sub>	15.872677	-1559.0631
C <sub>2</sub> H <sub>6</sub>	18.400368	-2410.4807
C <sub>3</sub> H <sub>8</sub>	20.958631	-3109.3918
nC <sub>4</sub> H <sub>10</sub>	22.150557	-3407.2181

#### 4.6.2. Gas phase

The composition of gas phase at any state during the course of experiments can be known by gas-chromatograph. Then the mole number of gas at initial state ( $n_j^0$ ) and at equilibrium ( $n_j^{eq}$ ) can be calculated as following:

$$n = \frac{PV^G}{Z(P,T,y)RT} \quad (30)$$

where  $P$  is pressure,  $Z$  is compressibility factor which can be calculated from Soave-Redlich-Kwong equation of state [59]. The gas volume  $V^G$  at equilibrium is:

$$V^G = V^R - V^L - V^H \quad (31)$$

Volumes for the reactor ( $V^R$ ) are 2.23 and 2.36 liter.  $V^L$  in equation 31 is known at each state based on the procedure explained in section 4.6.1.  $V_H$  is hydrate volume and its calculation is explained hereafter (section 4.6.3).

### 4.6.3. Hydrate phase

Knowing the mass of water in liquid phase, and consequently the mass of water in the hydrate phase, the volume of hydrate at equilibrium can be calculated based on the theoretical density of structures I and II [1], as follow:

$$m_W^H = (V_0^L - V^L)\rho_W \quad (32)$$

$$V^H = m_W^H \times \rho^{H-\beta I} \quad \text{for sI} \quad (33)$$

$$V^H = m_W^H \times \rho^{H-\beta II} \quad \text{for sII} \quad (34)$$

where  $\rho_w$  is the density of water,  $m_W^H$  is the mass of water in hydrate structure.  $\rho^{H-\beta I}$  and  $\rho^{H-\beta II}$  are the density of empty hydrate density based on water molecules for sI and sII, respectively (790 kg/m<sup>3</sup> for sI and 785 kg/m<sup>3</sup> for sII).

Given the fact that the density difference between structures I and II, only based on water molecules ( $\beta$  reference state), is 5 kg/m<sup>3</sup>, therefore, if the wrong structure is assumed in the calculations, the error on the calculated hydrate volume is about 0.6%. If both structures are present, this error is even lower. That is why the reliability of the hydrate volume is not really affected by the structure assumption. In fact, ionic chromatography analysis is probably more affected by uncertainties.

Once the mole number of gas in gas and liquid phases is calculated, then the mole number and composition of each gas in hydrate phase can be calculated by equation 26.

The procedure of mass balance calculation is summarized in Figure 37.

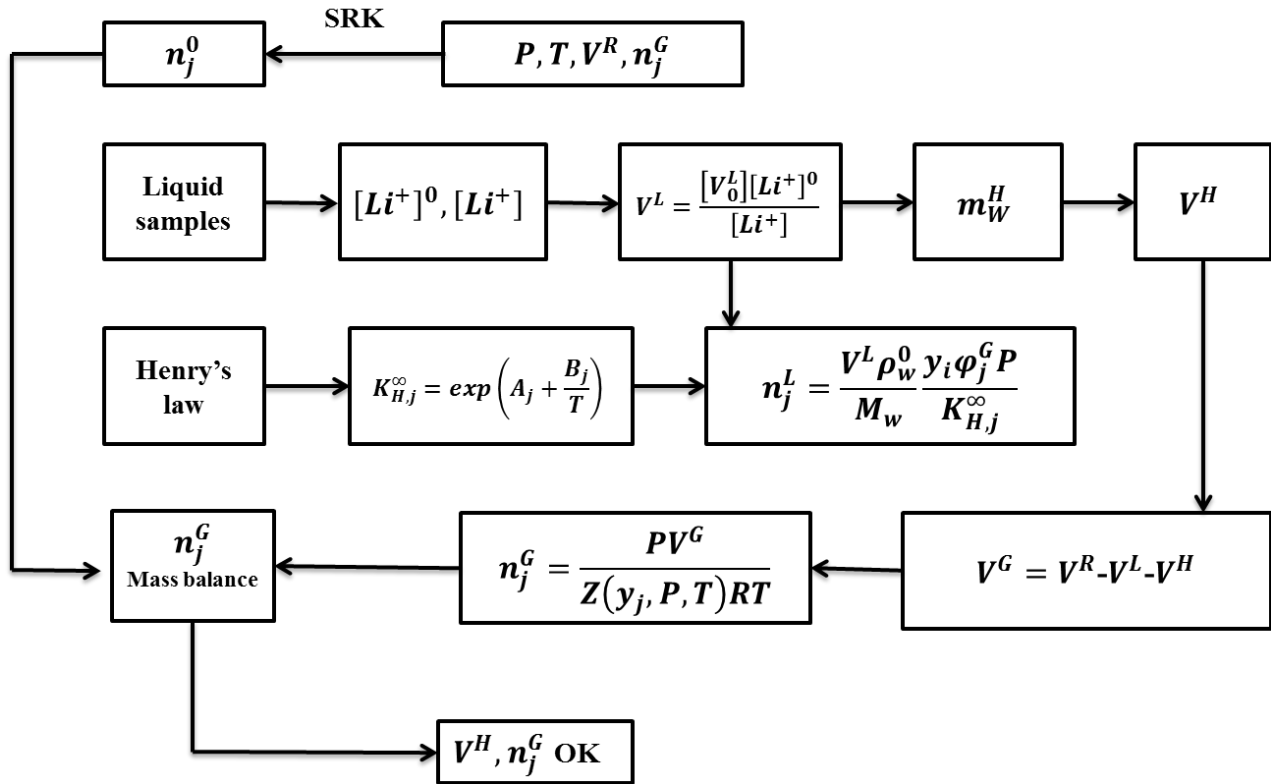


Figure 37. Mass balance calculation at equilibrium conditions

#### 4.6.4. Hydrate phase properties

This work provide not only new phase equilibrium data for mixed gas hydrates, but also contain hydrate phase properties such as hydration number, hydrate volume, storage capacity, water conversion and hydrate density. These rare properties are variable with temperature, pressure and the composition of associated fluid phases [1]. Therefore, they were determined at each stable state during the course of experiments. Note that, as stated before, stable state does not mean thermodynamic equilibrium.

The hydrate volume calculation was already explained in section 4.6. Water conversion is the percentage of water converted to hydrate (in % mass).

Storage capacity (SC) defines the volume of gas in hydrate phase at standard conditions per volume of hydrate ( $V^H$ ). The ideal gas law demonstrates that the molar volume of any gas at standard conditions ( $T=273K$  and  $P=1atm$ ) is 22.41 L/mol. Hence, the storage capacity is calculated as follow:

$$SC = \frac{22.41 \times 1000 \times \sum n_j^H}{V^H} \quad (35)$$

The hydrate density ( $\rho^H$ ) is the mass of water converted to hydrate ( $m_w^H$ ) plus the mass of encaged guest molecules ( $MW_j n_j^H$ , where  $MW_j$  is the molecular weight of component  $j$ ) per volume of hydrate:

$$\rho^H = \frac{m_w^H + \sum MW_j n_j^H}{V^H} \quad (36)$$

Hydration number ( $N_{hyd}$ ) is the water to gas ration in hydrate phase. Therefore:

$$N_{hyd} = \frac{m_w^H / MW_w}{\sum n_j^H} \quad (37)$$

#### 4.7. Experimental and instrumental uncertainties and assumptions

Determining uncertainties in any experimental procedures is essential. In this section, a brief description of sampling influence as well as errors is presented. Standard and absolute uncertainties of all measured and derived quantities are provided in Table 29 and in the footnotes of each data table. The different resources of instrumental errors, as well as their calculations, were explained in details in our previous works [113,121,135].

As aforementioned, each experiment of slow crystallization process takes about 60 days (about 25 days for quick crystallization process). Hence, it is not practical to investigate the reproducibility of each mixture and procedure. Nonetheless, we replicated two experiments under the same conditions on CH<sub>4</sub>/C<sub>3</sub>H<sub>8</sub> mixture in order to assess the quality of experimental data. The results showed that, at a given temperature, the pressure difference was less than 0.2 bar. The discrepancies in guest composition in gas and hydrate phases were about 0.006 and 0.008 mole fractions, respectively. Thus, it could be an evidence to ascertain the quality of our experimental data.

The amount of gas samples were about a few  $\mu\text{m}^3$ , hence negligible. At each stable state, about 1-2 mL of solution was sampled. Consequently, the amount of solution inside the reactor was actualized at each step according to the mass of water and lithium samples taken.



Moreover, as the hydrate volume and composition were obtained by changes in lithium concentrations, it seems obvious that larger amounts of hydrate lead to more accurate calculations. As a result, mass balance calculations sometimes fail near the total dissociation point. Indeed, when calculating with very small amounts of hydrates (close to zero) measurement uncertainties can lead to a negative mass for the hydrate. On the other hand, at the final state of crystallization, results are precise and reliable.

**Table 29. The experimental and instrumental uncertainties**

<b>Parameter</b>	<b>Absolute uncertainty</b>	<b>Source of uncertainty</b>
Temperature	0.2°C	Instrumental
Pressure	0.1 bar	Instrumental
Volume of reactor	0.001 L	Instrumental
Mass of water	0.1 g	Instrumental
Guest composition in gas phase	0.001 mole fraction	Instrumental
Guest composition in hydrate composition	0.003 mole fraction	Experimental
Guest composition in liquid phase	0.003 mole fraction	Experimental
Hydrate volume	0.4 cm <sup>3</sup>	Experimental
Hydration number	0.5	Experimental
Hydrate density	0.05 g/cm <sup>3</sup>	Experimental
Storage capacity	0.5 V/V	Experimental
Water conversion	0.4	Experimental
Gas solubility in the liquid phase	0.3 mmol/L	Experimental

## 5. Experimental results and modeling

In the present work, mixed gas hydrates from binary mixtures  $\text{CH}_4\text{-C}_3\text{H}_8$ ,  $\text{C}_2\text{H}_6\text{-C}_3\text{H}_8$ ,  $\text{CO}_2\text{-C}_3\text{H}_8$ ,  $\text{C}_2\text{H}_6\text{-nC}_4\text{H}_{10}$ ,  $\text{CH}_4\text{-nC}_4\text{H}_{10}$ , ternary mixtures  $\text{CO}_2\text{-C}_2\text{H}_6\text{-C}_3\text{H}_8$ ,  $\text{CH}_4\text{-C}_2\text{H}_6\text{-nC}_4\text{H}_{10}$ ,  $\text{CO}_2\text{-N}_2\text{-C}_2\text{H}_6$  and quaternary  $\text{CH}_4\text{-C}_2\text{H}_6\text{-C}_3\text{H}_8\text{-nC}_4\text{H}_{10}$  have been studied. The results obtained provide detailed information about temperature, pressure, guest composition in all phases (gas, liquid and hydrate), hydrate volume and density, hydration number, water conversion and storage capacity.

Furthermore, this work includes not only the investigation at final state, but also during the crystallization under non-equilibrium conditions. The influence of the crystallization rate has also been evaluated in order to better understand the role of kinetics in mixed hydrate crystallization. Finally, the experimental results have been compared to van der Waals and Platteeuw approach using Kihara potential.

### 5.1. Initial conditions

Since the slow crystallization procedure begins at the end of quick crystallization method for each gas mixture, the initial molar feed composition, volume of reactor and initial gas temperature and pressure of both procedures were similar. The approximate amount of water sampled during the quick crystallization process, was injected into the reactor before starting the slow crystallization for each gas mixture. Table 30 presents the initial conditions of all experiments.

**Table 30. Initial conditions of the experiments**

Gas	Type of exp.	Water(g)	Feed molar composition						$V_R$ (L)	$T_g$ (°C)	$P_g$ (bar)
			$N_2$	$CO_2$	$CH_4$	$C_2H_6$	$C_3H_8$	$nC_4H_{10}$			
1	Quick	801.4	-	-	0.861	-	0.139	-	2.36	10.9	16.8
	Slow	802.4									
2	Quick	798.6	-	-	-	0.811	0.189	-	2.23	16.3	13.7
	Slow	799.1									
3	Quick	1022.3	-	0.956	-	-	0.044	-	2.36	16.3	26.1
	Slow	1023.0									
4	Quick	801.0	-	-	-	0.956	-	0.044	2.23	16.3	16.6
	Slow	802.4									
5	Quick	801.8	-	-	0.959	-	-	0.041	2.36	16.0	16.5
	Slow	803.9									
6	Quick	1000.2	-	-	0.838	0.107	-	0.055	2.23	16.7	18.5
	Slow	1000.4									
7	Quick	1000.2	-	0.385	-	0.403	0.212	-	2.36	17.3	12.9
	Slow	1001.2									
8	Quick	800.8	0.205	0.261	-	0.534	-	-	2.23	20.2	18.9
	Slow	813.7									
9	Quick	801.4	-	-	0.737	0.120	0.124	0.019	2.36	15.8	15.5
Absolute uncertainty		±0.1 g	±0.001 mole fraction						±0.001 L	±0.2°C	±0.1 bar

## 5.2. Pressure and temperature evolution during the quick crystallization

An example of the procedures on  $C_2H_6/C_3H_8$  mixed hydrate will be presented in this section. Figure 38 illustrates the changes of temperature and pressure during the quick crystallization for ethane-butane mixture. The experiment was started at initial point (A). The solution was then rapidly cooled down near  $1^\circ C$  and after a while (depending on the gas mixture), crystallization started (B). Due to hydrate formation, the pressure decreased. We waited until the end of crystallization, point C (where there were no longer changes in temperature and pressure for 48 hours). Once gas hydrate formation was completed, the temperature was increased incrementally and every two days, gas and liquid samples were taken for analysis. The dissociation process was repeated until the dissociation curve meets the cooling line (D). Then, the amount of sampled

water was then re-injected into the reactor. Temperature was reset to have the same initial conditions.

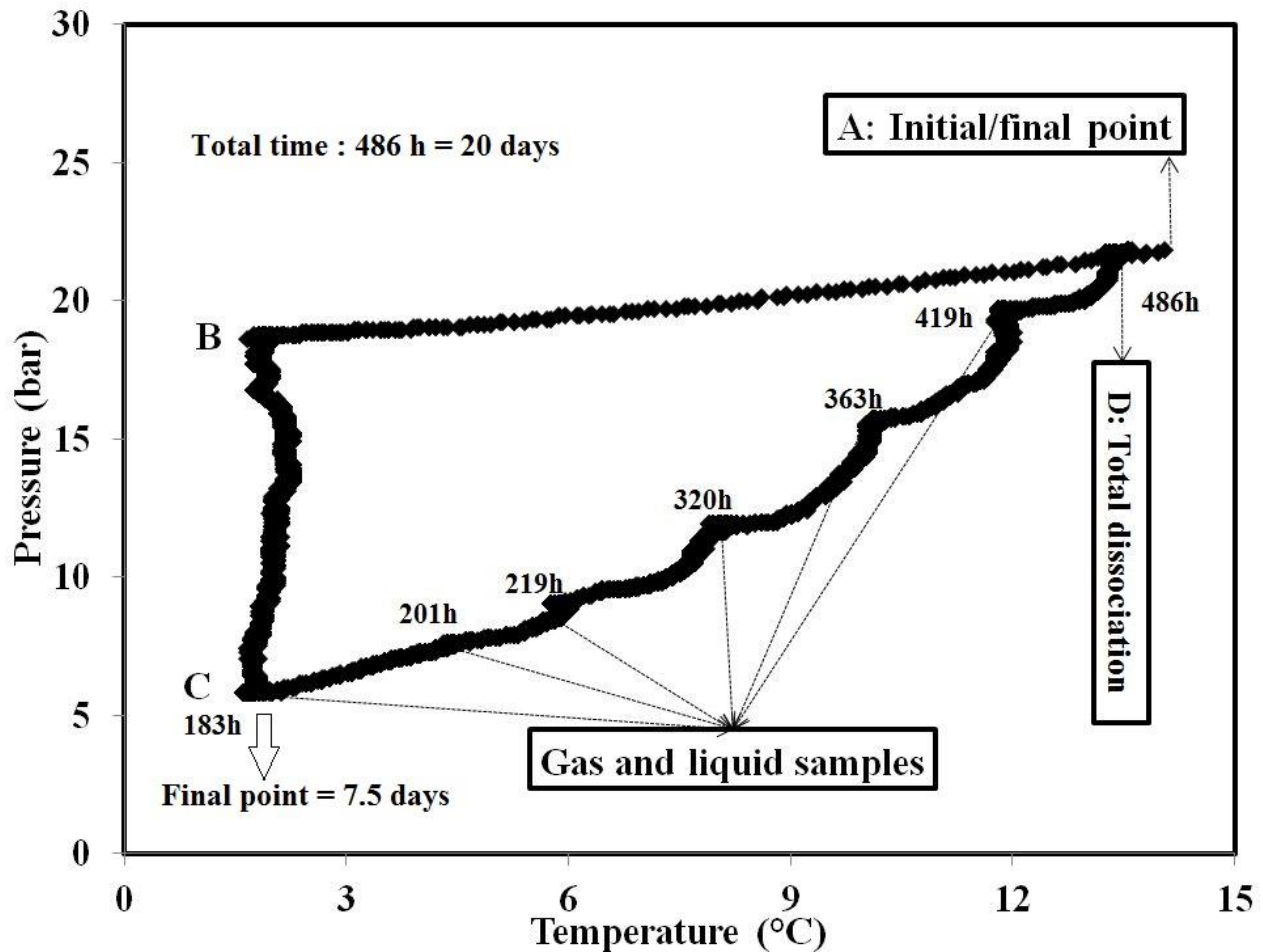


Figure 38. The pressure change versus temperature during the quick crystallization process in the case of ethane-butane mixture. The numbers in the figure correspond to the time of taking samples (from beginning of experiment)

### 5.3. Pressure and temperature evolution during the slow crystallization

Figure 39 shows temperature- pressure evolution during the slow crystallization procedure for ethane-butane mixture. As seen in this figure, the process was started with the same initial conditions as quick crystallization (A). But in this procedure, the temperature was decreased in a slow stepwise manner to negate the influence of kinetics as much as possible. This procedure is closer to the steady state processes. B was the first vapor-liquid-hydrate equilibrium point. The temperature was then decreased step by step until the end of crystallization (C). Several gas and liquid samples were taken for analysis.

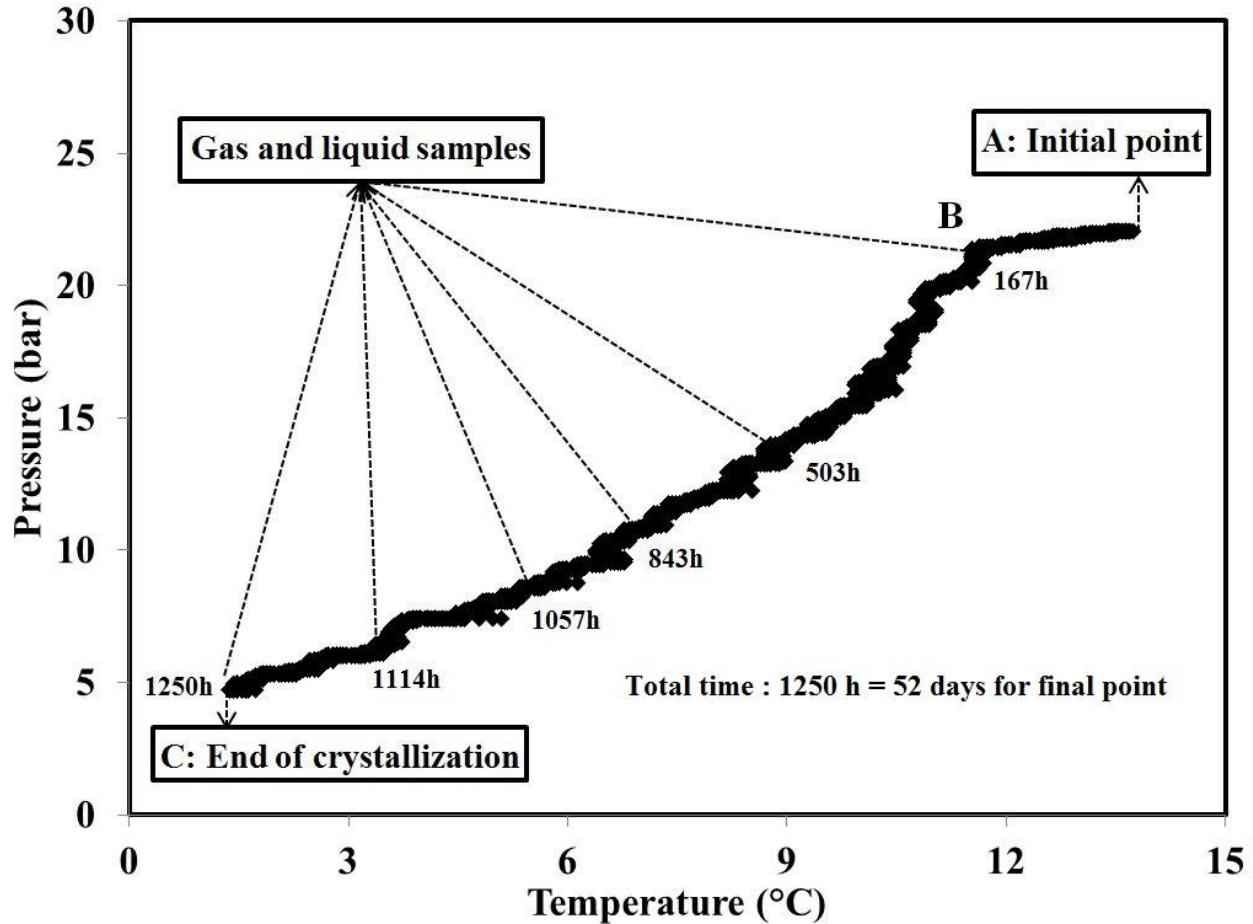


Figure 39. Temperature- pressure evolution during the slow crystallization procedure for ethane-butane mixture. The numbers in the figure correspond to the time of taking samples (from beginning of experiment)

These two procedures were performed for all the mentioned mixtures. The results are provided in the following sections.

## 5.4. Experimental results

### 5.4.1. New phase equilibrium data

In this section, the experimental results concerning V-L<sub>w</sub>-H equilibrium data are presented. Table 31 provides experimental results including not only temperature, pressure and composition of associated fluid phases, but also the distribution of guests in hydrate phase. Moreover, the gas solubility in liquid phase calculated from Henry's law is also presented in Table 32.

**Table 31. Experimental results of guest composition in all phases regarding to the equilibrium temperature and pressure for two rates of crystallization**

Gas	method	T (°C)	P (bar)	Molar gas composition ( $\pm 0.001$ )						Molar liquid composition (water free)						Molar hydrate composition (water free)					
				CO <sub>2</sub>	N <sub>2</sub>	CH <sub>4</sub>	C <sub>2</sub> H <sub>6</sub>	C <sub>3</sub> H <sub>8</sub>	C <sub>4</sub> H <sub>10</sub>	CO <sub>2</sub>	N <sub>2</sub>	CH <sub>4</sub>	C <sub>2</sub> H <sub>6</sub>	C <sub>3</sub> H <sub>8</sub>	C <sub>4</sub> H <sub>10</sub>	CO <sub>2</sub>	N <sub>2</sub>	CH <sub>4</sub>	C <sub>2</sub> H <sub>6</sub>	C <sub>3</sub> H <sub>8</sub>	C <sub>4</sub> H <sub>10</sub>
1	Quick	0.45	14.5	-	-	0.993	-	0.007	-	-	-	0.988	-	0.012	-	-	-	0.691	-	0.309	-
		1.50	14.6	-	-	0.991	-	0.009	-	-	-	0.985	-	0.015	-	-	-	0.688	-	0.312	-
		4.00	15.1	-	-	0.984	-	0.016	-	-	-	0.975	-	0.025	-	-	-	0.686	-	0.314	-
		5.80	15.9	-	-	0.975	-	0.025	-	-	-	0.962	-	0.038	-	-	-	0.675	-	0.325	-
		7.90	17.0	-	-	0.962	-	0.038	-	-	-	0.946	-	0.054	-	-	-	0.661	-	0.339	-
		10.40	18.9	-	-	0.939	-	0.061	-	-	-	0.916	-	0.084	-	-	-	0.638	-	0.362	-
		11.90	20.5	-	-	0.919	-	0.071	-	-	-	0.890	-	0.107	-	-	-	0.611	-	0.382	-
		13.60	23.2	-	-	0.890	-	0.110	-	-	-	a	-	a	-	-	-	a	-	a	-
	Slow	11.35	20.8	-	-	0.926	-	0.07	-	-	-	0.902	-	0.098	-	-	-	0.559	-	0.44	-
		10.35	20.0	-	-	0.936	-	0.064	-	-	-	0.913	-	0.087	-	-	-	0.574	-	0.43	-
		7.95	18.1	-	-	0.964	-	0.036	-	-	-	0.948	-	0.052	-	-	-	0.602	-	0.398	-
		5.70	17.0	-	-	0.980	-	0.020	-	-	-	0.969	-	0.031	-	-	-	0.614	-	0.386	-
		4.00	16.5	-	-	0.986	-	0.014	-	-	-	0.978	-	0.022	-	-	-	0.622	-	0.378	-
		2.55	16	-	-	0.991	-	0.009	-	-	-	0.985	-	0.015	-	-	-	0.627	-	0.373	-
1.55		15.8	-	-	0.993	-	0.007	-	-	-	0.988	-	0.012	-	-	-	0.629	-	0.371	-	
0.90		15.6	-	-	0.994	-	0.006	-	-	-	0.989	-	0.011	-	-	-	0.629	-	0.371	-	
2	Quick	0.95	6.1	-	-	-	0.756	0.244	-	-	-	0.758	0.242	-	-	-	-	0.832	0.168	-	
		4.60	10.3	-	-	-	0.712	0.288	-	-	-	0.721	0.279	-	-	-	-	0.908	0.092	-	
		6.05	12.2	-	-	-	0.734	0.266	-	-	-	0.745	0.255	-	-	-	-	0.929	0.071	-	
		9.15	16.5	-	-	-	0.812	0.188	-	-	-	0.824	0.176	-	-	-	-	0.803	0.197	-	
	Slow	7.80	14.0	-	-	-	0.801	0.199	-	-	-	0.812	0.188	-	-	-	-	0.833	0.167	-	
		6.40	11.7	-	-	-	0.770	0.230	-	-	-	0.780	0.220	-	-	-	-	0.866	0.134	-	

		4.55	9.5	-	-	-	0.723	0.277	-	-	-	-	0.731	0.269	-	-	-	-	0.885	0.115	-	
		1.05	4.9	-	-	-	0.792	0.208	-	-	-	-	0.794	0.206	-	-	-	-	0.816	0.184	-	
3	Quick	1.8	16.4	0.965	-	-	-	0.035	-	0.998	-	-	-	0.002	-	0.922	-	-	-	0.078	-	
		4.1	20.0	0.955	-	-	-	0.045	-	0.997	-	-	-	0.003	-	0.908	-	-	-	0.092	-	
		4.7	21.6	0.959	-	-	-	0.041	-	0.998	-	-	-	0.002	-	0.872	-	-	-	0.128	-	
		5.7	24.1	0.962	-	-	-	0.038	-	0.998	-	-	-	0.002	-	0.657	-	-	-	0.343	-	
		6.6	24.6	0.959	-	-	-	0.041	-	0.998	-	-	-	0.002	-	0.630	-	-	-	0.370	-	
		7.9	25.6	0.947	-	-	-	0.053	-	0.997	-	-	-	0.003	-	0.606	-	-	-	0.394	-	
		9.0	26.7	0.924	-	-	-	0.076	-	a	-	-	-	a	-	a	-	-	-	a	-	
	Slow	1.8	14.3	0.964	-	-	-	0.036	-	0.998	-	-	-	0.002	-	0.935	-	-	-	0.065	-	
		4.1	19.5	0.964	-	-	-	0.036	-	0.998	-	-	-	0.002	-	0.893	-	-	-	0.107	-	
		5.8	22.8	0.961	-	-	-	0.039	-	0.998	-	-	-	0.002	-	0.762	-	-	-	0.238	-	
		6.7	23.8	0.959	-	-	-	0.041	-	a	-	-	-	a	-	a	-	-	-	a	-	
	4	Quick	1.7	5.8	-	-	-	0.918	-	0.082	-	-	-	0.926	-	0.074	-	-	-	0.967	-	0.033
			4.4	7.6	-	-	-	0.926	-	0.074	-	-	-	0.936	-	0.064	-	-	-	0.968	-	0.032
			5.8	9.0	-	-	-	0.918	-	0.082	-	-	-	0.930	-	0.070	-	-	-	0.976	-	0.024
8.2			11.9	-	-	-	0.936	-	0.064	-	-	-	0.947	-	0.053	-	-	-	0.973	-	0.027	
10.2			15.7	-	-	-	0.951	-	0.049	-	-	-	0.961	-	0.039	-	-	-	0.965	-	0.035	
11.9			19.7	-	-	-	0.960	-	0.040	-	-	-	0.968	-	0.032	-	-	-	0.937	-	0.063	
Slow		1.6	4.7	-	-	-	0.867	-	0.133	-	-	-	0.880	-	0.120	-	-	-	0.975	-	0.025	
		4.6	7.4	-	-	-	0.907	-	0.093	-	-	-	0.920	-	0.080	-	-	-	0.975	-	0.025	
		5.8	8.7	-	-	-	0.918	-	0.082	-	-	-	0.931	-	0.069	-	-	-	0.975	-	0.025	
		8.3	12.3	-	-	-	0.938	-	0.062	-	-	-	0.949	-	0.051	-	-	-	0.973	-	0.027	
		10.3	16.0	-	-	-	0.952	-	0.048	-	-	-	0.962	-	0.038	-	-	-	0.964	-	0.036	
		11.4	21.3	-	-	-	0.962	-	0.038	-	-	-	a	-	a	-	-	-	a	-	a	
5	Q	0.9	20.9	-	-	0.984	-	-	0.016	-	-	0.976	-	-	0.024	-	-	0.708	-	-	0.292	
	S	0.9	20.6	-	-	0.983	-	-	0.017	-	-	0.974	-	-	0.026	-	-	0.755	-	-	0.245	
6	Quick	1.7	17.8	-	-	0.947	0.035	-	0.018	-	-	0.917	0.057	-	0.026	-	-	0.694	0.202	-	0.104	
		3.8	19.4	-	-	0.928	0.048	-	0.024	-	-	0.891	0.076	-	0.033	-	-	0.693	0.201	-	0.106	

		5.3	21.2	-	-	0.909	0.062	-	0.029	-	-	0.866	0.096	-	0.038	-	-	0.691	0.200	-	0.109
		6.7	23.9	-	-	0.885	0.078	-	0.037	-	-	0.835	0.118	-	0.047	-	-	0.684	0.201	-	0.115
		8.8	28.6	-	-	0.847	0.102	-	0.051	-	-	0.791	0.149	-	0.060	-	-	0.691	0.174	-	0.135
	Slow	1.7	18.2	-	-	0.954	0.033	-	0.013	-	-	0.927	0.054	-	0.019	-	-	0.683	0.209	-	0.108
		5.3	23.5	-	-	0.895	0.072	-	0.033	-	-	0.846	0.110	-	0.044	-	-	0.668	0.218	-	0.114
		6.5	25.1	-	-	0.880	0.080	-	0.040	-	-	0.830	0.121	-	0.049	-	-	0.668	0.219	-	0.113
7	Quick	0.1	9.0	0.277	-	-	0.525	0.198	-	0.862	-	-	0.100	0.038	-	0.368	-	-	0.369	0.263	-
		2.7	9.2	0.282	-	-	0.523	0.195	-	0.868	-	-	0.097	0.035	-	0.367	-	-	0.367	0.266	-
		4.3	11.1	0.281	-	-	0.511	0.208	-	0.869	-	-	0.094	0.037	-	0.367	-	-	0.355	0.278	-
		7.0	15.3	0.269	-	-	0.498	0.233	-	0.864	-	-	0.094	0.042	-	0.494	-	-	0.148	0.358	-
	S	0.0	6.5	0.332	-	-	0.540	0.128	-	0.891	-	-	0.088	0.021	-	0.176	-	-	0.492	0.332	-
8	Quick	1.8	11.3	0.198	0.428	-	0.374	-	-	0.869	0.032	-	0.099	-	-	0.246	0.072	-	0.682	-	-
		6.5	14.3	0.202	0.363	-	0.435	-	-	0.863	0.027	-	0.110	-	-	0.243	0.695	-	0.695	-	-
		9.2	20.7	0.198	0.263	-	0.539	-	-	0.846	0.019	-	0.135	-	-	0.234	0.708	-	0.708	-	-
		10.9	23.4	0.195	0.236	-	0.569	-	-	0.840	0.018	-	0.142	-	-	0.254	0.707	-	0.707	-	-
	Slow	9.0	20.9	0.196	0.267	-	0.537	-	-	0.845	0.020	-	0.135	-	-	0.224	0.038	-	0.738	-	-
		6.2	16.5	0.207	0.327	-	0.466	-	-	0.862	0.023	-	0.115	-	-	0.216	0.053	-	0.731	-	-
		1.05	10.2	0.221	0.477	-	0.302	-	-	0.893	0.033	-	0.074	-	-	0.228	0.070	-	0.702	-	-
9	Quick	1.4	10.1	-	-	0.879	0.092	0.016	0.013	-	-	0.813	0.144	0.025	0.018	-	-	0.628	0.141	0.208	0.022
		4.3	11.0	-	-	0.861	0.094	0.031	0.014	-	-	0.795	0.143	0.044	0.018	-	-	0.626	0.143	0.209	0.022
		7.2	13.4	-	-	0.823	0.107	0.054	0.016	-	-	0.752	0.155	0.074	0.019	-	-	0.619	0.138	0.221	0.022
		10.6	18.0	-	-	0.771	0.118	0.093	0.018	-	-	0.699	0.165	0.117	0.019	-	-	0.607	0.124	0.248	0.021
		13.3	21.7	-	-	0.743	0.118	0.121	0.018	-	-	0.676	0.160	0.146	0.018	-	-	0.439	0.232	0.274	0.056
u <sup>b</sup>	±0.2 °C	±0.1 bar	±0.001 mole fraction						±0.003 mole fraction						±0.003 mole fraction						
<sup>a</sup> Near total dissociation/first VLH equilibrium point. Q and S are Quick and Slow, respectively. <sup>b</sup> Absolute uncertainty																					



**Table 32. Gas solubility in liquid phase during the course of experiments**

Gas	method	T (°C)	P (bar)	Gas solubility in liquid phase (mmol/L)					
				CO <sub>2</sub>	N <sub>2</sub>	CH <sub>4</sub>	C <sub>2</sub> H <sub>6</sub>	C <sub>3</sub> H <sub>8</sub>	C <sub>4</sub> H <sub>10</sub>
1	Quick	0.45	14.5	-	-	31.8	-	0.4	-
		1.50	14.6	-	-	32.8	-	0.5	-
		4.00	15.1	-	-	31.9	-	0.8	-
		5.80	15.9	-	-	32.5	-	1.3	-
		7.90	17.0	-	-	33.2	-	1.9	-
		10.40	18.9	-	-	34.7	-	3.2	-
		11.90	20.5	-	-	36.2	-	4.3	-
		13.60	23.2	-	-	39.1	-	6.4	-
	Slow	11.35	20.8	-	-	34.0	-	3.7	-
		10.35	20.0	-	-	33.2	-	3.2	-
		7.95	18.1	-	-	31.5	-	1.7	-
		5.70	17.0	-	-	31.2	-	1.0	-
		4.00	16.5	-	-	29.8	-	0.7	-
		2.55	16	-	-	30.5	-	0.5	-
		1.55	15.8	-	-	30.1	-	0.4	-
0.90	15.6	-	-	30.9	-	0.3	-		
2	Quick	0.95	6.1	-	-	-	16.9	5.4	-
		4.60	10.3	-	-	-	26.9	10.4	-
		6.05	12.2	-	-	-	32.3	11.1	-
		9.15	16.5	-	-	-	47.1	10.1	-
	Slow	7.80	14.0	-	-	-	32.8	7.6	-
		6.40	11.7	-	-	-	27.0	7.6	-
		4.55	9.5	-	-	-	21.4	7.9	-
		1.05	4.9	-	-	-	11.8	3.1	-
3	Quick	1.8	16.4	935.2	-	-	-	2.0	-
		4.1	20.0	1123.1	-	-	-	3.0	-
		4.7	21.6	1206.8	-	-	-	2.9	-
		5.7	24.1	1351.4	-	-	-	3.0	-
		6.6	24.6	1341.6	-	-	-	3.2	-
		7.9	25.6	1329.5	-	-	-	4.1	-
		9.0	26.7	1309.3	-	-	-	5.8	-
	S	1.8	14.3	662.2	-	-	-	1.4	-

		4.1	19.5	977.7	-	-	-	2.1	-
		5.8	22.8	1180.6	-	-	-	2.7	-
		6.7	23.8	1343.8	-	-	-	3.4	-
4	Quick	1.7	5.8	-	-	-	19.0	-	1.6
		4.4	7.6	-	-	-	23.0	-	1.6
		5.8	9.0	-	-	-	26.2	-	2.0
		8.2	11.9	-	-	-	34.2	-	1.9
		10.2	15.7	-	-	-	45.1	-	1.8
		11.9	19.7	-	-	-	59.8	-	1.9
	Slow	1.6	4.7	-	-	-	10.7	-	1.5
		4.6	7.4	-	-	-	17.5	-	1.5
		5.8	8.7	-	-	-	20.4	-	1.5
		8.3	12.3	-	-	-	29.2	-	1.6
		10.3	16.0	-	-	-	36.8	-	1.5
		11.4	21.3	-	-	-	53.2	-	1.7
5	Q	0.9	20.9	-	-	43.3	-	-	1.1
	S	0.9	20.6	-	-	42.7	-	-	1.1
6	Quick	1.7	17.8	-	-	35.5	2.2	-	1.0
		3.8	19.4	-	-	37.2	3.2	-	1.4
		5.3	21.2	-	-	37.7	4.2	-	1.7
		6.7	23.9	-	-	40.3	5.7	-	2.2
		8.8	28.6	-	-	45.8	8.6	-	3.5
	Slow	1.7	18.2	-	-	34.6	2.0	-	0.7
		5.3	23.5	-	-	40.5	5.3	-	2.1
		6.5	25.1	-	-	41.3	6.0	-	2.4
7	Quick	0.1	9.0	153.9	-	-	17.8	6.7	-
		2.7	9.2	150.4	-	-	16.8	6.1	-
		4.3	11.1	175.3	-	-	19.1	7.4	-
		7.0	15.3	229.5	-	-	25.0	11.0	-
	S	0.0	6.5	121.1	-	-	12.0	2.8	-
8	Quick	1.8	11.3	131.3	4.8	-	14.9	-	-
		6.5	14.3	150.5	4.6	-	19.2	-	-
		9.25	20.7	211.5	4.8	-	33.6	-	-
		10.95	23.4	236.0	4.9	-	40.0	-	-
	Slow	9.0	20.9	196.2	4.6	-	31.4	-	-
		6.2	16.5	166.8	4.5	-	22.2	-	-
		1.05	10.2	118.5	4.3	-	9.8	-	-
9	Quick	1.4	10.1	-	-	18.8	3.3	0.6	0.4
		4.3	11.0	-	-	18.8	3.4	1.1	0.4

		7.2	13.4	-	-	21.2	4.4	2.1	0.5
		10.6	18.0	-	-	25.8	6.1	4.3	0.7
		13.3	21.7	-	-	29.8	7.0	6.5	0.8
<b>u<sup>a</sup></b>		±0.2 °C	±0.1bar	±0.3 mmol/L					
Q and S are Quick and slow, respectively.									
<sup>a</sup> Absolute uncertainty									

These tables provide several remarkable results. At a given temperature, the equilibrium pressure at final state was different according to the rate of crystallization. For instance, for CO<sub>2</sub>-C<sub>3</sub>H<sub>8</sub> mixture, at final state (1.8°C), the equilibrium pressures for quick and slow processes were notably 16.4 and 14.3 bar, respectively. The same consideration was observed for CO<sub>2</sub>-C<sub>2</sub>H<sub>6</sub>-C<sub>3</sub>H<sub>8</sub> which the pressure difference of slow and quick crystallizations at final state was significant (at 0.1°C, 9 and 6.5 bars for quick and slow crystallization procedures, respectively). Figure 40 and Figure 41 illustrate temperature-pressure diagram of all the mixtures for both crystallization procedures. The figures clearly show that the pressure at final states differed with respect to the crystallization rate. This clarifies that kinetics have a substantial impact on the final equilibrium. However, in the case of mixtures involving butane, the final pressure was almost equal. For example for ternary mixture of CH<sub>4</sub>-C<sub>2</sub>H<sub>6</sub>-C<sub>4</sub>H<sub>10</sub>, the pressures at final state for quick and slow at 1.7°C were 17.8 and 18.2 bar.

Furthermore, the experimental results indicated that although the P-T diagram of some mixed hydrates at slow crystallization located at upper position than at quick crystallization, for some others the inverse was observed. For instance, methane-propane mixture, at a given temperature the equilibrium pressure at slow crystallization process is higher than at quick crystallization process (For example at 7.9°C and 10.3°C), the opposite was detected for ethane-propane mixture (For example at 4.6°C).

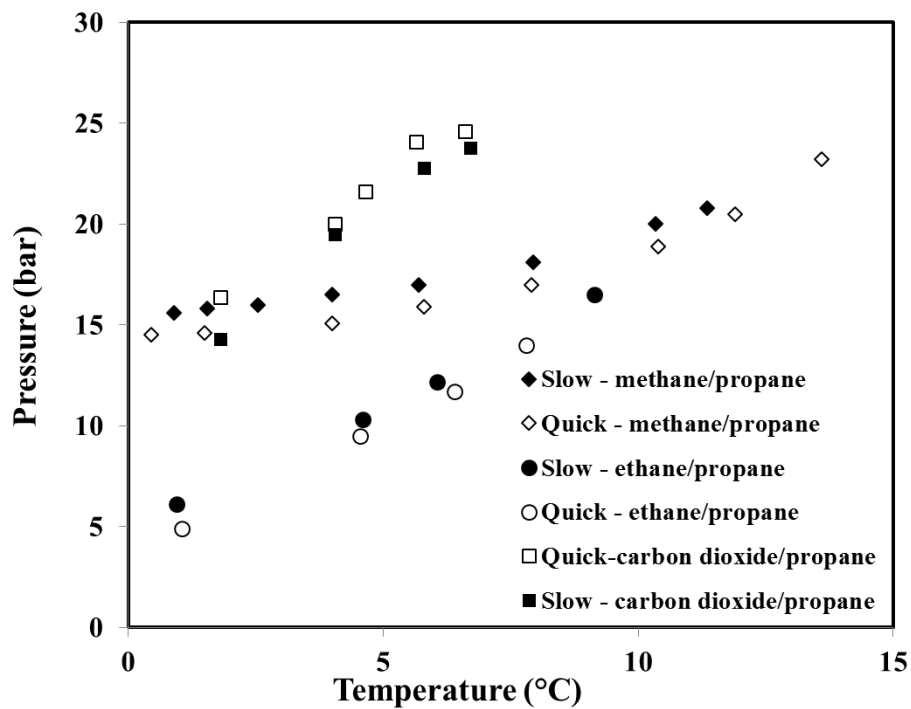


Figure 40. Pressure-temperature diagram of two different methods for methane/propane, ethane/propane and carbon dioxide/propane mixtures

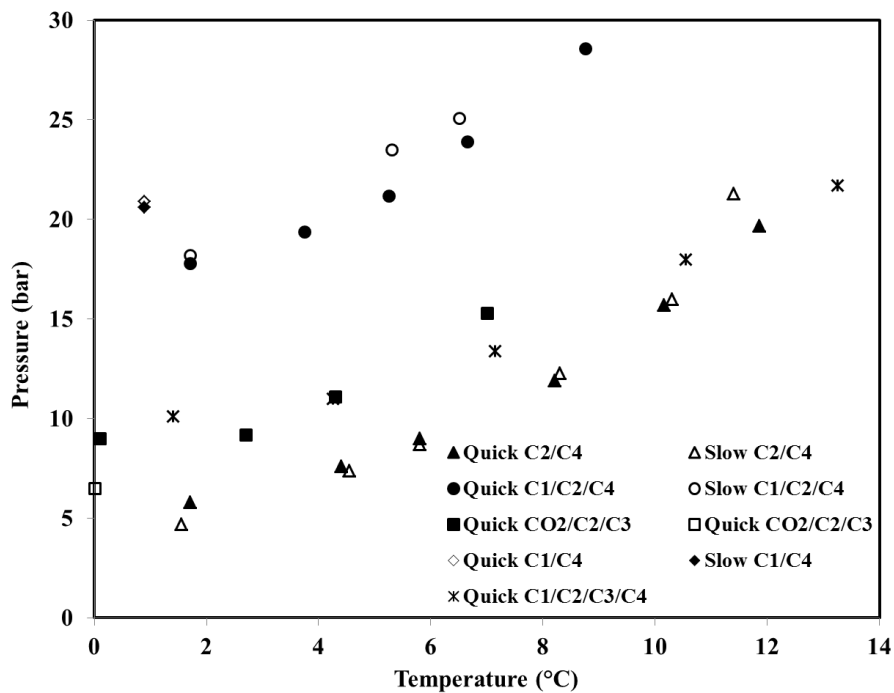


Figure 41. Pressure-temperature diagram of two different methods for methane/n-butane, ethane/n-butane and methane/ethane/n-butane, carbon dioxide/ethane/propane and methane/ethane/propane/n-butane mixtures

The results also revealed that guest distribution in hydrate phase differed as the rate of crystallization changed. Figure 42 shows the change in composition of propane in hydrate phase in different mixed gas hydrates according to the rate of crystallization. This is obvious from the figure that the propane composition in hydrate phase for each mixture at slow crystallization was higher than at quick crystallization. Moreover, the changes in hydrate composition versus the temperature seemed to be approximately identical. Additionally, propane hydrate composition in mixed CO<sub>2</sub>/C<sub>3</sub>H<sub>8</sub> hydrate considerably decreased at below 6°C. This could be due to the larger enclathration of CO<sub>2</sub> in hydrate cages. This could be an evidence of phase transition. Therefore, CO<sub>2</sub>/C<sub>3</sub>H<sub>8</sub> mixed hydrate was also analyzed and investigated by Raman spectroscopy measurements in order to detect and clarify the reason of this hydrate composition behavior. The results revealed that CO<sub>2</sub>/C<sub>3</sub>H<sub>8</sub> mixture at high concentration of CO<sub>2</sub> could form simultaneously both structures (sI and sII). This will be explained in details in following sections.

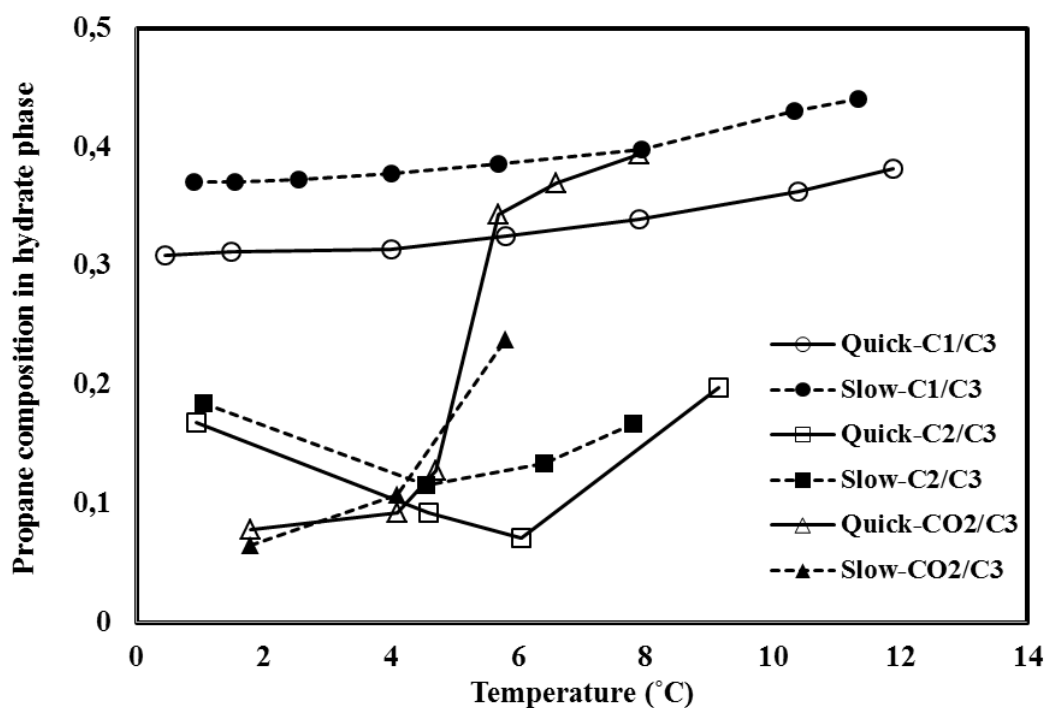


Figure 42. Composition of propane in hydrate phase in different mixed gas hydrates according to the rate of crystallization

This is also noticed that the composition of heavier hydrocarbons in hydrate phase was significantly higher than in the gas phase. Figure 43 illustrates obviously that the compositions of propane and butane in hydrate phase at any states were considerably larger than in gas phase. This is more obvious for encaged propane in hydrate phase. Nevertheless, the inverse

phenomenon was observed for binary mixtures including ethane. This might be considered as ethane can occupy both small and large cavities of hydrate structures. Therefore, the distribution of guest molecules in hydrate cavities in presence of ethane in binary mixed hydrates could be differed from the presence of other components.

Finally, the composition of propane and butane in hydrate phase decreased from the first vapor-liquid-hydrate equilibrium point to the final state in both crystallization mechanisms. As an illustration, the butane composition in  $C_2H_6-C_4H_{10}$  mixture at the first VLH equilibrium for quick process was 0.063 mole fraction, but at the final state, it changed to 0.033 mole fraction. This demonstrates that the enclathration of heavier molecules at the start of crystallization plays more important role than near the final state.

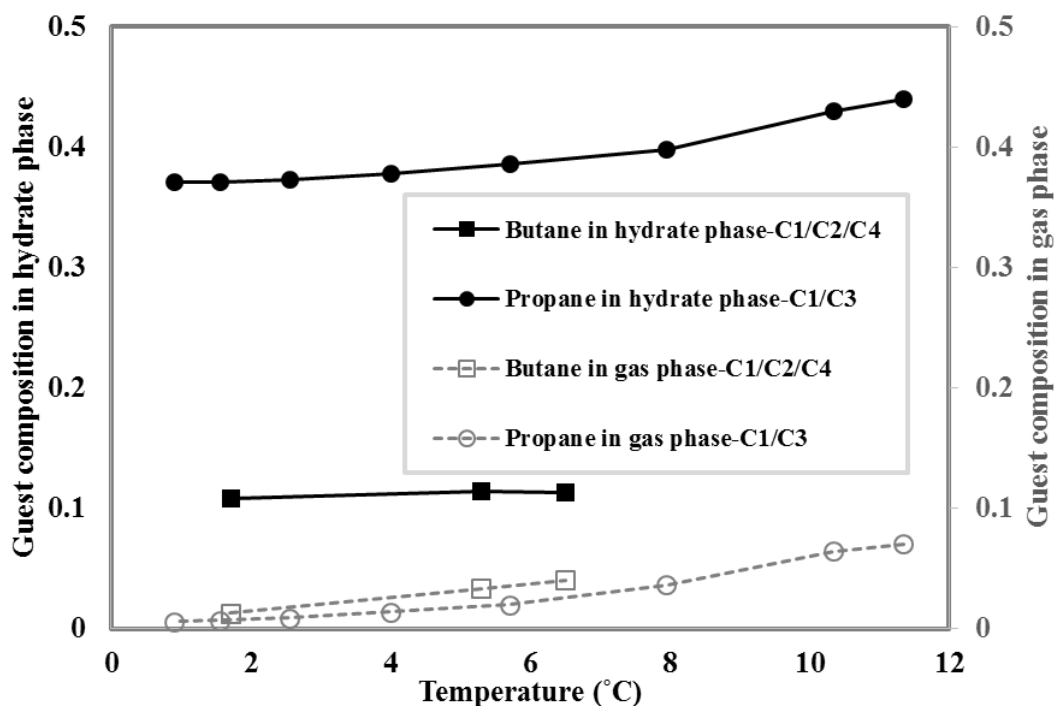


Figure 43. The changes in compositions of propane and butane in gas and hydrate phases.

One of the most interesting observations in Table 31 is the enclathration of propane. As the table indicates, at final state for all the mixtures, the composition of propane in hydrate phase at slow crystallization process is larger than the quick process (for example, for methane-propane mixture at quick and slow crystallizations, they are 0.31 and 0.37, respectively). This is more obvious on Figure 42. As the figure shows, at slow crystallization process, the propane composition in

hydrate phase at each desired temperature is located at higher position than quick crystallization. This shows that in a hydrocarbon mixture at slow crystallization rate, enclathration of heavier hydrocarbon is more substantial.

### 5.4.2. Hydrate phase properties results

As aforementioned, the experimental results obtained provide not only detailed information about temperature, pressure, guest composition in all phases (gas, liquid and hydrate), but also hydrate phase properties such as hydrate volume and density, hydration number, water conversion and storage capacity.

These investigations on hydrate properties could formulate, change or suggest the new fundamental questions and ideas based on the thermodynamic equilibrium of mixed gas hydrates. Additionally, these clarifications would alter how we will use clathrate hydrate applications which thermodynamic equilibrium is essentially taken into account such as energy storage and transportation or carbon capture sequestration.

Table 33 shows the experimental results including hydrate volume and density, water conversion, hydration number and storage capacity for all the mixed gas hydrates comparing quick and slow crystallization rates.

**Table 33. Hydrate phase properties during the course of experiments for two different crystallization rates**

Gas	Method	T(°C)	P(bar)	Hydrate volume (cm <sup>3</sup> )	Hydration number	Hydrate density (g/cm <sup>3</sup> )	Storage capacity (V/V)	Water conversion (%)
1	Quick	0.45	14.5	207.9	11.9	0.88	82.4	20.5
		1.50	14.6	162.7	9.4	0.90	103.5	16.1
		4.00	15.1	157.1	9.5	0.90	102.8	15.6
		5.80	15.9	139.8	9.2	0.91	106.2	14.0
		7.90	17.0	126.3	9.4	0.91	103.7	12.7
		10.40	18.9	110.5	10.9	0.90	90.1	11.2
		11.90	20.5	96.3	13.1	0.88	74.5	9.8
		13.60	23.2	71.3	a	0.84	32.1	7.3
	Slow	11.35	20.8	53.6	7.7	0.95	126.8	5.3
		10.35	20.0	60.4	7.4	0.96	132.7	6.0
		7.95	18.1	81.9	7.2	0.95	135.3	8.2

		5.70	17.0	84.8	6.5	0.97	149.5	8.6
		4.00	16.5	a	9.4	0.91	103.8	a
		2.55	16	108.2	7.5	0.94	129.4	11.1
		1.55	15.8	123.3	8.5	0.93	115.4	12.7
		0.90	15.6	a	6.4	0.97	151.5	a
2	Quick	0.95	6.1	278.7	11.3	0.92	86.7	27.6
		4.60	10.3	177.7	10.4	0.92	94.2	17.7
		6.05	12.2	146.5	10.9	0.91	89.6	14.6
	Slow	9.15	16.5	73.5	a	0.88	60.9	7.4
		7.80	14.0	79.8	7.9	0.97	123.5	7.9
		6.40	11.7	92.1	6.4	1.01	153.5	9.1
		4.55	9.5	106.3	5.7	1.03	169.5	10.6
	1.05	4.9	219.0	8.2	0.96	118.6	22.0	
3	Quick	1.8	16.4	172.6	6.4	1.09	153.6	13.3
		4.1	20.0	100.5	6.0	1.11	163.6	7.8
		4.7	21.6	87.0	7.2	1.06	136.4	6.8
		5.7	24.1	48.1	11.3	0.96	86.6	3.8
		6.6	24.6	42.3	12.1	0.95	81.5	3.3
		7.9	25.6	37.8	21.4	0.88	46.0	3.0
	Slow	9.0	26.7	a	a	a	a	a
		1.8	14.3	105.0	3.1	1.40	NA	8.2
		4.1	19.5	42.9	2.5	1.56	NA	3.3
		5.8	22.8	22.4	3.5	1.34	NA	1.7
	6.7	23.8	a	a	a	a	a	
4	Quick	1.7	5.8	259.6	7.8	0.96	125.6	25.6
		4.4	7.6	252.7	8.3	0.95	117.9	25.1
		5.8	9.0	234.2	8.4	0.95	117.2	23.4
		8.2	11.9	196.2	8.6	0.95	114.3	19.7
		10.2	15.7	150.8	9.7	0.93	100.8	15.2
		11.9	19.7	56.4	8.7	0.95	112.8	5.7
	Slow	1.6	4.7	253.8	7.3	0.97	134.8	25.6
		4.6	7.4	184.6	6.1	1.00	161.9	18.6
		5.8	8.7	173.4	6.1	1.00	160.2	17.4
		8.3	12.3	119.8	5.5	1.03	179.9	11.9
		10.3	16.0	107.6	7.2	0.97	136.4	10.7
	11.4	21.3	a	a	a	a	a	



5	Quick	0.9	20.9	38.3	11.6	0.90	88.0	3.8
	Slow	0.9	20.6	37.3	9.3	0.91	104.7	3.67
6	Quick	1.7	17.8	108.0	6.1	0.96	162.1	8.5
		3.8	19.4	57.0	3.6	1.07	271.2	4.5
		5.3	21.2	81.2	6.1	0.96	161.8	6.5
		6.7	23.9	70.2	7.4	0.93	132.0	5.6
		8.8	28.6	20.7	10.0	0.90	98.6	1.7
	Slow	1.7	18.2	85.6	4.9	1.00	199.1	6.8
		5.3	23.5	32.0	3.3	1.11	NA	2.5
7	Quick	6.5	25.1	40.4	5.3	0.99	186.6	3.2
		0.1	9.0	159.5	10.3	0.96	95.5	12.6
		2.7	9.2	142.8	9.3	0.97	105.8	11.3
		4.3	11.1	123.3	10.6	0.95	92.9	9.8
	7.0	15.3	42.4	16.2	0.90	60.8	3.4	
Slow	0.0	6.5	141.0	6.9	1.02	142.2	11.1	
8	Quick	0.0	6.5	141.0	6.9	1.02	142.2	11.1
		1.8	11.3	173.1	7.0	1.01	140.3	17.1
		6.5	14.3	160.1	8.0	0.98	122.2	15.8
		9.25	20.7	97.3	12.5	0.91	78.9	9.7
	10.95	23.4	46.9	20.8	0.86	47.2	4.7	
	Slow	9.0	20.9	66,2	8,8	0,95	110,8	6,4
		6.2	16.5	119,9	7,6	0,98	128,2	11,6
1.05		10.2	179,6	6,7	1,01	144,9	17,4	
9	Quick	1.4	10.1	169.2	8.1	0.92	120.9	16.7
		4.3	11.0	166.6	8.6	0.92	114.7	16.5
		7.2	13.4	136.4	8.8	0.91	111.3	13.6
		10.6	18.0	94.5	12.7	0.88	77.1	9.5
		13.3	21.7	42.2	74.3	0.81	13.2	4.2
Absolute uncertainty		±0.2	±0.1	±0.4	±0.5	±0.05	±0.5	±0.4

This table shows that for a mixed gas hydrate, water conversion at slow crystallization is generally lower than in the quick crystallization rate at final state. This means that less hydrate crystals have been formed with higher cavities occupation.

Storage cavity defines as the volume of the gas in hydrate phase at standard conditions per volume of hydrate. This is a vital factor in gas storage and transportation (like hydrogen or natural gas) or carbon capture sequestration processes, since more gas storage in a lower volume is favorable.

Experimental results showed that storage capacity and hydration number for mixed gas hydrates were also different according the rate of crystallization. In all cases, higher storage capacity occurred at slow crystallization (Figure 44 clearly shows the differences). For instance, the storage capacity of CO<sub>2</sub>-C<sub>2</sub>H<sub>6</sub>-C<sub>3</sub>H<sub>8</sub> hydrates at final state (0.1°C), for slow crystallization was 142.2 V/V compare to 95.5 V/V for quick crystallization. This may prove significant when storing natural gas for transportation use. In addition note that the hydration numbers at final state for slow and quick crystallization were 6.9 and 10.3, respectively. As explained earlier, the hydration number is the water to gas ration in hydrate. Therefore, the lower hydration number indicates the more gas molecules encaged in hydrate crystals.

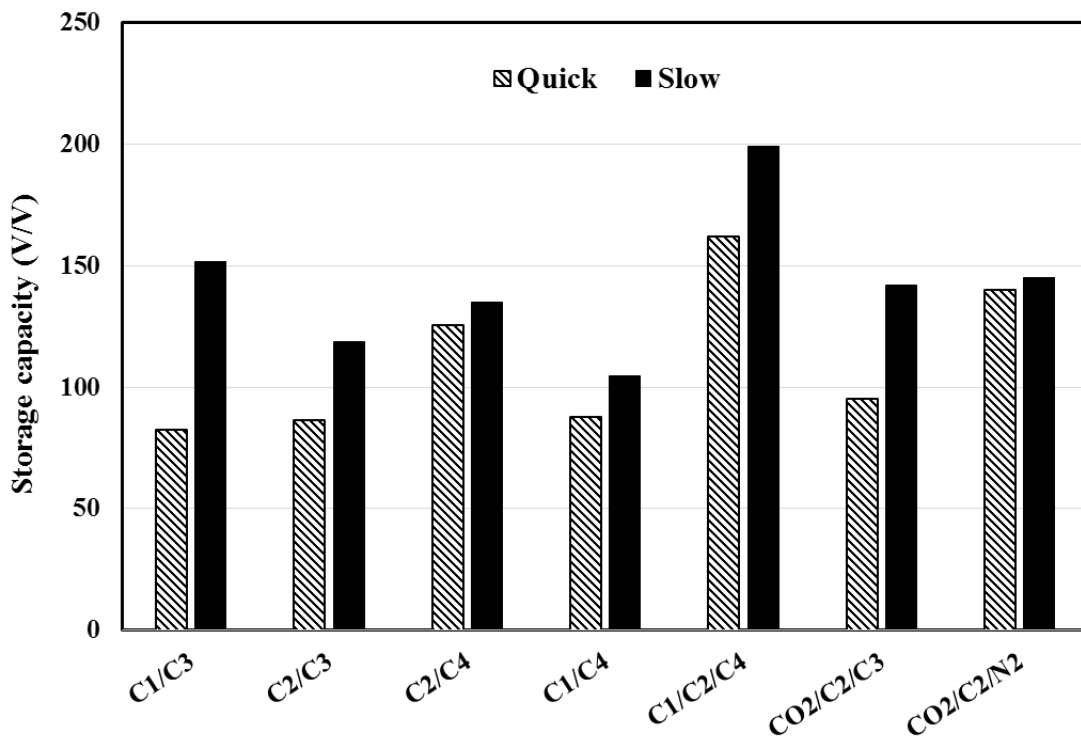
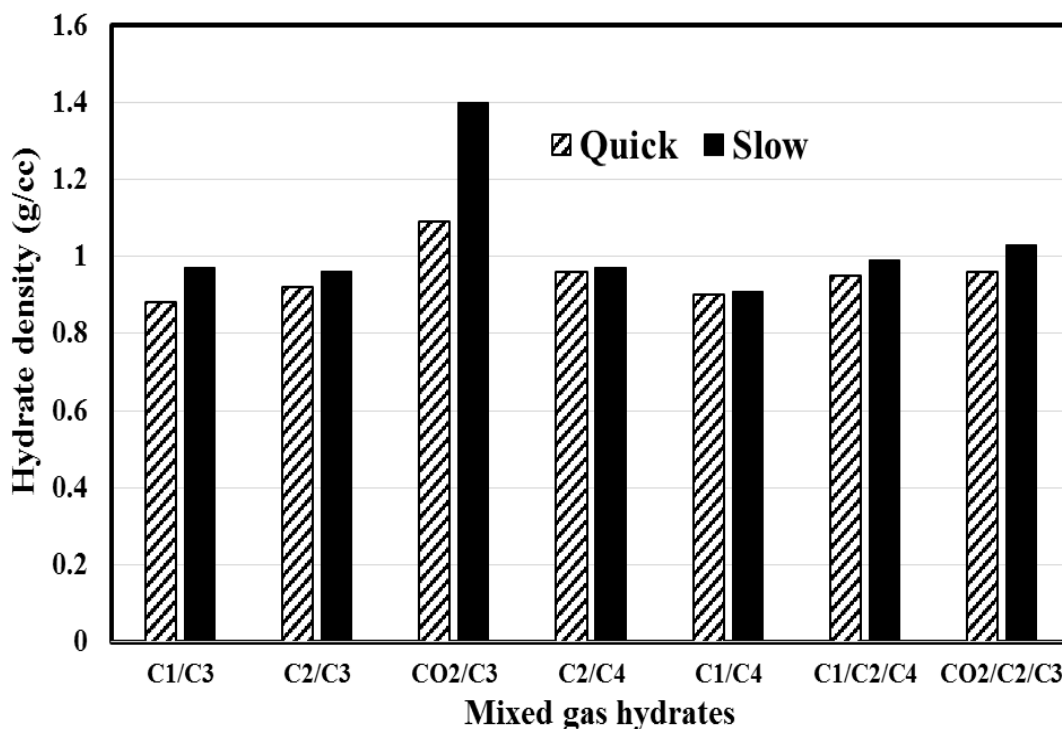


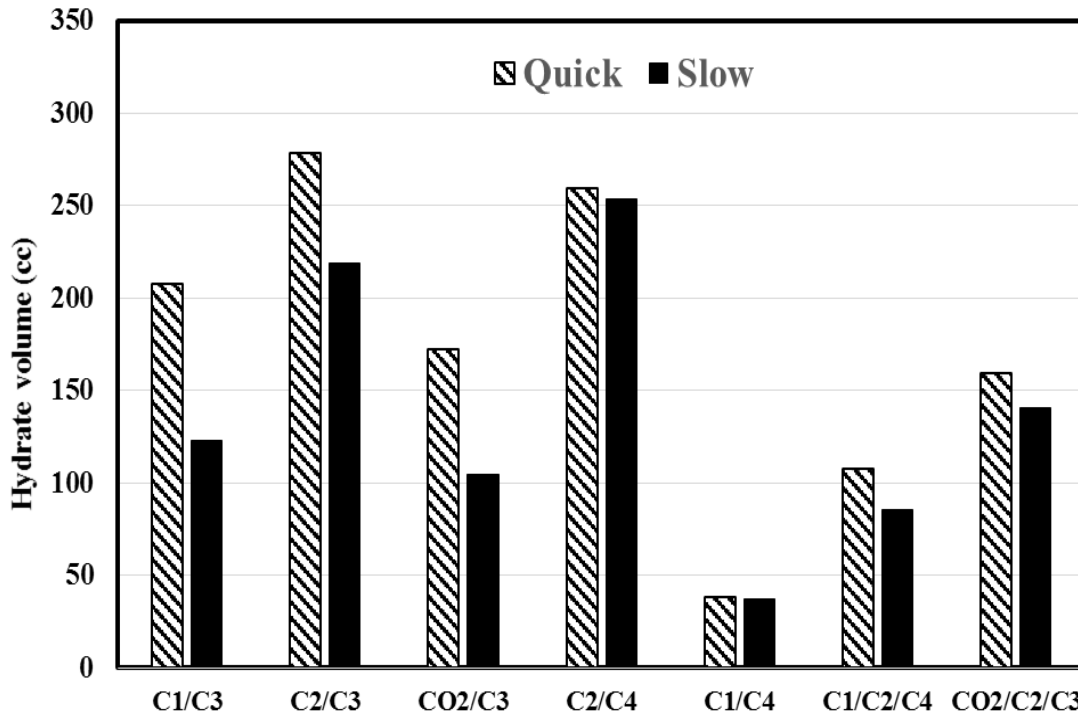
Figure 44. Storage capacity of mixed gas hydrates at final state according to the rate of crystallization

Figure 45 illustrates the hydrate density of mixed gas hydrates at final state concerning the both crystallization methods. Although for the hydrocarbon mixtures, the hydrate densities were almost similar for both crystallization rates, for the mixtures that included carbon dioxide the difference was considerable (for example, hydrate density of CO<sub>2</sub>-C<sub>3</sub>H<sub>8</sub> mixture at final state for quick and slow was 1.09 and 1.40 g/cm<sup>3</sup>, respectively). At slow crystallization for this mixture, the hydrate volume was significantly lower than quick crystallization (105 cm<sup>3</sup> at slow compared to 172 cm<sup>3</sup> for quick at 1.8°C). Moreover, the hydration number at slow crystallization was about two times less than quick crystallization. This means that more guest molecules were encased in hydrate phase. Hence, the hydrate densities at slow crystallization for CO<sub>2</sub>-C<sub>3</sub>H<sub>8</sub> were much larger than quick crystallization. In general, the hydrate density of mixed gas hydrates at slow crystallization was about 8% higher than at quick crystallization (average value by considering all the mixtures).



**Figure 45. Hydrate density of mixed gas hydrates at final state concerning the both crystallization methods**

One of the most important observations regarding to the hydrate properties in Table 33, is the hydrate volume findings. Figure 46 presents evidently the differences in hydrate volume according to the rate of crystallization.



**Figure 46. Hydrate volume for different mixtures for quick and slow crystallization procedures**

As seen on this figure, at slow crystallization procedure for all the mixtures, the hydrate volume was noticeably lower than at quick crystallization. This is more obvious for binary mixed hydrates involving propane. For instance, the hydrate volume of CO<sub>2</sub>/C<sub>3</sub>H<sub>8</sub> at final state for quick crystallization method was 172.6 cm<sup>3</sup> compared to 105.0 cm<sup>3</sup> for slow crystallization process. This means that the hydrate volume at quick process was about 64% larger than at slow process.

The findings about hydrate volume in this work could help to determine more realistically the amount of kinetic inhibitors (KHI) to use in flow-assurance. At slow crystallization method which is closer to a steady state process, the hydrate volume is less than quick crystallization. Therefore, a smaller amount of low dosage hydrate inhibitors (LDHIs) such as kinetic hydrate inhibitors (KHIs) or anti-agglomerants (AAs) is required to prevent hydrate formation or agglomeration. This means that the operational costs could be potentially reduced, leading to saving countless dollars in the current energy industry.

These outcomes from the previous sections explain the effect of kinetics on hydrate formation, crystallization and properties. This is to say that the enclathration and distribution of guest

molecules in hydrate phase as well as their selectivity intensely depend on the driving force of crystallization. Moreover, the differences in final pressure and composition highlight the nagging question about the thermodynamic equilibrium. Is it certain that the thermodynamic equilibrium has been reached? The results of thermodynamic model in the following section clarify some crucial indications on how to better understand the kinetic effects on equilibrium state of mixed hydrates.

## **5.5. Modeling results**

In this section, the experimental results were compared to the model of van der Waals and Platteeuw using Kihara parameters to evaluate the kinetic effects on thermodynamic equilibrium. The experimental results obtained for guest composition in gas and hydrate phases as well as pressure (temperature) were simulated by the thermodynamic model for all mixtures and both crystallization methods. The thermodynamic model used in this work was already explained by details in section 2.2.5.

It should be noted that the structure of gas hydrates might depend on the feed gas composition. Unfortunately, without expensive special instruments, such as Raman spectroscopy, it was impossible for our team to be 100% certain about the structure of these hydrates. Therefore, simulation results for both sI and sII are performed and the structure which has lower average deviation from experimental data is selected.

Before going deeper into the modeling results, the attention should be paid that experimental data from literature as well as data obtained from our experiments were tested with the thermodynamic model. Surprisingly, the modeling results concerning propane in mixed gas hydrates significantly deviated from experimental data in terms of hydrate pressure and composition. It seemed that Kihara parameters of propane were not adequately optimized. Thus, it was a motivation for us to optimize a new set of Kihara parameters for propane. Then, the prediction results of new optimized parameters are compared with the other Kihara parameters in literature.

### **5.5.1. Kihara parameters optimization for propane**

The algorithm for Kihara parameters optimization is described in section 2.2.5.3 and illustrated in Figure 14. In order to optimize the Kihara parameters for a guest molecule, it is necessary to

choose a set of liquid-hydrate equilibrium data. To avoid the impact of kinetic and non-equilibrium conditions, it is better to use equilibrium data for pure gas hydrates since there is no enclathration competition between guest molecules. Moreover the set of data must be consistent. This set of Kihara parameters must provide the equilibrium pressure which satisfies equation 6. When the deviation is a function of Kihara parameters, the minimum of deviation selects the best set of Kihara parameters. This is not the case for pure propane; the minimum of deviation function cannot be found. Hence, the equilibrium data from a mixture containing propane furnishes a satisfactory solution. However, the Kihara parameters for other components must be known. The other difficulty is that the experimental data for the mixed gas hydrates must be at thermodynamic equilibrium. It means that for the mixed gas hydrates data, the impact of kinetic effects must be minimized as much as possible. Therefore, the equilibrium results from slow crystallization of methane/propane mixture seem to be an important key in retrieving the Kihara parameters for propane. About 61 experimental points from literature as well as our results of slow crystallization were used to optimize Kihara parameters of propane [61,62,72,79,181,182].

Figure 47 presents the optimization of  $\varepsilon/k_B$ ,  $\sigma$  values and their corresponding average deviations for three different mixtures including propane as well as pure propane's experimental data. As it is clear in the figure, for pure propane a global minimum of average deviation cannot be found to generate the best set of Kihara parameters. Ergo, we used our experimental results from slow crystallization of methane-propane mixed hydrates as well as experimental results for xenon-propane and carbon dioxide-propane from literature [181,182]. It should be noted that, these experimental results from literature were carefully selected based on the fact that the Kihara parameters for methane, xenon and carbon dioxide had been satisfactorily obtained by our team and they are given in Table 8 [113,120].

**Table 34.  $\varepsilon/K$  and  $\sigma$  for the guest molecules from our previous work [113,120], “a” from literature [119,183]**

<b>Guest molecule</b>	<b><math>\varepsilon/k_B</math> (K)</b>	<b><math>\sigma</math> (Å)</b>	<b>a (Å)</b>
<b>Carbon dioxide</b>	178.21	2.873	0.6805
<b>Methane</b>	166.36	3.050	0.3834
<b>Xenon</b>	224.99	3.094	0.2280
<b>Ethane</b>	177.46	3.205	0.5651

As illustrated in Figure 47, the Kihara parameters curves for methane-propane (slow crystallization), carbon dioxide-propane and xenon-propane meet each other at a point specified on the curve. This point provides the best set of Kihara parameters for propane in the mixtures.  $\epsilon/k$  and  $\sigma$  for propane based on this point is 195.0 and 3.34, respectively.

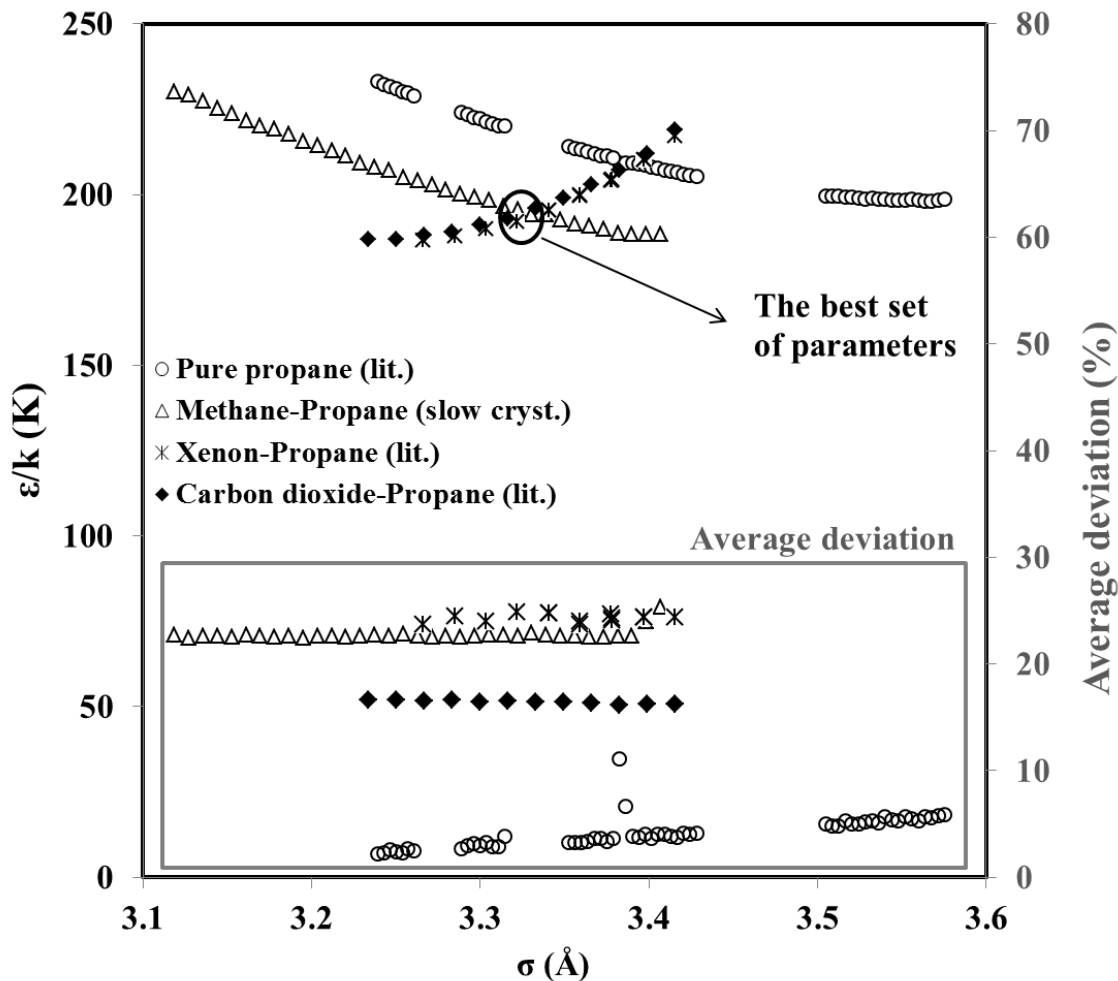


Figure 47.  $\epsilon/k$  versus  $\sigma$  for pure propane and three different mixtures including propane corresponding to average deviation by implementing experimental data from this paper and literature [61,62,72]

### 5.5.2. Test of the thermodynamic model based on the new set of Kihara parameters for propane to other sets in the literature

Different Kihara parameters for propane can be found in the literature due to the usage of the various experimental data and also thermodynamic properties. They are listed in Table 9.

**Table 35. Different sets of Kihara parameters for propane**

Reference	$\epsilon/k$ (K)	$\sigma$ (Å)	$a$ (Å)
(Sloan, 1998) [119]	203.31	3.3093	0.6502
(Ng and Robinson, 1977) [184]	213.58	3.2296	0.6700
(Barkan and Sheinin, 1993) [185]	194.55	3.3144	0.8340
(Moradi and Khosravani, 2013) [186]	493.70	4.5190	0.6502
<b>This work for GasHyDyn</b>	195.00	3.3400	0.6502

The accuracy of these sets of propane's Kihara parameters for predicting the hydrate equilibrium pressure has been calculated and compared to several experimental data of mixed gas hydrates from the literature. The results are presented in Table 10.

A wide range of experimental equilibrium data from literature and our experiments (198 equilibrium points) have been used to investigate the accuracy of the thermodynamic model based on our new set of Kihara parameters and also Kihara parameters from the other researchers. As demonstrated in the table, the average deviation of our thermodynamic model based on the new Kihara parameters is 14.5% and it is considerably lower than the other better known sets (26.9% for Sloan, 30.6% for Ng and Robinson, 32.2% for Barkan and Sheinin and 142.1% for Moradi and Khosravani). Figure 48 illustrates clearly the average deviation of thermodynamic model according to different sets of propane Kihara parameters. The average deviation of thermodynamic model to predict equilibrium pressure is determined as follow:

$$AADp\% = \frac{100}{N} \sum_i^N \left( \left| \frac{P_i^{exp} - P_i^{pre}}{P_i^{exp}} \right| \right) \quad (38)$$



**Table 36. The comparison between the different sets of propane Kihara parameters for predicting hydrate equilibrium pressure**

Mixtures	Experimental data resources	Structure	Number of equilibrium points	Kihara parameters (The values were presented in Table 9)				
				Ng and Robinson	Barkan and Sheinin	Sloan	Moradi and Khosravani	This work
				Average Deviation (%)				
CH <sub>4</sub> -C <sub>3</sub> H <sub>8</sub>	(McLeod and Campbell, 1961) [70]	II	17	38.7	51.0	37.4 <sup>I</sup>	85.0	26.6 <sup>I</sup>
	(Deaton and Frost, 1946) [62]	II	24	20.5	30.2	20.4	306.0	18.0
	(Nixdorf and Oellrich, 1997) [72]	II	7	27.4	42.0	26.8	103.9	14.5
	(Verma et al., 1975) [74]	II	12	33.9	8.8	34.7	386.0 <sup>I</sup>	24.4 <sup>I</sup>
	Our results (Quick crys.)	II	8	14.8	29.8	14.1	177.0	3.2
	(Song and Kobayashi, 1982) [187]	II	11	13.7	28.9	13.0	397.0	9.7
C <sub>2</sub> H <sub>6</sub> -C <sub>3</sub> H <sub>8</sub>	(Mooijer – van den Heuvel, 2004) [188]	I	11	67.8 <sup>II</sup>	67.8	65.7	67.8 <sup>II</sup>	15.8
	(Jager, 2001) [189]	I	7	71.8 <sup>II</sup>	71.8 <sup>II</sup>	66.2	71.9	11.0
	(Nixdorf and Oellrich, 1997) [72]	I	6	73.8	7.5	42.0	8.0	17.5
	Our results (Quick crys.)	I	4	82.6	18.2	55.7	19.0	24.0
	Our results (Slow crys.)	I	4	79.8	26.8	49.7	27.6	16.0
CO <sub>2</sub> -C <sub>3</sub> H <sub>8</sub>	(Robinson and Metha, 1971) [79]	II	37	34.0	52.5	33.6	216.0	14.6 <sup>I</sup>
CH <sub>4</sub> -C <sub>2</sub> H <sub>6</sub> -C <sub>3</sub> H <sub>8</sub>	(Nixdorf and Oellrich, 1997) [72]	II	7	13.0	29.0	12.6	69.2 <sup>I</sup>	4.5
	(Dharmawardhana et al., 1980) [190]	I	11	50.9 <sup>II</sup>	7.0	44.2	7.0	24.5
	(Yasuda and Ohmura, 2008) [61]	II	20	16.2	29.4	7.9 <sup>I</sup>	65.6	12.5
	(Le Quang et al., 2015) [121]	I	8	15.5	22.0	10.8	13.5 <sup>II</sup>	16.8
CO <sub>2</sub> -CH <sub>4</sub> -C <sub>3</sub> H <sub>8</sub>	(Bishnoi and Dholabhai, 1999) [191]	II	4	29.7	42.5	23.2 <sup>I</sup>	75.0	20.1
<i>AAD<sub>p</sub></i> (%)			<b>198</b>	<b>30.6</b>	<b>32.2</b>	<b>26.9</b>	<b>142.1</b>	<b>14.5</b>

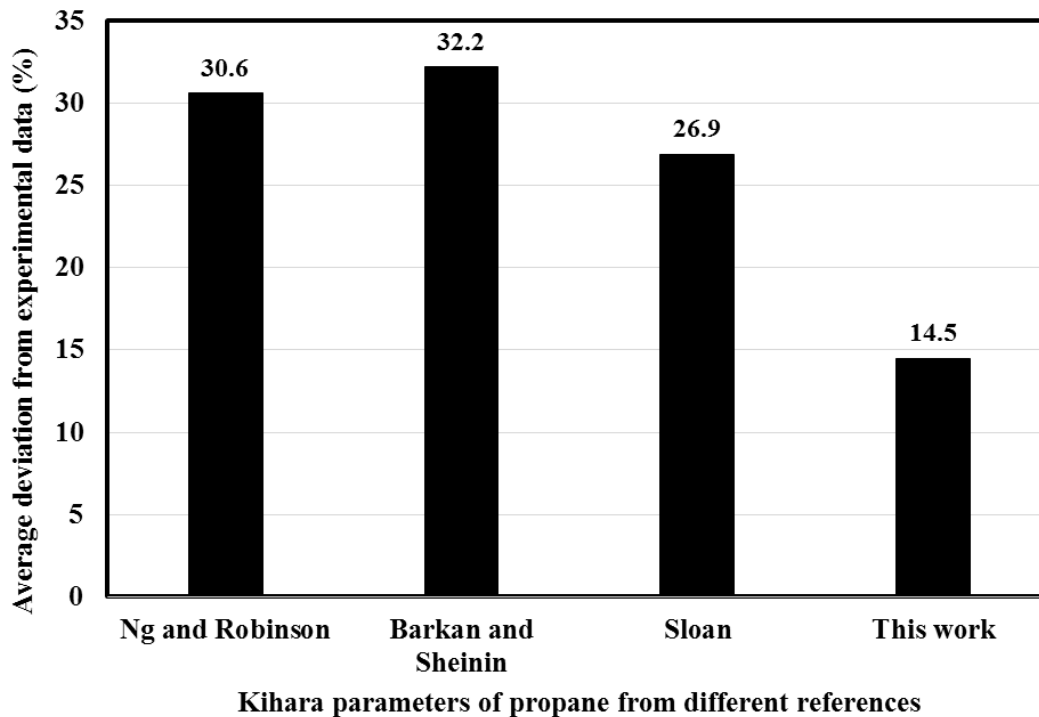


Figure 48. The average deviation of thermodynamic model based on different Kihara parameters of propane in literature and our work (The deviation results from Moradi and Khosravani were not presented in the figure since its deviation was significantly larger than others).

The other advantage of our new set of Kihara parameters for propane (in mixtures) is uniformity. In other words: for all the mixtures, the average deviation is relatively quite small, whilst the average deviation of the other sets varies significantly, according to the components of the mixtures and also literature resources. Another interesting observation in Table 36 is that for  $C_2H_6-C_3H_8$  mixture, the result of thermodynamic model for slow crystallization rate is better than quick crystallization rate (16% compare to 24%). This clarifies that the crystallization of mixed gas hydrate at slow crystallization rate can occur at thermodynamic equilibrium. As mentioned, at quick crystallization, the kinetics consideration may affect the results. This will be described in details in the following section.

### 5.5.3. Experimental data versus thermodynamic modeling results

As stated earlier, the gas composition in hydrate phase is a new challenge and it is very difficult to find pertinent data in literature. Our objectives were to investigate the hydrate temperature-pressure and gas composition dynamically in hydrate phase; not only at the final state (overall

thermodynamic equilibrium), but also during the crystallization at non-equilibrium conditions (local equilibrium). Hence, the thermodynamic model based on Kihara potential was used to model the evolution of hydrate composition from the initial state to final state. The issue in experimental measurements of guest distribution in hydrate phase is that its value is an average data. In fact, the crystal growth has not been taken into account. Therefore, the thermodynamic modeling might be compared to a state which is not at thermodynamic equilibrium. Table 37 shows modeling results including hydrate pressure and composition, not only for the final state of equilibrium, but also during the crystallization process. It should be highlighted that the results of slow crystallization process for methane-propane mixture are not presented in this table, as its results had been already used for the thermodynamic model (parameter optimization).

**Table 37. Results of thermodynamic model for hydrate pressure and composition**

Gas*	Method	Texp (C) ( $\pm 0.2$ )	Pexp (bar) ( $\pm 0.1$ )	Structure I (simulated results)						Structure II (simulated results)							
				Ppre (bar)	Hydrate composition (water free)						Ppre (bar)	Hydrate composition (water free)					
					CO <sub>2</sub>	N <sub>2</sub>	CH <sub>4</sub>	C <sub>2</sub> H <sub>6</sub>	C <sub>3</sub> H <sub>8</sub>	C <sub>4</sub> H <sub>10</sub>		CO <sub>2</sub>	N <sub>2</sub>	CH <sub>4</sub>	C <sub>2</sub> H <sub>6</sub>	C <sub>3</sub> H <sub>8</sub>	C <sub>4</sub> H <sub>10</sub>
1	Quick	0.45	14.5	25.0	-	-	0.909	-	0.091	-	13.0	-	-	0.732	-	0.268	-
		1.5	14.6	27.3	-	-	0.894	-	0.106	-	13.6	-	-	0.721	-	0.279	-
		4	15.1	32.7	-	-	0.844	-	0.156	-	14.7	-	-	0.695	-	0.306	-
		5.8	15.9	36.2	-	-	0.787	-	0.213	-	15.5	-	-	0.678	-	0.323	-
		7.9	17	41.4	-	-	0.737	-	0.263	-	17.1	-	-	0.668	-	0.332	-
		10.4	18.9	47.7	-	-	0.668	-	0.332	-	19.0	-	-	0.659	-	0.341	-
		11.9	20.5	51.7	-	-	0.627	-	0.373	-	20.5	-	-	0.655	-	0.345	-
		13.6	23.2	57.0	-	-	a	-	a	-	22.5	-	-	a	-	a	-
	<b>dev.</b>	<b>124%</b>	<b>0.117</b>						<b>3.2%</b>	<b>0.023</b>							
2	Quick	0.95	6.1	4.6	-	-	-	0.654	0.346	-	17.8	-	-	-	NA	NA	-
		4.60	10.3	7.2	-	-	-	0.616	0.384	-	18.0	-	-	-	NA	NA	-
		6.05	12.2	8.7	-	-	-	0.649	0.351	-	19.1	-	-	-	NA	NA	-
		9.15	16.5	13.8	-	-	-	0.757	0.243	-	32.5	-	-	-	NA	NA	-
	<b>dev.</b>	<b>24.9%</b>	<b>0.200</b>						<b>105%</b>								
	Slow	7.80	14.0	11.4	-	-	-	0.737	0.263	-	31.9	-	-	-	NA	NA	-
		6.40	11.7	9.3	-	-	-	0.692	0.308	-	20.3	-	-	-	NA	NA	-
		4.55	9.5	7.2	-	-	-	0.629	0.371	-	18.4	-	-	-	NA	NA	-
		1.05	4.9	4.8	-	-	-	0.700	0.300	-	18.9	-	-	-	NA	NA	-
<b>dev.</b>	<b>16.5%</b>	<b>0.161</b>						<b>145%</b>									

3	Quick	1.8	16.4	12.7	0.819	-	-	-	0.181	-	8.2	0.673	-	-	-	0.327	-
		4.1	20.0	15.6	0.789	-	-	-	0.211	-	9.8	0.668	-	-	-	0.332	-
		4.7	21.6	17.1	0.807	-	-	-	0.193	-	10.8	0.674	-	-	-	0.326	-
		5.7	24.1	19.6	0.823	-	-	-	0.177	-	12.6	0.680	-	-	-	0.320	-
		6.6	24.6	21.7	0.817	-	-	-	0.183	-	13.7	0.679	-	-	-	0.321	-
		7.9	25.6	24.0	0.783	-	-	-	0.217	-	14.6	0.671	-	-	-	0.329	-
		9.0	26.7	24.9	NA	-	-	-	NA	-	14.6	NA	-	-	-	NA	-
	<b>dev.</b>	<b>15.5%</b>			<b>0.136</b>						<b>47.3%</b>	<b>0.137</b>					
	Slow	1.8	14.3	12.60	0.812	-	-	-	0.188	-	8.1	0.671	-	-	-	0.329	-
		4.1	19.5	16.30	0.822	-	-	-	0.178	-	10.5	0.677	-	-	-	0.323	-
		5.8	22.8	19.90	0.821	-	-	-	0.179	-	12.7	0.680	-	-	-	0.320	-
		6.7	23.8	21.90	NA	-	-	-	NA	-	13.9	NA	-	-	-	NA	-
	<b>dev.</b>	<b>12.3%</b>			<b>0.084</b>						<b>43.8%</b>	<b>0.187</b>					
4	Quick	1.7	5.8	3.6	-	-	-	0.572	-	0.428	28.3	-	-	-	a	-	a
		4.4	7.6	5.3	-	-	-	0.615	-	0.385	28.1	-	-	-	a	-	a
		5.8	9.0	6.1	-	-	-	0.596	-	0.404	28.4	-	-	-	a	-	a
		8.2	11.9	9.1	-	-	-	0.678	-	0.322	33.8	-	-	-	a	-	a
		10.2	15.7	12.9	-	-	-	0.754	-	0.246	34.3	-	-	-	a	-	a
		11.9	19.7	17.3	-	-	-	0.807	-	0.193	34.6	-	-	-	a	-	a
	<b>dev.</b>	<b>28.2%</b>			<b>0.294</b>						<b>208%</b>	<b>a</b>					
	Slow	1.6	4.7	2.8	-	-	-	0.435	-	0.565	28.4	-	-	-	a	-	a
		4.6	7.4	4.9	-	-	-	0.555	-	0.445	28.2	-	-	-	a	-	a
		5.8	8.7	6.1	-	-	-	0.598	-	0.402	28.4	-	-	-	a	-	a
		8.3	12.3	9.3	-	-	-	0.687	-	0.313	34.0	-	-	-	a	-	a
		10.3	16.0	13.2	-	-	-	0.758	-	0.242	34.2	-	-	-	a	-	a
		11.4	21.3	16.3	-	-	-	NA	-	NA	34.5	-	-	-	a	-	a

	<b>dev.</b>	<b>26.0%</b>			<b>0.316</b>					<b>227%</b>	<b>a</b>						
5	Q <sup>b</sup>	0.9	20.9	13.0	-	-	0.521	-	-	0.479	16.8	-	-	0.806	-	-	0.194
	<b>dev.</b>	<b>37.7%</b>			<b>0.187</b>					<b>19.6%</b>	<b>0.098</b>						
	S <sup>b</sup>	0.9	20.6	12.5	-	-	0.507	-	-	0.493	16.8	-	-	0.800	-	-	0.200
	<b>dev.</b>	<b>39.4%</b>			<b>0.248</b>					<b>18.4%</b>	<b>0.045</b>						
6	Quick	1.7	17.8	12.0	-	-	0.237	0.098	-	0.335	17.2	-	-	0.765	0.069	-	0.166
		3.8	19.4	12.8	-	-	0.275	0.085	-	0.360	20.2	-	-	0.748	0.078	-	0.175
		5.3	21.2	13.3	-	-	0.300	0.069	-	0.368	22.8	-	-	0.736	0.087	-	0.176
		6.7	23.9	13.4	-	-	0.322	0.063	-	0.385	25.3	-	-	0.724	0.093	-	0.183
		8.8	28.6	13.8	-	-	0.361	0.032	-	0.393	30.2	-	-	0.711	0.099	-	0.190
	<b>dev.</b>	<b>40.0%</b>			-	-	<b>0.299</b>	-	-	<b>0.368</b>	<b>5.3%</b>	-	-	<b>0.046</b>	<b>0.111</b>	-	<b>0.064</b>
	Slow	1.7	18.2	14.0	-	-	0.509	0.118	-	0.373	18.2	-	-	0.787	0.075	-	0.138
		5.3	23.5	12.2	-	-	0.370	0.137	-	0.493	22.0	-	-	0.726	0.092	-	0.182
		6.5	25.1	12.4	-	-	0.351	0.134	-	0.515	24.3	-	-	0.719	0.091	-	0.190
		<b>dev.</b>	<b>40.4%</b>			-	-	<b>0.263</b>	<b>0.087</b>	-	<b>0.349</b>	<b>3.1%</b>	-	-	<b>0.071</b>	<b>0.130</b>	-
7	Quick	0.1	9.0	4.1	0.204	-	-	0.485	0.311	-	6.9	0.557	-	-	0.046	0.397	-
		2.7	9.2	5.5	0.217	-	-	0.485	0.298	-	9.6	0.575	-	-	0.047	0.378	-
		4.3	11.1	6.5	0.222	-	-	0.471	0.307	-	11.5	0.582	-	-	0.045	0.373	-
		7.0	15.3	8.6	0.225	-	-	0.449	0.326	-	16.2	0.593	-	-	0.042	0.365	-
	<b>dev.</b>	<b>44.6%</b>			<b>0.182</b>	-	-	<b>0.163</b>	<b>0.035</b>	-	<b>9.3%</b>	<b>0.178</b>	-	-	<b>0.264</b>	<b>0.087</b>	-
	S <sup>b</sup>	0.0	6.8	4.3	0.231	-	-	0.547	0.222	-	7.2	0.577	-	-	0.064	0.359	-
	<b>dev.</b>	<b>37.0%</b>			<b>0.055</b>	-	-	<b>0.055</b>	<b>0.110</b>	-	<b>5.5%</b>	<b>0.401</b>	-	-	<b>0.428</b>	<b>0.027</b>	-
8	Quick	1.8	11.3	10.2	0.231	0.044	-	0.726	-	-	32.4	0.517	0.139	-	0.344	-	-
		6.5	14.3	15.5	0.234	0.040	-	0.726	-	-	61.9	0.508	0.157	-	0.335	-	-

		9.25	20.7	18.0	0.226	0.031	-	0.743	-	-	113.5	0.469	0.205	-	0.327	-	-
		10.95	23.4	21.3	0.226	0.029	-	0.744	-	-	176.1	0.444	0.234	-	0.322	-	-
	<b>dev.</b>	<b>9.9%</b>			<b>0.015</b>	<b>0.022</b>	-	<b>0.037</b>	-	-	<b>405%</b>	<b>0.240</b>	<b>0.125</b>	-	<b>0.366</b>	-	-
	Slow	9.0	20.9	17.6	0.224	0.031	-	0.744	-	-	107.4	0.471	0.201	-	0.328	-	-
		6.2	16.5	14.1	0.232	0.035	-	0.733	-	-	56.9	0.523	0.138	-	0.339	-	-
		1.05	10.2	10.7	0.261	0.049	-	0.690	-	-	29.4	0.530	0.137	-	0.333	-	-
	<b>dev.</b>	<b>11.9%</b>			<b>0.016</b>	<b>0.015</b>	-	<b>0.007</b>	-	-	<b>282%</b>	<b>0.285</b>	<b>0.105</b>	-	<b>0.391</b>	-	-
6	Quick	1.4	10.1	10.5	-	-	0.407	0.239	0.069	0.284	10.9	-	-	0.667	0.055	0.239	0.039
		4.3	11.0	13.2	-	-	0.400	0.225	0.117	0.257	12.5	-	-	0.656	0.037	0.281	0.026
		7.2	13.4	16.2	-	-	0.378	0.217	0.172	0.232	14.6	-	-	0.647	0.027	0.307	0.018
		10.6	18.0	21.1	-	-	0.358	0.204	0.235	0.203	18.4	-	-	0.643	0.020	0.324	0.013
		13.3	21.7	28.1	-	-	0.361	0.192	0.274	0.173	23.3	-	-	0.644	0.017	0.329	0.009
		<b>dev.</b>	<b>18.2%</b>			-	-	<b>0.203</b>	<b>0.076</b>	<b>0.058</b>	<b>0.201</b>	<b>8.0%</b>	-	-	<b>0.068</b>	<b>0.124</b>	<b>0.064</b>
	* Guest compositions in vapor phase were already provided in Table 31.																
<sup>a</sup> The thermodynamic model did not converge for the condition.																	
<sup>b</sup> Q and S correspond to quick and slow, respectively.																	

As Table 37 clarifies, for methane-propane mixture, the simulation results considering sII have a satisfactory accordance with experimental hydrate composition results (the average deviation of hydrate composition is 0.023 in mole fraction). Moreover, the equilibrium pressures at temperatures ranging from 0 to 14°C of this mixture were also adequately predicted by an average deviation about 3%. To summarize the simulation results for methane/propane mixture, Figure 49 is provided.

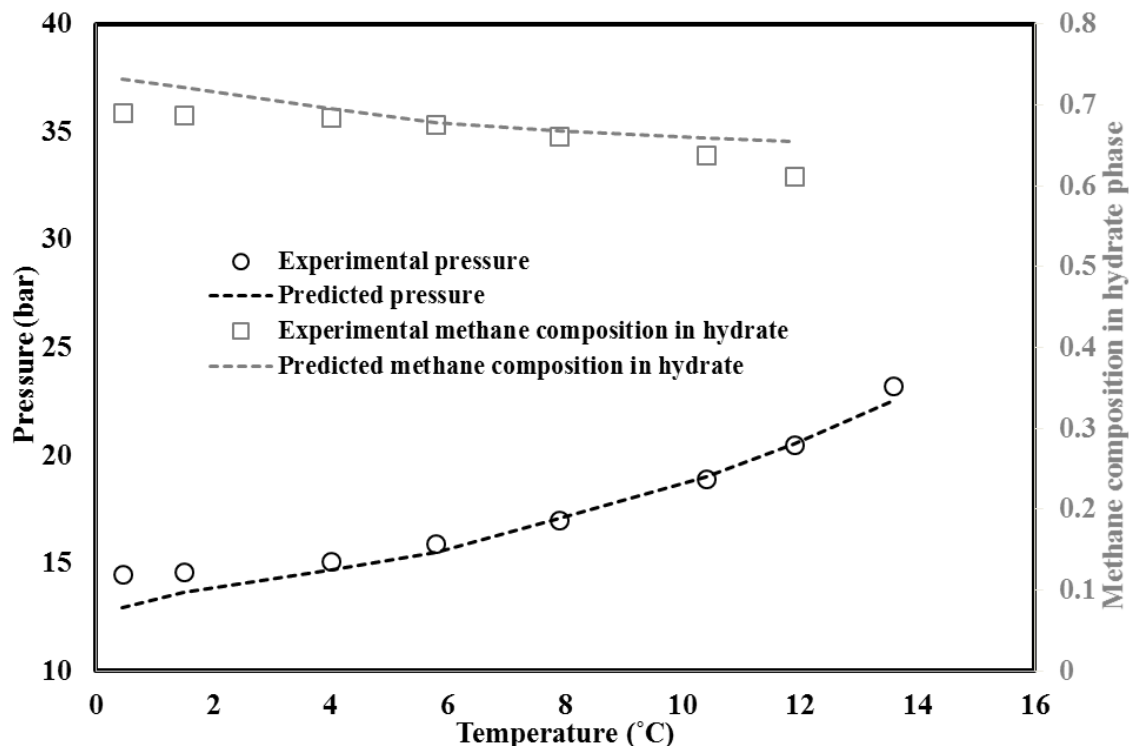


**Figure 49. The experimental data versus simulation results in terms of pressure and hydrate composition for methane/propane mixed hydrate, sII.**

For ethane-propane mixture, the prediction results for pressure and hydrate composition were not effectively accurate. Nevertheless, the average deviations of thermodynamic model for slow crystallization concerning both pressure and hydrate composition were less than quick crystallization.

Furthermore, as seen in Table 37 for binary mixtures, in the case of  $\text{CO}_2\text{-C}_3\text{H}_8$ , the results of thermodynamic model had a better accordance with the experimental data from slow crystallization for equilibrium pressure (12.3% for slow compare to 15.5% for quick). This is more obvious for hydrate composition. The average absolute deviation for hydrate composition



for slow process is about 0.08, whilst near 0.14 for quick crystallization. Moreover, this should be noted that pure CO<sub>2</sub> forms sI hydrate. However, in presence of small amount of propane in gas phase, CO<sub>2</sub>-C<sub>3</sub>H<sub>8</sub> mixture could form sII [1]. Nevertheless, Adisasmito and Sloan [181] reported that at CO<sub>2</sub> compositions higher than 95% (mole fraction) in gas phase, hydrate sI forms. CO<sub>2</sub> composition in gas phase in our experiment for CO<sub>2</sub>-C<sub>3</sub>H<sub>8</sub> mixed hydrate was usually higher than 95%. Therefore, hydrate sI was expected to form. The simulation results for both structures showed that the thermodynamic model well predicted hydrate structure (sI).

However for binary mixtures including C<sub>4</sub>H<sub>10</sub>, the thermodynamic model almost failed to predict hydrate pressure and composition. It could be due to the Kihara parameters of butane. Ideally, a wide range of pure equilibrium data for each guest molecule is required to optimize Kihara parameters. Butane does not form hydrates by itself. Nevertheless in the presence of other hydrate formers, it can enter into the cavities. As a result, the Kihara parameters for butane are quite complicated to obtain. Secondly, for binary mixtures involving butane, the kinetic effects might have a significant influence on hydrate formation; hence the results of experiments and thermodynamic model diverge considerably.

For ternary mixtures, the modeling results show that both mixtures including heavier hydrocarbons formed structure II. Furthermore, thermodynamic model agreed well with the experimental results of slow crystallization (average deviation of 3.1% and 5.5% for CO<sub>2</sub>-C<sub>2</sub>H<sub>6</sub>-C<sub>3</sub>H<sub>8</sub> and CH<sub>4</sub>-C<sub>2</sub>H<sub>6</sub>-n-C<sub>4</sub>H<sub>10</sub>, respectively). However, the guest composition in hydrate phase for both crystallization rates was not well simulated. Actually, in both mixtures, the composition of ethane in hydrate phase was poorly computed. Given the fact that Kihara parameters for ethane had been already satisfactorily optimized and tested [121], the question then arises concerning structural transition or co-existence of both structures sI and sII. For instance, Subramanian et al. [88] stated that the hydrate structure of CH<sub>4</sub>-C<sub>2</sub>H<sub>6</sub> could change regarding to the gas phase composition. The same consideration was indicated for CO<sub>2</sub>-C<sub>3</sub>H<sub>8</sub> mixed hydrate [181]. Therefore, as aforementioned, the thermodynamic model could not simulate satisfactorily hydrate phase in term of structural transitions.

The hydrate pressure and composition of CO<sub>2</sub>-C<sub>2</sub>H<sub>6</sub>-N<sub>2</sub> were simulated by considering sI. The average absolute deviation of pressure for quick and slow crystallizations was 9.9 and 11.9%, respectively. More appropriate results were obtained for hydrate composition at slow

crystallization. The average absolute deviation of composition for all three components was less than 0.016 at slow crystallization process. Figure 50 illustrates the experimental and simulation results for this mixture at slow crystallization rate.

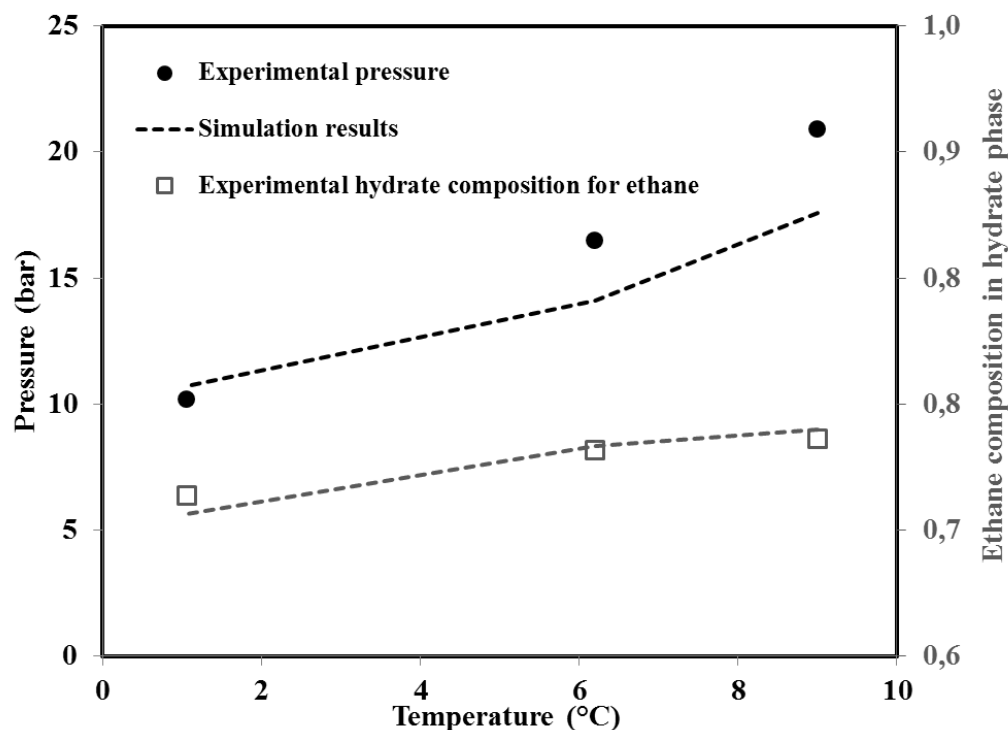


**Figure 50. Experimental and simulation results of hydrate pressure and ethane composition in solid phase at slow crystallization for CO<sub>2</sub>-N<sub>2</sub>-C<sub>2</sub>H<sub>6</sub> mixed hydrates (sI)**

The thermodynamic model predicted relatively well the hydrate formation pressure (average deviation: 8%) and guest composition in hydrate phase for mixed CH<sub>4</sub>-C<sub>2</sub>H<sub>6</sub>-C<sub>3</sub>H<sub>8</sub>-nC<sub>4</sub>H<sub>10</sub> hydrates.

Moreover, it should be emphasized that it is difficult to optimize a unique set of Kihara parameters to model both pure propane hydrate and mixtures that include propane. Hence we concluded that for using van der Waals and Platteeuw model based on Kihara approach, it is necessary to use different sets of Kihara parameters based on the kind of feed gas (pure propane or a mixture involving propane).

The results obtained elucidate that at quick crystallization process where the driving force is high, kinetics effects could dominate. Indeed, gas dissolution in liquid phase depends on the driving

force, mass transfer coefficients as well as the characteristics of the contact surface. Therefore, instantaneous gas concentration in the liquid phase should not be at thermodynamic equilibrium. Finally, the driving force for the crystallization does not match what we could expect from only one gas's thermodynamic considerations. The final solid phase should be the result of all mass transfer considerations [121].

These clarifications reveal some surprising consequences. The experimental results of slow crystallization process seemed to be closer to thermodynamic equilibrium (unlike the thermodynamic model). This suggests that the hydrate formation would be at thermodynamic equilibrium, if the kinetic effects could be circumvented as much as possible. Furthermore, the hydrate crystals at slow crystallization might be more homogeneous than quick crystallization process. Finally, the impact of kinetic considerations in both crystallization processes could not be ignored. Therefore, the hydrate formation of gas mixtures is clearly occurs at non-equilibrium conditions.

## **5.6. Raman spectroscopic measurements of clathrate hydrates**

### **5.6.1. Basic principles of Raman spectroscopy**

Spectroscopy is the study of the absorption, emission or scattering of light and other radiation by matter [192]. Sir C.V. Raman was experimentally observed the inelastic scattering of light in 1920 and since then, this phenomenon has been called “Raman Spectroscopy” [193]. Raman spectroscopy is an instrumental technique based on an inelastic light scattering by molecules in order to detect rotational, vibrational and other low-frequency modes in a system. Indeed, in Raman spectroscopic measurement, a photon is scattered into surroundings in all directions due to interactions with a molecule. As a result, the photon gains or loses collision energy which can be then spotted and evaluated [194–197].

Raman spectroscopy is a multipurpose and adoptable technique which can be used for a wide range of scientific cases. Bumbrah and sharma [192] stated that Raman spectroscopy has less limitations compared to other spectroscopic methods. Thus, it is widely utilized to investigate chemical structures and physical forms as well as identifying the chemical substances. This technique is used not only for the qualitative analysis of samples by measuring the frequency of

scattered radiations, but also to determine the concentration of samples by computing their intensities [192].

In the present study, vibrational Raman spectroscopy was used to provide qualitative and quantitative information about the solid hydrate phase. Note that, two studies with Raman spectroscopy have been conducted in order to analyze directly the properties and molecular aspects of CO<sub>2</sub>/C<sub>3</sub>H<sub>8</sub> mixed hydrate such as hydrate structure and composition as well as guest molecule position investigations. First study was performed at Ecole Nationale Supérieure des Mines de Saint-Etienne and is presented in section 5.6.2. The second study was conducted in cooperation with and at the Institute of Molecular Sciences at University of Bordeaux (ISM), France and is presented in section 5.6.3.

Before going into further details, I would like to gratefully acknowledge the funding received from CNRS “GdR2026” through this collaborative work. I am also very grateful to Professor Arnaud Desmedt (and his team) for his active involvement and constructive scientific suggestions and discussions which improved effectively the microscopic part of this work.

### **5.6.2. Raman spectra of CO<sub>2</sub>/C<sub>3</sub>H<sub>8</sub> binary hydrate at isochoric conditions**

The present section provides qualitative and quantitative insights into the enclathration of guest molecules (CO<sub>2</sub>/C<sub>3</sub>H<sub>8</sub> mixture) in hydrate phase as well as gas phase concentration changes. Raman shifts of different vibrational modes of each guest during the crystallization and dissociation processes are identified and presented. In addition, the band frequencies of trapped molecules in small and large cavities of hydrate structures are discussed. They are also compared to the available data in the literature. For vapor and hydrate phases composition measurements, the calibration of Raman spectroscopy was required. This was determined by injecting CO<sub>2</sub>/C<sub>3</sub>H<sub>8</sub> mixtures (different compositions) and will be presented in the following sections.

#### **5.6.2.1. High pressure optical cell and Raman spectrometer**

The experiments were performed in a high pressure cell which consisted of a sapphire window allowing the laser light of Raman for spectroscopic observations of the samples. The diameter and height of sample chamber are 19.8 and 4mm, respectively. The volume of sample chamber without the bore volumes is approximately 1.2cm<sup>3</sup>. The cell comprises two channels which connected to the cryostat (HUBER Ministat 240). The internal temperature of the cell can be

controlled between -20 and 40°C by a 60/40 V/V water-ethanol. The temperature is monitored by a Pt100 probe which is located about 5mm inside the internal volume of the cell through a canal. The maximum operational pressure of the cell is 100bar. The pressure is measured by a KELLER PA-23S sensor. There are two mechanical valves for gas and liquid injection. A schematic diagram of experimental set-up is presented in Figure 51.

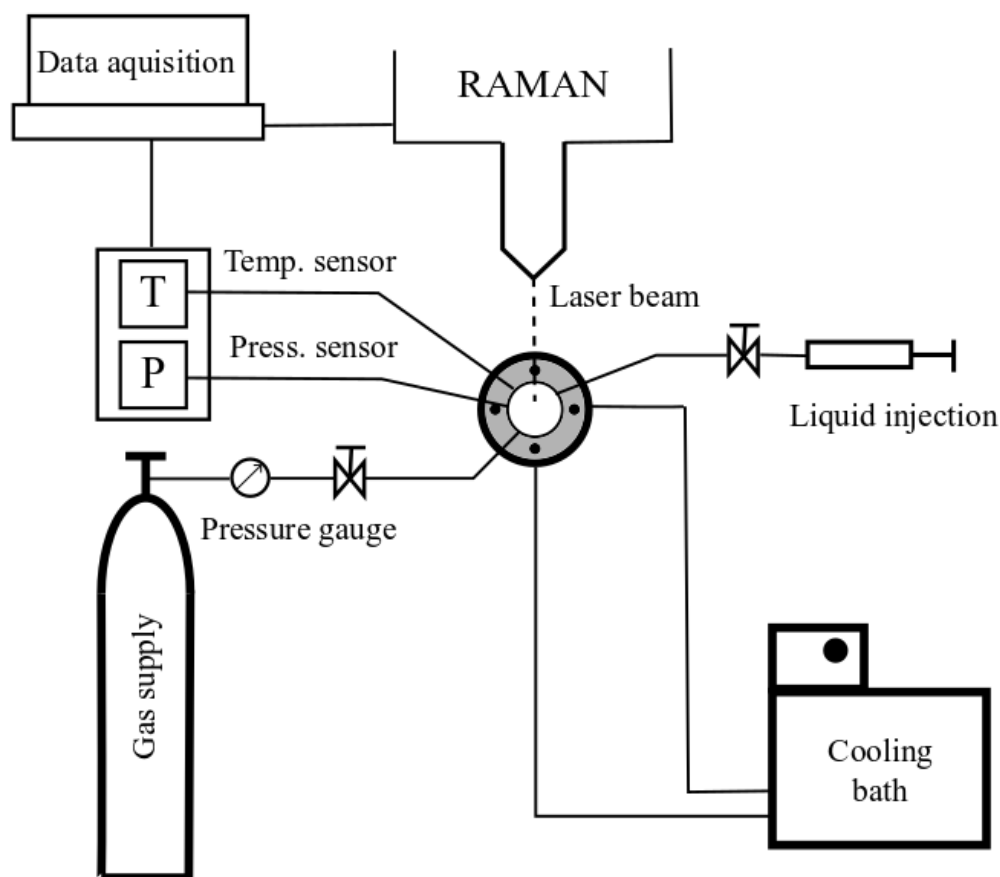


**Figure 51. Schematic of experimental set-up used for Raman spectroscopic measurements**

A confocal Raman spectrometer HORIBA JOBIN YVON was used in this study. The laser light could be focused on the desired spot of existence fluids inside the cell chamber. Backscattered light was filtered using a 2400 grooves/mm grating. A CCD detector which operated at -69°C was used to spot the peak frequencies in the spectrum. The excitation power of argon laser emitting green light was 30mW with a wavelength of 532 nm as an excitation source. A 10X Olympus microscope objective was used to focus the laser on the sample. Different regions of Raman spectra were analyzed according the vibrational modes of CO<sub>2</sub> and C<sub>3</sub>H<sub>8</sub>. The spectra

from each location of sample were collected by 10 accumulations; each comprised 10 seconds of integration time. The Raman spectrometer was calibrated by Silicon ( $521\text{ cm}^{-1}$ ) before the experiments.

#### **5.6.2.2. Experimental protocol**

At the beginning, the reactor is washed and cleaned. The deionized water (about  $0.7\text{ cm}^3$ ) is then introduced into the cell. The temperature of cooling bath is set on  $0.5^\circ\text{C}$  in order to obtain a temperature near  $1^\circ\text{C}$  inside the cell. A gas mixture of  $\text{CO}_2/\text{C}_3\text{H}_8$  (0.777/0.223 mole fraction) is injected into the high pressure cell at approximately 15 bar. A pressure drop (about 1 bar) is observed due to gas dissolution (mostly carbon dioxide, since its solubility is significantly greater than propane). After one day, hydrate formation starts. At this point, the temperature slightly increases due to exothermic reaction of hydrate crystallization. The system pressure is then decreased as a result of guest enclathration in hydrate cavities. We wait for the stabilization of pressure and temperature (end of crystallization). During the crystallization, Raman spectra of vapor and hydrate phases are collected and analyzed. Then the dissociation begins by increasing stepwise the system temperature. At each step, when the equilibrium condition is achieved, Raman spectra of vapor and hydrate phases are collected. The procedure is repeated until there is no more crystal in the cell. Figure 52 illustrates the procedure of crystallization and dissociation of  $\text{CO}_2/\text{C}_3\text{H}_8$  mixed hydrate.

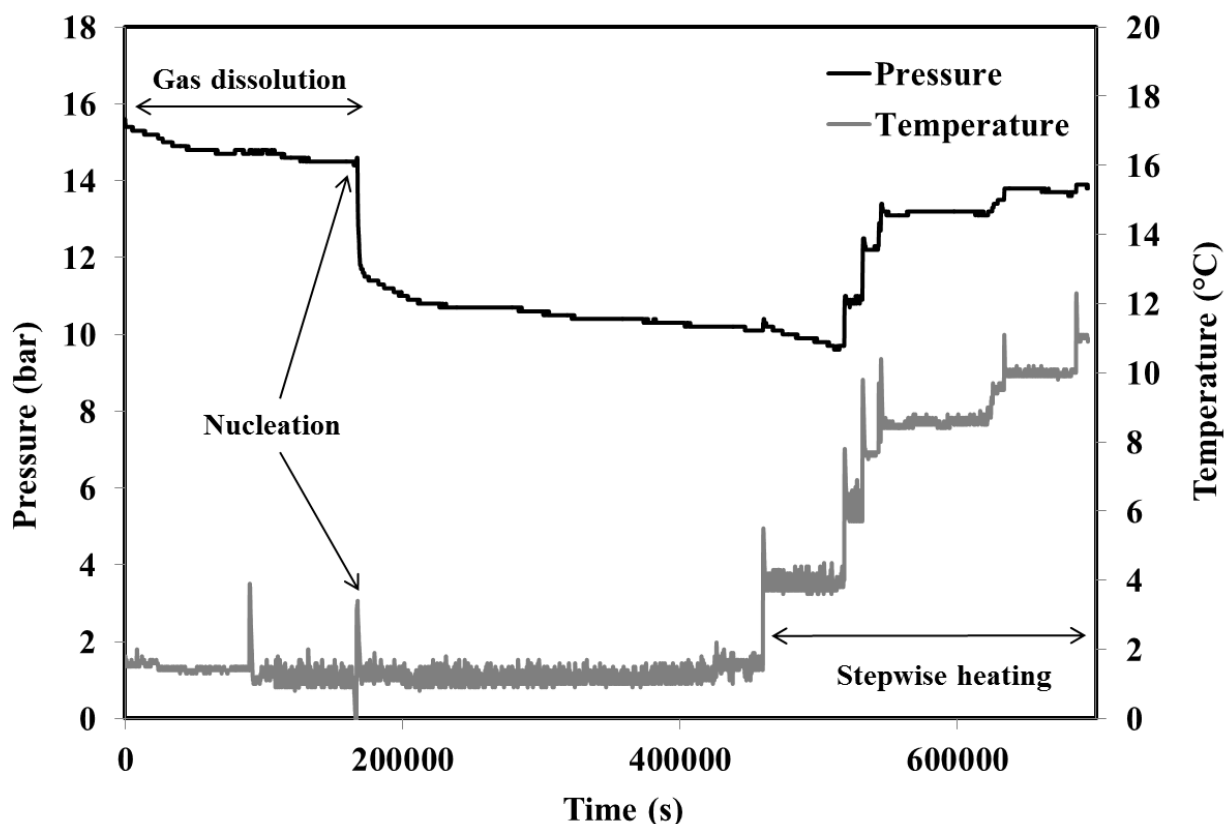
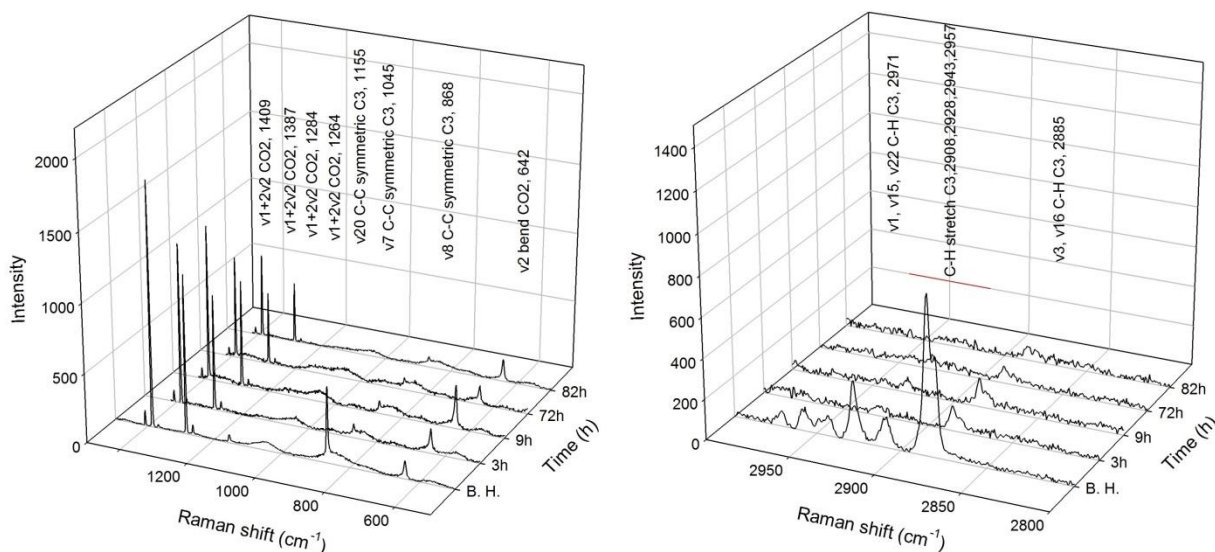


Figure 52. Pressure-Temperature evolution during hydrate formation and dissociation of  $\text{CO}_2/\text{C}_3\text{H}_8$  mixed hydrate

### 5.6.2.3. Raman spectra of $\text{CO}_2$ and $\text{C}_3\text{H}_8$ during crystallization

A detailed analysis of  $\text{CO}_2$  and  $\text{C}_3\text{H}_8$  Raman band frequencies in vapor phase as well as small and large cavities of sI and sII is presented now. Since the bands of  $\text{CO}_2$  and  $\text{C}_3\text{H}_8$  are located in different regions of Raman shifts, the gas and hydrate phases were investigated in different sections; 500-1420 and 2800-3000  $\text{cm}^{-1}$ . Figure 53 presents these regions during the crystallization process and the band positions of  $\text{CO}_2$  and  $\text{C}_3\text{H}_8$  were highlighted. The figures have been plotted by “SigmaPlot” software. The analysis of gas phase before crystallization was also added to the figures to clarify the gas phase changes during the crystallization.



**Figure 53. The gas phase changes during the crystallization. (B. H. corresponds to “before hydrate formation”)**

As seen on the figures, the peak areas during crystallization differed considerably from the initial state (before crystallization). These changes in band areas were more considerable for C-C and C-H stretches of  $C_3H_8$ . Only three hours after starting the crystallization, the peaks of propane notably shrank. This means that at the beginning of crystallization process, the enclathration of propane molecules was more considerable than of  $CO_2$ . In fact, during our experiments in SECOHYA and ACACIA reactors, this was also observed that the encapsulation of propane and butane at the first steps of crystallization were more significant than lighter hydrocarbons. However, the main vibrational modes of carbon dioxide in gas phase ( $1284$  and  $1387\text{ cm}^{-1}$ ) continuously shortened from the beginning to the end of crystallization.

Table 38 shows the Raman shifts obtained in this work as well as in the literature for the different bands of  $CO_2$  and  $C_3H_8$ . This is clear that the shifts measured of vibrational modes for two gases were obtained with the good agreement with the literature. However, the dominate peaks of carbon dioxide and propane were taken into account in this study to analyze the phase behavior changes. They are highlighted in the following table.



**Table 38. The Raman shifts for CO<sub>2</sub> and C<sub>3</sub>H<sub>8</sub> in gas phase, obtained in this work and in literature**

Gas	Type	Vibrational mode	Shift measured (cm <sup>-1</sup> )	shift literature (cm <sup>-1</sup> )	Ref.
Propane	C-C stretch	v8 symmetric	868	871	[198]
		v20	1045	1054	[199]
		v7	1155	1157	[199]
	C-H stretch	v3,v16	2885	2887	[199]
		N.A	2908	2910	[199]
		N.A	2928	2929	[199]
		N.A	2943	-	-
		N.A	2957	2960	[199]
	v1,v22,v15,v1	2971	2971	[199,200]	
Carbon dioxide	-	v2 bend CO <sub>2</sub>	642	667	[198]
		v1+2v2	1264	1266	[165]
		v1+2v2	1284	1286	[165]
		v1+2v2	1387	1389	[165]
		v1+2v2	1409	1410	[165]

The hydrate phase behavior during the crystallization was studied in three different regions of Raman shifts as indicated in Figure 54. Table 39 shows the Raman shifts obtained in this work as well as in the literature for the different bands of CO<sub>2</sub> and C<sub>3</sub>H<sub>8</sub>.

**Table 39. The Raman spectra for CO<sub>2</sub> and C<sub>3</sub>H<sub>8</sub> in hydrate phase, during the crystallization**

Gas	Type	Vibrational mode	Cavity type	Shift measured (cm <sup>-1</sup> )	shift literature (cm <sup>-1</sup> )	Ref.
C <sub>3</sub> H <sub>8</sub>	C-C stretch	v8 symmetric	sII large	871	878	[198]
	C-H stretch	v3	sII large	2869	2870	[201]
		v16	sII large	2877	2878	[201]
		N.A	sII large	2917	-	-
CO <sub>2</sub>	-	V1+2v2	sII large	1271	1276	[170]
		V1+2v2	sII large	1379	1381	[170]

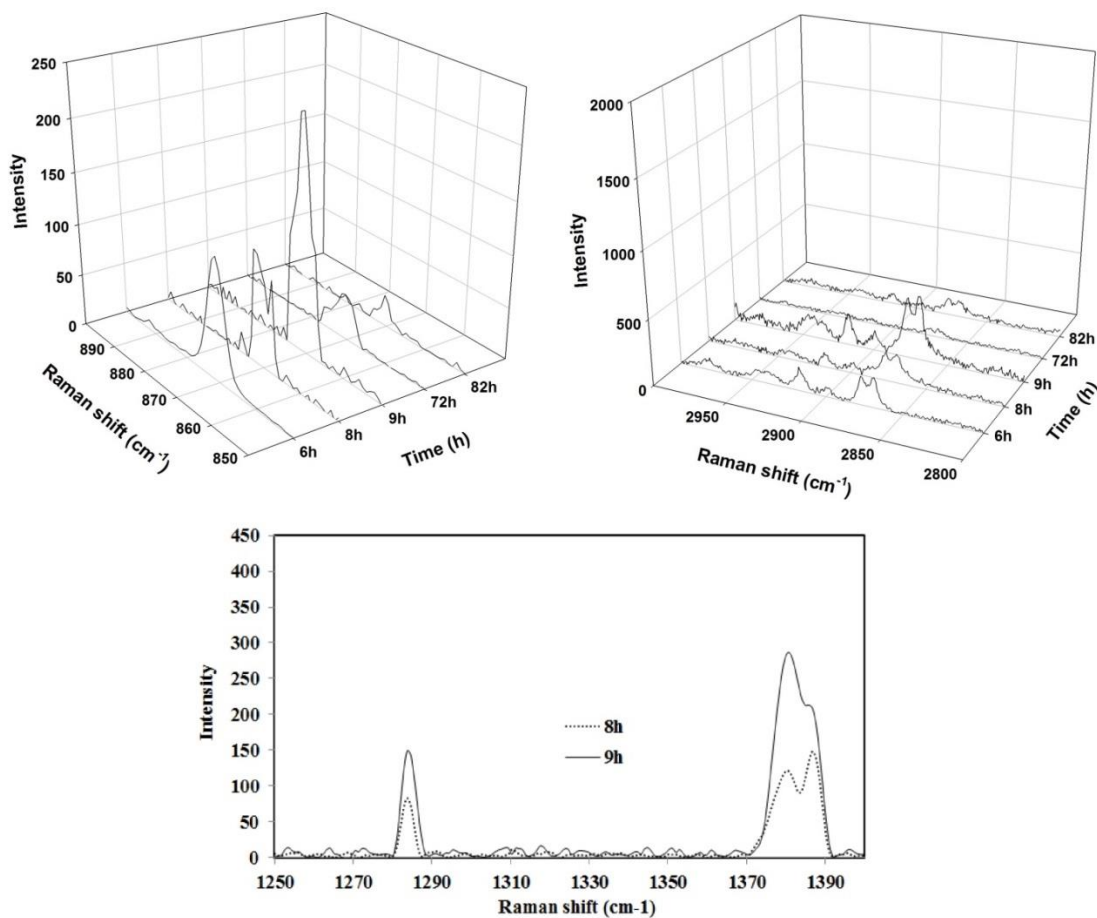


**Figure 54. Hydrate phase changes during the crystallization process. Top left: C-C stretch of propane. Top right: C-H stretch of propane. Bottom: CO<sub>2</sub> Fermi resonance**

As Figure 54 shows, at the beginning of the crystallization process, the propane molecules encapsulated rapidly the  $5^{12}6^4$  large cavities of sII. In other words, the enclathration rate of propane molecules at the beginning of the process was much faster than CO<sub>2</sub> molecules. This is also in accordance with the evidence investigated for the gas phase changes. Hence, the composition of propane in hydrate phase at this period could be much higher than in the gas phase.

Mixed hydrate of CO<sub>2</sub>/C<sub>3</sub>H<sub>8</sub> is supposed to form sII. As the molecular diameter of propane is 0.6568 nm, they are encapsulated in large cavities of sII ( $5^{12}6^4$ ) and it is not likely to be captured in small cavities [202,203]. There is a double-band at 2869 and 2877 cm<sup>-1</sup> which is correspond to C-H symmetric vibration of propane. Interestingly, the simple propane hydrate has only one vibration band in this region (this will be explained in the following sections). Hence, it is

concluded that propane molecules have been trapped in two different environments. The first band is considered to the propane molecules encapsulated in the large cavities of sII ( $5^{12}6^4$ ). The second band could be assigned whether the occluded propane molecules in hydrate particles or encaged propane in large cavities of sI ( $5^{12}6^2$ ). This is also excluded from a small peak on the shoulder of C-C stretch of propane at  $871\text{ cm}^{-1}$ .

The same phenomenon was observed for the main peaks of carbon dioxide. There was a double-band of  $\text{CO}_2$  at around  $1386\text{ cm}^{-1}$ . The carbon dioxide molecules occupy the large cavities of sI and sII. However, Fleyfel and Devlin reported that  $\text{CO}_2$  molecules can occupy small cavities [204]. Therefore, the double-band of  $\text{CO}_2$  in this work might be assigned to large cavities of sI and sII ( $5^{12}6^2$  and  $5^{12}6^4$ ) or small and large cavities of sII ( $5^{12}$  and  $5^{12}6^4$ ). This will be also compared to the Raman bands of  $\text{CO}_2$  in the gas phase and simple hydrate phase in the following sections.

The existence of sI is not far away from reality. As aforementioned in the previous section, the composition of  $\text{CO}_2$  in the gas phase was significantly higher than of propane at the end of crystallization. Hence, there was a possibility of sI formation since simple  $\text{CO}_2$  forms sI, and since Adisasmito and Sloan already reported that at high compositions of  $\text{CO}_2$  in the gas phase,  $\text{CO}_2/\text{C}_3\text{H}_8$  mixtures might form sI [181].

However, at the final states of crystallization, the relative area peaks of carbon dioxide to propane seemed to be large ( $A_{\text{CO}_2}/A_{\text{C}_3\text{H}_8}$ ). Moreover, the peak areas of C-C and C-H stretches of propane at the end of crystallization shrank compared to the beginning of the crystallization. This means that the composition of  $\text{CO}_2$  at the end of crystallization is significantly higher than  $\text{C}_3\text{H}_8$ .

#### **5.6.2.4. Raman spectra of $\text{CO}_2$ and $\text{C}_3\text{H}_8$ during dissociation process**

At the end of crystallization, the temperature was stepwise increased and at each step, the gas and hydrate phases were accordingly analyzed by Raman spectroscopy. Figure 55 presents the gas phase behavior during the dissociation process according the Raman spectra. As clear on the figure, during the first steps of dissociation, the peaks ratio of  $A_{\text{CO}_2}/A_{\text{C}_3\text{H}_8}$  was high, meaning that the composition of  $\text{CO}_2$  in gas phase was considerably higher than  $\text{C}_3\text{H}_8$ .

Furthermore, the results show that the change in peak areas of propane was more significant than of carbon dioxide. This means that the declathration of propane molecules during the dissociation process was faster than of carbon dioxide molecules.

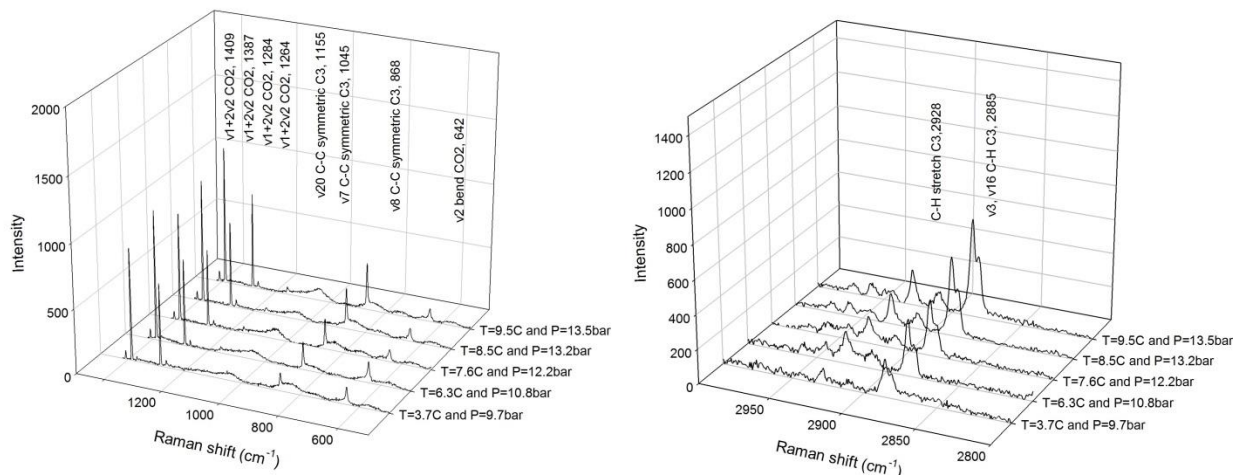


Figure 55. The gas phase changes during the dissociation process

The hydrate phase during the dissociation procedure was analyzed in order to investigate the guest behavior in hydrate phase at different  $P$ - $T$ - $y$  conditions. Figure 56 and Figure 57 illustrate the hydrate phase analyses and Raman spectra of CO<sub>2</sub>/C<sub>3</sub>H<sub>8</sub> binary hydrate at each dissociation point.

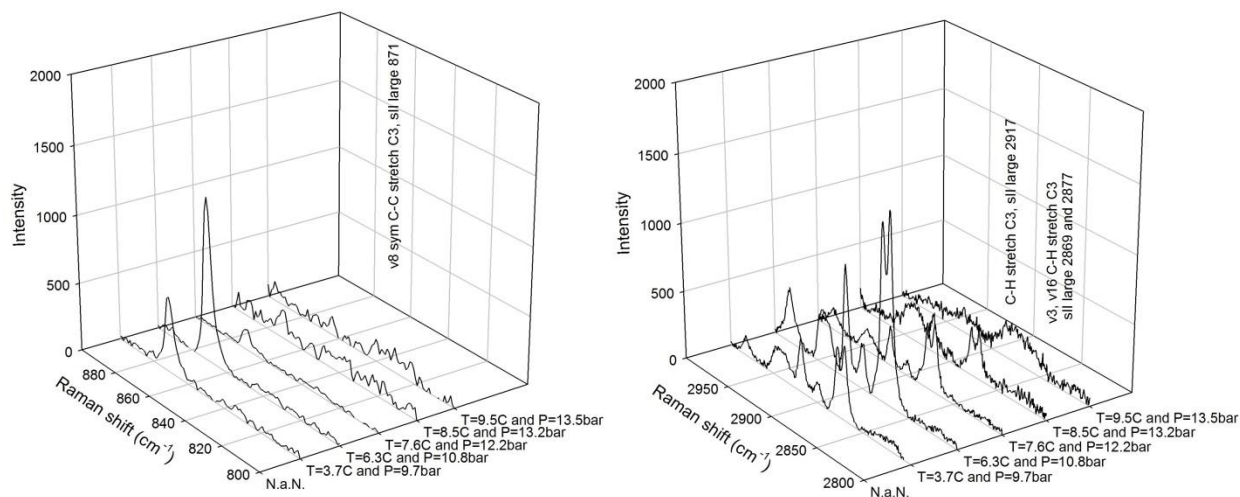


Figure 56. Hydrate phase analyses and Raman spectra of CO<sub>2</sub>/C<sub>3</sub>H<sub>8</sub> binary hydrate. Left: C-C stretch of propane vibrations. Right: C-H stretch of propane

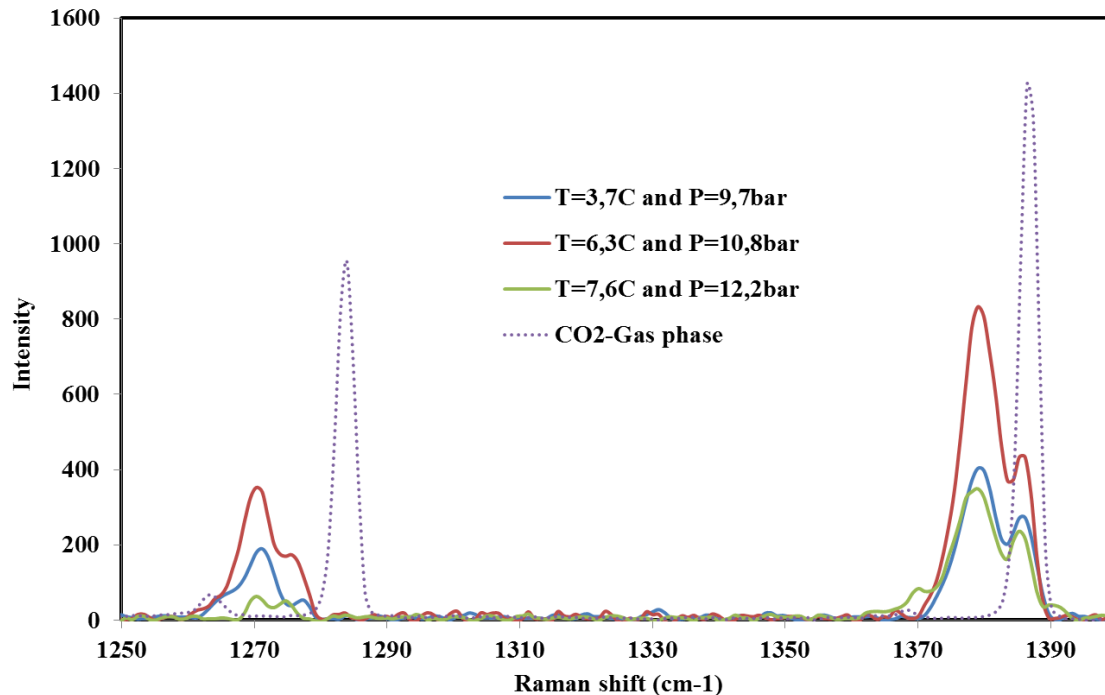


Figure 57. Hydrate phase analysis CO<sub>2</sub> in hydrate phase compared to CO<sub>2</sub> gas

At the first steps of dissociation process, the results of relative peak areas of CO<sub>2</sub> and C<sub>3</sub>H<sub>8</sub> show that the carbon dioxide molecules dissociated rapidly than propane molecules. Unfortunately, the CO<sub>2</sub> signals near total dissociation were entirely disrupted; therefore, they are not presented in the figure. At temperatures higher than 6.3°C, the both peak area of propane (C-C and C-H stretches) shrank notably (in the following section, the composition of guest molecules in gas and hydrate phases will be calculated and discussed based on the peak areas). As for the period of the crystallization, during the dissociation process, the double-peak at 2869 and 2877 cm<sup>-1</sup> corresponding to the C-H vibrational mode of propane was observed. If we consider the existence of both structures based on this double-peak, the declathration rate of propane molecules in both structures is significantly different at the low temperature. However, it seemed to be almost the same following the dissociation procedure.

Figure 57 provides the collected Raman spectra of carbon dioxide in mixed CO<sub>2</sub>/C<sub>3</sub>H<sub>8</sub> hydrate. As seen on the figure, on the shoulder of two main peaks of carbon dioxide (1271 and 1379 cm<sup>-1</sup>), there are two vibrational bands. The vibrational bands of CO<sub>2</sub> in the gas phase has been added to the figure and it clarifies that the peak on the shoulder of 1379 cm<sup>-1</sup> band could be associated to the gaseous non-enclathrated CO<sub>2</sub> molecules since it is correctly located at 1386 cm<sup>-1</sup> (the band of

CO<sub>2</sub> in gas phase). Although, the same explanation could be described to the peak at the shoulder of band 1271 cm<sup>-1</sup> (the vibrational mode of CO<sub>2</sub> in hydrate cages), it is 7cm<sup>-1</sup> far from the vibration band in gas phase.

#### 5.6.2.5. Compositional analysis

Guest molecules inside the hydrate cavities are surrounded by different environment as in liquid or vapor phase. However, encaged molecules have enough space for rotation and vibration. Thus, the gas-gas or gas-water interactions are mainly directed by van der Waals forces. As a result, the Raman scattering cross sections of guest molecules do not differ significantly after being encapsulated in hydrate cavities. Therefore, a calibration curve based on the vapor concentration could be used to determine hydrate composition [165,198].

For binary mixture of CO<sub>2</sub>/C<sub>3</sub>H<sub>8</sub>, the ratio area under the peaks of carbon dioxide and propane (C-C stretches) attributes the relative quantity of these gases. Therefore, three different gas mixture of CO<sub>2</sub>/C<sub>3</sub>H<sub>8</sub> were prepared and analyzed by Raman spectroscopy (Their compositions are provided in Table 40). The peak area of each vibrational mode of carbon dioxide and propane, and consequently the ratio area were determined for each mixture. The calibration curve is presented in Figure 58.

**Table 40. Mixtures used for calibration of Raman spectroscopic measurements**

Mixture	CO <sub>2</sub>	C <sub>3</sub> H <sub>8</sub>
a	0.633	0.367
b	0.863	0.137
c	0.937	0.063

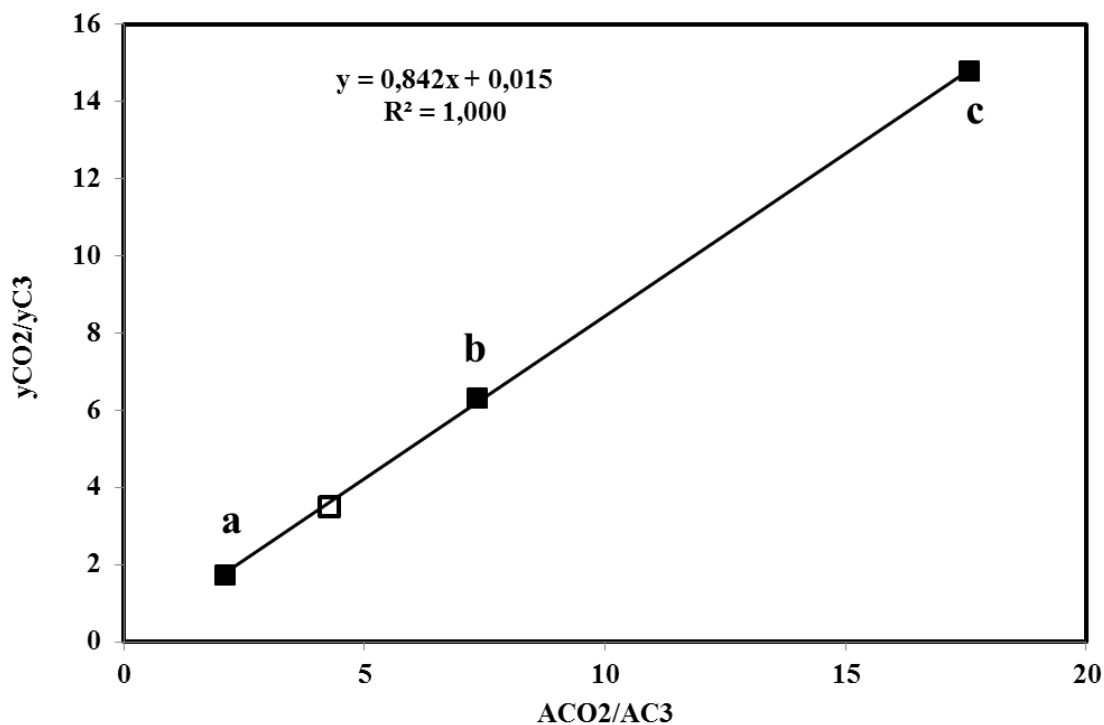


**Figure 58. Calibration curve of carbon dioxide/propane mixture based on vapor measurements to estimate vapor and hydrate compositions (points a, b and c are the mixtures presented in Table 40)**

The figure clearly represents that the peak area ratio was a linear function relative composition ( $R^2=1.000$  with a correlation coefficient of 0.842). The black squares are the gas mixtures used for calibration and the empty square is the mixture which was used to study gas hydrate formation and dissociation. This empty square was presented to confirm the results of calibration.

Guest concentration in vapor phase was determined according to the peak areas for each spectroscopic measurement. Indeed, at each state, the laser beam was focused into the vapor phase and Raman spectra of guest molecules were obtained. Then, peak area of carbon dioxide and propane ( $A_{CO_2}$  and  $A_{C_3H_8}$ , respectively) were calculated by Raman spectroscopy software (LabSpec5). The relative composition of carbon dioxide and propane ( $y_{CO_2}/y_{C_3H_8}$ ) was then determined based on the calibration curve provided in Figure 58. Finally, the composition of each guest was computed ( $y_{CO_2} + y_{C_3H_8} = 1$ ).

To determine the guest composition in hydrate phase, it is supposed that Raman scattering cross sections of carbon dioxide (Fermi Dyed) and propane ( $\nu_8$  C-C stretching mode) does not significantly change upon enclathration into hydrate structures. Given the fact that there is no

chemical bonding between the encaged guest molecules and water molecules of hydrate structure, it can be expected that the rotations and vibrations of trapped molecules in hydrate lattice are the same as in free vapor phase. As a result, the Raman scattering cross sections of carbon dioxide and propane molecules encaged in hydrate structure are almost identical to free vapor phase [165,198].

Based on this assumption the guest composition in hydrate phase was determined. At each state, the laser beam was focused into the hydrate phase and Raman spectra were collected and analyzed. The peak areas of carbon dioxide (Fermi Dyed) and propane (v8 C-C stretching mode) were then determined by Raman spectroscopy software (LabSpec5). The peak area ratio ( $A_{CO_2}/A_{C_3H_8}$ ) was calculated. The mole fraction ratio of carbon dioxide and propane in hydrate phase ( $x_{CO_2}/x_{C_3H_8}$ ) was then computed by the correlation coefficient provided in Figure 58 (0.842). The hydrate composition was then determined based on the equal unity of guest composition in on water free basis ( $x_{CO_2} + x_{C_3H_8} = 1$ ).

The compositional analysis of gas and hydrate phases during the dissociation steps are provided in Table 41.

**Table 41. Compositional analysis of CO<sub>2</sub>/C<sub>3</sub>H<sub>8</sub> mixed hydrate by Raman spectroscopy; vapor and hydrate phases**

T (°C) (±0.1)	P (MPa) (±0.01)	Vapor phase (±0.001)		Hydrate phase (±0.001)	
		CO <sub>2</sub>	C <sub>3</sub> H <sub>8</sub>	CO <sub>2</sub>	C <sub>3</sub> H <sub>8</sub>
3.7	0.97	0.895	0.105	0.521	0.479
6.3	1.08	0.838	0.162	0.486	0.514
7.6	1.22	0.819	0.181	0.786	0.214
8.5	1.32	0.767	0.233	0.504	0.496
9.5	1.35	0.700	0.300	0.672	0.328

The table illustrates that at the composition of carbon dioxide in vapor phase gradually decreased from the final state of crystallization to the final step of dissociation (0.895 to 0.700 mole fraction). One of the most remarkable observations of hydrate phase is the concentration of propane in hydrate phase which was always larger than in vapor phase as well as the initial state of experiment (0.223 mole fraction). Moreover, at 7.6°C and final state of dissociation process,



the composition of carbon dioxide in hydrate phase was notably increased. The experimental measurements were simulated by the thermodynamic model in order to clarify and reveal the differences in hydrate composition determinations and predictions. The results are provided in Table 42.

**Table 42. Hydrate composition simulation of CO<sub>2</sub>/C<sub>3</sub>H<sub>8</sub> mixed hydrate with GasHyDyn**

T (°C) (±0.1)	P (MPa) (±0.01)	Hydrate phase (±0.001)		Simulation results (sI)			Simulation results (sII)		
		CO <sub>2</sub>	C <sub>3</sub> H <sub>8</sub>	P (MPa)	CO <sub>2</sub>	C <sub>3</sub> H <sub>8</sub>	P (MPa)	CO <sub>2</sub>	C <sub>3</sub> H <sub>8</sub>
3.7	0.97	0.521	0.479	1.15	0.621	0.379	0.70	0.637	0.363
6.3	1.08	0.486	0.514	1.32	0.538	0.462	0.83	0.631	0.369
7.6	1.22	0.786	0.214	1.47	0.521	0.479	0.93	0.632	0.368
8.5	1.32	0.504	0.496	1.44	0.469	0.531	0.98	0.627	0.373
9.5	1.35	0.672	0.328	1.44	0.418	0.582	1.04	0.622	0.378
Average deviation				15%	0.141		25%	0.117	

The experimental results from Raman spectroscopic measurements were simulated by the thermodynamic modeling for both sI and sII. The predictions results show that hydrate pressure were better simulated by considering sI (average deviation 15% for sI compared to 25% for sII). However, the hydrate composition seemed to be more challenging to be comprehended. Average absolute deviation of the thermodynamic model in sII was less than sI. Nevertheless, there are some equilibrium conditions which hydrate compositions were better simulated by sI (for example at 6.3 and 8.5°C). Interestingly, two equilibrium points which were not well simulated by sI (at 7.6 and 9.5°C), had better agreements with the prediction results of sII. In other words, by considering the co-existence of both structures in this system as explained in the previous sections, and by taking into account the best simulation results for both structures, the average absolute deviation decreased to 0.078.

### 5.6.3. Raman spectra of CO<sub>2</sub>/C<sub>3</sub>H<sub>8</sub> binary hydrate at isobaric conditions

Another set of experiments on Raman spectroscopic investigations of simple CO<sub>2</sub> and C<sub>3</sub>H<sub>8</sub> hydrates as well as CO<sub>2</sub>/C<sub>3</sub>H<sub>8</sub> mixed hydrate at isobaric conditions was conducted as part of the present work. This study was conducted in cooperation with and at the Institute of Molecular Sciences at University of Bordeaux (ISM), France.

In fact, our first study at Mines Saint-Etienne about Raman spectroscopic measurements of mixed hydrates revealed the co-existence of structures I and II in CO<sub>2</sub>/C<sub>3</sub>H<sub>8</sub> mixed hydrate. Although the vapor phase was adequately analyzed, the intensities of Raman spectra of hydrate phase were sometimes weak. Therefore, we continued our investigation at the Institute of Molecular Sciences at University of Bordeaux (ISM) for complementary analyzes and evaluations, since they have a strong expertise on Raman spectroscopic measurements, and they have also more accurate devices from the same manufacturer (Horiba Jobin-Yvon).

In this study, Raman spectra were recorded with a confocal micro-Raman spectrometer LabRAM HR Evolution (Horiba Jobin Yvon, Villeneuve d'Ascq, France) using a 532 nm radiation from a diode pumped solid state laser. The incident laser beam was focused onto the sample through a microscope with a 50× objective (NA = 0.45, Olympus) allowing the sample to be probed with a micrometric spatial resolution. Scattered light was dispersed by 1800 grooves/mm holographic grating system and collected in the backscattered geometry with a CCD detector. The spectral resolution was ca. 1.3 cm<sup>-1</sup>. The calibration of the spectrometer wavenumbers was carried out using the 520.7 cm<sup>-1</sup> mode of a silicon sample. The sample temperatures were maintained at the desired value (± 0.1 K) during the acquisition by using the lab-modified temperature controlled stage (Linkam Scientific Instruments Ltd., UK), including a lab-made high-pressure optical cell equipped with a 2 mm thick sapphire optical window. The sample pressure was controlled by the ISCO High Pressure pump previously described. Such experimental conditions lead to isochoric and isobaric measurements at equilibrium since the sample cell (volume of 0.5cm<sup>3</sup>) is connected to the automatic D-260 syringe pump having a 260 cm<sup>3</sup> reservoir.

The experimental set-up was almost the same as Figure 51. The only differences were that the high pressure cell could be positioned into two directions, vertical or horizontal. In our experiment, the high pressure cell was placed in vertical position in order to distinguish visibly the vapor and hydrate (liquid) phases. The experimental procedure was as following. The reactor was washed and cleaned. At a desired pressure and ambient temperature, the gas (or gas mixture) was injected to the reactor. The gas was analyzed by Raman spectroscopy to detect the vibrational bands of each gas. Then, the reactor was purged by a vacuum pump. About 7ml of liquid ultra-pure water (Milli-Q quality) was injected into the reactor. Then, gas was re-injected through the reactor at ambient temperature (near 25°C) and 30bar. The experiment was

performed with a continuous gas flow at constant pressure (which simulates an infinite gas reservoir) to avoid any changes in the composition of feed gas. At this moment and before cooling process, the confocal of Raman spectroscopy was set on the interface of gas-water at the bottom of reactor as shown in Figure 59.

This should be note that the gas mixture has been prepared with a homemade set up composed of two syringe pumps including a D-260 High Pressure syringe pump (Teledyne Isco, Lincoln, USA) and a PM High Pressure syringe pump (Top Industrie, Vaux-le-Penil, France) with which the two gases are mixed by compression/decompression procedure (similar procedure to that describe in [205]).

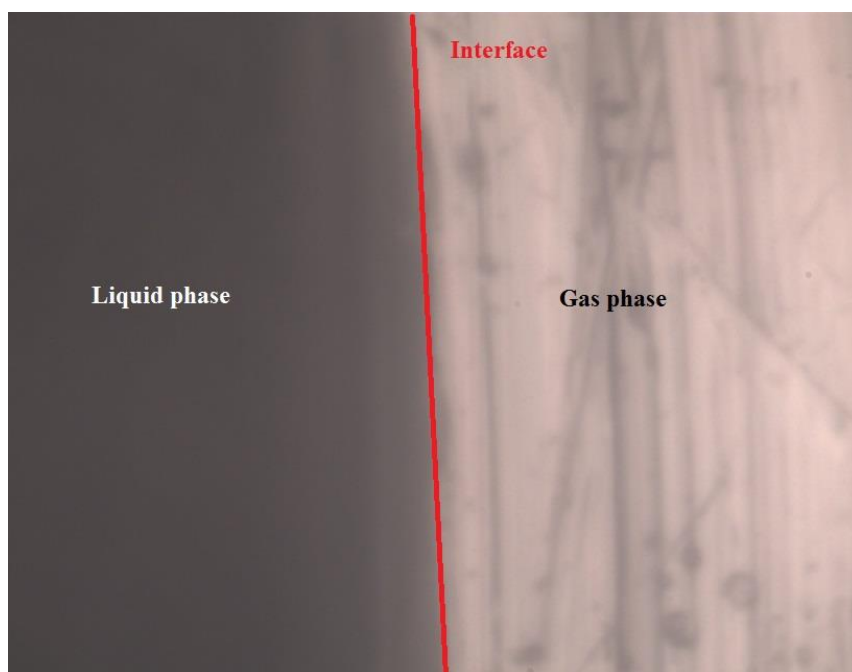


**Figure 59. A typical gas-water interface before the cooling process**

The reactor temperature was then decreased to  $-23^{\circ}\text{C}$  by liquid nitrogen to initiate and promote the hydrate crystallization. Then, the temperature was increased to  $1^{\circ}\text{C}$  to melt the ice particles. This process was repeated several times to increase the water conversion into hydrate. At the last step (at  $1^{\circ}\text{C}$ ), the hydrate phase was examined by Raman spectroscopy to identify the vibrational bands of guest molecules in hydrate phase. Finally, the results were investigated and discussed by considering the Raman shifts in gas phase, hydrate phase as well as in the mixture.

The results are presented in three figures which correspond to the vibrational bands of CO<sub>2</sub> and C<sub>3</sub>H<sub>8</sub> in gas and hydrate phases.

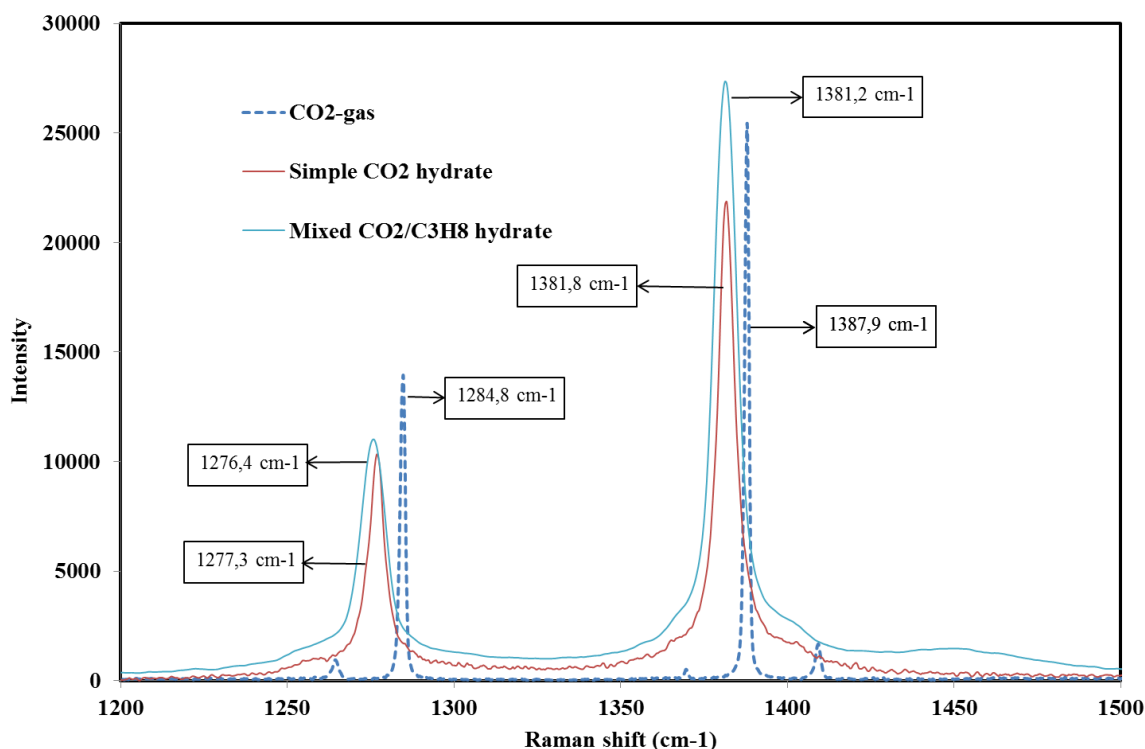


Figure 60. Vibrational bands of CO<sub>2</sub> gas, simple hydrate and CO<sub>2</sub>/C<sub>3</sub>H<sub>8</sub> mixed hydrate

Figure 60 presents the Raman spectra of CO<sub>2</sub> gas, simple CO<sub>2</sub> hydrate and CO<sub>2</sub>/C<sub>3</sub>H<sub>8</sub> mixed hydrate. The Fermi vibrational bands of CO<sub>2</sub> gas were located at 1284.8 and 1387.9 cm<sup>-1</sup> (the Raman spectra of CO<sub>2</sub> in mixed CO<sub>2</sub>/C<sub>3</sub>H<sub>8</sub> gas were taken and they were almost at the same bands of CO<sub>2</sub> gas). The simple CO<sub>2</sub> hydrate forms sI and carbon dioxide molecules commonly occupy the large cavities of this structure (5<sup>12-6</sup> cavities). Therefore, two vibrational bands of simple CO<sub>2</sub> hydrate at 1277.3 and 1381.8 cm<sup>-1</sup> could be considered as the large cavities of sI which were lowered by approximately 6-7 cm<sup>-1</sup> compared to the gas phase.

The Raman spectra of mixed CO<sub>2</sub>/C<sub>3</sub>H<sub>8</sub> hydrate were also taken and analyzed. This mixture was supposed to form sII and carbon dioxide molecules theoretically occupy the large cavities of this structure (5<sup>12-6</sup>). The CO<sub>2</sub> bands of the mixed hydrate were positioned at 1276.4 and 1381.2 cm<sup>-1</sup> which were moved between 0.6 to 0.9 cm<sup>-1</sup> to higher Raman shifts. Since the shift differences are higher than 0.5 cm<sup>-1</sup>, it could be concluded that the assumption of sII is correct.

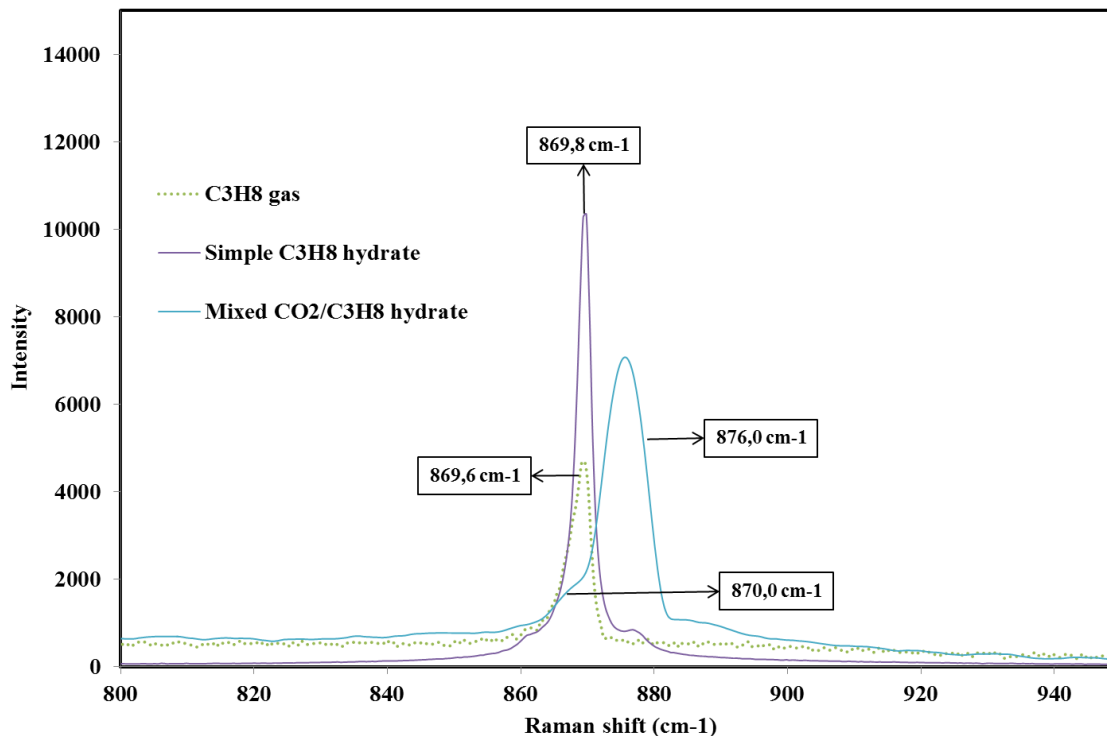


Figure 61. C-C stretch mode of propane in gas, simple hydrate and mixed hydrate

The Raman spectra of propane were taken and analyzed in two different regions; C-C stretch mode near  $870\text{ cm}^{-1}$  and C-H stretch vibration near  $2900\text{ cm}^{-1}$ . Figure 61 shows the C-C band of propane in pure gas, simple propane hydrate and  $\text{CO}_2/\text{C}_3\text{H}_8$  mixed hydrate. As clear on the figure, the Raman shift pure propane gas was at  $869.6\text{ cm}^{-1}$ . The simple propane hydrate forms sII and the propane molecules can be trapped in the  $5^{12}6^4$  cavities of sII. As aforementioned, the molecular diameter of propane is larger than the diameter of small cavities. Therefore, they cannot be encapsulated in the small cavities ( $5^{12}$ ). As a result, the C-C band of simple propane hydrate which was located at  $869.8\text{ cm}^{-1}$  is assigned to the large cavities of sII.

The  $\text{CO}_2/\text{C}_3\text{H}_8$  mixed hydrate was supposed to form sII. However, the Raman shift of C-C stretch vibration of propane in mixed hydrate was extended to higher Raman shift at  $876.0\text{ cm}^{-1}$ . This could be due to the presence of  $\text{CO}_2$  molecules in adjacent cages. Interestingly, there was another peak on the shoulder of C-C stretch of propane in mixed hydrate at  $870.0\text{ cm}^{-1}$ . This small peak might be considered as non-enclathrated propane molecules in the hydrate phase. Another possibility could be assigned to the occupancy of large cavities of sI ( $5^{12}6^2$ ) by propane molecules. The former could be more probable since the difference in Raman shifts compared to

simple hydrate is about only  $0.2 \text{ cm}^{-1}$ . The same results were obtained at C-H vibrational region of propane.

Figure 62 Presents C-H band shifts of propane in pure gas, simple propane hydrate and  $\text{CO}_2/\text{C}_3\text{H}_8$  mixed hydrate.

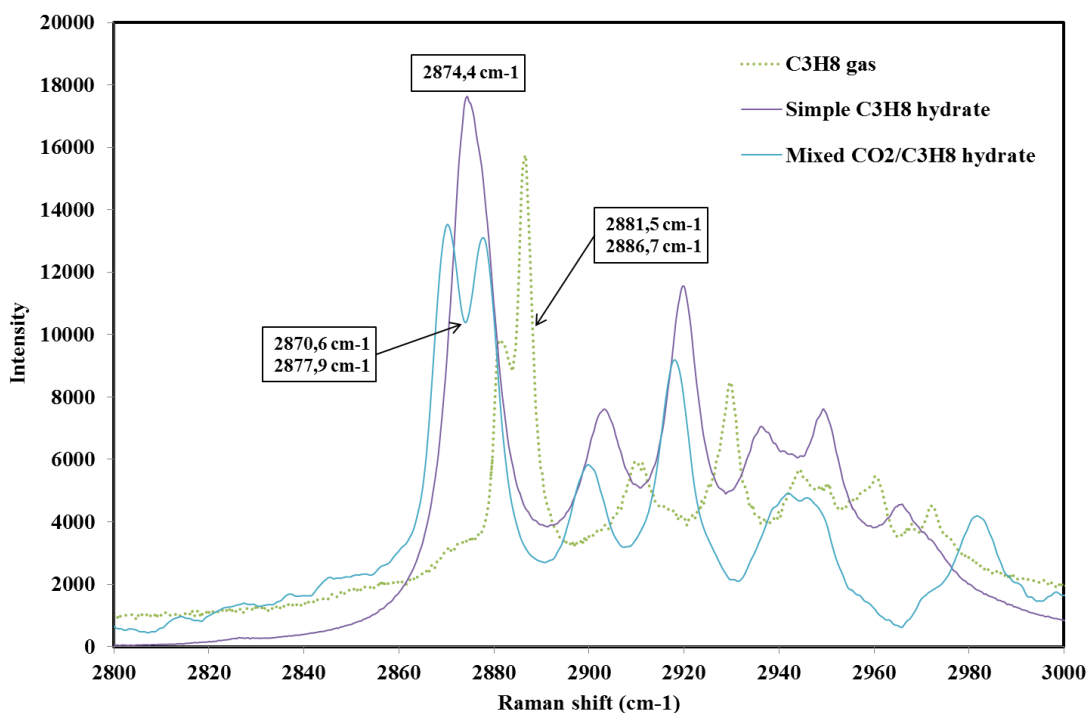


Figure 62. C-H stretch mode of propane in gas, simple hydrate and mixed hydrate

As clear on the figure, pure propane molecule in the gas phase has two main peaks of C-H stretch at  $2881.5$  and  $2886.7 \text{ cm}^{-1}$  and several bands following the shift region at  $2909.9$  and  $2929.6 \text{ cm}^{-1}$ . The Raman spectra analyses of simple propane hydrate showed that the main two peaks of propane was accumulated into one peak at  $2874.4 \text{ cm}^{-1}$ . This peak is assigned to the large cavities of sII since simple propane forms sII.

The results of Raman spectra for binary  $\text{CO}_2/\text{C}_3\text{H}_8$  mixed hydrate unexpectedly revealed a double-peak at  $2870.6$  and  $2877.9 \text{ cm}^{-1}$ . This is in accordance with the results of Raman spectra of C-C stretch of propane in binary hydrate mixture. As the Raman shifts of propane in binary hydrate were lowered by approximately  $3 \text{ cm}^{-1}$  compared to the simple propane hydrate, it could be concluded that the peak of  $2870.6 \text{ cm}^{-1}$  at mixed binary hydrate corresponds to the large cavities of sII. Thus, the second peak of mixture at  $2877.9 \text{ cm}^{-1}$  could be assigned to whether the

large cavities of sI or propane molecules trapped between the hydrate particles (non-encapsulated molecules in hydrate structure).

Since the results of Raman spectra at C-C stretch elucidated that the co-existence of both structures I and II is more probable, it was concluded that binary CO<sub>2</sub>/C<sub>3</sub>H<sub>8</sub> hydrate at high composition of carbon dioxide in the vapor phase might form both structures. These investigations could explain why hydrate composition significantly changed during our experiments at quick and slow crystallization procedures (the results obtained in section 5.4.1 and Figure 42).

Moreover, this co-existence of sI and sII in binary CO<sub>2</sub>/C<sub>3</sub>H<sub>8</sub> mixed hydrate is also a reason to explain why thermodynamic modeling was not capable to predict adequately the guest composition in hydrate phase regarding to binary CO<sub>2</sub>/C<sub>3</sub>H<sub>8</sub> mixed hydrate. As a matter of fact, our simulation results demonstrated that, when phase transition or co-existence of structures occurs in a system, the thermodynamic model is no longer accurate since an assumption of only one structure is considered. In addition, our results elucidated that, when phase transition happens in a system, the guest distribution in hydrate phase significantly changes due to different occupation of cavities. Thus, thermodynamic modeling cannot satisfactorily predict guest composition in hydrate structure. Failure to predict these phenomena such as structural transition or co-existence of structures is one of the main challenges for applying successfully the thermodynamic models.

In conclusion, the evidence obtained by Raman spectroscopy in this study show that hydrate phase could be well characterized by this technique in order to measure directly the properties and molecular aspects of clathrate hydrates such as hydrate structure, cage occupancy, hydrate composition etc.

## **6. Flash calculations**

The results obtained and presented in the previous chapters revealed that the crystallization rate could affect the final state of the system. Therefore, thermodynamic modeling was taken into account to clarify the exact order of magnitude. However, the comparison provided by thermodynamic modeling does not seem to be sufficient to reach a clear conclusion. In fact, thermodynamic modeling provides the composition of first nuclei at first vapor-liquid-hydrate

equilibrium point. The hydrate composition at this point could not be experimentally determined due to difficulties in measurements. Therefore, a significant volume of hydrate was formed to measure accurately hydrate composition. Given the fact that hydrate formation is a non-stoichiometric process, the hydrate composition measurements provide only an average value which is not in accordance with thermodynamic modeling. Thus, without considering the crystallization process, the thermodynamic modeling could deviate from experimental results.

In this chapter, the motivation is to take into account both thermodynamic modeling and non-stoichiometric crystallization process by flash calculation algorithms in order to simulate the phase equilibria of mixed gas hydrates as well as hydrate volume and composition.

### 6.1. Standard flash calculations

Flash calculations are an integral part of all process engineering calculations. They are required when the aim is to determine the amount and composition of components in co-existing phases at given temperature, pressure and overall composition of feed. The most common two-phase flash calculations are vapor-liquid equilibrium flash [206]. A simple case of this situation is schematically shown in Figure 63.

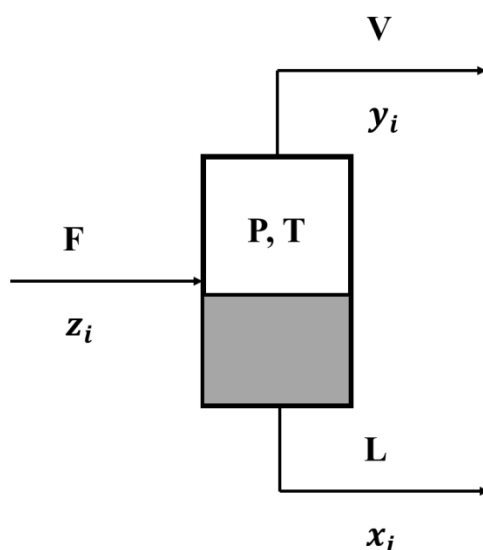


Figure 63. Isothermal flash calculation



In the figure,  $F$ ,  $V$  and  $L$  are flow of feed, vapor and liquid, respectively.  $P$  and  $T$  stand for temperature and pressure.  $z_i$ ,  $y_i$  and  $x_i$  correspond to the composition of component  $i$  in feed, gas and vapor. At given temperature and pressure and by knowing the feed properties:

$$F = V + L \quad (38)$$

$$z_i F = y_i V + x_i L \quad (39)$$

by defining  $K_i = \frac{y_i}{x_i}$  the following equations can be found:

$$x_i = \frac{F z_i}{V(K_i - 1) + F} \quad (40)$$

$$y_i = \frac{F z_i K_i}{V(K_i - 1) + F} \quad (41)$$

Given the fact that  $\sum(x_i - y_i) = 0$  and by combining the last two equations:

$$\sum(y_i - x_i) = \frac{F z_i K_i - F z_i}{V(K_i - 1) + F} = 0 \quad (42)$$

$K_i$  is ratio of fugacity coefficients and can be calculated by Raoult's law, Lewis fugacity rule or Henry's law [207]. In a generalized case, the Gibbs energy minimization, through the tangent plane criterion is widely used [122].

To solve equation 42, an iteration procedure is required.  $K_i$  at given temperature and pressure is defined. A value is then assumed for  $V$  and check by equation 42. If the value does not satisfy the equation, another value for  $V$  is chosen. This iteration is repeated in order to achieve a value which satisfies equation 42. The composition of vapor and liquid phases is then calculated.

## 6.2. Flash calculations for clathrate hydrates

Bishnoi et al. [208] presented a methodology for the isobaric-isothermal flash calculations for hydrate systems. They stated that these computations were never reported previously. Based on the methodology, they calculated the amounts and the composition of all co-existing phases by minimizing Gibbs free energy. The distribution ratio of component  $i$  in phase  $j$  was calculated as following:

$$K_{ij} = \frac{\varphi_{ir}}{\varphi_{ij}} \quad (43)$$

$r$  is the reference state.  $\varphi_{ij}$  for non-hydrate phases can be calculated from EoS and for hydrate phase as below:

$$\varphi_{ij} = \frac{f_{ij}}{x_{ij}P} \quad (44)$$

The fugacity of water is determined from van der Waals and Platteeuw approach [111] and for other components in hydrate phase is equal to the fugacity of the reference state. Finally the equilibrium equations (46 and 47) for a system are provided by defining a stability variable ( $\theta_j$ ) and combining with mass balance and mole fraction summation equations:

$$\theta_j = \frac{f_{ij}}{f_{ir}} \quad (45)$$

$$\frac{x_{ij}}{x_{ir}} = K_{ij}e^{\theta_j} \quad (46)$$

$$\alpha_j\theta_j = 0 \quad (47)$$

where  $\alpha_j$  is the phase fraction. They examined the methodology for hydrate systems containing water-methane-propane and mixtures of oil condensate and varying amounts of water.

The same similar approach was proposed by Cole and Goodwin [209] and they calculated the hydrate phase properties and hydrate composition in a cyclopropane-water system, temperature ranging from 273 to 280K. Their work included the readjustment of hydrate model to a form compatible with the Michelsen flash algorithm [210,211], to provide precise definitions for the fugacities of all the components in hydrate phase as functions of the overall composition of the hydrate phase [209]. However, due to lack of experimental data for hydrate composition and volume, the approach has been not well evaluated.

Segtovich et al. [212] proposed an algorithm for phase equilibrium calculations involving hydrates to apply stability analysis simultaneously to flash calculations. Their study was based on the algorithms of Gupta et al. [213] and Ballard and Sloan [214], with modifications that contribute to both speed and robustness of these calculations. The fugacity coefficients of all components in hydrate phase were calculated from thermodynamic modeling at given conditions. The algorithm was then used to simulate the pressure-temperature diagrams of hydrate systems containing vapor, liquid and hydrate phases [212].

Tavasoli and Feyzi [215] proposed a three-phase flash algorithm based on the equality of fugacities of components in all vapor, liquid and hydrate phases. To model the gas and liquid phases, Valderrama modification of the Patel-Teja equation of state [216] combined with non-density dependent mixing rules [217] were used and hydrate phase was considered as an ideal solid solution. The calculation procedures start with vapor-liquid equilibrium flash calculations by Rachford-Rice method at temperature and pressure of the system. The guest composition in hydrate phase is determined at the operating pressure. The fugacities of water and guest molecules in hydrate phase are then calculated. Given the fact that hydrate composition changes during hydrate formation, a new operating pressure is predicted. The equilibrium pressure at known temperature is determined. Finally, the phase fraction of each phase is calculated. They compared the algorithm with CSMGem and HWHYD thermodynamic prediction tools and stated that the convergence ability is an advantage of the proposed algorithm compared to the mentioned thermodynamic prediction tools.

As aforementioned, due to serious lack of experimental data concerning guest composition in hydrate phase as well as phase fractions, these algorithms of isothermal flash calculations cannot be well assessed.

In conclusion, since hydrate formation is a non-stoichiometric process, the final state of crystallization is not at thermodynamic equilibrium. Therefore, utilizing partition coefficient is no longer valid. This is why non-equilibrium flash calculations can be taken into account.

### **6.3. Non-equilibrium flash calculations**

The hydrate phase in the methodology of non-equilibrium flash calculation is considered as a nonhomogeneous phase and it is not a consequence of crystallization process. In addition, although the hydrate formation occurs under non-equilibrium conditions, the local thermodynamic can be assumed and consequently, the thermodynamic equilibrium calculations are considered.

Moreover, in this approach, the change in guest composition in hydrate phase and hydrate volume increase are taken simultaneously into account as the guest composition in gas phase changes during crystallization due to gas consumption (this should be noted that constant volume in a batch condition is considered in this approach). Thus, it is required to discretize the crystal

growth in the calculations. When an amount of hydrate is formed, it can remain in the system as metastable, and can be removed from the calculations. Thus, this approach can be considered as successive flash calculations [122]. Figure 64 illustrates two different mechanisms encountered for hydrate crystallization growth.

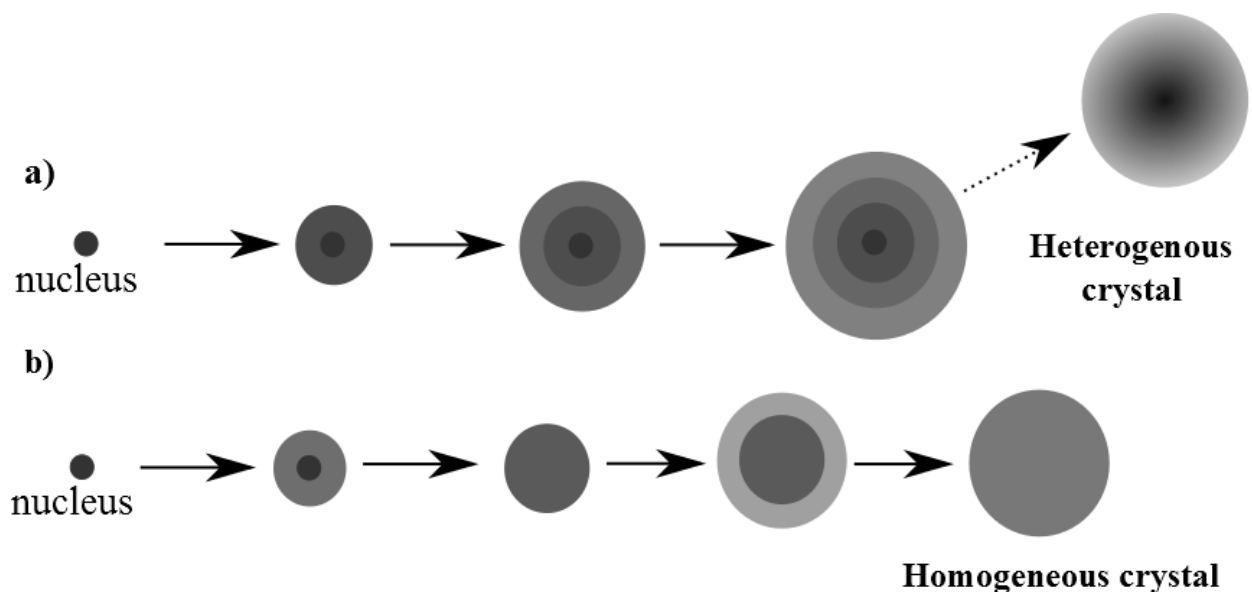


**Figure 64. Two mechanisms for hydrate growth [122]**

The first mechanism in the figure (a) represents a non-stoichiometric crystallization process. The guest composition in vapor phase changes as a result of gas consumption during crystal growth stages. The hydrate composition changes as well and it can be predicted by thermodynamic equilibrium at only the surface of crystal and its surrounding liquid. This means that at each stage, the core of hydrate crystal and other layers are not at thermodynamic equilibrium with the surrounding liquid. At the end of crystallization, the cavity occupations in the hydrate crystal are continuously developed from the core to the last hydrate layer. This situation can be occurred at high driving force, since crystal are growing at local thermodynamic equilibrium and it is too quick for the most stable phase to appear. This could signify the startup of a crystallization process like production in pipelines[122].

In the second mechanism in Figure 64 (b), there is a reorganization of hydrate crystals at each layer during the crystallization process. Although this process is almost similar to the standard flash calculation, the guest composition in hydrate phase is not a result of initial gas composition since the gas consumption is taken into account.

Bouillot and Herri [136] developed a framework for clathrate hydrate flash calculations at constant volume and given temperature considering both stoichiometric and non-stoichiometric crystallizations. Figure 65 presents the flash calculations algorithm for non-stoichiometric crystallization.

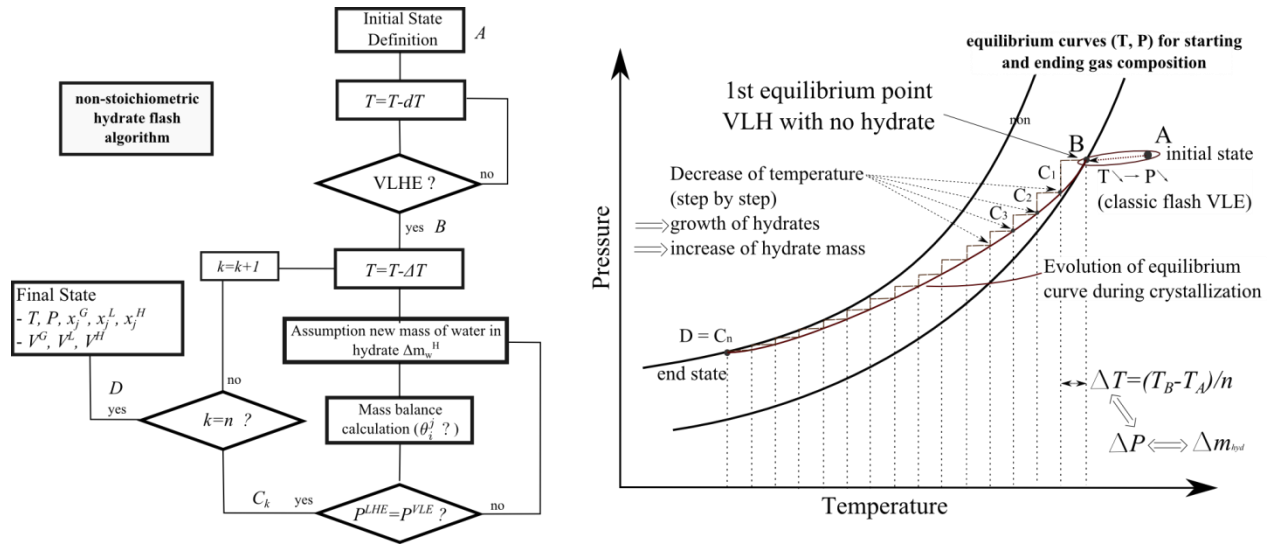


Figure 65. Non-stoichiometric flash calculations, algorithm and procedure [122]

The process starts after gas and liquid injection at point A (Vapor-liquid equilibrium) which is located outside of hydrate forming region. At this point, flash calculations by decreasing stepwise the temperature are performed to find a pressure which is equal at both vapor-liquid and liquid-hydrate equilibrium conditions (point B). This is the first liquid-hydrate equilibrium point and crystallization begins from this point. The crystal growth process is then discretized into several steps and successive flash calculations are implemented. The iteration number,  $n$ , gives the temperature step ( $\Delta T = (T_B - T_D)/n$ ). At each iteration ( $k$ ), a new mass of water in hydrate phase ( $\Delta m_{w,k}^H$ ) is considered and it can be adjusted during successive flash calculations. At a known  $\Delta m_{w,k}^H$ , the hydrate volume ( $V^H$ ) can be determined by the fact that density of empty hydrate only based on water molecules ( $\beta$  reference state) is  $790 \text{ kg/m}^3$  for sI and  $785 \text{ kg/m}^3$  for sII. Therefore:

$$V^H = \sum_k \Delta V_k^H = \sum_k \frac{\Delta m_{w,k}^H}{\rho^{H-\beta}} \quad (48)$$

The amount of guest molecules in the hydrate phase can be calculated from the occupancy factor. The occupancy factor can be determined from guest composition in the liquid phase at the beginning of iteration or after it. The calculation process could be more complicated if the second case is taken into account. Nevertheless, Bouillot and Herri [136] stated that with more than 20 iterations, it is sufficient for the two approaches to converge. Therefore, the first case can be utilized.

To verify the assumed new mass of water in hydrate is correct or not, a vapor-liquid flash calculation is performed to obtain the pressure  $P^{VLE}$ . If this value is equal to the liquid-hydrate equilibrium pressure,  $P^{LHE}$ , means that the assumed new mass of water in hydrate ( $\Delta m_{w,k}^H$ ) is correct. The procedure is then repeated for each iteration to obtain the final temperature ( $T_D$ ). The hydrate volume and guest composition in vapor and hydrate phases are also determined.

This algorithm can be also used to converge to a stoichiometric crystallization process. For that, a loop on the occupancy factor is also needed. This loop corresponds to the equality of the occupancy factor at the end of crystallization and thermodynamic equilibrium predicted considering the surrounding liquid phase. The algorithm is illustrated in Figure 66.

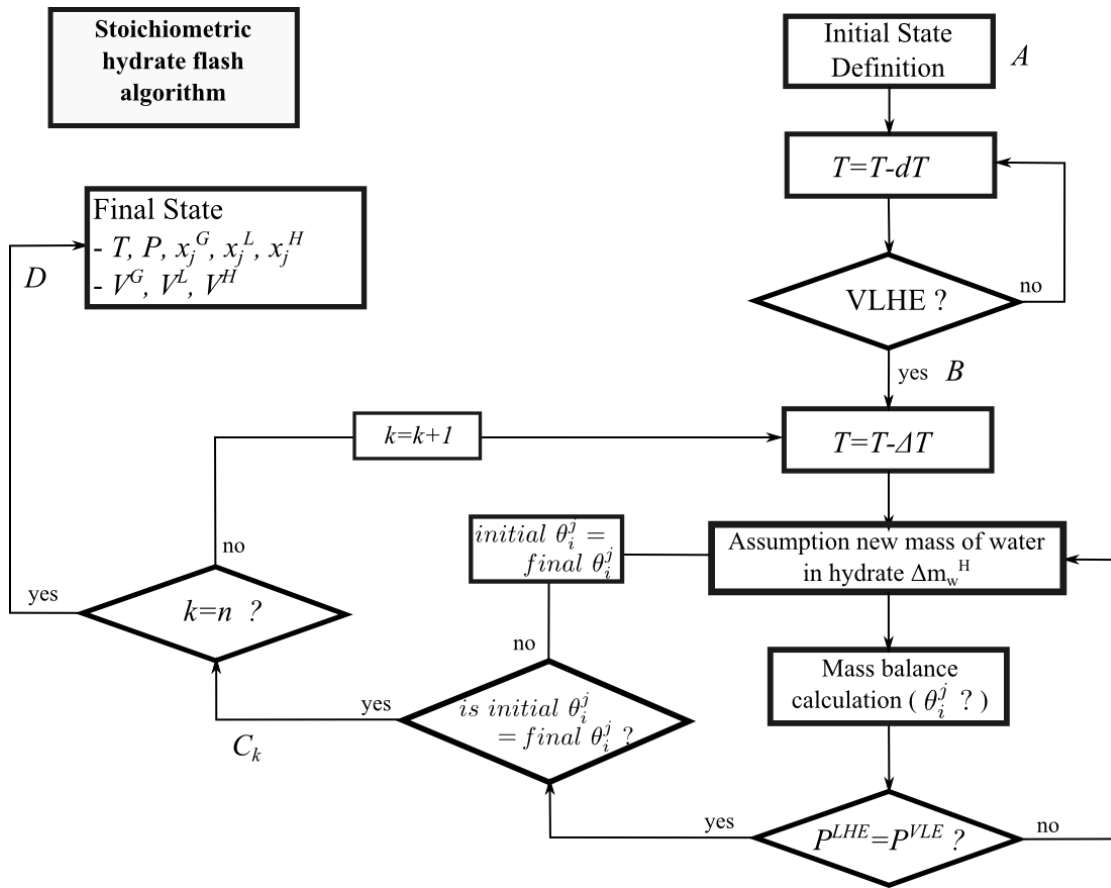


Figure 66. Stoichiometric flash algorithm [122]

#### 6.4. Flash calculations results

In this section, our experimental data for  $N_2$ - $CO_2$ - $C_2H_6$  mixed hydrates at quick and slow crystallization were compared to Bouillot and Herri's isochoric flash algorithm concerning homogenous and heterogeneous structures [136]. Table 43 presents the final state parameters (temperature, pressure, guest distribution in vapor and hydrate phases, hydrate volume and water conversion) according to the different rates of crystallization with the same initial operational conditions. The thermodynamic path of hydrate formation (for both crystallization procedures) is also shown in Figure 67.

Table 43. Experimental results for N<sub>2</sub>-CO<sub>2</sub>-C<sub>2</sub>H<sub>6</sub> mixed hydrates at final state of quick and slow crystallization

Method	Final state		Final gas composition			Final hydrate composition			V <sub>f</sub> (cc)
	T <sub>f</sub> (°C)	P <sub>f</sub> (bar)	CO <sub>2</sub>	N <sub>2</sub>	C <sub>2</sub> H <sub>6</sub>	CO <sub>2</sub>	N <sub>2</sub>	C <sub>2</sub> H <sub>6</sub>	
Quick	1.8	11.3	0.198	0.428	0.374	0.246	0.072	0.682	173.1
Slow	1.1	10.2	0.221	0.477	0.302	0.228	0.070	0.702	179.6
Absolute uncertainty	±0.2	±0.1	±0.001			±0.003			±0.4

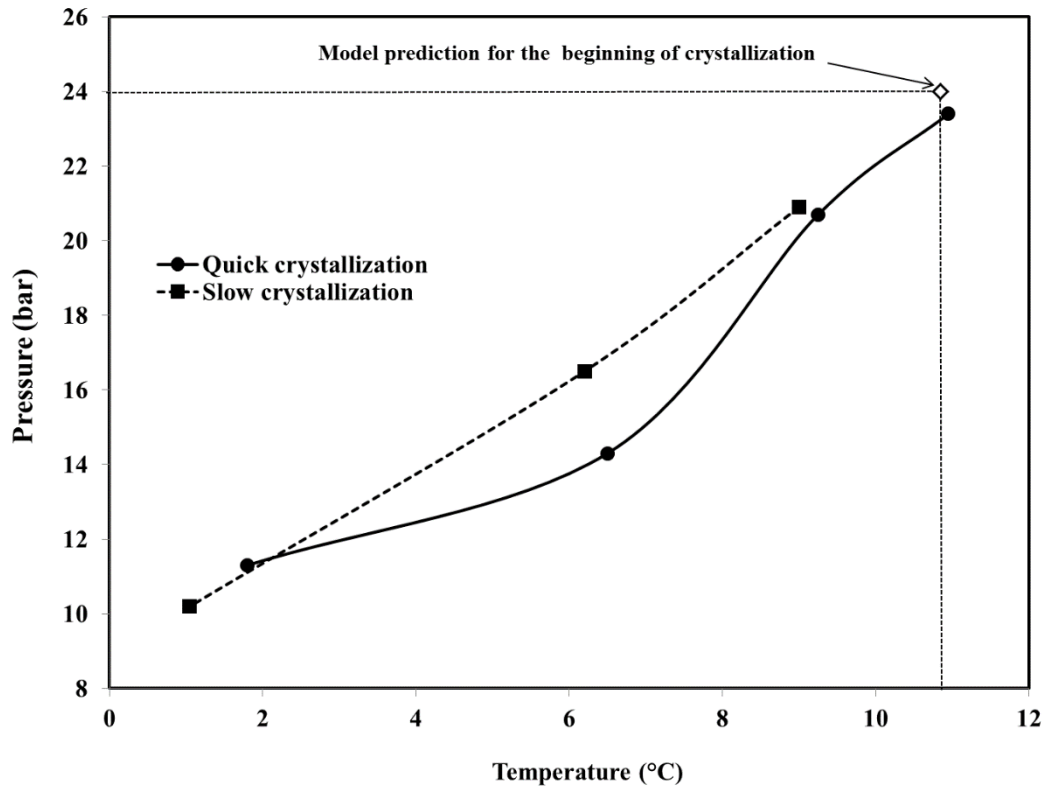


Figure 67. Thermodynamic path of mixed N<sub>2</sub>-CO<sub>2</sub>-C<sub>2</sub>H<sub>6</sub> hydrate at slow and quick crystallization

Before discussing the isochoric flash calculation results, it should be noted that the results of thermodynamic modeling in Table 37 provided overall evidence about the hydrate structure of N<sub>2</sub>-CO<sub>2</sub>-C<sub>2</sub>H<sub>6</sub> at the operational condition of this work. The average absolute deviation of the thermodynamic modeling for hydrate pressure concerning sI was considerably lower than sII



(about 10% for sI compared to more than 200% for sII). Therefore, for the flash calculation procedures, sI is considered.

The results of isochoric flash algorithms (heterogeneous and homogenous frameworks as illustrated in Figure 64) for quick crystallization process are presented in Table 44 and Table 45.

**Table 44. Experimental versus prediction results of N<sub>2</sub>-CO<sub>2</sub>-C<sub>2</sub>H<sub>6</sub> mixed hydrates at quick crystallization rate by considering non-stoichiometric and stoichiometric flash algorithms**

Method	Experimental results			Non-stoichiometric				Stoichiometric		
				N=8		N=20				
Quick	T <sub>f</sub> (°C) (±0.2)	P <sub>f</sub> (bar) (±0.1)	V <sub>H</sub> (cc) (±0.4)	P <sub>f</sub> (bar)	V <sub>H</sub> (cc)	P <sub>f</sub> (bar)	V <sub>H</sub> (cc)	P <sub>f</sub> (bar)	V <sub>H</sub> (cc)	
		1.8	11.3	174.2	11.9	150.2	11.8	150.6	11.4	158.2
		Average deviation			5.3%	13%	4.4%	13%	0.9%	9%

**Table 45. Experimental hydrate composition of N<sub>2</sub>-CO<sub>2</sub>-C<sub>2</sub>H<sub>6</sub> mixed hydrates at quick crystallization versus non-stoichiometric and stoichiometric flash algorithms**

Method	Exp. Final hydrate composition (±0.003)			Non-stoichiometric						Stoichiometric			
				N=8			N=20						
Quick	CO <sub>2</sub>	N <sub>2</sub>	C <sub>2</sub> H <sub>6</sub>	CO <sub>2</sub>	N <sub>2</sub>	C <sub>2</sub> H <sub>6</sub>	CO <sub>2</sub>	N <sub>2</sub>	C <sub>2</sub> H <sub>6</sub>	CO <sub>2</sub>	N <sub>2</sub>	C <sub>2</sub> H <sub>6</sub>	
		0.246	0.072	0.681	0.207	0.052	0.741	0.208	0.053	0.739	0.224	0.069	0.706
		Average deviation			0.039	0.020	0.060	0.038	0.019	0.058	0.022	0.003	0.025

The prediction results of all frameworks showed that the hydrate formation should start at 10.85°C and 24bar (see Figure 67). In other words, the first hydrate crystal in the bulk should appear at this condition. Therefore, this is the first three-phase equilibrium point (Vapor-Liquid-Hydrate) of N<sub>2</sub>-CO<sub>2</sub>-C<sub>2</sub>H<sub>6</sub> mixture which is point B on Figure 65. The crystal growth initiated from this step and it continued to the final step (point D on Figure 65). N is the number of iterations and it defines heterogeneity of the hydrate phase. To be clear, the lower number of iterations means the more heterogeneous the hydrate phase. The simulation results of hydrate final pressure and volume (Table 44) show that for the non-stoichiometric framework, the number of iterations had only a slight effect on the prediction of final state. The average deviation

of final hydrate pressure was 5.3% for N=8 compared to 4.4% for N=20. The final hydrate volume was simulated by an average deviation of 13% for both numbers of iterations. The hydrate final composition was also simulated by the non-stoichiometric algorithm with 8 and 20 iterations and the results were almost the same with an average deviation of 0.039.

The simulation results based on the stoichiometric framework revealed surprising investigations. The hydrate final pressure and composition were adequately predicted. The average deviation of pressure and composition were 0.9% and 0.017, respectively. Moreover, the final hydrate volume was predicted by an average deviation of 9% which is slightly less than the deviation of the non-stoichiometric flash algorithm. This means that thermodynamic equilibrium has been probably achieved for N<sub>2</sub>-CO<sub>2</sub>-C<sub>2</sub>H<sub>6</sub> mixed hydrate at high driving force and the hydrate crystal seemed to be homogenous.

The experimental results of N<sub>2</sub>-CO<sub>2</sub>-C<sub>2</sub>H<sub>6</sub> mixed hydrate at slow crystallization rate were also simulated by non-stoichiometric (N=10) and stoichiometric frameworks and they are presented in Table 46 and Table 47.

**Table 46. Experimental versus prediction results of N<sub>2</sub>-CO<sub>2</sub>-C<sub>2</sub>H<sub>6</sub> mixed hydrates at slow crystallization rate by considering non-stoichiometric and stoichiometric flash algorithms**

Method	Experimental results			Non-stoichiometric (N=10)		Stoichiometric	
Slow	T <sub>f</sub> (°C) (±0.2)	P <sub>f</sub> (bar) (±0.1)	V <sub>H</sub> (cc) (±0.4)	P <sub>f</sub> (bar)	V <sub>H</sub> (cc)	P <sub>f</sub> (bar)	V <sub>H</sub> (cc)
	1.1	10.2	179.6	11.4	156.5	10.8	165.4
	Average deviation			11.8%	13%	5.8%	8%

**Table 47. Experimental hydrate composition of N<sub>2</sub>-CO<sub>2</sub>-C<sub>2</sub>H<sub>6</sub> mixed hydrates at quick crystallization versus non-stoichiometric and stoichiometric flash algorithms**

Method	Exp. Final hydrate composition (±0.003)			Non-stoichiometric (N=10)			Stoichiometric		
Slow	CO <sub>2</sub>	N <sub>2</sub>	C <sub>2</sub> H <sub>6</sub>	CO <sub>2</sub>	N <sub>2</sub>	C <sub>2</sub> H <sub>6</sub>	CO <sub>2</sub>	N <sub>2</sub>	C <sub>2</sub> H <sub>6</sub>
	0.228	0.070	0.702	0.208	0.054	0.738	0.226	0.072	0.702
	Average deviation			0.020	0.016	0.036	0.002	0.002	0

The prediction results of slow crystallization process were as we expected. The final hydrate pressure was better simulated by stoichiometric flash algorithm by an average deviation of 5.8% which is almost two times less than by non-stoichiometric algorithm (11.8%). Furthermore, the final hydrate volume was also satisfactorily predicted by stoichiometric framework (average deviation was 8%).

The final hydrate composition was efficiently predicted by stoichiometric framework. The average deviation was almost zero. This means that at slow crystallization rate which the kinetic effects are not significant, the hydrate phase was completely homogenous.

Finally, all the frameworks provided relatively precise results concerning final hydrate pressure and composition. In the case of hydrate volume, the stoichiometric algorithm presented slightly more accurate results compared to non-stoichiometric framework. To sum up, it could be concluded that  $N_2$ - $CO_2$ - $C_2H_6$  mixed hydrate was not significantly affected by kinetics. However, since the investigation of hydrate crystallization at low driving force is time-consuming and several problems might be faced such as leakage etc., these algorithms could provide and propose a comprehensive insight into the hydrate nucleation and growth (crystal reorganization and homogeneity), final state of crystallization as well as hydrate phase properties. Moreover, they could provide some fundamental answers when the question of non-equilibrium crystallization of mixed hydrate arises.

## Conclusions, final remarks and perspectives

In this work, crystallization of mixed gas hydrates has been investigated under equilibrium and non-equilibrium conditions. Mixed gas hydrates including  $\text{CH}_4\text{-C}_2\text{H}_6\text{-C}_3\text{H}_8\text{-nC}_4\text{H}_{10}\text{-CO}_2\text{-N}_2$  were experimentally studied not only at equilibrium but also during the crystallization at non-equilibrium conditions. For that purpose, two procedures with different rates of crystallization (with the same initial conditions) were used in a batch-type reactor; quick and slow. The results included the classical temperature-pressure-vapor composition (P-T-y), as well as hydrate phase properties such as hydrate composition and volume, storage capacity, density, hydration number and water conversion. In addition, a thermodynamic modeling based on van der Waals and Platteeuw approach and Kihara potential approach was used to simulate the hydrate pressure and composition and to clarify the assumptions and hypothesis. Furthermore, an important and comprehensive review of the literature on hydrate composition has been done in order to overview, summarize and classify the experimental data on guest composition and to compare them to thermodynamic modeling. Indeed, this work aims to investigate:

- 1) Is the final hydrate phase at thermodynamic equilibrium?
- 2) Does the solid phase minimize Gibbs free energy?
- 3) What are the influences of kinetic phenomena on the hydrate formation of gas mixtures?
- 4) How is guest distribution in hydrate phase and how hydrate properties vary according to the rate of crystallization?

Experimental results showed that equilibrium pressures at final state are dissimilar with respect to the crystallization rate. Moreover, the crystallization rate also affected guest composition in solid phase, resulting the different hydrate composition at final state. The composition of heavier hydrocarbon (propane and butane) demonstrated that the enclathration of heavier molecules at the start of crystallization plays more important role than near the final state. Another interesting result was the hydrate volume. At slow crystallization rate which is similar to a steady state process, hydrate volume was significantly lower than at quick crystallization rate. This is important because the amount of kinetic hydrate inhibitors (KHI) or anti-agglomerants (AA) in flow assurance concerns depends on the hydrate volume. Therefore, obtained result in this study could help to adjust more accurately the amount of these inhibitors. In addition, in gas storage

and transportation via hydrate-based applications, the key parameter is storage capacity. In this work, the results revealed that at slow crystallization, the storage capacity is larger than at quick crystallization, meaning that more gas can be stored in solid phase.

The results of thermodynamic modeling showed that the hydrate crystallization of a gas mixture is usually closer to the thermodynamic equilibrium at slow crystallization rates where the impact of kinetics is slight. However, the impact of kinetic considerations in both crystallization processes could not be ignored. Therefore, the hydrate formation of gas mixtures is clearly occurs at non-equilibrium conditions. In addition, a new set of Kihara parameter for propane was obtained and compared to the other sets provided by other authors. A wide range of experimental equilibrium data from literature and our experiments (198 equilibrium points) have been used to investigate the accuracy of the thermodynamic model based on our new set of Kihara parameters and also Kihara parameters from the other researchers.

Despite experimental difficulties in hydrate composition measurement, there is still valuable experimental data in the literature. This information could be very useful to develop and improve the processes involving hydrate formation and dissociation. Unfortunately, there is not any reference in the literature which overviews and summarizes this information. Hence, we attempted to collect and classify the experimental data on guest composition in hydrate phase at equilibrium conditions in the open literature. Then, we investigated the capability of thermodynamic modeling to simulate hydrate composition. The modeling results revealed the drawbacks and advantages of the thermodynamic model in terms of hydrate composition, structure, phase transition as well as kinetic considerations.

Furthermore, in the present manuscript, we provided qualitative and quantitative investigations of  $\text{CO}_2/\text{C}_3\text{H}_8$  mixed hydrate in order to study enclathration of guest molecules in gas and hydrate phases as well as hydrate structure. For gas and hydrate composition measurements, Raman spectroscopy was calibrated. The results showed that there might be a co-existence of both sI and sII at high concentrations of  $\text{CO}_2$ , which was not theoretically expected.

In addition, non-equilibrium flash algorithms adequately predicted the guest composition in hydrate phase and pressure of  $\text{CO}_2/\text{N}_2/\text{C}_2\text{H}_6$  mixture and provide vital information about crystal reorganization and homogeneity. These frameworks can be also very advantageous not only for

academic purposes but also for industry since they can provide final hydrate volume which is definitely essential for hydrate-based applications as well as flow assurance.

In conclusion, the authors suggest that in all applications of mixed clathrate hydrates where the thermodynamic equilibrium is taken into account, the kinetic effects could be a vital key to re-design the approach to have more accurate and realistic data.

Finally, the following suggestions are recommended for the continuation of this work:

1) Since the rate of crystallization affects the final state of equilibrium, more comprehensive experimental data is still required to investigate the non-equilibrium thermodynamics of mixed gas hydrates. Moreover, this database could be used to develop the thermodynamic model or improve the model parameters like Kihara potential of butane.

2) There is still a lack of data concerning storage capacity, volume and composition of hydrates. Thus, it is essential to extend the experimental database in order to develop more efficiently the hydrate-based applications like gas separation or storage.

3) As a matter of fact, clathrate hydrate formation normally occurs at high pressure and low temperature. Since providing these conditions increases operational costs for hydrate-based applications, additives can be used to not only normalize these conditions, but also to enhance the hydrate formation rate. Thus, we suggest studying effects of additives such as sodium dodecyl sulfate (SDS) or cyclopentane (CP) on hydrate formation, dissociation and stability.

4) To the best of our knowledge, it is the first time that the co-existence of sI and sII in  $\text{CO}_2/\text{C}_3\text{H}_8$  mixed hydrate is experimentally discovered and investigated. However, more investigations are still required to evaluate and determine the occupation small and large cavities of both structures. In addition, the portion of each structure is of great interest. Therefore, it is recommended to couple microscopic tools such as Raman spectroscopy, Nuclear magnetic resonance (NMR) and X-ray diffraction (XRD) in order to provide further quantitative and qualitative information about enclathration of guest molecules in hydrate structure, cage occupancy as well as phase transition.

## References

- [1] E.D. Sloan, C.A. Koh, *Clathrate Hydrates of Natural Gases*, 3rd ed., CRC Press, 2007.
- [2] J.F. Gabitto, C. Tsouris, *Physical Properties of Gas Hydrates: A Review*, *J. Thermodyn.* (2010). doi:10.1155/2010/271291.
- [3] E.D. Sloan, *Fundamental principles and applications of natural gas hydrates*, *Nature*. (2003). doi:10.1038/nature02135.
- [4] M. v. Stackelberg, *Feste Gashydrate*, *Naturwissenschaften*. 36 (1949) 359–362. doi:10.1007/BF00627172.
- [5] W.F. Kuhs, B. Chazallon, P.G. Radaelli, F. Pauer, *Cage occupancy and compressibility of deuterated N<sub>2</sub>-clathrate hydrate by neutron diffraction*, *J. Incl. Phenom. Mol. Recognit. Chem.* 29 (1997) 65–77. doi:10.1023/A:1007960217691.
- [6] W.F. Kuhs, B. Chazallon, A. Klapproth, F. Pauer, *Filling-Isotherms in Clathrate-Hydrates*, *Rev. High Press. Sci. Technol.* 7 (1998) 1147–1149. doi:10.4131/jshpreview.7.1147.
- [7] B. Chazallon, W.F. Kuhs, *In situ structural properties of N<sub>2</sub>-, O<sub>2</sub>-, and air-clathrates by neutron diffraction*, *J. Chem. Phys.* 117 (2002) 308–320. doi:10.1063/1.1480861.
- [8] E.D. Sloan, *A changing hydrate paradigm—from apprehension to avoidance to risk management*, *Fluid Phase Equilibria*. 228 (2005) 67–74. doi:10.1016/j.fluid.2004.08.009.
- [9] J.L. Creek, *Efficient Hydrate Plug Prevention*, *Energy Fuels*. 26 (2012) 4112–4116. doi:10.1021/ef300280e.
- [10] M.A. Kelland, T.M. Svartaas, L. Dybvik, *Studies on New Gas Hydrate Inhibitors*, in: *Society of Petroleum Engineers*, 1995. doi:10.2118/30420-MS.
- [11] C. Cooley, B.K. Wallace, R. Gudimetla, *Hydrate Prevention and Methanol Distribution on Canyon Express*, in: *Society of Petroleum Engineers*, 2003. doi:10.2118/84350-MS.
- [12] P.K. Notz, *The Study of Separation of Nitrogen from Methane by Hydrate Formation Using a Novel Apparatus*, *Ann. N. Y. Acad. Sci.* 715 (1994) 425–429. doi:10.1111/j.1749-6632.1994.tb38855.x.
- [13] A. Perrin, O.M. Musa, J.W. Steed, *The chemistry of low dosage clathrate hydrate inhibitors*, *Chem. Soc. Rev.* 42 (2013) 1996–2015. doi:10.1039/C2CS35340G.
- [14] L.W. Clark, L.M. Frostman, J. Anderson, *Low Dosage Hydrate Inhibitors (LDHI): Advances in Flow Assurance Technology for Offshore Gas Production Systems*, in: *International Petroleum Technology Conference*, 2005. doi:10.2523/IPTC-10562-MS.

- [15] M.A. Kelland, History of the Development of Low Dosage Hydrate Inhibitors, *Energy Fuels*. 20 (2006) 825–847. doi:10.1021/ef050427x.
- [16] A. Memon, H.-J. Ng, Effectiveness of Low-Dosage Hydrate Inhibitors and their Rheological Behavior for Gas Condensate/Water Systems, *J. Chem. Eng. Data*. 60 (2015) 293–298. doi:10.1021/je500590y.
- [17] C. Zou, Chapter 14 - Natural Gas Hydrate, in: *Unconv. Pet. Geol. Second Ed.*, Elsevier, 2017: pp. 391–404. doi:10.1016/B978-0-12-812234-1.00014-5.
- [18] J.B. Klauda, S.I. Sandler, Global Distribution of Methane Hydrate in Ocean Sediment, *Energy Fuels*. 19 (2005) 459–470. doi:10.1021/ef049798o.
- [19] Y.F. Makogon, S.A. Holditch, T.Y. Makogon, Natural gas-hydrates — A potential energy source for the 21st Century, *J. Pet. Sci. Eng.* 56 (2007) 14–31. doi:10.1016/j.petrol.2005.10.009.
- [20] Z.R. Chong, S.H.B. Yang, P. Babu, P. Linga, X.-S. Li, Review of natural gas hydrates as an energy resource: Prospects and challenges, *Appl. Energy*. 162 (2016) 1633–1652. doi:10.1016/j.apenergy.2014.12.061.
- [21] Y.F. Makogon, Natural gas hydrates – A promising source of energy, *J. Nat. Gas Sci. Eng.* 2 (2010) 49–59. doi:10.1016/j.jngse.2009.12.004.
- [22] B. Anderson, R. Boswell, T.S. Collett, H. Farrell, S. Ohtsuki, M. White, M. Zyrianova, Review of the findings of the Ignick Sikumi CO<sub>2</sub>–CH<sub>4</sub> gas hydrate exchange field trial, in: *Proc. 8th Int. Conf. Gas Hydrates ICGH8-2014*, 2014.
- [23] B.P. McGrail, H.T. Schaef, M.D. White, T. Zhu, A.S. Kulkarni, R.B. Hunter, S.L. Patil, A.T. Owen, P.F. Martin, Using carbon dioxide to enhance recovery of methane from gas hydrate reservoirs: final summary report, Pacific Northwest National Laboratory (PNNL), Richland, WA (US), 2007.
- [24] K. Ohgaki, K. Takano, H. Sangawa, T. Matsubara, S. Nakano, Methane exploitation by carbon dioxide from gas hydrates. Phase equilibria for CO<sub>2</sub>-CH<sub>4</sub> mixed hydrate system., *J. Chem. Eng. Jpn.* 29 (1996) 478–483. doi:10.1252/jcej.29.478.
- [25] David Schoderbek, Helen Farrell, Keith Hester, James Howard, Kevin Raterman, Suntichai Silpngarmert, Kenneth Lloyd Martin, Bruce Smith, Perry Klein, ConocoPhillips Gas Hydrate Production Test Final Technical Report, ConocoPhillips Company, 2013.
- [26] X.-S. Li, C.-G. Xu, Y. Zhang, X.-K. Ruan, G. Li, Y. Wang, Investigation into gas production from natural gas hydrate: A review, *Appl. Energy*. 172 (2016) 286–322. doi:10.1016/j.apenergy.2016.03.101.



- [27] A. Oyama, S. Masutani, A. Oyama, S.M. Masutani, A Review of the Methane Hydrate Program in Japan, *Energies*. 10 (2017) 1447. doi:10.3390/en10101447.
- [28] Z. Sun, R. Wang, R. Ma, K. Guo, S. Fan, Natural gas storage in hydrates with the presence of promoters, *Energy Convers. Manag.* 44 (2003) 2733–2742. doi:10.1016/S0196-8904(03)00048-7.
- [29] S. Maghsoodloo Babakhani, A. Alamdari, Effect of maize starch on methane hydrate formation/dissociation rates and stability, *J. Nat. Gas Sci. Eng.* 26 (2015) 1–5. doi:10.1016/j.jngse.2015.05.026.
- [30] Z. Taheri, M.R. Shabani, K. Nazari, A. Mehdizaheh, Natural gas transportation and storage by hydrate technology: Iran case study, *J. Nat. Gas Sci. Eng.* 21 (2014) 846–849. doi:10.1016/j.jngse.2014.09.026.
- [31] Y.F. Makogon, *Hydrates of Hydrocarbons*, 1 edition, Pennwell Corp, Tulsa, Okla, 1997.
- [32] A.. Khokhar, J.. Gudmundsson, E.. Sloan, Gas storage in structure H hydrates, *Fluid Phase Equilibria*. 150–151 (1998) 383–392. doi:10.1016/S0378-3812(98)00338-0.
- [33] J.-S. Gudmundsson, M. Parlaktuna, A.A. Khokhar, Storage of Natural Gas as Frozen Hydrate, *SPE Prod. Facil.* 9 (1994) 69–73. doi:10.2118/24924-PA.
- [34] N.-J. Kim, J. Hwan Lee, Y.S. Cho, W. Chun, Formation enhancement of methane hydrate for natural gas transport and storage, *Energy*. 35 (2010) 2717–2722. doi:10.1016/j.energy.2009.07.020.
- [35] M. Ozaki, S. Tomura, R. Ohmura, Y.H. Mori, Comparative study of large-scale hydrogen storage technologies: Is hydrate-based storage at advantage over existing technologies?, *Int. J. Hydrog. Energy*. 39 (2014) 3327–3341. doi:10.1016/j.ijhydene.2013.12.080.
- [36] T.A. Strobel, K.C. Hester, C.A. Koh, A.K. Sum, E.D. Sloan, Properties of the clathrates of hydrogen and developments in their applicability for hydrogen storage, *Chem. Phys. Lett.* 478 (2009) 97–109. doi:10.1016/j.cplett.2009.07.030.
- [37] H.P. Veluswamy, R. Kumar, P. Linga, Hydrogen storage in clathrate hydrates: Current state of the art and future directions, *Appl. Energy*. 122 (2014) 112–132. doi:10.1016/j.apenergy.2014.01.063.
- [38] J.-H. Cha, Y. Seol, Increasing Gas Hydrate Formation Temperature for Desalination of High Salinity Produced Water with Secondary Guests, *ACS Sustain. Chem. Eng.* 1 (2013) 1218–1224. doi:10.1021/sc400160u.

- [39] Y. Zhang, S.-M. Sheng, X.-D. Shen, X.-B. Zhou, W.-Z. Wu, X.-P. Wu, D.-Q. Liang, Phase Equilibrium of Cyclopentane + Carbon Dioxide Binary Hydrates in Aqueous Sodium Chloride Solutions, *J. Chem. Eng. Data.* 62 (2017) 2461–2465. doi:10.1021/acs.jced.7b00404.
- [40] A.J. Barduhn, H.E. Towilson, Y.C. Hu, The properties of some new gas hydrates and their use in demineralizing sea water, *AIChE J.* 8 (1962) 176–183. doi:10.1002/aic.690080210.
- [41] H. Lee, H. Ryu, J.-H. Lim, J.-O. Kim, J.D. Lee, S. Kim, An optimal design approach of gas hydrate and reverse osmosis hybrid system for seawater desalination, *Desalination Water Treat.* 57 (2016) 9009–9017. doi:10.1080/19443994.2015.1049405.
- [42] S. Ho-Van, B. Bouillot, J. Douzet, S. Maghsoodloo Babakhani, J.M. Herri, Experimental measurement and thermodynamic modeling of cyclopentane hydrates with NaCl, KCl, CaCl<sub>2</sub>, or NaCl-KCl present, *AIChE J.* In press (2018). doi:10.1002/aic.16067.
- [43] Y. Yang, D. Shin, S. Choi, Y. Woo, J.-W. Lee, D. Kim, H.-Y. Shin, M. Cha, J.-H. Yoon, Selective Encaging of N<sub>2</sub>O in N<sub>2</sub>O-N<sub>2</sub> Binary Gas Hydrates via Hydrate-Based Gas Separation, *Environ. Sci. Technol.* 51 (2017) 3550–3557. doi:10.1021/acs.est.6b05978.
- [44] N.G. Zanjani, K. Nazari, A.Z. Moghaddam, M.M. Taheri, M. Sina, Methane Purification by Sequential Gas Hydrate Formation in Porous Media, in: *Proc. 7th Int. Conf. Gas Hydrates Edinb. Scotl. U. K. July, 2011*: pp. 17–21.
- [45] E. Kim, G. Ko, Y. Seo, Greenhouse Gas (CHF<sub>3</sub>) Separation by Gas Hydrate Formation, *ACS Sustain. Chem. Eng.* 5 (2017) 5485–5492. doi:10.1021/acssuschemeng.7b00821.
- [46] M.S. Onn, A.A. Seman, Z. Kassim, M.A. Esa, CO<sub>2</sub> Separation from Natural Gas Through Hydrate Formation, in: *Offshore Technology Conference, 2014*. doi:10.4043/24930-MS.
- [47] V.M. Vorotyntsev, V.M. Malyshev, G.M. Mochalov, P.G. Taraburov, Separation of gas mixtures by the gas hydrate crystallization method, *Theor. Found. Chem. Eng.* 35 (2001) 119–123.
- [48] J.-M. Herri, A. Bouchemoua, M. Kwaterski, P. Brântuas, A. Galfré, B. Bouillot, J. Douzet, Y. Ouabbas, A. Cameirao, Enhanced Selectivity of the Separation of CO<sub>2</sub> from N<sub>2</sub> during Crystallization of Semi-Clathrates from Quaternary Ammonium Solutions, *Oil Gas Sci. Technol. – Rev. D’IFP Energ. Nouv.* 69 (2014) 947–968. doi:10.2516/ogst/2013201.
- [49] Y. Lee, Y. Seo, T. Ahn, J. Lee, J.Y. Lee, S.-J. Kim, Y. Seo, CH<sub>4</sub> – Flue gas replacement occurring in sH hydrates and its significance for CH<sub>4</sub> recovery and CO<sub>2</sub> sequestration, *Chem. Eng. J.* 308 (2017) 50–58. doi:10.1016/j.cej.2016.09.031.
- [50] M. Yang, Y. Song, L. Jiang, Y. Zhao, X. Ruan, Y. Zhang, S. Wang, Hydrate-based technology for CO<sub>2</sub> capture from fossil fuel power plants, *Appl. Energy.* 116 (2014) 26–40. doi:10.1016/j.apenergy.2013.11.031.

- [51] Z. Xia, X. Li, Z. Chen, K. Yan, C. Xu, J. Cai, Hydrate-based hydrogen purification from simulated syngas with synergic additives, *Int. J. Hydrog. Energy*. 41 (2016) 2649–2659. doi:10.1016/j.ijhydene.2015.12.065.
- [52] Z. Xia, X. Li, Z. Chen, G. Li, Y. Wang, C. Jing, Z. Li, Q. Lv, Hydrate-based Synchronously Capture of CO<sub>2</sub> and H<sub>2</sub>S for Clean H<sub>2</sub> with New Synergic Additives, *Energy Procedia*. 142 (2017) 3427–3432. doi:10.1016/j.egypro.2017.12.225.
- [53] S. Fan, X. Wang, X. Lang, Y. Wang, Energy efficiency simulation of the process of gas hydrate exploitation from flue gas in an electric power plant, *Nat. Gas Ind. B*. 4 (2017) 470–476. doi:10.1016/j.ngib.2017.09.009.
- [54] C.-G. Xu, J. Cai, Y.-S. Yu, Z.-Y. Chen, X.-S. Li, Research on micro-mechanism and efficiency of CH<sub>4</sub> exploitation via CH<sub>4</sub>-CO<sub>2</sub> replacement from natural gas hydrates, *Fuel*. 216 (2018) 255–265. doi:10.1016/j.fuel.2017.12.022.
- [55] C.-G. Xu, X.-S. Li, Research progress of hydrate-based CO<sub>2</sub> separation and capture from gas mixtures, *RSC Adv*. 4 (2014) 18301–18316. doi:10.1039/C4RA00611A.
- [56] Z.-Y. Chen, C. Chen, Y. Zhang, Z.-M. Xia, K.-F. Yan, X.-S. Li, Carbon dioxide and sulfur dioxide capture from flue gas by gas hydrate based process, *Energy Procedia*. 142 (2017) 3454–3459. doi:10.1016/j.egypro.2017.12.229.
- [57] J.W. Mullin, *Crystallization*, 4 edition, Butterworth-Heinemann, Oxford ; Boston, 2001.
- [58] M.N. Khan, P. Warriar, C.J. Peters, C.A. Koh, Review of vapor-liquid equilibria of gas hydrate formers and phase equilibria of hydrates, *J. Nat. Gas Sci. Eng.* 35, Part B (2016) 1388–1404. doi:10.1016/j.jngse.2016.06.043.
- [59] A. Danesh, *PVT and Phase Behaviour Of Petroleum Reservoir Fluids*, Elsevier Science, Amsterdam ; New York, 1998.
- [60] B.J. Falabella, *A STUDY OF NATURAL GAS HYDRATES.*, University of Massachusetts Amherst, 1975. <https://scholarworks.umass.edu/dissertations/AAI7605849>.
- [61] K. Yasuda, R. Ohmura, Phase Equilibrium for Clathrate Hydrates Formed with Methane, Ethane, Propane, or Carbon Dioxide at Temperatures below the Freezing Point of Water, *J. Chem. Eng. Data*. 53 (2008) 2182–2188. doi:10.1021/je800396v.
- [62] W.M. Deaton, E.M. Frost, *Gas hydrates and their relation to the operation of natural-gas pipe lines*, Printed by the American Gas Association, 1946.
- [63] T.Y. Makogon, E.D.J. Sloan, Phase Equilibrium for Methane Hydrate from 190 to 262 K, *J. Chem. Eng. Data*. 39 (1994) 351–353. doi:10.1021/je00014a035.

- [64] A.H. Mohammadi, D. Richon, Ice–Clathrate Hydrate–Gas Phase Equilibria for Air, Oxygen, Nitrogen, Carbon Monoxide, Methane, or Ethane + Water System, *Ind. Eng. Chem. Res.* 49 (2010) 3976–3979. doi:10.1021/ie901820u.
- [65] N. Fray, U. Marboeuf, O. Brissaud, B. Schmitt, Equilibrium Data of Methane, Carbon Dioxide, and Xenon Clathrate Hydrates below the Freezing Point of Water. Applications to Astrophysical Environments, *J. Chem. Eng. Data.* 55 (2010) 5101–5108. doi:10.1021/je1006604.
- [66] Y. Dyadin, E. Aladko, Decomposition of the methane hydrate up to 10 kbar, in: Toulouse, France, n.d.
- [67] S. Adisasmitho, R.J. Frank, E.D. Sloan, Hydrates of carbon dioxide and methane mixtures, *J. Chem. Eng. Data.* 36 (1991) 68–71. doi:10.1021/je00001a020.
- [68] J. Jhaveri, D.B. Robinson, Hydrates in the methane-nitrogen system, *Can. J. Chem. Eng.* 43 (1965) 75–78. doi:10.1002/cjce.5450430207.
- [69] R. Kobayashi, D.L. Katz, Methane Hydrate at High Pressure, *J. Pet. Technol.* 1 (1949) 66–70. doi:10.2118/949066-G.
- [70] H.O. McLeod, J.M. Campbell, Natural Gas Hydrates at Pressures to 10,000 psia, *J. Pet. Technol.* 13 (1961) 590–594. doi:10.2118/1566-G-PA.
- [71] P. Englezos, Y.T. Ngan, Incipient equilibrium data for propane hydrate formation in aqueous solutions of sodium chloride, potassium chloride and calcium chloride, *J. Chem. Eng. Data.* 38 (1993) 250–253. doi:10.1021/je00010a017.
- [72] J. Nixdorf, L.R. Oellrich, Experimental determination of hydrate equilibrium conditions for pure gases, binary and ternary mixtures and natural gases, *Fluid Phase Equilibria.* 139 (1997) 325–333. doi:10.1016/S0378-3812(97)00141-6.
- [73] W.I. Wilcox, D.B. Carson, D.L. Katz, Natural Gas Hydrates, *Ind. Eng. Chem.* 33 (1941) 662–665. doi:10.1021/ie50377a027.
- [74] Y.K. Verma, J.H. Hand, D.L. Katz, Gas hydrates from liquid hydrocarbons methane-propane-water system, in: *GVCAIChE Jt. Meet., Munich, Germany, 1975*: p. 10.
- [75] Holder G. D., Godbole S. P., Measurement and prediction of dissociation pressures of isobutane and propane hydrates below the ice point, *AIChE J.* 28 (1982) 930–934. doi:10.1002/aic.690280607.
- [76] J.L. Thakore, G.D. Holder, Solid vapor azeotropes in hydrate-forming systems, *Ind. Eng. Chem. Res.* 26 (1987) 462–469. doi:10.1021/ie00063a011.

- [77] S.L. Miller, W.D. Smythe, Carbon dioxide clathrate in the martian ice cap, *Science*. 170 (1970) 531–533. doi:10.1126/science.170.3957.531.
- [78] S.D. Larson, Phase studies of the two component carbon dioxide-water system involving the carbon dioxide hydrate, 1955.
- [79] D.B. Robinson, B.R. Metha, Hydrates In the PropaneCarbon Dioxide- Water System, *J. Can. Pet. Technol.* 10 (1971). doi:10.2118/71-01-04.
- [80] H.-J. Ng, D.B. Robinson, Hydrate formation in systems containing methane, ethane, propane, carbon dioxide or hydrogen sulfide in the presence of methanol, *Fluid Phase Equilibria*. 21 (1985) 145–155. doi:10.1016/0378-3812(85)90065-2.
- [81] G.D. Holder, G.C. Grigoriou, Hydrate dissociation pressures of (methane + ethane + water) existence of a locus of minimum pressures, *J. Chem. Thermodyn.* 12 (1980) 1093–1104. doi:10.1016/0021-9614(80)90166-4.
- [82] O.L. Roberts, E.R. Brownscombe, L.S. Howe, Constitution diagrams and composition of methane and ethane hydrates, *Oil Gas J.* 39 (1940) 37–43.
- [83] D.R. Marshall, S. Saito, R. Kobayashi, Hydrates at high pressures: Part I. Methane-water, argon-water, and nitrogen-water systems, *AIChE J.* 10 (1964) 202–205. doi:10.1002/aic.690100214.
- [84] K. Sugahara, Y. Tanaka, T. Sugahara, K. Ohgaki, Thermodynamic stability and structure of nitrogen hydrate crystal, *J. Supramol. Chem.* 4–5 (2002) 365–368. doi:10.1016/S1472-7862(03)00060-1.
- [85] A. van Cleeff, G. a. M. Diepen, Gas hydrates of nitrogen and oxygen, *Recl. Trav. Chim. Pays-Bas.* 79 (1960) 582–586. doi:10.1002/recl.19600790606.
- [86] J.M. Schicks, R. Naumann, J. Erzinger, K.C. Hester, C.A. Koh, E.D. Sloan, Phase Transitions in Mixed Gas Hydrates: Experimental Observations versus Calculated Data, *J. Phys. Chem. B.* 110 (2006) 11468–11474. doi:10.1021/jp0612580.
- [87] J.-W. Lee, D.-Y. Kim, H. Lee, Phase behavior and structure transition of the mixed methane and nitrogen hydrates, *Korean J. Chem. Eng.* 23 (2006) 299–302. doi:10.1007/BF02705731.
- [88] S. Subramanian, A.. Ballard, R.. Kini, S.. Dec, E.. Sloan, Structural transitions in methane+ethane gas hydrates — Part I: upper transition point and applications, *Chem. Eng. Sci.* 55 (2000) 5763–5771. doi:10.1016/S0009-2509(00)00162-7.

- [89] S. Subramanian, R.A. Kini, S.F. Dec, E.D. Sloan, Evidence of structure II hydrate formation from methane+ethane mixtures, *Chem. Eng. Sci.* 55 (2000) 1981–1999. doi:10.1016/S0009-2509(99)00389-9.
- [90] A.L. Ballard, D.E. Sloan, Structural transitions in methane+ethane gas hydrates — Part II: modeling beyond incipient conditions, *Chem. Eng. Sci.* 55 (2000) 5773–5782. doi:10.1016/S0009-2509(00)00163-9.
- [91] M. Kwon, J.-W. Lee, H. Lee, Temperature-Dependent Structural Transitions in Methane–Ethane Mixed Gas Hydrates, *J. Phys. Chem. C.* 118 (2014) 28906–28913. doi:10.1021/jp5102219.
- [92] H. Ohno, T.A. Strobel, S.F. Dec, E.D. Sloan, C.A. Koh, RAMAN STUDIES OF METHANE-ETHANE HYDRATE STRUCTURAL TRANSITION, (2008). doi:10.14288/1.0041038.
- [93] O.S. Rouher, A.J. Barduhn, Hydrates of iso- and normal butane and their mixtures, *Desalination.* 6 (1969) 57–73. doi:10.1016/S0011-9164(00)80011-9.
- [94] B.-J. Wu, D.B. Robinson, H.-J. Ng, Three- and four-phase hydrate forming conditions in methane + isobutane + water, *J. Chem. Thermodyn.* 8 (1976) 461–469. doi:10.1016/0021-9614(76)90067-7.
- [95] H. Kubota, K. Shimizu, Y. Tanaka, T. Makita, Thermodynamic properties of R13 (CCIF<sub>3</sub>), R23 (CHF<sub>3</sub>), R152a (C<sub>2</sub>H<sub>4</sub>F<sub>2</sub>), and propane hydrates for desalination of sea water, *J. Chem. Eng. Jpn.* 17 (1984) 423–429. doi:10.1252/jcej.17.423.
- [96] Holder G. D., Hand J. H., Multiple-phase equilibria in hydrates from methane, ethane, propane and water mixtures, *AIChE J.* 28 (2004) 440–447. doi:10.1002/aic.690280312.
- [97] D.L. Katz, Prediction of Conditions for Hydrate Formation in Natural Gases, *Trans. AIME.* 160 (1945) 140–149. doi:10.2118/945140-G.
- [98] M.R.N. Loh, E.J.H. James, New hydrate formation data reveal differences, *Oil Gas J.* 81 (1983) 96–98.
- [99] S. Shahnazar, N. Hasan, Gas hydrate formation condition: Review on experimental and modeling approaches, *Fluid Phase Equilibria.* 379 (2014) 72–85. doi:10.1016/j.fluid.2014.07.012.
- [100] D.B. Carson, D.L. Katz, Natural Gas Hydrates, *Trans. AIME.* 146 (1942) 150–158. doi:10.2118/942150-G.
- [101] A.A. Elgibaly, A.M. Elkamel, A new correlation for predicting hydrate formation conditions for various gas mixtures and inhibitors, *Fluid Phase Equilibria.* 152 (1998) 23–42. doi:10.1016/S0378-3812(98)00368-9.

- [102] R.G. Kobayashi, K.Y. Song, E.D. Sloan, Phase Behavior of Water/Hydrocarbon Systems (1987 PEH Chapter 25), *Pet. Eng. Handb.* (1987). doi:NA.
- [103] A. Bahadori, Correlation Accurately Predicts Hydrate Forming Pressure of Pure Components, *J. Can. Pet. Technol.* 47 (2008). doi:10.2118/08-02-13-TN.
- [104] O. Omole, O.A. Falode, A.O. Arinkoola, Development of empirical correlations for predicting formation of gas hydrate, *Int. J. Oil Gas Coal Technol.* 2 (2009) 24. doi:10.1504/IJOGCT.2009.023628.
- [105] J. Zupan, J. Gasteiger, Neural networks: A new method for solving chemical problems or just a passing phase?, *Anal. Chim. Acta.* 248 (1991) 1–30. doi:10.1016/S0003-2670(00)80865-X.
- [106] G.G. Andersson, P. Kaufmann, Development of a generalized neural network, *Chemom. Intell. Lab. Syst.* 50 (2000) 101–105. doi:10.1016/S0169-7439(99)00051-9.
- [107] A. Jouyban, M.-R. Majidi, F. Jabbaribar, K. Asadpour-Zeynali, Solubility prediction of anthracene in binary and ternary solvents by artificial neural networks (ANNs), *Fluid Phase Equilibria.* 225 (2004) 133–139. doi:10.1016/j.fluid.2004.08.031.
- [108] A.H. Mohammadi, J.F. Martínez-López, D. Richon, Determining phase diagrams of tetrahydrofuran+methane, carbon dioxide or nitrogen clathrate hydrates using an artificial neural network algorithm, *Chem. Eng. Sci.* 65 (2010) 6059–6063. doi:10.1016/j.ces.2010.07.013.
- [109] S. Maghsoodloo Babakhani, M. Bahmani, J. Shariati, K. Badr, Y. Balouchi, Comparing the capability of artificial neural network (ANN) and CSMHYD program for predicting of hydrate formation pressure in binary mixtures, *J. Pet. Sci. Eng.* 136 (2015) 78–87. doi:10.1016/j.petrol.2015.11.002.
- [110] G. Zahedi, Z. Karami, H. Yaghoobi, Prediction of hydrate formation temperature by both statistical models and artificial neural network approaches, *Energy Convers. Manag.* 50 (2009) 2052–2059. doi:10.1016/j.enconman.2009.04.005.
- [111] J.H. van der Waals, J.C. Platteeuw, Clathrate Solutions, in: I. Prigogine (Ed.), *Adv. Chem. Phys.*, John Wiley & Sons, Inc., Hoboken, NJ, USA, 1959: pp. 1–57. <http://doi.wiley.com/10.1002/9780470143483.ch1> (accessed December 22, 2015).
- [112] M. v. Stackelberg, H.R. Müller, On the Structure of Gas Hydrates, *J. Chem. Phys.* 19 (1951) 1319. doi:10.1063/1.1748038.
- [113] J.-M. Herri, A. Bouchemoua, M. Kwaterski, A. Fezoua, Y. Ouabbas, A. Cameirao, Gas hydrate equilibria for CO<sub>2</sub>–N<sub>2</sub> and CO<sub>2</sub>–CH<sub>4</sub> gas mixtures—Experimental studies and thermodynamic modelling, *Fluid Phase Equilibria.* 301 (2011) 171–190. doi:10.1016/j.fluid.2010.09.041.

- [114] W.R. Parrish, J.M. Prausnitz, Dissociation Pressures of Gas Hydrates Formed by Gas Mixtures, *Ind. Eng. Chem. Process Des. Dev.* 11 (1972) 26–35. doi:10.1021/i260041a006.
- [115] J. Munck, S. Skjold-Jørgensen, P. Rasmussen, Computations of the formation of gas hydrates, *Chem. Eng. Sci.* 43 (1988) 2661–2672. doi:10.1016/0009-2509(88)80010-1.
- [116] V. McKoy, O. Sinanoğlu, Theory of Dissociation Pressures of Some Gas Hydrates, *J. Chem. Phys.* 38 (1963) 2946. doi:10.1063/1.1733625.
- [117] L.S. Tee, S. Gotoh, W.E. Stewart, Molecular Parameters for Normal Fluids. Kihara Potential with Spherical Core, *Ind. Eng. Chem. Fundam.* 5 (1966b) 363–367. doi:10.1021/i160019a012.
- [118] A.E. Sherwood, J.M. Prausnitz, Intermolecular Potential Functions and the Second and Third Virial Coefficients, *J. Chem. Phys.* 41 (1964) 429. doi:10.1063/1.1725884.
- [119] J.E.D. Sloan, *Clathrate Hydrates of Natural Gases*, Second Edition, Revised and Expanded, CRC Press, 1998.
- [120] J.-M. Herri, E. Chassefière, Carbon dioxide, argon, nitrogen and methane clathrate hydrates: Thermodynamic modelling, investigation of their stability in Martian atmospheric conditions and variability of methane trapping, *Planet. Space Sci.* 73 (2012) 376–386. doi:10.1016/j.pss.2012.07.028.
- [121] D. Le Quang, D. Le Quang, B. Bouillot, J.-M. Herri, P. Glenat, P. Duchet-Suchaux, Experimental procedure and results to measure the composition of gas hydrate, during crystallization and at equilibrium, from N<sub>2</sub>–CO<sub>2</sub>–CH<sub>4</sub>–C<sub>2</sub>H<sub>6</sub>–C<sub>3</sub>H<sub>8</sub>–C<sub>4</sub>H<sub>10</sub> gas mixtures, *Fluid Phase Equilibria*. (2015). doi:10.1016/j.fluid.2015.10.022.
- [122] B. Bouillot, J.-M. Herri, Volume and Non-Equilibrium Crystallization of Clathrate Hydrates, in: *Gas Hydrates Fundam. Charact. Model.*, Wiley, 2017: pp. 227–282.
- [123] B. Kvamme, T. Kuznetsova, B. Jensen, S. Stensholt, J. Bauman, S. Sjøblom, K. Nes Lervik, Consequences of CO<sub>2</sub> solubility for hydrate formation from carbon dioxide containing water and other impurities, *Phys Chem Chem Phys.* 16 (2014) 8623–8638. doi:10.1039/C3CP53858C.
- [124] T. Uchida, S. Takeya, Y. Kamata, I.Y. Ikeda, J. Nagao, T. Ebinuma, H. Narita, O. Zatsepina, B.A. Buffett, Spectroscopic Observations and Thermodynamic Calculations on Clathrate Hydrates of Mixed Gas Containing Methane and Ethane: Determination of Structure, Composition and Cage Occupancy, *J. Phys. Chem. B.* 106 (2002) 12426–12431. doi:10.1021/jp025884i.



- [125] J.M. Schicks, J.A. Ripmeester, The Coexistence of Two Different Methane Hydrate Phases under Moderate Pressure and Temperature Conditions: Kinetic versus Thermodynamic Products, *Angew. Chem.* 116 (2004) 3372–3375. doi:10.1002/ange.200453898.
- [126] J.-M. Herri, F. Gruy, J.-S. Pic, M. Cournil, B. Cingotti, A. Sinquin, Interest of in situ turbidimetry for the characterization of methane hydrate crystallization: application to the study of kinetic inhibitors, *Chem. Eng. Sci.* 54 (1999a) 1849–1858.
- [127] J.L. Peytavy, J.P. Monfort, C. Gaillard, Investigation of Methane Hydrate Formation in a Recirculating Flow Loop: Modeling of the Kinetics and Tests of Efficiency of Chemical Additives on Hydrate Inhibition, *Oil Gas Sci. Technol.* 54 (n.d.) 365–374. doi:10.2516/ogst:1999033.
- [128] P.J. Murphy, S. Roberts, Melting and nucleation behaviour of clathrates in multivolatile fluid inclusions: evidence of thermodynamic disequilibrium, *Chem. Geol.* 135 (1997) 1–20. doi:10.1016/S0009-2541(96)00101-5.
- [129] A.N. Salamatin, A. Falenty, W.F. Kuhs, Diffusion Model for Gas Replacement in an Isostructural CH<sub>4</sub>–CO<sub>2</sub> Hydrate System, *J. Phys. Chem. C.* 121 (2017) 17603–17616. doi:10.1021/acs.jpcc.7b04391.
- [130] J. Vatamanu, P.G. Kusalik, Molecular Insights into the Heterogeneous Crystal Growth of sI Methane Hydrate, *J. Phys. Chem. B.* 110 (2006) 15896–15904. doi:10.1021/jp061684l.
- [131] M.R. Walsh, C.A. Koh, E.D. Sloan, A.K. Sum, D.T. Wu, Microsecond Simulations of Spontaneous Methane Hydrate Nucleation and Growth, *Science.* 326 (2009) 1095–1098. doi:10.1126/science.1174010.
- [132] L.C. Jacobson, W. Hujo, V. Molinero, Amorphous Precursors in the Nucleation of Clathrate Hydrates, *J. Am. Chem. Soc.* 132 (2010) 11806–11811. doi:10.1021/ja1051445.
- [133] W. Shin, S. Park, H. Ro, D.-Y. Koh, J. Seol, H. Lee, Spectroscopic Confirmation of Metastable Structure Formation Occurring in Natural Gas Hydrates, *Chem. – Asian J.* 7 (2012) 2235–2238. doi:10.1002/asia.201200040.
- [134] A.H. Nguyen, L.C. Jacobson, V. Molinero, Structure of the Clathrate/Solution Interface and Mechanism of Cross-Nucleation of Clathrate Hydrates, *J. Phys. Chem. C.* 116 (2012) 19828–19838. doi:10.1021/jp305468s.
- [135] S. Maghsoodloo Babakhani, B. Bouillot, J. Douzet, S. Ho-Van, J.M. Herri, A new approach of studying mixed gas hydrates involving propane at non-equilibrium conditions and final state: An experimental study and modeling, *Chem. Eng. Sci.* 179 (2018) 150–160. doi:10.1016/j.ces.2018.01.017.

- [136] B. Bouillot, J.-M. Herri, Framework for clathrate hydrate flash calculations and implications on the crystal structure and final equilibrium of mixed hydrates, *Fluid Phase Equilibria*. (2015). doi:10.1016/j.fluid.2015.10.023.
- [137] S. Han, Y.-W. Rhee, S.-P. Kang, Investigation of salt removal using cyclopentane hydrate formation and washing treatment for seawater desalination, *Desalination*. 404 (2017) 132–137. doi:10.1016/j.desal.2016.11.016.
- [138] A.Y. Manakov, A.D. Duchkov, Laboratory modeling of hydrate formation in rock specimens (a review), *Russ. Geol. Geophys.* 58 (2017) 240–252. doi:10.1016/j.rgg.2016.01.023.
- [139] Y. Song, L. Yang, J. Zhao, W. Liu, M. Yang, Y. Li, Y. Liu, Q. Li, The status of natural gas hydrate research in China: A review, *Renew. Sustain. Energy Rev.* 31 (2014) 778–791. doi:10.1016/j.rser.2013.12.025.
- [140] Q. Sun, Y.T. Kang, Review on CO<sub>2</sub> hydrate formation/dissociation and its cold energy application, *Renew. Sustain. Energy Rev.* 62 (2016) 478–494. doi:10.1016/j.rser.2016.04.062.
- [141] Z. Yin, Z.R. Chong, H.K. Tan, P. Linga, Review of gas hydrate dissociation kinetic models for energy recovery, *J. Nat. Gas Sci. Eng.* 35, Part B (2016) 1362–1387. doi:10.1016/j.jngse.2016.04.050.
- [142] T. Kawasaki, K. Kikuchi, D. Terasaki, T. Okui, K. Myata, H. Hirayama, M. Ihara, Composition of Guests in Hydrates from Gas Mixture, in: Yokohama, Japan, 2002: pp. 424–427.
- [143] S.-P. Kang, H. Lee, C.-S. Lee, W.-M. Sung, Hydrate phase equilibria of the guest mixtures containing CO<sub>2</sub>, N<sub>2</sub> and tetrahydrofuran, *Fluid Phase Equilibria*. 185 (2001) 101–109. doi:10.1016/S0378-3812(01)00460-5.
- [144] S. Angus, J.B. Armstrong, K.M. de Reuck, R.D. McCarthy, R.T. Jacobsen, W. Wagner, International thermodynamic tables of the fluid state. Methane 5 5, 1978.
- [145] S. Angus, B. Armstrong, K.M. de Reuck, International thermodynamic tables of the fluid state: carbon dioxide, Pergamon Press, Oxford; New York, 1976.
- [146] V. Belandria, A. Eslamimanesh, A.H. Mohammadi, P. Théveneau, H. Legendre, D. Richon, Compositional Analysis and Hydrate Dissociation Conditions Measurements for Carbon Dioxide + Methane + Water System, *Ind. Eng. Chem. Res.* 50 (2011) 5783–5794. doi:10.1021/ie101959t.
- [147] V. Belandria, A. Eslamimanesh, A.H. Mohammadi, D. Richon, Gas Hydrate Formation in Carbon Dioxide + Nitrogen + Water System: Compositional Analysis of Equilibrium Phases, *Ind. Eng. Chem. Res.* 50 (2011) 4722–4730. doi:10.1021/ie101635k.

- [148] Y.-T. Seo, S.-P. Kang, H. Lee, C.-S. Lee, W.-M. Sung, Hydrate phase equilibria for gas mixtures containing carbon dioxide: A proof-of-concept to carbon dioxide recovery from multicomponent gas stream, *Korean J. Chem. Eng.* 17 (2000) 659–667.
- [149] H.-J. Ng, Hydrate Phase Composition for Multicomponent Gas Mixtures, *Ann. N. Y. Acad. Sci.* 912 (2000) 1034–1039. doi:10.1111/j.1749-6632.2000.tb06858.x.
- [150] A. Desmedt, R.E. Lechner, J.-C. Lassegues, F. Guillaume, D. Cavagnat, J. Grondin, Hydronium dynamics in the perchloric acid clathrate hydrate, *Solid State Ion.* 252 (2013) 19–25. doi:10.1016/j.ssi.2013.06.004.
- [151] J. Jia, Y. Liang, T. Tsuji, S. Murata, T. Matsuoka, Microscopic Origin of Strain Hardening in Methane Hydrate, *Sci. Rep.* 6 (2016) 23548. doi:10.1038/srep23548.
- [152] L.A. Stern, S.H. Kirby, S. Circone, W.B. Durham, Scanning Electron Microscopy investigations of laboratory-grown gas clathrate hydrates formed from melting ice, and comparison to natural hydrates, *Am. Mineral.* 89 (2004) 1162–1175. doi:10.2138/am-2004-8-902.
- [153] F. Javadpour, M. Moravvej Farshi, M. Amrein, Atomic-Force Microscopy: A New Tool for Gas-Shale Characterization, *J. Can. Pet. Technol.* 51 (2012) 236–243. doi:10.2118/161015-PA.
- [154] A. Klapproth, E. Goreshnik, D. Staykova, H. Klein, W.F. Kuhs, Structural studies of gas hydrates, *Can. J. Phys.* 81 (2003) 503–518. doi:10.1139/p03-024.
- [155] C. Deusner, S. Gupta, E. Kossel, N. Bigalke, M. Haeckel, Hydro-geomechanical behaviour of gas-hydrate bearing soils during gas production through depressurization and CO<sub>2</sub> injection, *AGU Fall Meet. Abstr.* 12 (2015) B12B-03.
- [156] W.L. Du Frane, L.A. Stern, K.A. Weitemeyer, S. Constable, J.C. Pinkston, J.J. Roberts, Electrical properties of polycrystalline methane hydrate: ELECTRICAL PROPERTIES OF METHANE HYDRATE, *Geophys. Res. Lett.* 38 (2011) n/a-n/a. doi:10.1029/2011GL047243.
- [157] M. Holland, P. Schultheiss, Comparison of methane mass balance and X-ray computed tomographic methods for calculation of gas hydrate content of pressure cores, *Mar. Pet. Geol.* 58 (2014) 168–177. doi:10.1016/j.marpetgeo.2014.07.016.
- [158] R. Susilo, J.A. Ripmeester, P. Englezos, Characterization of gas hydrates with PXRD, DSC, NMR, and Raman spectroscopy, *Chem. Eng. Sci.* 62 (2007) 3930–3939. doi:10.1016/j.ces.2007.03.045.
- [159] C. Petuya, F. Damay, B. Chazallon, J.-L. Bruneel, A. Desmedt, Guest Partitioning and Metastability of the Nitrogen Gas Hydrate, *J. Phys. Chem. C.* 122 (2018) 566–573. doi:10.1021/acs.jpcc.7b10151.

- [160] B. Chazallon, C. Focsa, J.-L. Charlou, C. Bourry, J.-P. Donval, A comparative Raman spectroscopic study of natural gas hydrates collected at different geological sites, *Chem. Geol.* 244 (2007) 175–185. doi:10.1016/j.chemgeo.2007.06.012.
- [161] S. Ignea, L. Alfvén, *Characterization of Gas Hydrates*, (n.d.) 34.
- [162] M.T. Kirchner, R. Boese, W.E. Billups, L.R. Norman, Gas Hydrate Single-Crystal Structure Analyses, *J. Am. Chem. Soc.* 126 (2004) 9407–9412. doi:10.1021/ja049247c.
- [163] H. Kadobayashi, H. Hirai, H. Ohfuji, M. Ohtake, Y. Yamamoto, In situ Raman and X-ray diffraction studies on the high pressure and temperature stability of methane hydrate up to 55 GPa, *J. Chem. Phys.* 148 (2018) 164503. doi:10.1063/1.5013302.
- [164] A. Desmedt, D. Broseta, L. Ruffine, *Gas Hydrates 1: Fundamentals, Characterization and Modeling*, John Wiley & Sons, 2017.
- [165] A.K. Sum, R.C. Burruss, E.D. Sloan, Measurement of Clathrate Hydrates via Raman Spectroscopy, *J. Phys. Chem. B.* 101 (1997) 7371–7377. doi:10.1021/jp970768e.
- [166] Y.-T. Seo, H. Lee, Structure and Guest Distribution of the Mixed Carbon Dioxide and Nitrogen Hydrates As Revealed by X-ray Diffraction and <sup>13</sup>C NMR Spectroscopy, *J. Phys. Chem. B.* 108 (2004) 530–534. doi:10.1021/jp0351371.
- [167] T. Uchida, S. Takeya, Y. Kamata, R. Ohmura, H. Narita, Spectroscopic Measurements on Binary, Ternary, and Quaternary Mixed-Gas Molecules in Clathrate Structures, *Ind. Eng. Chem. Res.* 46 (2007) 5080–5087. doi:10.1021/ie070153w.
- [168] D.W. Davidson, S.K. Garg, S.R. Gough, R.E. Hawkins, J.A. Ripmeester, Characterization of natural gas hydrates by nuclear magnetic resonance and dielectric relaxation, *Can. J. Chem.* 55 (1977) 3641–3650. doi:10.1139/v77-512.
- [169] J.A. Ripmeester, C.I. Ratcliffe, The Diverse Nature of Dodecahedral Cages in Clathrate Hydrates As Revealed by <sup>129</sup>Xe and <sup>13</sup>C NMR Spectroscopy: CO<sub>2</sub> as a Small-Cage Guest, *Energy Fuels.* 12 (1998) 197–200. doi:10.1021/ef970171y.
- [170] S. Nakano, M. Moritoki, K. Ohgaki, High-Pressure Phase Equilibrium and Raman Microprobe Spectroscopic Studies on the CO<sub>2</sub> Hydrate System, *J. Chem. Eng. Data.* 43 (1998) 807–810. doi:10.1021/je9800555.
- [171] I.L. Moudrakovski, G.E. McLaurin, C.I. Ratcliffe, J.A. Ripmeester, Methane and Carbon Dioxide Hydrate Formation in Water Droplets: Spatially Resolved Measurements from Magnetic Resonance Microimaging, *J. Phys. Chem. B.* 108 (2004) 17591–17595. doi:10.1021/jp0473220.

- [172] S. Subramanian, E.D. Sloan, Microscopic Measurements and Modeling of Hydrate Formation Kinetics, *Ann. N. Y. Acad. Sci.* 912 (2006) 583–592. doi:10.1111/j.1749-6632.2000.tb06813.x.
- [173] S. Gao, W.G. Chapman, W. House, NMR and Viscosity Investigation of Clathrate Hydrate Formation and Dissociation, *Ind. Eng. Chem. Res.* 44 (2005) 7373–7379. doi:10.1021/ie050464b.
- [174] K.C. Hester, T.A. Strobel, E.D. Sloan, C.A. Koh, A. Huq, A.J. Schultz, Molecular Hydrogen Occupancy in Binary THF–H<sub>2</sub> Clathrate Hydrates by High Resolution Neutron Diffraction, *J. Phys. Chem. B.* 110 (2006) 14024–14027. doi:10.1021/jp063164w.
- [175] R. Kumar, P. Englezos, I. Moudrakovski, J.A. Ripmeester, Structure and composition of CO<sub>2</sub>/H<sub>2</sub> and CO<sub>2</sub>/H<sub>2</sub>/C<sub>3</sub>H<sub>8</sub> hydrate in relation to simultaneous CO<sub>2</sub> capture and H<sub>2</sub> production, *AIChE J.* 55 (2009) 1584–1594. doi:10.1002/aic.11844.
- [176] S. Maghsoodloo Babakhani, B. Bouillot, S. Ho-Van, J. Douzet, J.-M. Herri, A review on hydrate composition and capability of thermodynamic modeling to predict hydrate pressure and composition, *Fluid Phase Equilibria.* 472 (2018) 22–38. doi:10.1016/j.fluid.2018.05.007.
- [177] A. Galfré, Captage du dioxyde de carbone par cristallisation de clathrate hydrate en présence de cyclopentane : Etude thermodynamique et cinétique, Ecole des Mines de Saint-Etienne, 2014.
- [178] D. Le Quang, Equilibre des hydrates de gaz en présence d'un mélange d'hydrocarbures gazeux, Ecole des mines de Saint-Etienne, 2013.
- [179] G.D. Holder, G. Corbin, K.D. Papadopoulos, Thermodynamic and Molecular Properties of Gas Hydrates from Mixtures Containing Methane, Argon, and Krypton, *Ind. Eng. Chem. Fundam.* 19 (1980) 282–286. doi:10.1021/i160075a008.
- [180] G.D. Holder, S.P. Zetts, N. Pradhan, Phase Behavior in Systems Containing Clathrate Hydrates: A Review, *Rev. Chem. Eng.* 5 (1988) 1–70. doi:10.1515/REVCE.1988.5.1-4.1.
- [181] S. Adisasmito, D.E. Sloan, Hydrates of Hydrocarbon Gases Containing Carbon Dioxide, *J. Chem. Eng. Data.* 37 (1992) 343–349. doi:DOI: 10.1021/je00007a020.
- [182] B. Tohidi, R.W. Burgass, A. Danesh, A.C. Todd, Measurement and Prediction of Amount and Composition of Equilibrium Phases in Heterogeneous Systems Containing Gas Hydrates, in: Aberdeen, UK, 1993.
- [183] R.M. Barrer, A.V.J. Edge, Gas Hydrates Containing Argon, Krypton and Xenon: Kinetics and Energetics of Formation and Equilibria, *Proc. R. Soc. Math. Phys. Eng. Sci.* 300 (1967) 1–24. doi:10.1098/rspa.1967.0154.

- [184] H.-J. Ng, D.B. Robinson, The prediction of hydrate formation in condensed systems, *AIChE J.* 23 (1977) 477–482. doi:10.1002/aic.690230411.
- [185] E.S. Barkan, D.A. Sheinin, A general technique for the calculation of formation conditions of natural gas hydrates, *Fluid Phase Equilibria.* 86 (1993) 111–136. doi:10.1016/0378-3812(93)87171-V.
- [186] G. Moradi, E. Khosravani, Modeling of hydrate formation conditions for CH<sub>4</sub>, C<sub>2</sub>H<sub>6</sub>, C<sub>3</sub>H<sub>8</sub>, N<sub>2</sub>, CO<sub>2</sub> and their mixtures using the PRSV2 equation of state and obtaining the Kihara potential parameters for these components, *Fluid Phase Equilibria.* 338 (2013) 179–187. doi:10.1016/j.fluid.2012.11.010.
- [187] K.Y. Song, R. Kobayashi, Measurement and interpretation of the water content of a methane-propane mixture in the gaseous state in equilibrium with hydrate, *Ind. Eng. Chem. Fundam.* 21 (1982) 391–395. doi:10.1021/i100008a013.
- [188] M.. Mooijer – van den Heuvel, Phase Behaviour and Structural Aspects of Ternary Clathrate Hydrate Systems The Role of Additives, Technische Universiteit Delft, 2004.
- [189] M.D. Jager, High Pressure Studies of Hydrate Phase Inhibition Using Raman Spectroscopy, Ph.D. Chemical Engineering Thesis, Colorado School of Mines, 2001.
- [190] P.B. Dharmawardhana, W.R. Parrish, E.D. Sloan, Experimental Thermodynamic Parameters for the Prediction of Natural Gas Hydrate Dissociation Conditions, *Ind. Eng. Chem. Fundam.* 19 (1980) 410–414. doi:10.1021/i160076a015.
- [191] P.. Bishnoi, P.D. Dholabhai, Equilibrium conditions for hydrate formation for a ternary mixture of methane, propane and carbon dioxide, and a natural gas mixture in the presence of electrolytes and methanol, *Fluid Phase Equilibria.* 158–160 (1999) 821–827. doi:10.1016/S0378-3812(99)00103-X.
- [192] G.S. Bumrah, R.M. Sharma, Raman spectroscopy – Basic principle, instrumentation and selected applications for the characterization of drugs of abuse, *Egypt. J. Forensic Sci.* 6 (2016) 209–215. doi:10.1016/j.ejfs.2015.06.001.
- [193] E. Smith, G. Dent, Introduction, Basic Theory and Principles, in: *Mod. Raman Spectrosc. – Pract. Approach*, Wiley-Blackwell, 2005: pp. 1–21. doi:10.1002/0470011831.ch1.
- [194] N. Ahlawat, RAMAN SPECTROSCOPY: A REVIEW, (2014) 6.
- [195] J. Kuligowski, B. Lendl, G. Quintás, Chapter 19 - Advanced IR and Raman detectors for identification and quantification, in: S. Fanali, P.R. Haddad, C.F. Poole, M.-L. Riekkola (Eds.), *Liq. Chromatogr. Second Ed.*, Elsevier, 2017: pp. 463–477. doi:10.1016/B978-0-12-805393-5.00019-1.

- [196] N.E. Schlotter, 21 - Raman Spectroscopy, in: G. Allen, J.C. Bevington (Eds.), *Compr. Polym. Sci. Suppl.*, Pergamon, Amsterdam, 1989: pp. 469–497. doi:10.1016/B978-0-08-096701-1.00021-5.
- [197] E.C. Le Ru, P.G. Etchegoin, Chapter 2 - Raman spectroscopy and related optical techniques, in: E.C. Le Ru, P.G. Etchegoin (Eds.), *Princ. Surf.-Enhanc. Raman Spectrosc.*, Elsevier, Amsterdam, 2009: pp. 29–120. doi:10.1016/B978-0-444-52779-0.00008-8.
- [198] S. Subramanian, *Measurements of Clathrate Hydrates Containing Methane and Ethane Using Raman Spectroscopy*, Colorado School of Mines, 2000.
- [199] G. Magnotti, U. Kc, P.L. Varghese, R.S. Barlow, Raman spectra of methane, ethylene, ethane, dimethyl ether, formaldehyde and propane for combustion applications, *J. Quant. Spectrosc. Radiat. Transf.* 163 (2015) 80–101. doi:10.1016/j.jqsrt.2015.04.018.
- [200] J. Martin, Raman intensities of propane in the gas phase, *J. Raman Spectrosc.* 16 (1985) 139–142. doi:10.1002/jrs.1250160302.
- [201] N. Daraboina, J. Ripmeester, V.K. Walker, P. Englezos, Natural Gas Hydrate Formation and Decomposition in the Presence of Kinetic Inhibitors. 3. Structural and Compositional Changes, *Energy Fuels.* 25 (2011) 4398–4404. doi:10.1021/ef200814z.
- [202] G.A. Jeffrey, Hydrate inclusion compounds, *J. Incl. Phenom.* 1 (1984) 211–222. doi:10.1007/BF00656757.
- [203] J.M. Schicks, M. Luzi-Helbing, Cage occupancy and structural changes during hydrate formation from initial stages to resulting hydrate phase, *Spectrochim. Acta. A. Mol. Biomol. Spectrosc.* 115 (2013) 528–536. doi:10.1016/j.saa.2013.06.065.
- [204] F. Fleyfel, J.P. Devlin, Carbon dioxide clathrate hydrate epitaxial growth: spectroscopic evidence for formation of the simple type-II carbon dioxide hydrate, *J. Phys. Chem.* 95 (1991) 3811–3815. doi:10.1021/j100162a068.
- [205] C. Petuya, F. Damay, S. Desplanche, D. Talaga, A. Desmedt, Selective trapping of CO<sub>2</sub> gas and cage occupancy in CO<sub>2</sub>-N<sub>2</sub> and CO<sub>2</sub>-CO mixed gas hydrates, *Chem. Commun.* 54 (2018) 4290–4293. doi:10.1039/C8CC00538A.
- [206] T. Ahmed, CHAPTER 3 - Flash Calculations, in: *Work. Guide Vap.-Liq. Phase Equilibria Calc.*, Gulf Professional Publishing, Boston, 2010: pp. 9–12. doi:10.1016/B978-1-85617-826-6.00003-0.
- [207] E. Soroush, A. Bahadori, Chapter Five - Vapor–Liquid Equilibrium (VLE) Calculations, in: *Fluid Phase Behav. Conv. Unconv. Oil Gas Reserv.*, Gulf Professional Publishing, Boston, 2017: pp. 249–291. doi:10.1016/B978-0-12-803437-8.00005-1.

- [208] P.R. Bishnoi, A.K. Gupta, P. Englezos, N. Kalogerakis, Multiphase equilibrium flash calculations for systems containing gas hydrates, *Fluid Phase Equilibria*. 53 (1989) 97–104. doi:10.1016/0378-3812(89)80076-7.
- [209] W.A. Cole, G. Stephen P., Flash calculations for gas hydrates: A rigorous approach, *Chem. Eng. Sci.* 45 (1990) 569–573. doi:10.1016/0009-2509(90)87001-9.
- [210] M.L. Michelsen, The isothermal flash problem. Part I. Stability, *Fluid Phase Equilibria*. 9 (1982) 1–19. doi:10.1016/0378-3812(82)85001-2.
- [211] M.L. Michelsen, The isothermal flash problem. Part II. Phase-split calculation, *Fluid Phase Equilibria*. 9 (1982) 21–40. doi:10.1016/0378-3812(82)85002-4.
- [212] I.S.V. Segtovich, A.G. Barreto, F.W. Tavares, Simultaneous multiphase flash and stability analysis calculations including hydrates, *Fluid Phase Equilibria*. 413 (2016) 196–208. doi:10.1016/j.fluid.2015.10.030.
- [213] A.K. Gupta, P. Raj Bishnoi, N. Kalogerakis, A method for the simultaneous phase equilibria and stability calculations for multiphase reacting and non-reacting systems, *Fluid Phase Equilibria*. 63 (1991) 65–89. doi:10.1016/0378-3812(91)80021-M.
- [214] A.L. Ballard, E.D. Sloan, The next generation of hydrate prediction: Part III. Gibbs energy minimization formalism, *Fluid Phase Equilibria*. 218 (2004) 15–31. doi:10.1016/j.fluid.2003.08.005.
- [215] H. Tavasoli, F. Feyzi, Compositional data calculation of vapor–aqueous–hydrate systems in batch operations by a new algorithm, *J. Nat. Gas Sci. Eng.* 24 (2015) 473–488. doi:10.1016/j.jngse.2015.04.003.
- [216] J.O. Valderrama, A Generalized Patel-Teja Equation of State for Polar and Nonpolar Fluids and Their Mixtures, *J. Chem. Eng. Jpn.* 23 (1990) 87–91. doi:10.1252/jcej.23.87.
- [217] D. Avlonitis, A. Danesh, A.C. Todd, Prediction of VL and VLL equilibria of mixtures containing petroleum reservoir fluids and methanol with a cubic EoS, *Fluid Phase Equilibria*. 94 (1994) 181–216. doi:10.1016/0378-3812(94)87057-8.



## Scientific production (2015-2018)

### Publications in peer-reviewed journals

- Maghsoodloo Babakhani, S., Bouillot, B., Douzet, J., Ho-Van, S., Herri, J.M., 2018. PVT<sub>x</sub> measurements of mixed clathrate hydrates in batch conditions under different crystallization rates: influence on equilibrium. *Journal of Chemical Thermodynamics*. 122, 73–84.
- Maghsoodloo Babakhani, S., Bouillot, B., Douzet, J., Ho-Van, S., Herri, J.M., 2018. A new approach of studying mixed gas hydrates involving propane at non-equilibrium conditions and final state: An experimental study and modeling. *Journal of Chemical Engineering Science*. 179, 150–160.
- Maghsoodloo Babakhani, S., Bouillot, B., Ho-Van, S., Douzet, J., Herri, J.-M., 2018. A review on hydrate composition and capability of thermodynamic modeling to predict hydrate pressure and composition. *Fluid Phase Equilibria*. 472, 22–38.
- Ho-Van, S., Bouillot, B., Douzet, J., Maghsoodloo Babakhani, S., Herri, J.M., 2018. Experimental measurement and thermodynamic modeling of cyclopentane hydrates with NaCl, KCl, CaCl<sub>2</sub>, or NaCl-KCl present. *AIChE Journal*. 64, 2207-2218.

### International Conferences

- Maghsoodloo Babakhani, S., Ho-Van, S., Bouillot B., Douzet, J., Herri, J.M. Four phase equilibrium conditions of cyclopentane/carbon dioxide binary hydrate in brine solutions: A potential application in water desalination. The 25th international conference on industrial crystallization, Rouen, France. September 2018.
- Maghsoodloo Babakhani, S., Bouillot B., Herri, J.M. A new experimental and modelling study on non-equilibrium crystallization of mixed gas hydrates involving hydrate volume and composition. The 10th World Congress of Chemical Engineering, Barcelona, Spain. October 2017.

- Maghsoodloo Babakhani, S., Bouillot B., Herri, J.M. A new approach of experimental and modelling study of mixed gas hydrates under non-equilibrium conditions. 16ème Congrès de la Société Française de Génie des Procédés, Nancy, France. July 2017.
- Maghsoodloo Babakhani, S., Bouillot B., Herri, J.M. Influence of the crystallization rate on the mixed hydrates: experimental and modelling work. The 9th International Conference on Gas Hydrates, Denver, Colorado USA. June 2017.
- Ho-Van, S., Bouillot B., Douzet, J., Maghsoodloo Babakhani, S., Herri, J.M. Phase Equilibrium Data of Cyclopentane Hydrates in Saline Systems of  $\text{Na}_2\text{SO}_4\text{-H}_2\text{O}$ ,  $\text{MgCl}_2\text{-H}_2\text{O}$ ,  $\text{MgCl}_2\text{-NaCl-H}_2\text{O}$ , and  $\text{MgCl}_2\text{-NaCl-KCl-H}_2\text{O}$ : Experimental and Modelling. The 25th international conference on industrial crystallization, Rouen, France. September 2018.
- Ho-Van, S., Bouillot B., Douzet, J., Maghsoodloo Babakhani, S., Herri, J.M. Morphological Study of Cyclopentane Hydrates in Saline Water for Desalination Application. The 25th international conference on industrial crystallization, Rouen, France. September 2018.

#### **Other publications in in peer-reviewed journals**

- Maghsoodloo Babakhani, S., Alamdari, A., 2015. Effects of maize starch on methane hydrate formation/dissociation rates and stability. *Journal of Natural Gas Science and Engineering*. 26, 1–5.
- Maghsoodloo Babakhani, S., Bahmani, M., Shariati, J., Badr, K., Balouchi, Y., 2015. Comparing the capability of artificial neural network (ANN) and CSMHYD program for predicting of hydrate formation pressure in binary mixtures. *Journal of Petroleum Science and Engineering*. 136, 78–87.

## Appendix A

**Table A. 1. Experimental results of Jhaveri and Robinson [68] for methane-nitrogen mixture hydrates and simulation results (sII).**

T <sub>exp</sub> (K)	P <sub>exp</sub> (MPa)	P <sub>pre</sub> (MPa)	S	Gas composition (exp)		Hydrate composition (exp)		Hydrate composition (pre)	
				N <sub>2</sub>	CH <sub>4</sub>	N <sub>2</sub>	CH <sub>4</sub>	N <sub>2</sub>	CH <sub>4</sub>
273.2	2.640	2.102	II	0.000	1.000	0.000	1.000	0.000	1.000
273.2	3.620	2.457	II	0.160	0.840	0.065	0.935	0.033	0.967
273.2	4.310	2.915	II	0.310	0.690	0.098	0.902	0.074	0.926
273.2	5.350	3.996	II	0.530	0.470	0.200	0.800	0.167	0.833
273.2	6.550	4.946	II	0.645	0.355	0.350	0.650	0.244	0.756
273.2	7.750	5.915	II	0.725	0.275	0.425	0.575	0.319	0.681
273.2	10.640	7.561	II	0.815	0.185	0.620	0.380	0.440	0.560
273.2	11.650	9.322	II	0.880	0.120	0.710	0.290	0.567	0.433
273.2	12.770	10.177	II	0.900	0.100	0.765	0.235	0.617	0.383
277.4	3.860	3.192	II	0.000	1.000	0.000	1.000	0.000	1.000
277.4	5.200	5.358	II	0.440	0.560	0.180	0.820	0.130	0.870
277.4	8.110	7.492	II	0.630	0.370	0.310	0.690	0.245	0.755
277.4	10.340	9.664	II	0.740	0.260	0.470	0.530	0.354	0.646
277.4	12.060	10.778	II	0.780	0.220	0.560	0.440	0.406	0.594
277.4	13.320	17.909	II	0.925	0.075	0.810	0.190	0.708	0.292
277.4	14.590	19.049	II	0.940	0.060	0.860	0.140	0.755	0.245
277.4	16.210	25.914	II	1.000	0.000	1.000	0.000	1.000	0.000
279.8	5.140	4.072	II	0.000	1.000	0.000	1.000	0.000	1.000
279.8	7.140	6.073	II	0.350	0.650	0.091	0.909	0.096	0.904
279.8	8.370	7.143	II	0.460	0.540	0.224	0.776	0.145	0.855
279.8	15.550	13.020	II	0.750	0.250	0.550	0.450	0.379	0.621
279.8	20.670	17.073	II	0.840	0.160	0.680	0.320	0.519	0.481
279.8	25.230	22.469	II	0.914	0.086	0.802	0.198	0.688	0.312
279.8	32.420	33.741	II	1.000	0.000	1.000	0.000	1.000	0.000
<b>AADp</b>		<b>20.70%</b>		<b>AADc</b>				<b>0.080</b>	

**Table A. 2. Experimental results of Kang et al. [143] and simulation (sII).**

T <sub>exp</sub> (K) (±0.1)	P <sub>exp</sub> (MPa) (±0.01)	P <sub>pre</sub> (MPa)	S	Gas composition (exp)		Hydrate composition (exp)		Hydrate composition (pre)	
				CO <sub>2</sub>	N <sub>2</sub>	CO <sub>2</sub>	N <sub>2</sub>	CO <sub>2</sub>	N <sub>2</sub>
274.0	1.36	1.87	II	1.00	0.00	1.00	0.00	1.000	0.000
274.0	1.73	2.32	II	0.82	0.18	0.99	0.02	0.971	0.029
274.0	2.30	3.15	II	0.60	0.40	0.95	0.05	0.915	0.085
274.0	2.77	3.72	II	0.50	0.50	0.93	0.07	0.877	0.123
274.0	3.48	4.60	II	0.40	0.60	0.90	0.10	0.819	0.181
274.0	7.07	7.75	II	0.21	0.79	0.58	0.42	0.617	0.383
274.0	10.95	10.78	II	0.12	0.88	0.34	0.66	0.431	0.569
274.0	14.59	14.26	II	0.05	0.95	0.18	0.82	0.221	0.779
274.0	17.52	17.99	II	0.00	1.00	0.00	1.00	0.000	1.000
277.0	1.91	2.76	II	1.00	0.00	1.00	0.00	1.000	0.000
277.0	2.54	3.29	II	0.85	0.15	0.98	0.02	0.973	0.027
277.0	3.30	5.05	II	0.57	0.43	0.95	0.05	0.888	0.112
277.0	5.12	7.27	II	0.39	0.61	0.89	0.11	0.783	0.217
277.0	11.71	13.07	II	0.18	0.82	0.54	0.46	0.516	0.484
277.0	15.15	15.81	II	0.12	0.88	0.35	0.65	0.394	0.606
277.0	18.74	19.23	II	0.07	0.93	0.19	0.81	0.246	0.754
277.0	23.50	24.72	II	0.00	1.00	0.00	1.00	0.000	1.000
277.0	1.91	2.76	II	1.00	0.00	1.00	0.00	1.000	0.000
277.0	2.54	3.29	II	0.85	0.15	0.98	0.02	0.973	0.027
280.0	2.74	4.28	II	1.00	0.00	1.00	0.00	1.000	0.000
280.0	3.52	5.47	II	0.83	0.17	0.98	0.02	0.959	0.041
280.0	4.14	6.79	II	0.70	0.30	0.96	0.04	0.915	0.085
280.0	4.95	8.30	II	0.59	0.41	0.94	0.06	0.865	0.135
280.0	8.09	12.46	II	0.39	0.61	0.86	0.14	0.726	0.274
280.0	14.64	17.30	II	0.25	0.75	0.64	0.36	0.568	0.432
280.0	20.29	21.08	II	0.17	0.83	0.45	0.55	0.443	0.557
280.0	26.09	26.14	II	0.09	0.91	0.22	0.78	0.274	0.726
280.0	31.58	34.50	II	0.00	1.00	0.00	1.00	0.000	1.000
<b>AADp</b>		<b>29%</b>		<b>AADc</b>				<b>0.04</b>	

**Table A. 3. Experimental results of Belandria et al. [147] for nitrogen-carbon dioxide mixture hydrates and simulation results (sII).**

T (K) (±0.02)	P <sub>exp</sub> (MPa) (±0.002)	P <sub>pre</sub> (MPa)	S	Gas composition (exp)		Hydrate composition (exp) (±1%)		Hydrate composition (pre)	
				CO <sub>2</sub>	N <sub>2</sub>	CO <sub>2</sub>	N <sub>2</sub>	CO <sub>2</sub>	N <sub>2</sub>
273.6	2.03	2,92	II	0.62	0.38	0.97	0.03	0,92	0,08
273.6	8.15	8,30	II	0.17	0.83	0.66	0.34	0,56	0,44
273.6	11.94	8,06	II	0.18	0.82	0.37	0.63	0,58	0,42
273.6	2.96	4,09	II	0.43	0.57	0.90	0.10	0,84	0,16
274.6	2.54	2,82	II	0.73	0.27	0.74	0.26	0,95	0,05
274.9	5.20	2,98	II	0.72	0.28	0.79	0.21	0,95	0,05
275.2	2.29	3,38	II	0.66	0.34	0.90	0.10	0,93	0,07
275.2	2.64	3,04	II	0.73	0.27	0.89	0.11	0,95	0,05
275.2	3.26	4,88	II	0.45	0.55	0.88	0.12	0,84	0,16
275.2	7.45	10,22	II	0.17	0.83	0.82	0.18	0,54	0,46
275.2	8.25	10,13	II	0.18	0.82	0.80	0.20	0,55	0,45
275.2	12.75	10,64	II	0.16	0.84	0.38	0.62	0,52	0,48
275.6	2.71	3,20	II	0.73	0.27	0.76	0.24	0,95	0,05
275.8	5.38	3,34	II	0.72	0.28	0.80	0.20	0,95	0,05
276.1	2.50	3,68	II	0.68	0.32	0.98	0.02	0,93	0,07
276.1	2.87	3,42	II	0.73	0.27	0.79	0.21	0,95	0,05
276.1	3.70	5,13	II	0.49	0.51	0.70	0.30	0,86	0,14
276.1	4.40	6,23	II	0.40	0.60	0.69	0.31	0,80	0,20
276.1	8.58	10,80	II	0.20	0.80	0.57	0.43	0,57	0,43
276.7	3.70	5,61	II	0.49	0.51	0.70	0.30	0,85	0,15
277.1	2.71	4,09	II	0.71	0.30	0.84	0.16	0,94	0,06
277.3	3.13	4,05	II	0.73	0.27	0.83	0.17	0,94	0,06
277.8	6.16	4,26	II	0.75	0.25	0.86	0.14	0,95	0,05
278.1	2.97	4,59	II	0.73	0.27	0.89	0.11	0,94	0,06
278.1	3.41	4,46	II	0.73	0.27	0.75	0.25	0,94	0,06
278.1	4.19	6,59	II	0.52	0.48	0.66	0.35	0,86	0,14
278.1	9.15	13,30	I	0.23	0.77	0.54	0.46	0,58	0,42
278.1	14.26	18,09	II	0.13	0.87	0.51	0.49	0,39	0,61
279.7	4.82	8,31	II	0.56	0.44	0.70	0.30	0,85	0,15
279.7	10.02	15,93	II	0.26	0.74	0.61	0.39	0,59	0,41
279.7	15.82	21,43	II	0.15	0.85	0.55	0.45	0,41	0,59

281.2	17.63	25,03	I	0.18	0.82	0.58	0.42	0,43	0,57
281.7	6.33	10,94	II	0.75	0.25	0.81	0.19	0,88	0,12
<b>AADp</b>		<b>38.1%</b>	<b>AADc</b>				<b>0.13</b>		

**Table A. 4. Experimental results from Herri et al. [113] and simulation results (sII) for carbon dioxide-nitrogen mixture**

T (K) (±0.1)	P <sub>exp</sub> (MPa) (±0.01)	P <sub>pre</sub> (MPa)	S	Gas composition (exp) (±0.001)		Hydrate composition (exp) (±0.003)		Hydrate composition (pre)	
				CO <sub>2</sub>	N <sub>2</sub>	CO <sub>2</sub>	N <sub>2</sub>	CO <sub>2</sub>	N <sub>2</sub>
273.4	6.10	8.50	II	0.16	0.84	0.66	0.34	0.54	0.46
274.5	6.20	9.60	II	0.16	0.84	0.66	0.34	0.53	0.47
275.4	6.40	10.03	II	0.19	0.82	0.66	0.34	0.56	0.44
276.5	6.60	11.30	II	0.20	0.80	0.58	0.42	0.57	0.43
273.9	5.90	6.61	II	0.25	0.75	0.75	0.25	0.69	0.31
274.7	5.90	7.30	II	0.26	0.75	0.73	0.27	0.68	0.32
276.0	5.90	8.66	II	0.26	0.74	0.70	0.30	0.67	0.33
276.9	6.00	9.89	II	0.27	0.74	0.70	0.30	0.66	0.34
277.8	6.30	10.65	II	0.29	0.71	0.67	0.33	0.67	0.33
278.1	6.40	11.04	II	0.30	0.71	0.69	0.31	0.67	0.33
278.4	6.40	11.68	II	0.30	0.71	0.72	0.29	0.66	0.34
278.6	6.50	11.91	II	0.30	0.70	0.70	0.31	0.67	0.33
275.4	6.10	9.54	II	0.20	0.80	0.67	0.33	0.59	0.41
276.0	6.20	9.89	II	0.22	0.78	0.65	0.35	0.61	0.39
280.1	5.30	9.04	II	0.56	0.44	0.85	0.16	0.84	0.16
281.1	5.60	11.15	II	0.59	0.42	0.82	0.18	0.83	0.17
<b>AADp</b>		<b>60.1%</b>	<b>AADc</b>				<b>0.05</b>		

**Table A. 5. Carbon dioxide-methane and carbon dioxide-nitrogen hydrate mixtures, experimental data [121] and simulation results**

T (°C) (±0.1)	P <sub>exp</sub> (MPa) (±0.01)	P <sub>pre</sub> (MPa)	S	Gas composition (exp) (±0.001)		Hydrate composition (exp) (±0.003)		Hydrate composition (pre)		
				N <sub>2</sub>	CO <sub>2</sub>	N <sub>2</sub>	CO <sub>2</sub>	N <sub>2</sub>	CO <sub>2</sub>	
2.3	2.46	3,44	II	0.33	0.67	0.06	0.94	0,07	0,93	
3.1	2.60	3,71	II	0.31	0.69	0.07	0.93	0,06	0,94	
3.3	2.66	3,76	II	0.30	0.70	0.07	0.93	0,06	0,94	
4.3	2.87	4,19	II	0.28	0.72	0.09	0.91	0,06	0,94	
5.2	3.13	4,65	II	0.25	0.75	0.12	0.88	0,06	0,94	
<b>AADp</b>		<b>43.7%</b>	<b>AADc</b>				<b>0.03</b>			